New Challenge of Integrating an Accident Research System with the Medical and Engineering Network in Japan

Susumu Ejima
Shinichi Takayama
Koji Mikami
Koshiro Ono
Japan Automobile Research Institute
Japan
Kunihiro Mashiko, Yuuichi Motomura
Nippon Medical Hospital Chiba Hokuso Hospital
Japan
Hideyuki Ohashi
Institute for Traffic Accident Research and Data Analysis
Japan
Paper Number 11-0129

ABSTRACT

This study introduces the accident research system integrated with the medical and engineering network in Japan. Based on the collaborative study by Japan Automobile Research Institute (JARI), Nippon Medical School Chiba Hokuso Hospital and ITARDA (Institute for Traffic Accident Research and Data Analysis), detailed accident data have been collected, and crash, vehicle damage, and injury data were analyzed. This system provides us with the "mechanism" of injury by employing in-depth accident investigation with physical evidence, biomechanical knowledge, and medical knowledge for depicting the injury causation scenario. Moreover, vehicle safety improvement is not the only essential concern for the reduction of road accident casualties and injuries; immediate medical care, such as emergency medical treatment during road accidents, is also necessary. Therefore, the information of emergency medical activities in the post-crash was also collected in this system. This paper introduces the prototype research of the integrated pertinent medical and engineering information and proposes an effective injury-reduction system in actual traffic accidents. The case examples are provided to demonstrate the ability of this system to improve crash /injury assessment. In addition, the accident reconstruction simulation supplements this function of this accident analysis system.

INTRODUCTION

Accident investigation provides the crash information with regard to the vehicle type, the crash configuration, the restraint system, the involvement and the resulting injuries. These data are important to depict the accident scenario and utilize it for reducing the causality in road traffic crashes. ITARDA has been collecting accident data to update its databases of vehicle crashes with varying amounts of data in Japan. The traffic accident-related data derived from the police accident reports links to establishing accident database. In order to obtain detailed information of traffic accidents, ITARDA [1] conducts the in-depth accident investigation in the local area (Tsukuba) and collects the crash information respect to the crash environment, vehicle, occupants, and injury. These data provide the detailed crash environments and vehicle damage; however, the data collection system has a limited amount of data on occupant injury outcome. In the U.S., the hospital-based accident research system called CIREN (Crash Injury Research Engineering Network) [2] was set up, and this program has been working for over twelve years. CIREN center has integrated the detailed accident information such as vehicle, occupant, and injury information, and it has used a methodology known as "Bio Tab" [3] to analyze and document the cause of injuries resulted from passenger vehicle crashes.

In the discussion of automobile crash safety, it is considered that the occupant injury depends on the crash configurations, age, gender, and physiques; thus, it is essential to examine the injury mechanisms from a medical perspective by employing medical information. Moreover, when we consider the traffic safety, it is important to figure out the relationship between the accident and the injury of the occupant who has individual characteristics. Therefore, it is necessary to study the following key points to reduce the casualty from motor vehicle crashes.

1. The impact relating to the injury outcome
2. The physiological change caused by the injury
3. Injury pattern based on the human body structure

To start discussing these points, the accident reconstruction based on the accident investigation

and the analysis of the difference of the occupant individuality should be considered. The connection between the crash condition and injury was investigated with the medical image data taken by the CT/X-ray or MRI by emergency medical doctor. **Figure 1** illustrates the injury-reduction methodology for reducing the casualty. The data-collection system includes not only the accident data but also the detailed medical records. First, a detailed accident case study is performed to estimate the injury pattern and the kinematics of the person involved in the accident. These investigation are linked to detailed medical records of the human injuries, in which emergency medical care progress, radiological image, and treatment are included. Reviews of cases are conducted to examine the causation of human injuries based on the physical evidences. In addition, a digital human model is utilized to reconstruct the injury outcome based on the accident data to understand more about the injury mechanisms of the persons involved. In this process, results from the simulation are validated against the accident data to ensure consistency.

In Japan, automobile crash safety engineering has focused on the development and improvement of safer vehicles so far. However, since the upgrading of emergency medical care during the post-crash time is essential for the reduction of road accident casualties and injuries, it is also important to integrate pertinent medical and engineering information. But this kind of research has not been done in Japan. This paper introduces the pilot study of the medical and engineering network system by employing a concrete traffic accident example. If an integrated accident crash research system with the medical and engineering networks is established, it is possible to pursue injury causation mechanisms in order to further upgrade automobile safety in Japan.

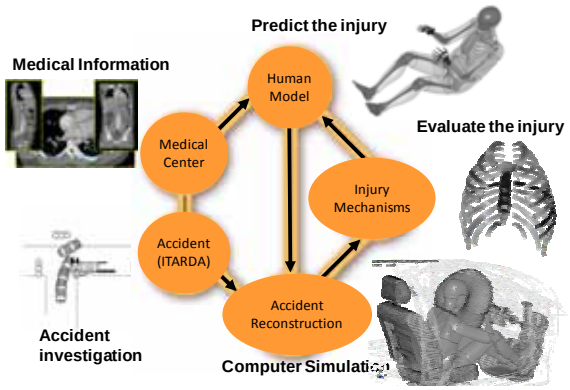

Figure 1. Medicine and Engineering Networking

METHOD

Integrating an Accident Research System

The new challenge of integrating an accident research program started to collect the detailed crash, vehicle, occupant, and injury information, most of which sustained at least one serious or more severe injuries (AIS3+). In general, in the selection of case occupant, ITARDA selects on the basis of a severe injury of the crashed vehicle occupant. In-depth investigations of the case occupant's vehicle and crash scene are investigated via ITARDA protocol. Detailed accident case study is performed to estimate the injury pattern and the kinematics of the person involved in the accident. The accident data are linked to detailed medical records of the case occupant's injuries. These records include emergency medical care, radiological image, clinical progress, treatment, and discharge reports. The multidisciplinary review and discussion of each case are conducted by an experienced ITARDA accident investigator, a biomechanical engineer with experience in impact biomechanics research, and a trauma physician to derive the causation of the injuries based on the physical evidences, medical knowledge and injury biomechanics from the engineering point of view. In addition, a digital computer model is utilized to reconstruct the vehicle motion and injury outcome based on the accident data to understand more about the injury mechanisms of the persons involved. These reviews reconfirm the crash severity and injury assessment in the real accident.

Multidisciplinary Review of the Accident Case

In-depth injury investigation based on the engineering and medical information – The foci of this integration of accident research system are on the identification and documentation of injury causation, and this system can define all the factors that have been believed necessary for the occurrence and/or severity of injury. Compared to the traditional accident data collection, the integrated data includes medical image data such as CT/X-ray and MRI, which indicate the location of the bone fracture or the tissue damage constituting the injury. In addition, the image data provide the effective information for predicting the injury pattern related to the particular type of loading or mechanical response that can estimate the strength of the bone with BMD (Bone Mineral Density). In this system, the accident investigator, the trauma physician, and the biomechanical engineer collaborate to discuss and examine the injury causation considering the source of energy, direction, and physical components involved.

Accident Reconstruction with Computer Simulation - In-depth accident investigation provides the injury causation scenario that can estimate the physical motion of the occupant under the crash condition. However, it is difficult to

confirm the actual occupant condition in the complex accident case. Therefore, the occupant kinematic caused by crash condition is predicted via computer simulation (combination of multi-body model and finite element model) [4]. This approach consists of two phases as shown in **Figure 2**. First, the vehicle motion at the accident scene is estimated from the multi-body vehicle model by using CARS3D [5] [6]. Second, the crash pulse calculated from the multi-body vehicle model is directly applied to the interior compartment of the finite element vehicle model, to which the human model is installed [7]. The advantage of this approach is to estimate the crash pulse and the vehicle motion from the multi-body model with simple geometry. On the other hand, the vehicle deformation under the external load is not calculated in the interior compartment of the finite element vehicle model. Therefore, this approach has a limitation when the target case occupant vehicle has a large deformation in the vehicle interior. The vehicle interior model consists of a standard three-point belt system, an airbag, a steering wheel, an instrumental panel, and a toe pan. The mechanical property of each component is validated with the experimental study. In this computer simulation, the occupant kinematic is simulated to complement the scenario derived from the in-depth accident investigation of the crash condition.

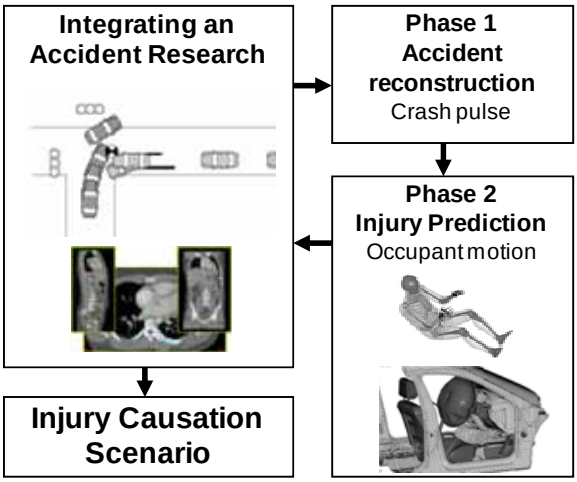

Figure 2. Injury prediction approach based on the actual car crash accident

Emergency medical information – When the occupants are injured in their vehicles in the traffic accident, the first priority is to ensure that they can receive the best medical treatment as quickly as possible. For the purpose of analyzing the injury severity based on the physiological information, the integration of accident research system collects the emergency medical activities. To understand the emergency medical activities just after the accident, Pre-hospital Record and Evaluation Sheet is utilized. This sheet is organized by the department of emergency and rescue, and the detailed medical information of the injured is recoded on it. This sheet covers such items as a large variety of emergency process, the injury condition, activity (transportation time history), vital signs, initial evaluation, emergency medical care, medical decision, and trauma score.

On-site accident picture - For the purpose of medication, Nippon Medical School Chiba Hokuso Hospital has been taking the photographs at the accident scene with the support of the emergency medical service. The picture mainly focuses on the vehicle damage and the occupant condition. The photograph taken at the accident site is immediately transferred to the medical hospital via mobile phone. Based on this photograph, medical doctor evaluates the injury and prepare for the treatment in advanced.

RESULTS OF THE APPLICATION OF THE INTEGRATED SYSTEM

Collected Accident Case

Based on the collaborative study by JARI, Nippon Medical School Chiba Hokuso Hospital, and ITARDA, 18 accident cases were collected and particularly 8 of them were investigated with the medical and engineering network system. The accident types in this study were vehicle-to-vehicle, single-vehicle, and vehicle-to-pedestrian. **Table 1** shows the brief summary of each accident case and the collected items in the system are as follows.

Table 1 Summary of accident case

No.	Crash configration	Vehicle	Age	Gender	Position	Injury severity
1	Frontal	A1	23	M	Driver	Serious
		B1	62	M	Driver	Slight
2	Frontal	A2	73	M	Passenger	Serious
		A1	20	M	Driver	Slight
		B1	50	M	Driver	Slight
3	While working on road	A1	37	F	Driver	Non
		B1	92	M	Seniorcar	Fatal
4	Crossing collision	A1	31	F	Driver	Slight
		B1	30	M	Driver	Non
5	Others	B1	1	M	Pedestrian	Serious
6	Rear	A1	26	M	Driver	Fatal
7	Crossing collision	A1	20	M	Driver	Slight
		B1	55	M	Driver	Slight
8	Single-vheicle	A1	22	M	Driver	Serious

The list of the items

1. Crash and medical summary
2. Accident site information
   - Environment: roadway, traffic, and weather
   - Type: collision angle, speed, and CDC
3. Accident car information
   -Vehicle: make/model/year, size, weight
   - Analysis result: delta V, EBS
4. Detailed medical records
   - Emergency medical process
   - Radiological image and report
   - Clinical process
   - Discharge report

Example of Injury Causation Analysis Using Integrating an Accident Research

Case Review 1 - This case involves a 23-year-old unbelted male driver involved head-on collision in a small car as shown in **Figure 3** (green vehicle). He failed to negotiate the left turn and collided with the oncoming car, when his small vehicle was approaching a gentle curve to the left at a high speed. The delta V was 70 km/h and the vehicle damage (CDC code = 12FZEW5), which is shown in **Figure 4**, was to the front and major, there was intrusion of the vehicle interior components into the driver space, and the steering-wheel airbag was not installed in this vehicle. As shown by the CT scan of **Figure 5**, the driver sustained fracture of the pelvis and femur. These fractures are classified as an AIS 2 injury for pelvis and AIS 3 for femur. The chest also contacted with the steering and got a bruise and the bilateral lung contusion (AIS 3) in this case occupant. The injury causation scenario for this injury is as follows:

The narrow offset frontal impact caused both the deceleration and the rotation of the vehicle, which caused the driver to move right forward relative to the vehicle interior. With no airbag deployment and relatively little space between the driver's lower extremity and the instrumental panel, the driver's knee contacted with the lower panel. There was physical evidence of the lower extremity contact on the instrumental panel as shown in the picture (blue arrow), oblique pattern noted on the driver's right femur X-ray (red arrow), consistent with the compressing load. The contact generated compression of femur and, coupled with a resulting bending load of the femur head, caused the femur head and pelvis fractures observed in the pelvis 3D-CT image (red arrow). Because of the intrusion of the vehicle interior components, the bilateral lung contusion was caused by the steering assembly.

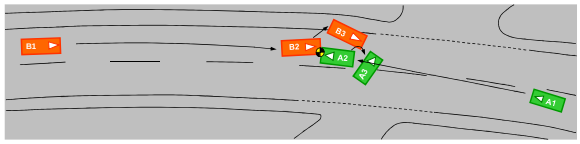

Figure 3. Case Review 1: Accident scenario with head-on collision

Figure 4. Case vehicle damage (head-on collision)

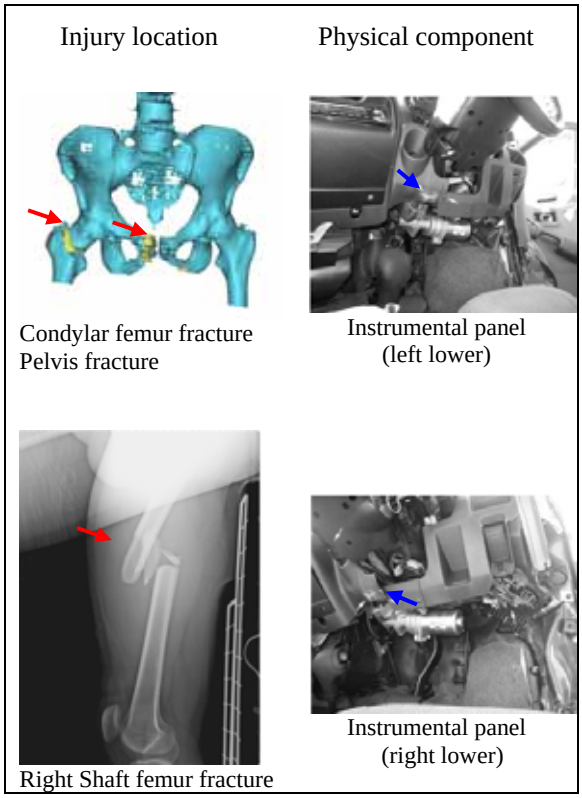

Figure 5. Occupant injury based on the physical evidence (Case Review 1)

Injury causation scenario was reconstructed by means of computer simulation. As previously described, the interior compartment of the finite element vehicle model did not calculate the large deformation of the interior compartment of the case occupant vehicle. Therefore, only the initial stage of the occupant kinematic motion was calculated in this accident reconstruction to complement the accident scenario. In this sense, the simulation approach of this prototype study has a limitation in reconstructing the exact accident situation. **Figure 6** shows the

crash behavior of the head-on collision with a rigid body model. First, the vehicle model whose size and weight were adjusted based on the specification and the boundary condition analyzed by the accident investigation was applied to both the vehicle models. This result shows that the final stop position of the target vehicle (blue vehicle) was close to the position which was investigated at the accident scene (**Figure 3**: A3 - green vehicle). If the curbstone is not taken into consideration, the opposite vehicle (white vehicle) stop position was different from the actual accident vehicle (**Figure 3**: B3 - orange vehicle). Next, the crash pulse was extracted from the vehicle, and this information was input into the interior car compartment to predict the occupant motion and injury mechanisms. **Figure 7** indicates the sequential image of predicted occupant motion at the initial stage (0 -100ms) after the impact by using the finite element human model. Because the driver was unbelted, the occupant hit his knee at the instrumental panel, and the impact load was transferred to the pelvis through the knee and femur. Because the chest contacted to the steering just after the knee contacted to the instrumental panel, the chest was fairly compressed. The occupant's torso restrained to the steering, and the head moved forward relative to the torso. As a result of this phenomenon, there is a possibility that the face contacted to the steering assembly or the windshield.

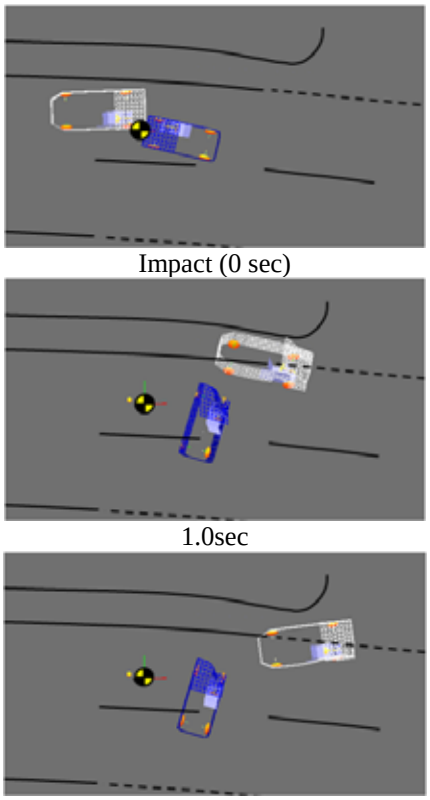

Figure 6. Accident reconstruction simulation with rigid-body model (CARS3D)

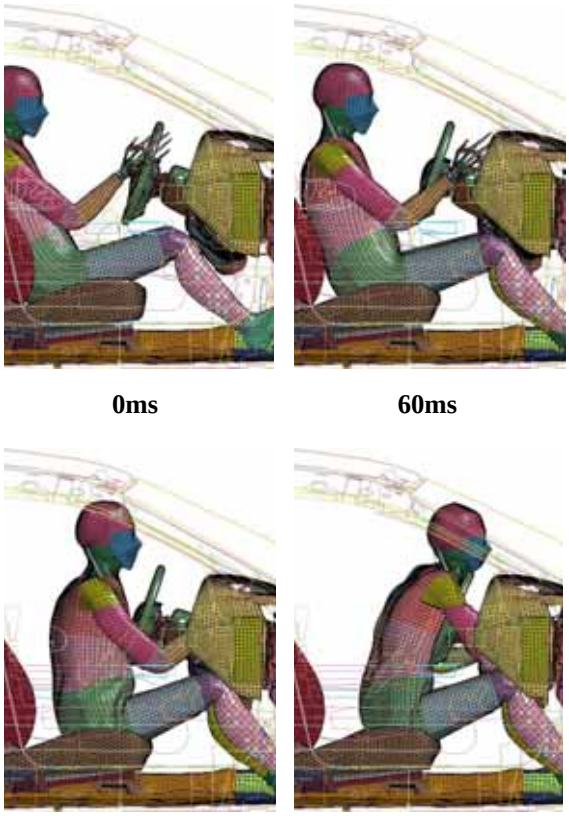

Figure 7. Prediction of the occupant motion by using finite element human model

Case Review 2 - In this crash, a 22-year-old male fell asleep at his wheel, and the vehicle diverged from the roadway, and the right front struck against a telephone pole as shown in **Figure 8**. The vehicle damage (CDC code = 01FRW4) shown in **Figure 9** was severe, and the delta V was calculated at 30 km/h. The lower extremity was caught between the seat and the intruded instrumental panel, and the occupant was pulled out alive from the damaged compartment by the rescue team. The case occupant sustained right medial malleolus tibia fracture and shaft fibula fracture as shown in the X-ray image of **Figure 10**. The injury causation scenario for these fracture are described as follow.

For the right fibula, intrusion of instrumental panel is a contributing factor of bending the long bone. The fracture pattern of fibula in **Figure 10** also explains the effect of bending from the X-ray image. For the right tibia, the telephone pole intruded inside the interior compartment and tope-pan was damaged because of the impact intrusion. This phenomenon is a critical factor of breaking the local region of the bone in the injury causation scenario.

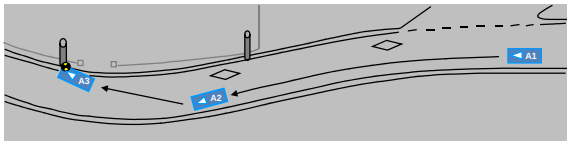

Figure 8. Case Review 2: Accident scenario with single-vehicle

Figure 9. Case vehicle damage (single-vehicle)

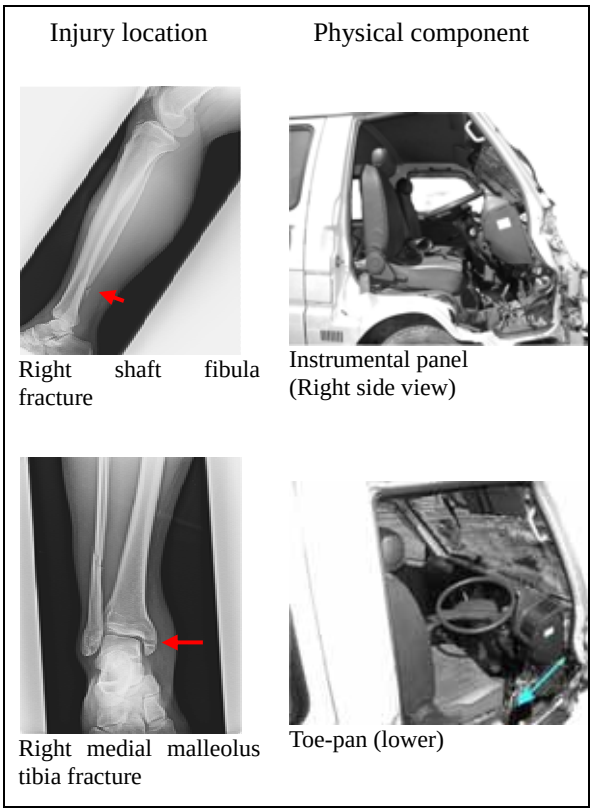

Figure 10. Occupant injury based on the physical evidence (Case Review 2)

In this case occupant, emergency medical summary was recorded. The occupant made an emergency call from his mobile phone after the accident, and it took 18 minutes to contact with EMS (Emergency Medical Service). Because of the rescue operation, it took extra 35 minutes to move the injured to the ambulance at the accident site. During the rescue operation, EMS took the on-site information (photograph) and transferred it to the medical center for the purpose of the injury evaluation by the trauma physician. On-site information shows that the telephone pole intruded in the driver side of the front bumper in the case occupant vehicle. This specific physical evidence is the valuable information for predicting the injury. After the rescue operation, the injured was brought to the ambulance, and the initial evaluation of each body region, which could not easily be done in the damaged vehicle, was conducted by emergency services. In this case, the right lower extremity recognized the tenderness, contusion, and bloating at the right leg region and malleolus medialis. EMS suspected the compartment syndrome with his leg at the accident site. Therefore, the emergency medical care center was selected to transfer the injured. **Table 2** shows the time history of the vital-sign from the accident site to the hospital.

Table 2. Time history of the occupant condition

			Transportaion					Hospital
Vital Signs	Time Period [min]		0	27	52	55	61	67
	JCS		I	Lucidity	Lucidity	Lucidity	Lucidity	0
	GCS	E	4					4
		V	5					5
		S	6					6
	Respiration [times/min]		Fast	24	24	24	24	22
	Beat [times/min.]		Normal		82	82	84	100
	BP	upper [mmHg]			137	136	158	170
		lower [mmHg]			79	94	82	120
	SpO_2	Oxygen[ℓ]		10	10	10	10	
		SpO_2 [%]			100	100	100	100

DISCUSSION

New integration of accident research system with medical and engineering network is applied to the real accident case to determine and document injury causation and injury mechanisms. Although the accident reconstruction simulation has a limitation, the detailed medical information with the computer simulation complement the injury causation scenario estimated from in-depth accident investigations and injury data.

In-depth accident analysis with medical and engineering network

The two cases described in this paper show the advantage of the integration of accident research system compared to the traditional approach of recording injury causation and mechanisms. These examples demonstrate how this system associates injuries with a particular crash event by using the physical evidence and medical image data to establish the injury causation scenario. In this process, injury causation was explained based both on the involved physical component inspected by the experienced and trained ITARDA accident investigator from the accident vehicle and on the medical information diagnosed by the emergency

medical doctor and the biomechanical engineer with experience in impact biomechanics research. In Case Review 1, there existed clear evidence of knee contact to the lower instrumental panel, and the typical lower extremity injury mechanism was explained with the medical image data. Moreover, in order to complement the injury causation scenario and the mechanism established in the accident investigation, the accident reconstruction simulation was demonstrated. This simulation was conducted as a preliminary computational study of the accident reconstruction under the limitation. The result of occupant behaviors complemented the scenario which was estimated in the discussion with the medical and engineering network. In Case Review 2, this integration of accident research system identified intrusion that are critical to the occupant injury in this case, and one-site picture contributed to providing the effective information to the medical doctor for preparation.

Probability of severity score

In general the survival possibility of a person involved in an accident can be evaluated by the "Golden Hour Principle" [8]. This phrase means the time period within which the casualty should be brought to the hospital following an accident. During this time period, the casualty has the best chance to avoid significant deterioration of his/her conditions.

By using Case Review 2, the Probability of severity score (Ps) [9], which is commonly employed for the evaluation of survival in the area of emergency medical care, is calculated. In this case occupants, it took 35 minutes to bring the injured to the ambulance at the accident site, because the vehicle occupants were trapped in their vehicles, and the rescue team was called for right after EMS arrived. Ps is calculated by the TRISS (Trauma and Injury Severity Score) [10] based on the physiological factor (RTS: Revised trauma score), anatomical damage score, (ISS: Injury Severity Score) and Age. Ps is utilized as the objective assessment index when the judgment of the preventable trauma death is made. RTS consists of GCS (Glasgow Coma Scale), SBP (Systolic Blood Pressure), and RR (Respiration Rate). Therefore, it should change from the accident site to the hospital. **Figure 11** indicates the Ps respect to the RTS. The Case Review 2 occupant has a relatively large Ps value, which increases during the transportation from the accident site to the hospital by the medication. Ps evaluates the physiological index of the case occupant, and this logic is effective information when the severity of injury at the accident site is discussed.

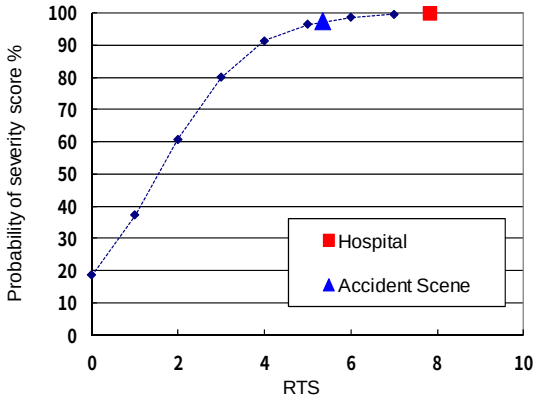

Figure 11. The case occupant Ps calculated from the TRISS method.

Limitation of this study and suggestion for further research

In the accident reconstruction simulation, the approach applied did not calculate the intrusion of the vehicle interior components. Therefore, the accuracy of the quantitative evaluation such as the dynamic loading condition to the lower extremity and the stain distribution in the long bone during the impact was not enough to predict the injury in the Case Review 1. The large deformation of vehicle interior should be the critical factor in estimating the injury in the accident. In the next phase of this research, the multi-body vehicle model should enhance the accuracy of the estimation of the intrusion during the accident, and these information should be applied to the interior compartment of the finite element vehicle model for more accurate injury prediction.

CONCLUSION

This data-collection system provides not only the detailed crash environments but also the causation of injuries in automobile crashes. Even though the intrusion of the vehicle is not calculated in the simulation, the digital human model helps to provide the possible occupant motion under the impact in the real traffic accident. Moreover, the emergency medical care process and the damaged vehicle photograph recorded by EMS (Emergency Medical Service) at the accident site provide effective information in predicting the situation and degree of human injury. In particular, the survival possibility of a person involved in an accident can be evaluated by employing the biological information reported at the instant of the emergency.

The research of this system has just started, and the number of the accident cases is limited. Therefore, accident data should be continually corrected and updated in order to understand the injury and reflect the result for the improvement of vehicle safety and emergency post-crash medical care. In addition, this

medical and engineering network was attempted for the first time in Japan, and the digital human model has a possibility to be an effective tool for predicting the degree and situation of occupant's injury.

ACKNOWLEGEMENT

We would like to express our appreciation to Toyota Motor Corporation, for funding the in-depth accident analysis with the medical and engineering network.

REFERENCES

[1] Accident Analysis Report (JAPAN) Institute for Traffic Accident Research and Data Analysis (ITARDA) 2005

[2] http://www.nhtsa.gov/CIREN

[3] Ridella, A.S., Scarboro, M.J., Rupp, D.J. and Schneider, W.L., "BioTab - An Improving Methodology for Injury Causation Analysis and Coding in CIREN." ESAR 2010 - Paper No.12 2010.

[4] Mikami, K., Antona, J. and Ejima, S. "Injury Prediction Method Using Mathematical Analysis." 2010 JSAE Annual Congress (Autumn), Proceeding No. 127-10. #203-20105193, Transaction of Society of Automotive Engineers of Japan

[5] Yamazaki, K., "Development of Rigid-Body Simulation Program for Car-Accident Analysis." Vol. 24 No. 11 JARI Research Journal (2002)

[6] Yamazaki, K., "Development of Simulation Program for Car-Accident Analysis on Rigid Body Dynamics." Vol. 25 No. 4 JARI Research Journal (2003)

[7] Zama, Y., Antona, M.J., Mikami, K., Ejima, S., Kamiji, K. and Yasuki, T., "Development of Finite Element Human Model for Assessment of Injuries in Front Impact." 2010 JSAE Annual Congress (Spring), No. 41-10 #203-20105193, Transaction of Society of Automotive Engineers of Japan

[8] Champion, H.R, Augenstein, JS, Blatt, A.J, Cushing B, Digges KH, Flanigan M.C, Hunt R.C, Lombardo L.V, Siegel J.H, "New Tools to Reduce Deaths and Disabilities by Improving Emergency Care: URGENCY Reducing Highway Deaths and Disabilities with Automatic Wireless Transmission of Serious Injury Probability Ratings from Vehicles in Crashes to EMS," Proceedings of the 19th International Technical Conference on the Enhanced Safety of Vehicles, May 19-22, 2005

[9] Boyd, C.R., Tolson, M.A. and Copes, W.S., Evaluating trauma care : The TRISS method Trauma Score and Injury Severity Score. Journal of Trauma Vol. 27, No. 4, pp. 370-378 (1987)

[10] Champion H.R., Sacco W.J., Gann D.S., Gennarelli T.A. and Flanagan M.E., A Revision of the Trauma Score, Journal of Trauma Vol. 29, No. 4, pp. 623-629 (1989)

HOW RELIABLE ARE INJURY RISK CURVES?

Norbert Praxl
PDB – Partnership for Dummy Technology and Biomechanics
Germany
Paper Number 11-0089

ABSTRACT

Injury risk curves are the basis for assessing automotive occupant safety. They are used in regulation, consumer test ratings, safety system design, and for the evaluation of the effectiveness of safety systems. Therefore, an injury risk curve should be accurate and credible. But how reliable is the risk prediction of an injury risk curve?

The objective of this study was to identify and illustrate factors influencing the reliability of injury risk curves. Thereby, highlight the need for a more thoughtful construction and use of injury risk curves as well as the need for additional statistical measures when publishing injury risk curves. The results of this study will lead to a better understanding of injury risk curves and can also be used for a better design of experiments in biomechanical testing.

Four factors affecting the reliability of injury risk predictions were evaluated exemplarily in this study:

- The sampling, i.e. the uncertainty due to statistical inference from a sample on the population.
- The censoring of data, i.e. the uncertainty introduced by the imprecision of the tolerance limit determination.
- The test severities, i.e. the uncertainty in injury risk prediction as a result of test severities used in the biomechanical tests.
- The statistical model, i.e. the bias introduced by the method used to calculate the injury risk curve.

Although all of the findings presented can be explained by statistical theory, this paper demonstrates the effects of different factors on the reliability of injury risk curves in a visual manner. Statistical simulation is used to replicate biomechanical testing and injury risk curve construction.

The statistical simulations comprise several steps including the definition of a distribution of the biomechanical tolerance limit in the population, the sampling and biomechanical testing of specimens as well as the construction of the injury risk curve.

The statistical simulations clearly illustrate the effect of the sample size and data censoring on the uncertainty of injury risk curves. It can be concluded that the interpretation of an injury risk curve without a proper measure of confidence is meaningless. Exact data of the biomechanical tolerance limit improve the reliability of the injury risk curve – however only with the use of an appropriate statistical method.

The range of criterion values used in the injury risk curve construction systematically affects the shape and reliability of the curve. Biomechanical tests should be done over a wide range of test severities in order to avoid bias in the risk estimation.

It is demonstrated that the use of an unsuitable - nevertheless widely used - statistical method for constructing the injury risk curve can lead to unrealistic injury risk predictions.

INTRODUCTION

Injury risk curves are used for the safety assessment of passenger cars regulated by law, for occupant safety ratings in consumer tests, for the design of safety systems, and for evaluating the effectiveness of safety systems. Injury risk curves are the basis for assessing, improving, and evaluating automotive occupant safety. The prediction of the injury risk by an injury risk curve plays an essential role in vehicle safety. Thus the risk prediction needs to be reliable.

But how reliable is the risk prediction of an injury risk curve?

Before looking at the reliability of injury risk curves, it should be clear what an injury risk curve is and how it relates to the biomechanical tolerance limit.

Biomechanical Tolerance Limit

The maximum mechanical load a person can withstand without getting injured is called the biomechanical tolerance limit of this person. Different persons – most likely – have different biomechanical tolerance limits. The biomechanical tolerance limit varies within the population.

The distribution of the varying biomechanical tolerance limit can be expressed by a probability density function (PDF), an example of a possible PDF is shown in figure 1. The real probability density function of the biomechanical tolerance limit of a population is unknown and generally can't be determined. The PDF or distribution can only be estimated statistically by using a random sample from the population of interest (if the sample isn't random, all conclusions will be highly biased!).

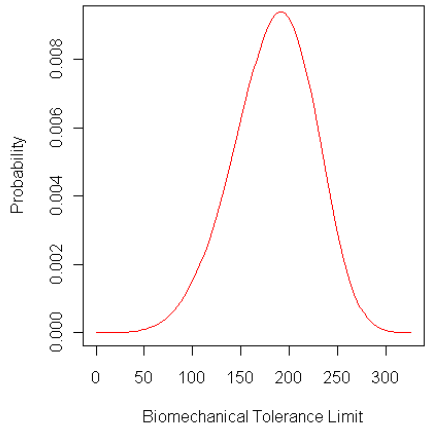

Figure 1. A possible probability density function (PDF) of the biomechanical tolerance limit of a population.

Injury Risk Curve

For an arbitrary person of a population of interest the injury risk curve shows the probability of getting injured at a specific mechanical load level. The mechanical load is expressed by an injury criterion value. This can be a physical measure like force or acceleration or more complex quantities like HIC or NIC. Figure 2 shows a possible injury risk curve.

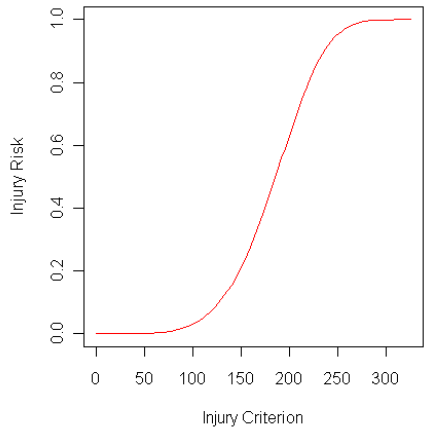

Figure 2. A possible injury risk curve or cumulative distribution function (CDF) of the biomechanical tolerance limit.

An injury risk curve displays the percentage of the population having a biomechanical tolerance limit lower than the associated criterion value. In the example used in this study (figure 2) 20% of the population have a biomechanical tolerance limit (expressed as an injury criterion value) lower than 150.

An injury risk curve is the cumulative distribution function (CDF) belonging to the distribution of the biomechanical tolerance limit. Consequently the distribution of the tolerance limit and the injury risk curve contains the same information. However, the presentation of this information is different.

Like the PDF of the biomechanical tolerance limit the injury risk curve of a population is not known and can only be estimated by statistical inference, i.e. inference from a sample on the population. The distribution of the biomechanical tolerance limit within the sample is the best estimate of the distribution of the biomechanical tolerance limit in the population and the best predictor for the injury risk of an arbitrary person of the population.

The injury risk curve is calculated on the basis of the biomechanical tolerance limits found in biomechanical tests mostly done on cadavers. The cadavers are the sample for the population of interest.

Since every injury risk curve is a statistical estimate, the question about the reliability of this estimate is obvious.

Objective

The development of an injury risk curve is a statistical procedure. Some of the problems and the complexity of this procedure are addressed in this paper.

The main intention of this study is to analyse and highlight factors adding to the uncertainty of an injury risk curve. Another objective is to provide the basis for an improved assessment of predicted injury risks and to show the need for a precautious interpretation as well as a more thoughtful construction and usage of injury risk curves. Furthermore, this study will reveal the benefit of additional statistical measures or supplementary information in the publication of injury risk curves.

The effect of different factors on the injury risk curve is demonstrated in a visual way using statistical simulation. All of the findings presented can be explained by theory. However, theoretical considerations are not the purpose of this study.

Only the baseline risk without any predictors (e.g. age) is used. The analysis of more complex

statistical models is not within the scope of this study.

METHODS

Four factors affecting the uncertainty of an injury risk curve have been evaluated exemplarily in this study:

- The uncertainty due to the statistical inference from a sample on the population, named the effect of sampling.
- The uncertainty and bias introduced by the imprecision of the determination of the biomechanical tolerance limit in biomechanical tests, denoted as effect of censoring.
- The bias in the injury risk curve as a result of the test severities used in the biomechanical tests, herein after called effect of testing.
- The effect of statistics, i.e. the bias in the injury risk curve as a result of the statistical method used in calculating the injury risk curve.

The effects of these four factors were evaluated by statistical simulation.

Statistical simulation

To simulate the process of biomechanical testing and injury risk curve construction an underlying ("real") distribution of the biomechanical tolerance limit in the population was predefined. A Weibull distribution [1] with shape parameter 5 and scale parameter 200 was used as underlying distribution of the biomechanical tolerance limit in the simulations (see figure 1), except for the additional analysis of the logistic regression (see figure 19 and 20). Here the shape parameter was changed to a value of 2.5. The CDF of the distribution shown in figure 1 is presented in figure 2. This is the "real" injury risk curve of the population and will be used for the analysis of the effect of the factors listed above.

The underlying distribution is an assumption for the purpose of the simulation study. There is no justification that the distribution of the biomechanical tolerance limit in a population is following a certain or even common statistical distribution. Nevertheless, the effect of the factors evaluated in this study will in principle be the same on similar distributions.

In the next step of the simulation process a random sample of biomechanical tolerance limits was taken from the predefined distribution of tolerance limits [2]. This equals a random sampling of specimens (cadavers) from the population of interest.

To simulate the biomechanical testing of the sample, a range of test severities was defined, i.e. a minimum and maximum test severity. The test severities in the simulation study are expressed as criterion values, thus, the same quantity as for the biomechanical tolerance limit was used. The test severity in the simulation study is not equal to the physical test condition (e.g. pendulum mass and velocity) but equivalent to the response of the physical test condition. Test severities were randomly taken out of the test severity range and randomly assigned to the sampled specimens [2].

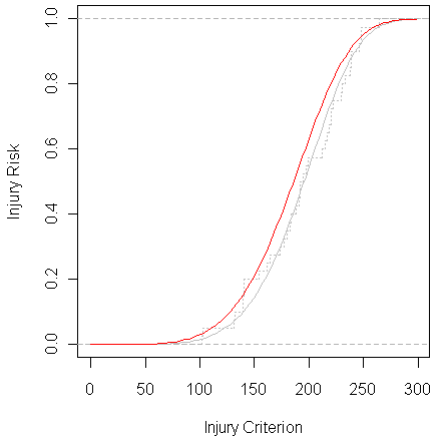

Figure 3. Sample injury risk curve (grey continuous line), "real" injury risk curve (red line), non-parametric CDF of the sample (grey dotted line).

By comparing the biomechanical tolerance limit of a specimen with the assigned test severity (expressed as resulting injury criterion value) a binary outcome is produced: injury or no injury.

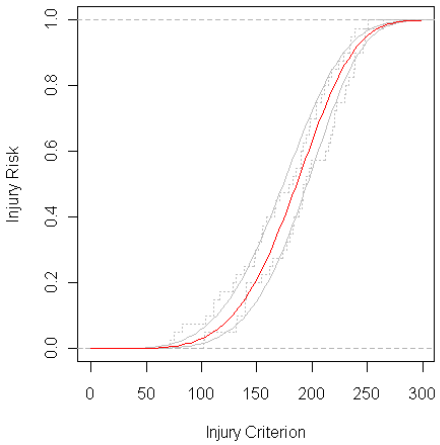

Figure 4. Injury risk curves of two samples (grey continuous lines), "real" injury risk curve (red line), non-parametric CDFs of the samples (grey dotted lines).

The last step of the statistical simulation was the calculation of the injury risk curve. Except for the analysis of the effect of statistics, a survival analysis with Weibull distribution assumption was used to calculate the injury risk curve of the samples [1, 3]. A baseline survival analysis, i.e. without predictors, equals a distribution fitting. The fitting of a Weibull distribution to data sampled from a Weibull distribution should give a reasonable estimation.

The statistical software R was used for the calculations and the plotting of the results [4].

Figure 3 shows a comparison of the result of one simulation run (sample size 40) with the "real" injury risk curve. Figure 4 shows a comparison of the results of two simulation runs (sample size 40) with the "real" injury risk curve.

The simulation process explained before was repeated hundred times and the resulting injury risk curves were compared to the "real" injury risk curve (see figure 5 as example). The scatter of the sample injury risk curves demonstrates the uncertainty of the injury risk curve estimation.

Effect of sampling

To show the effect of sample size on the reliability of the resulting injury risk prediction, hundred simulation runs with a sample size of 10, 40, and 160 have been performed.

Effect of censoring

Data censoring means that the exact biomechanical tolerance limit is not known for a specimen. If an injury is known to have occurred below a certain value of the injury criterion this data is called "left censored". If it is known that an injury will occur above a certain value of the injury criterion this value is called "right censored".

By comparing the biomechanical tolerance limit of a specimen from the sample with the assigned test severity, the binary result (injury or no injury) will lead to left and right censored data. If the assigned test severity is above the biomechanical tolerance limit, the outcome is an injury and the test severity is a left censored data and vice versa.

To simulate exact data, instead of using the test severity, the tolerance limit was used in the injury risk curve calculation when an injury was detected.

For the analysis of the influence of data censoring when using different statistical methods, injury risk curves with right censored and exact data were calculated with the use of logistic regression [1, 2] and survival analysis with logistic distribution assumption. The logistic distribution assumption in the survival analysis was used to avoid the influence of different distribution assumption in the compared methods.

Effect of testing

Usually, biomechanical tests are done at a certain mechanical load or at least within a certain range of loading severities. Very low and very high loadings are not used because it is assumed that such tests will not give valuable information since the outcome is known beforehand. To show the influence of the test severity range used in biomechanical testing on the injury risk curve, different ranges of test severities have been defined in the simulation: a low range, a small centred range, a high range and a large range. The lower and upper limit of the test severity range was defined with respect to the "real" distribution, i.e. quantiles of the "real" distribution were used for the definition of the test severity ranges (table 1).

Table 1.

Quantiles used for the definition of the test severity ranges

Range	Lower limit	Upper limit
low	0.001	0.25
high	0.75	0.999
small	0.35	0.65
large	0.01	0.99

Effect of statistics

To visualize an important effect of the statistical method on the injury risk curve, simulations using logistic regression as well as survival analysis with Weibull distribution assumption were performed. To show the dependency of this effect on the sample size, simulations with a sample size of 20 were conducted in addition to the simulations with a sample size of 40. In order to further analyse the influence of the statistical method on the injury risk curve, a different "real" distribution of biomechanical tolerance limits were used. The shape parameter of the Weibull distribution was changed from 5 to 2.5, i.e. the distribution was shifted to the left (compare figure 16 to figure 19).

RESULTS

Effect of sampling

In figure 3 the difference between the "real" underlying injury risk curve (red curve) and the calculated injury risk curve based on a random sample of size 40 is shown. The underlying risk curve is a Weibull distribution and the calculation method is a survival analysis with a Weibull distribution assumption (which basically is a fitting of a Weibull distribution).

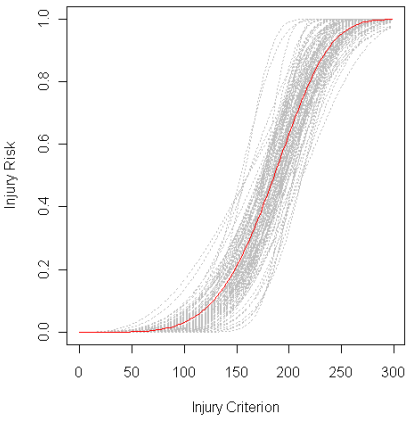

Figure 5. Scatter of injury risk curves in 100 simulation runs with a sample size of 10.

The difference between the underlying injury risk curve and the calculated risk curve is due to the sampling and not because of different distributions in the statistical calculation (the non parametric CDF additionally shown in figure 3 as dotted grey line supports this statement).

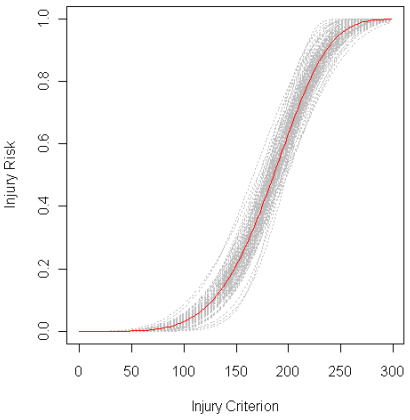

Figure 6. Scatter of injury risk curves in 100 simulation runs with a sample size of 40.

Figure 3 shows that a sample does not reproduce the "real" distribution. That is why the injury risk curve of a sample (most likely) will deviate from the "real" injury risk curve. The actual difference between the "real" injury risk curve and the injury risk curve based on a sample is up to the random sample. The randomness of sampling leads to uncertainty in the resulting injury risk curve, i.e. it is not known how good the calculated injury risk curve represents the real injury risk curve.

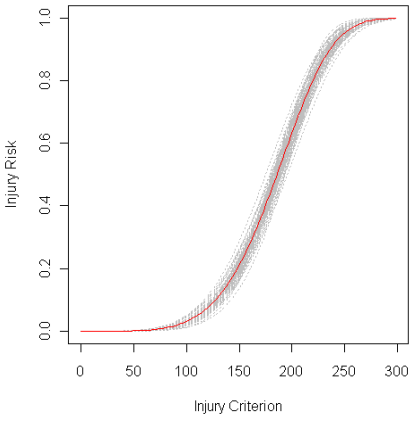

Figure 7. Scatter of injury risk curves in 100 simulation runs with a sample size of 160.

Figures 5 to 7 show the dependency of the difference between real and sample injury risk curve from the size of the sample. The smaller the sample size the bigger the uncertainty of the risk prediction (more scatter of the simulation results). In other words the reliability of an injury risk curve increases with increasing sample size.

Effect of censoring

Censored data substantially increases the uncertainty of an injury risk curve in comparison to the result of exact data (compare figure 8 and 9). Censored data contain less information, therefore, the risk prediction is less reliable. It is not shown here but can easily be imagined, that the more censored data are in the dataset the more scatter or uncertainty will be introduced. The example shown here (figure 8) illustrates the maximal effect because all data were left or right censored.

The censoring of data used in the calculation of the injury risk curve does not only introduce more uncertainty in the risk prediction (more scatter in the simulations) but can also lead to a bias in the risk prediction (shifting of the injury risk curve) when using an unsuitable calculation method. Logistic regression assumes left and right censored data. The use of right censored and exact data in logistic regression – as in all binary regression models – leads to a left shift of the injury risk curves (figure 10).

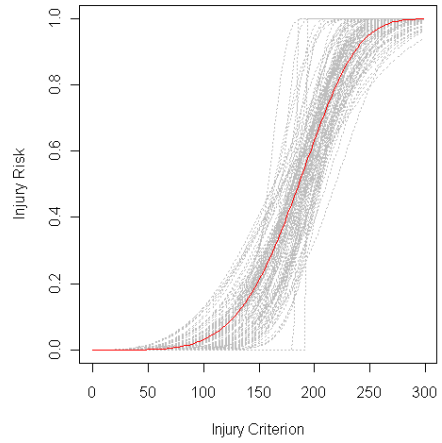

Figure 8. Simulated injury risk curves based on left and right censored data (sample size 40).

Using right censored and exact data with a survival analysis and logistic distribution assumption will have no bias (figure 11).

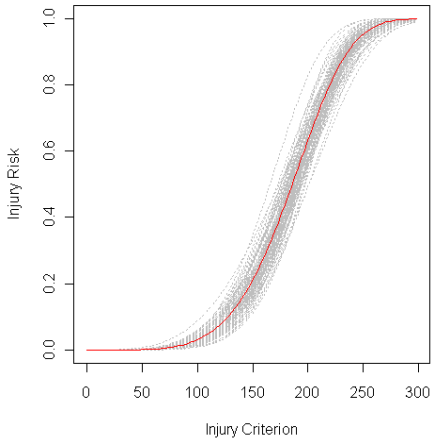

Figure 9. Simulated injury risk curves based on exact (uncensored) data (sample size 40).

The same distribution assumption (logistic) was used in survival analysis like in logistic regression. For this reason the result demonstrates that solely the calculation method (binary regression vs. survival analysis) is responsible for the bias in the injury risk curve and not the distribution assumption. The effects displayed in the figures 10 and 11 show the maximal effect since all injury data were treated as exact data. It is not shown but can easily be imagined that the strength of this effect depends on the percentage of exact data in the dataset: the more exact data the more bias in the injury risk curve calculated by logistic regression.

Effect of testing

The test severities used are influencing the injury risk curve. Outside the tested severity range the uncertainty is high. A low severity test range (figure 12) will probably lead to overestimated risks. In contrast a high severity test range (figure 13) can easily lead to underestimated risks. A small test severity range in the centre (figure 14) will likely lead to a steeper injury risk curve (overestimated risks above 50% risk and underestimated risks below 50% risk).

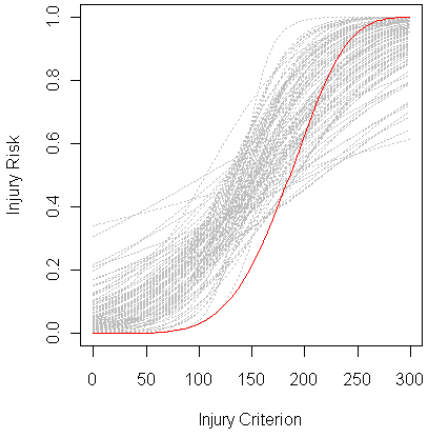

Figure 10. Logistic regression based on exact and right censored data (sample size 40).

These results are stochastic, i.e. a low test severity range does not necessarily lead to an overestimated risk. However, the probability of getting an overestimated risk is higher than getting a correct or underestimated risk.

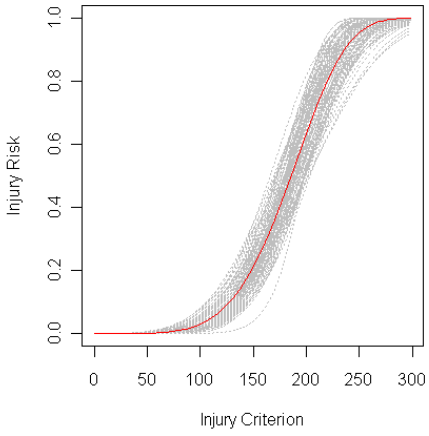

Figure 11. Survival analysis with logistic distribution assumption based on exact and right censored data (sample size 40).

The results for the other test severity ranges have to be seen analogous. A wide range of test severities gives the least bias in the injury risk prediction (figure 15). Due to the unknown "real"

injury risk curve the width of the test severity range with respect to the "real" injury risk curve (or tolerance limit distribution) cannot be assessed, unfortunately.

Effect of statistics

An unsuitable statistical model can lead to a bias in the risk prediction. An injury risk curve calculated with the logistic regression does not pass through zero and will always predict a non-zero risk at zero load.

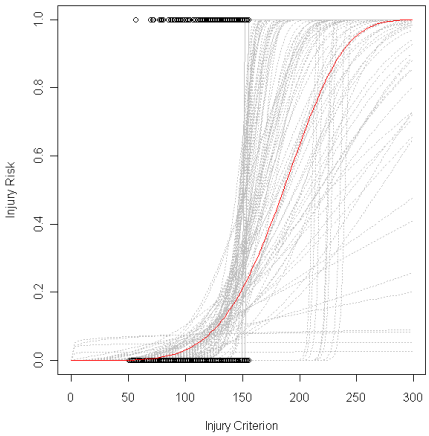

Figure 12. Low range of test severities (black dots showing the test results: 0.0=no injury, 1.0=injury).

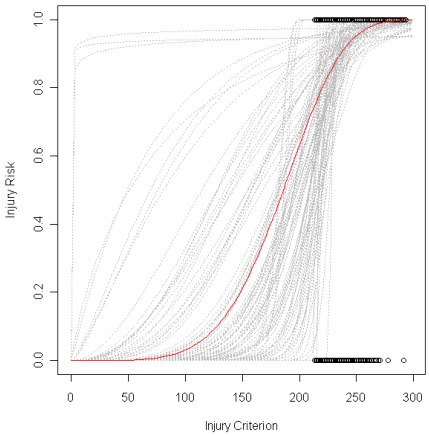

Figure 13. High range of test severities (black dots showing the test results: 0.0=no injury, 1.0=injury).

This is because a logistic distribution (like a normal distribution) is defined from minus eternity to plus eternity and is the basis of the injury risk curve calculation in logistic regression. This non-zero risk at zero load often is not obvious because the offset is very small (see figure 16). The probability of getting a substantial offset at zero risk depends on the sample size. The smaller the sample size the greater the probability of getting a substantial injury risk at zero load (compare figure 16 and 17).

If the underlying distribution has an early rise of the risk, the bias of a logistic regression injury risk curve will be more pronounced (figure 19).

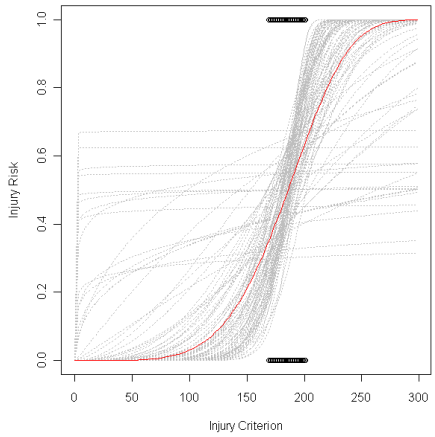

Figure 14. Small range of test severities (black dots showing the test results: 0.0=no injury, 1.0=injury).

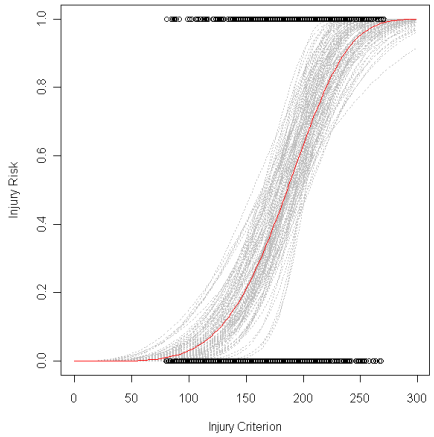

Figure 15. Large range of test severities (black dots showing the test results: 0.0=no injury, 1.0=injury).

A survival analysis with the assumption of a distribution which is defined only for positive values will always result in a injury risk curve passing through zero at zero load (as an example see figure 18 and 20 for a Weibull distribution).

CONCLUSION

This study shows factors influencing the injury risk curve, namely the data sampling, the data censoring, the test severities, and the statistical method. That means the reliability of the risk prediction of an injury risk curve depends on the size of the sample, the number of censored data,

the range of test severities and the method used in the injury risk curve development. One or more of these factors may affect the injury risk curve in a way that leads to a significant difference of the predicted risk from the real risk.

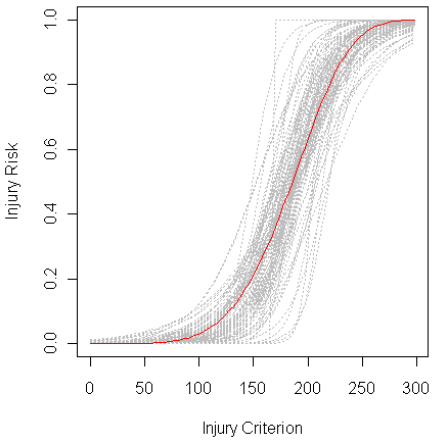

Figure 16. Logistic regression based on left and right censored data (sample size 40).

It is highly recommended to consider the reliability of an injury risk prediction in automotive safety. Before utilizing an injury risk curve the validity of the risk prediction should be assessed. Furthermore, the uncertainty of the injury risk prediction should be considered with respect to the required precision.

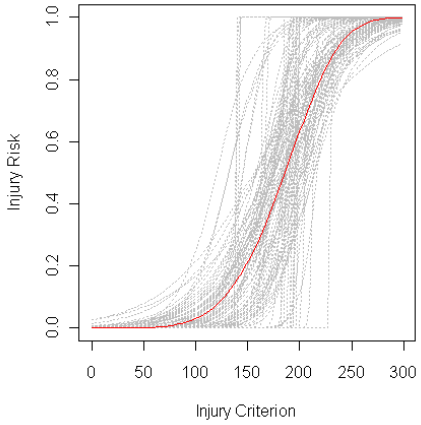

Figure 17. Logistic regression based on left and right censored data (sample size 20).

The calculation of a confidence interval (with description of the method used for its calculation) will give the user a measure of reliability. If there is no confidence interval given, the sample size and the number of censored data can provide an idea about the reliability of the risk prediction.

Logistic regression is not suitable for exact data in the dataset because it will lead to a bias in the injury risk curve and, therefore, in the risk prediction. Logistic regression should not be used with exact data. The same applies to all binary regression methods, e.g. probit regression.

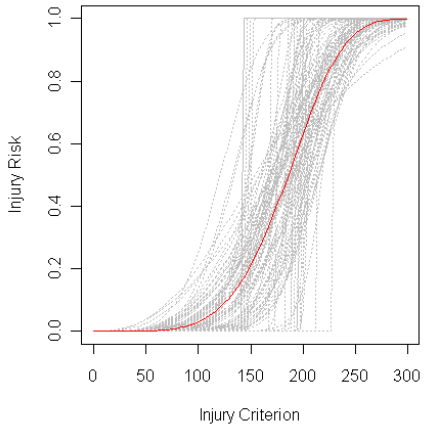

Figure 18. Survival analysis (Weibull) based on left and right censored data (sample size 20).

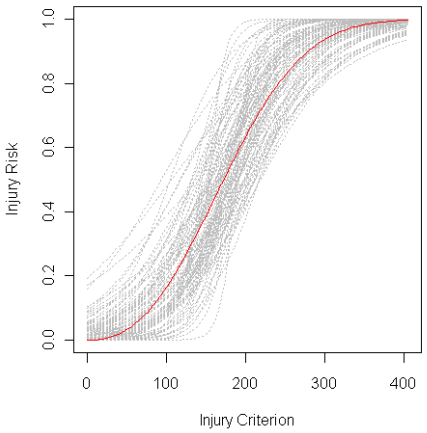

Figure 19. Logistic regression based on left and right censored data (sample size 40) and a early rising "real" distribution.

As have been demonstrated by this study the test severities used in the biomechanical tests have a significant influence on the result of the injury risk curve calculation. A wide range of test severities with respect to the underlying biomechanical tolerance limit distribution ensures a small bias in the risk prediction. In contrast to the simulation the underlying distribution of the biomechanical tolerance limits is not known in reality. Thus, the range of test severities is not known at which the specimens should be tested to be able to lead to optimal results. Nevertheless, it is clear that biomechanical tests should not be done in a small range of severities.

In general risk predictions outside the range of tested severities are less reliable than within the test severity range. Therefore, the range of test

severities should be presented with the injury risk curve.

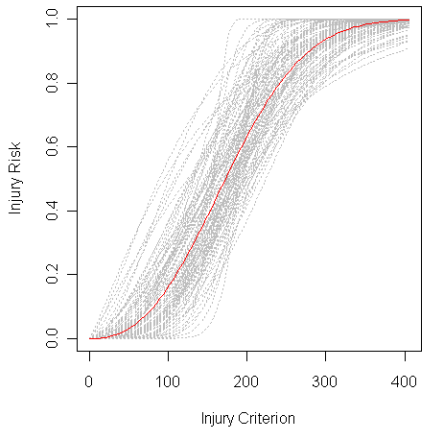

Figure 20. Survival analysis (Weibull) based on left and right censored data (sample size 40) and a early rising "real" distribution.

Exact data improves the reliability of injury risk curves, however, only with the use of an appropriate statistical method. The use of binary regression methods is critical because exact data will introduce bias in the injury risk prediction. In addition logistic regression shows an injury risk at zero load. This non-zero risk at zero load is more pronounced with lower sample size and with early rising "real" injury risk.

This study clearly shows, that an injury risk curve is affected by different factors and may lead to a unrealistic injury risk prediction. This can lead to misdirect the development of safety systems. Adapting safety systems to a misleading risk may have a negative impact on vehicle safety.

This study demonstrates that there is a need for a "quality control" for injury risk curves. Simply calculate a curve is not enough!

REFERENCES

[1] Sachs L. and Hedderich J. 2006. "Angewandte Statistik" Springer-Verlag, Berlin, Heidelberg.

[2] Dalgaard P. 2008. "Introductory Statistics with R" 2nd Edition, Springer Science +Business Media, LLC, New York.

[3] Hosmer D.W., Lemeshow S., May S. 2008. "Applied Survival Analysis" 2nd Edition, John Wiley & Sons, Inc., New Jersey.

[4] http://www.r-project.org

[5] Matloff N. 2008. "R for Programmers" http://heather.cs.ucdavis.edu/~matloff/R/RProg.pdf.

ANTHROPOMORPHIC TEST DUMMY LUMBAR LOAD VARIATION

Joseph A. Pellettiere,
David Moorcroft
Federal Aviation Administration
USA
Gerardo Olivares
National Institute for Aviation Research
USA
Paper Number 11-0157

ABSTRACT

The Federal Aviation Administration (FAA) has a number of standards and regulations that are designed to protect occupants in the event of a crash. Compliance with these regulations is described in the Code of Federal Regulations 14 CFR 25.562 for transport category aircraft, with similar regulations for other types of aircraft in parts 23, 27, and 29. One of these required tests is a seated dynamic impact with either a Hybrid II or FAA Hybrid III Anthropomorphic Test Device (ATD) with a pulse which has a primary vertical component. Vertical loading can be obtained in other environments such as under vehicle blast, ejection seat testing, or as part of a vehicle rollover. When the commonly used ATDs were developed, focus was placed on frontal impact performance with some consideration given to rear and lateral loading. It has recently been brought up that there could be significant variability in the compressive lumbar load measurement during vertical impacts. This variability could be between tests with the same ATD, between tests within the same ATD family, and between ATDs attempting to measure the same response. To quantify this issue, data from several test sources including from the Civil Aerospace Medical Institute, National Institute for Aviation Research and the Air Force Research Laboratory was collected. Cases were selected where the primary loading phase was in the vertical direction on a variety of ATDs including the Hybrid II, FAA Hybrid III, Hybrid III, and aerospace variants. These cases also included different configurations including restraint systems, cushions, and acceleration levels. This study was limited to only investigating the compressive variability and not the bending moment or in cases where significant multi axial loading could occur. Also, since these data were from different test laboratories, slight differences in test procedures could also have affected the results. Through this analysis it was shown that the Hybrid III had the most repeatable response whether it was the FAA Hybrid III or the aerospace Hybrid III. One issue noted was the lack of calibration methods for the lumbar spine to assess its current characteristics. Without this calibration method, there is no way other than visual inspection which would only show gross changes to determine when a lumbar spine segment has been degraded. Such a performance requirement should be developed for both ATDs currently in the field and those being newly developed and used such as the THOR.

BACKGROUND

The Federal Aviation Administration (FAA) has a number of standards and regulations that are designed to protect occupants in the event of a crash. As a part of these regulations dynamic testing and occupant injury assessment have been required for seats in newly certified aircraft since the adoption of Title 14 of the Code of Federal Regulations (CFR) Part 25, 25.562, and similar regulations in Parts 23, 27, and 29 [1]. There are two basic tests that must be conducted (Figure 1). For part 25 aircraft, Test 1 is a primarily vertical impact test with the characteristics of a minimum impact velocity of 35 fps with peak acceleration of 14 G's and an impact angle of 30 degrees off vertical. Test 2 is primarily a frontal test with a minimum impact velocity of 44 fps with peak acceleration of 16 G's and an impact angle of 10 degrees of yaw. Both tests also have limits on the rise time. Other aircraft categories have similar requirements. Both of these test conditions have associated injury metrics that must be met before a test is considered a pass and the seat is certified for use in aviation. These injury metrics include limits on lumbar and leg loads, limits on the Head Injury Criterion (HIC), limits on shoulder strap loads when used, and requirements that belts remain in place. For complete details, please see the applicable regulation. Of particular importance is the requirement that during Test 1, the peak compressive lumbar load in a Part 572 subpart B (Hybrid II) or equivalent must be below 1500 lb.

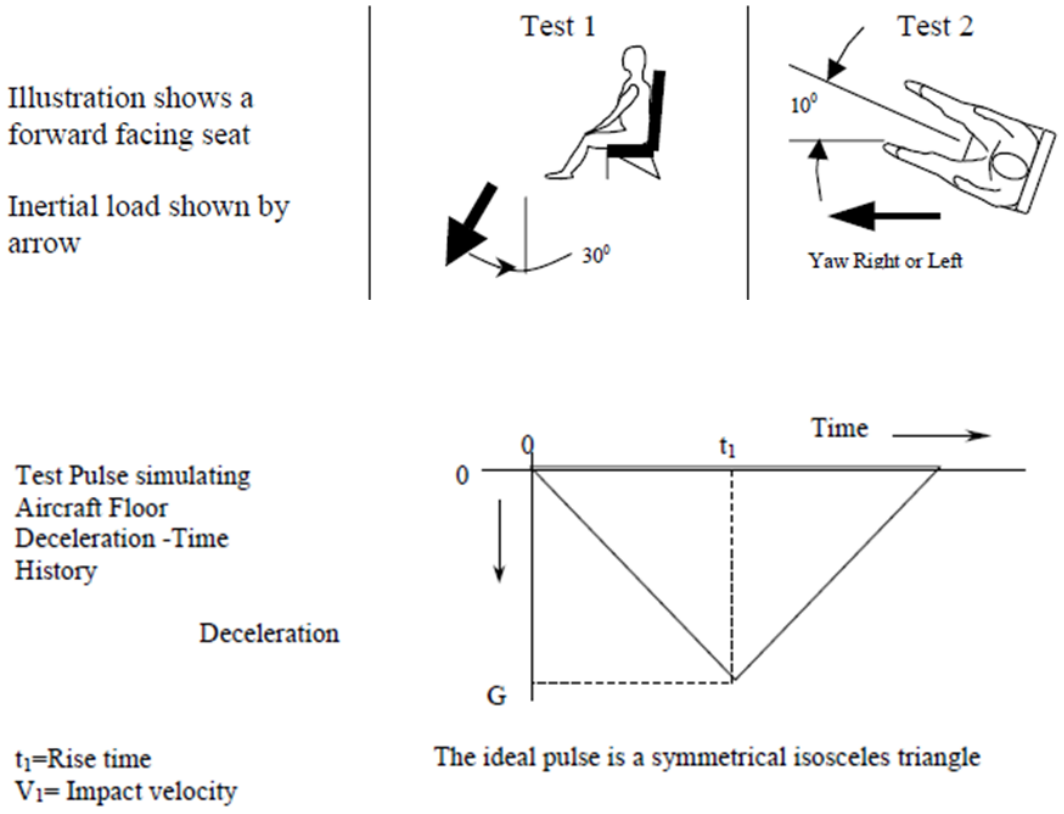

Figure 1. FAA Dynamic Seat Tests

LUMBAR INJURY

Over the years the criteria for assessing the safety of a system to vertical impacts has changed. Eiband [2] developed the earliest criterion in the 1950's. Using human volunteer and animal data, exposure limits for uninjured, moderately injured, and seriously injured occupants were developed. For vertical impacts, it was reported that human volunteers tolerated 10-G's for 0.1 seconds and 15-G's for 0.05 seconds (Figure 2).

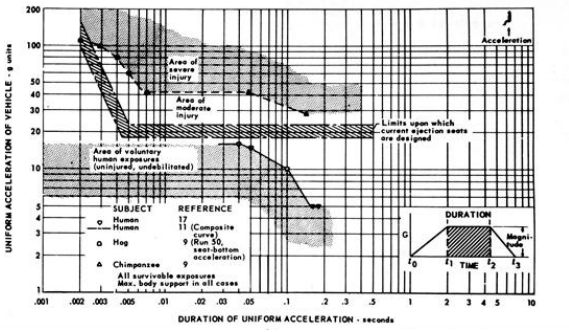

Figure 2: Human tolerance limits to vertical acceleration

Application of the Eiband curve had several limitations. It primarily characterized the response to whole body acceleration and did not break out injuries by body region. It also was not sensitive to changes in the pulse shape or mitigation methods that may have been developed. Initial ejection seat designs had acceleration limits in the 20-G range. This range falls at the boundary of moderate injury in the Eiband criteria. It was found that spinal fractures frequently occurred during ejection seat incidents and that improved seat designs were needed. As part of a revised ejection seat development program, a new criterion was also developed that is known as the Dynamic Response Index (DRI) [3]. The DRI model represents the spinal column of the human occupant as a lumped mass-spring-damper model. Input to the model consisted of seat pan accelerations and model output consisted of the acceleration time history of the DRI system. The maximum value of the DRI response was the parameter of interest. This value could then be correlated with operational injury data and an accepted value of 18 was selected (Figure 3).

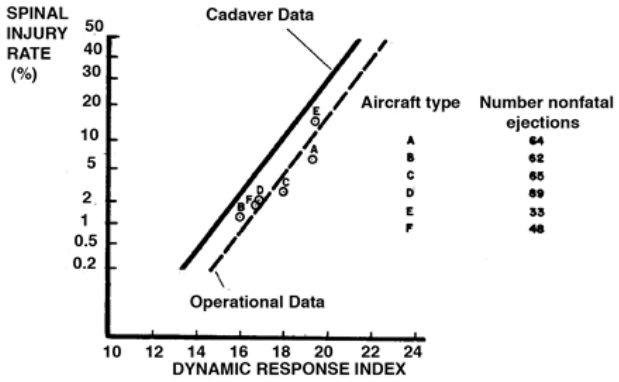

Figure 3: Spinal injury rate from ejection seats

The primary limitation of the DRI model is that it was developed for ejection seat pulses and is not sensitive to seat design changes such as different seat cushions, different restraint systems, or ATDs. While these changes may have only a minor effect on the overall seat acceleration, thereby changing the DRI only slightly, they can have a large effect on the risk of injury.. To address these issues, the FAA developed a lumbar load tolerance value. Since load in the lumbar region is the primary factor causing injuries, it was thought that a criterion based directly on measured lumbar load response was prudent. To determine the threshold, the FAA conducted a series of dynamic impact tests using aviation specific pulses. For each test, a lumbar load was measured and the DRI of the test condition was calculated. Based upon this correlation, a lumbar load of 1500-lb measured in the Hybrid II ATD was correlated to a DRI of 19 which was considered acceptable. One limitation is that these measurements were made using a Hybrid II ATD, but later tests included the FAA Hybrid III.

To expand the lumbar criteria to different anthropometries, tests and simulations were conducted using seating systems with different sized ATDs. The results of this effort formed the basis for the lumbar criteria used in the Joint Services Specification Guide (JSSG) [4]. The JSSG specified maximum lumbar loads for various sized occupants, some of which there was no equivalent ATD in existence. In a later analysis, it was shown that the JSSG limits were too high [5], based primarily on the analysis program that tended to calculate higher loads than what were measured during testing. Revised limits were proposed based on this re-analysis. The U.S. Air Force had been using the 1500-lb compressive limit for its mid-sized ATD's and used a linear mass scaling based upon the total ATD weight to generate limits for the other dummy sizes. These dummies were typically from the Aerospace Hybrid III family and had similar body weight distributions. These limits were applied to seat cushion development programs to select replacement cushions.

Recently, the modified limits (Table 4) proposed by Desjardins [5] were also proposed for a revised lumbar injury criterion to be applied to rotorcraft [6]. The limits provide a different tolerance value based upon dummy type. It should be noted here that the Mid-size Male Hybrid II type includes the FAA Hybrid III because of its similarity in response [7]. Since each size of ATD and even the different types were demonstrated to have slightly different responses, it is important that the response of any particular ATD be characterized before it can be used for injury determination.

Table 1. Maximum Values for Lumbar Injury for Specific Occupant Sizes

	Small Female Hybrid III Type ATD (103 to 118 lb)	Mid-Size Male Hybrid II Type ATD (170 lb)	Mid-Size Male Hybrid III Type ATD (170 lb)	Large Male Hybrid III Type ATD (200 to 245 lb)
Compression (lb)	933	1500	1395	1757

DUMMY DEVELOPMENT

In the FAA airworthiness standards 14 CFR Parts 23, 25, 27, and 29 Section 562 (Emergency Landing Dynamic Conditions) there is the requirement that "The tests must be conducted with an occupant simulated by a 170-pound anthropomorphic test dummy, as defined by 49 CFR Part 572, Subpart B, or its equivalent, sitting in the normal upright position." This dummy is more commonly referred to as the Hybrid II 50th percentile male ATD.

The Hybrid II can be characterized as having a solid, straight neck, an erect spine seated posture, a straight lumbar spine aligned with the thorax, 164 +- 3 lb weight with a 35.7 in sitting height. The Hybrid II was the original ATD specified in US automobile regulations (49 CFR 571.208) and was used for the development of aircraft dynamic seat standards. The lumbar load criterion in section 562 is based on the Hybrid II. However, the regulations do allow for an equivalent ATD. In order to address issues with the aging of the Hybrid II since its first development and to certify an additional ATD that would be equivalent, the FAA Hybrid III was [7] developed. The standard Hybrid III (49 CFR Part 572 Subpart E)

had several key differences to the Hybrid II, including a slouched spine sitting posture, a curved lumbar spine, a weight of 172 +- 2.4 lb with a 34.6 in sitting height. The FAA Hybrid III combined parts from the standard Hybrid II and Hybrid III to create a Hybrid III that mimicked the key features of the Hybrid II for the aviation environment. In order to maintain an upright sitting posture, the Hybrid II lumbar spine, load cell and pelvic adapter block are used. This required the creation of a unique upper lumbar-thorax adapter, which is described in the original paper [7]. To recreate the Hybrid II loading pattern into a seat, specifically for a vertical test, the Hybrid III abdominal insert, chest jacket, and lower leg assembly where replaced with Hybrid II parts (Figure 4).

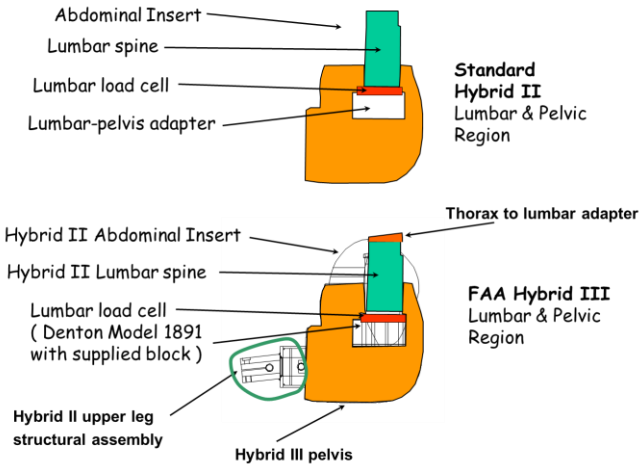

Figure 4. Hybrid II and FAA Hybrid III Pelvis

The United States Air Force also had a need for a dummy to respond to vertical accelerations. The USAF was actively involved in ejection seat testing and required a durable dummy which could be placed into a variety of seating positions and collect data onboard. The result of this effort was the development of the Hybrid III Aerospace line [8]. These dummies range in size from small (approximately 5th percentile female), mid-size (50th percentile male) and large (95th percentile male). The aerospace Hybrid IIIs have a straight spine, but unlike the FAA Hybrid III, the aerospace Hybrid III uses the spine from the pedestrian dummies. Because of this, the spine is made from natural rubber instead of the butyl rubber in the Hybrid II and it has a slightly different geometry. The material for the construction of the hard elements was also modified to withstand the extremes of ejection seat testing. However, the construction is mainly of a Hybrid III design, instead of borrowing Hybrid II components as was done for the FAA Hybrid III.

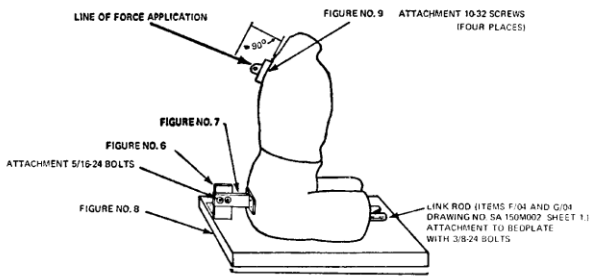

Figure 5. Lumbar flexion test

Since the various ATDs used in testing are commonly used for certification testing, there is a whole series of calibration tests that must be routinely conducted for each ATD. These tests include but are not limited to: chest compression, knee compression, neck flexion, and a quasi-static spinal flexion (Figure 5). The spinal flexion test is conducted to verify that the lumbar spine, abdominal insert and pelvis are properly functioning. This test is described in 49 CFR 572.9. The test consists of continuously applying a force to the thorax of the dummy and recording the flexion angle and force and allowing the ATD to return to its initial position afterwards. The response must fall within a prescribed corridor (Table 2). In addition, when the load is removed, the ATD must return to its initial position within 12 degrees.

Table 2. Lumbar spine calibration corridor

Flexion (degrees)	Force (+- 6 lb)
0	0
20	28
30	40
40	52

Besides this test, there is also a test to measure the compressibility of the abdominal insert separately (Figure 6). It should be noted that this test procedure is really measuring how the dummy will perform during a frontal flexion type of test. It is doing nothing to verify the compressibility of the lumbar spine itself. There is no test procedure to verify the condition of the ATD to vertical loading. The ATD is routinely inspected to determine if there is any damage to the lumbar spine or the dummy flesh itself

Figure 6. Abdominal insert compression test

DATA SOURCES

As part of a cushion replacement and modeling and simulation program, the USAF has conducted a number of vertical impact tests with various ATDs over the years. This data is available on a publicly accessible website, https://www.biodyn.wpafb.af.mil [9]. One study of importance for the discussion here is the Seat Cushion Lumbar Support (SCLS) study from 2003 [10]. This study was a series of vertical impacts with a mostly rigid seat. Tests consisted of conditions with and without seat cushions. The no cushion tests were investigated here as they will provide the most insight into the ATD response. The ATD used for these tests was the 50th percentile Hybrid III Aerospace dummy.

Table 3. Hybrid III 50th Aerospace Lumbar Loads

Test Number	Peak Acceleration (G's)	Peak Lumbar (lb)	Normalized Lumbar (lb)	AVG
V4583	8.04	706	703	710
V4584	8.03	735	733	STD
V4585	8.1	704	695	19.62
V4586	10.19	983	965	AVG
V4587	10.13	960	948	989
V4588	10.1	1071	1060	STD
V4589	10.14	995	981	49.70
V4590	11.21	1177	1260	AVG
V4891	11.59	1251	1296	1288
V4892	12.05	1286	1281	STD
V4893	11.97	1343	1346	36.08
V4894	12.08	1266	1258	

Twelve tests were conducted without seat cushions ranging from 8 to 12 G's (Table 3). The measured lumbar load was normalized to the target acceleration level as described in paragraph 5.3.9.5 of SAE AS8049B [11]. In addition, the Standard Deviation, based on the normalized load, was calculated for each acceleration range and ranged from 19 to 50 lb, or from 2.8 % to 5% of lumbar range. These results are consistent with other test series from this data source using the Hybrid III 50th percentile Aerospace dummy.

As part of the development of the FAA Hybrid III, a series of vertical impact tests were run at the Civil Aerospace Medical Institute (CAMI) with both the Hybrid II and the newly developed FAA Hybrid III [7]. The tests included a rigid seat with a thin cushion in a manner consistent with the 562 type tests. The peak acceleration was approximately 15G for the combined vertical test as opposed to 14G for a part 25 aircraft. While the tests were targeted for 15G, they were normalized here to 14G for comparison with other tests series (Table 4). For both dummies the average lumbar load was 1178 Lbs with a Standard Deviation of 20.5 or 1.7% of the average lumbar load for the Hybrid II and 26 or 2.2% of the average lumbar load for the FAA Hybrid III.

Table 4. FAA Hybrid III Development Tests

ATD	Test Number	Peak Acceleration (G's)	Peak Lumbar (lb)	Normalized Lumbar (lb)
H2	96041	15.96	1362	1195
H2	96042	16.0	1355	1186
H2	96043	15.6	1288	1155
FH3	98032	15.0	1236	1154
FH3	98033	15.2	1275	1174
FH3	99010	14.8	1275	1206
*H2= Hybrid II and FH3= FAA Hybrid III				

In 1999 the FAA completed a test program in coordination with industry to compare the results from testing at different facilities with the same test article [12]. Tests were conducted with a typical aircraft seat using the Hybrid II ATD in both the longitudinal and the vertical orientations. The facilities included two deceleration sleds, an acceleration sled, and a drop tower and included repeated testing. While these tests did have cushions and were not with rigid seats, because they were the same seat and cushion type tested at each facility and with similar pulses that were designed to meet the 562 type of testing, the results should be similar (Table 5).

Table 5. Hybrid II Facility Comparison Tests

Test Number	Peak Acceleration (G's)	Peak Lumbar (lb)	Normalized Lumbar (lb)
CAMI 92104	16.2	1547.39	1337.25
CAMI 94019	13.8	1149.2	1165.86
MGA1	14.1	1607.03	1595.63
MGA2	14.1	1408.06	1398.07
Sim1	15.5	-	
Sim2	15.5	1195.76	1080.04
WSU1	14.1	1202.16	1193.63
WSU2	14.3	1163.46	1139.05
AVG			1272.79
STD			181.11

While these tests would be expected to have a little more variability in them due to the fact that the test article (deformable seat and cushion at different facilities) should provide additional variation, the lumbar load from all the tests had a Standard Deviation of 181 lb or over 14% of the average measured lumbar load. Another way to consider this variability is to calculate the range from the lowest to the highest normalized lumbar load. In this test series the measured lumbar load varied over 500 lb or 40% of the average lumbar load.

The National Institute for Aviation Research (NIAR) at Wichita State University recently began investigating issues of lumbar load variability while trying to develop response corridors that could be used to validate computational models [13]. Two types of anthropomorphic test dummies per 49 CFR Part 572 Subpart B requirements were evaluated; the Hybrid II 50th percentile adult male ATD and the FAA Hybrid III 50th percentile adult male ATD. Two test series were conducted:

- Test series 06165: These tests were conducted on a rigid seat without a seat cushion. For this test series 14G Part 25 pulses were applied.
- Test series 07324: These tests were conducted on a rigid seat without a seat cushion (Figure 7). It should be noted that for this test series two Teflon sheets were used, one attached to the seat-pan aluminum surface and one additional sheet between the seat pan and the ATD pelvis. For this test series 19G Part 23 pulses were applied.

For 14G dynamic loads, the FAA Hybrid III measured higher average lumbar loads (10% higher) than the Hybrid II ATD (Figure 8). The test to test variability for this test series is very similar for both the Hybrid II and the FAA Hybrid III (standard deviations 38 and 63 lb respectively). For the 19G part 23 pulses the FAA Hybrid III consistently exceeds the 1500 Lbs limit, the average lumbar load value for this test configuration was 1737 lb. On the other hand, the Hybrid II did not show consistent results, the lumbar loads ranged from 1146 to 1698 lb with a standard deviation of 281 lb.

Table 6. NIAR Lumbar Comparison Tests

ATD	Teflon (# of sheets)	Test Number	Peak Acceleration (G's)	Peak Lumbar (lb)	Normalized Lumbar (lb)	
H2	2	07324-10	19.05	1410	1406	AVG
H2	2	07324-11	19.66	1757	1698	1399
H2	2	07324-12	19.43	1693	1655	STD
H2	1	07324-30	19.56	1120	1088	281
H2	2	07324-31	19.25	1161	1146	
H2	0	06165-5	14.7	858	817	AVG
H2	0	06165-6	14.6	960	921	862
H2	0	06165-25	14.65	837	800	STD
H2	0	06165-26	14.35	935	912.	63
FAA H3	2	07324-13	19.08	1713	1705	AVG
FAA H3	2	07324-14	19.14	1736	1723	1737
FAA H3	2	07324-15	19.18	1798	1781	STD 44
FAA H3	0	06165-7	14.6	1013	971	AVG
FAA H3	0	06165-8	14.8	1028	972	950
FAA H3	0	06165-28	14.28	924	906	STD 38

As shown in Figure 9 there are significant differences in the lumbar spine to upper torso interface geometry. The differences in the interface geometry and orientation with respect to the upper torso cg (Figure 9) are sufficient to change the slenderness ratio of the lumbar spine assembly; hence the differences in the dynamic behavior of the lumbar spines experienced during higher deceleration pulses. Preliminary data analysis indicates that the lumbar spine of the Hybrid II experiences limit point instability hence the scatter shown in the test data. NIAR is currently conducting a series of sled tests and simulations to identify the source of the test to test variability shown for higher deceleration loads. The parameters that will be analyzed in this study are geometric/inertia differences between ATDs, surface friction, seat pan stiffness (no seat cushion and various seat cushion material/thickness combinations), and ATD initial position.

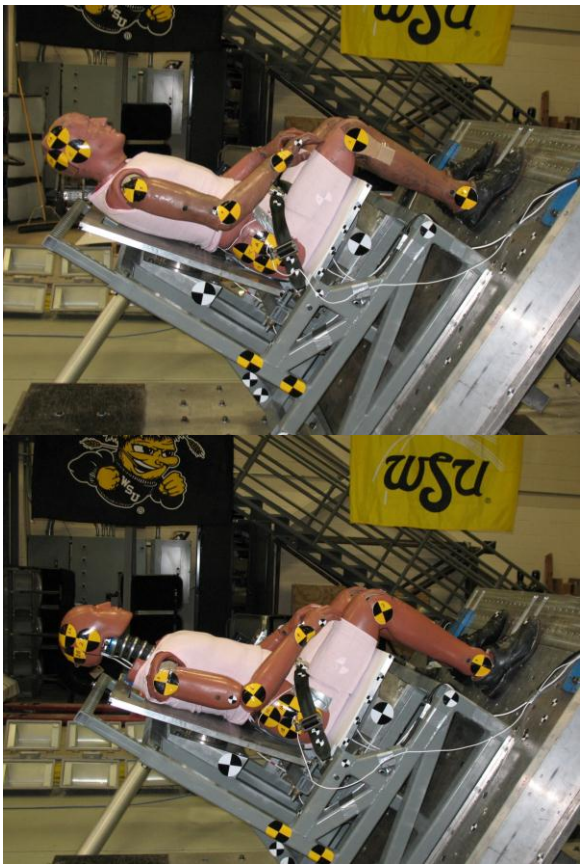

Figure 7. HII and FAA HIII NIAR test setup

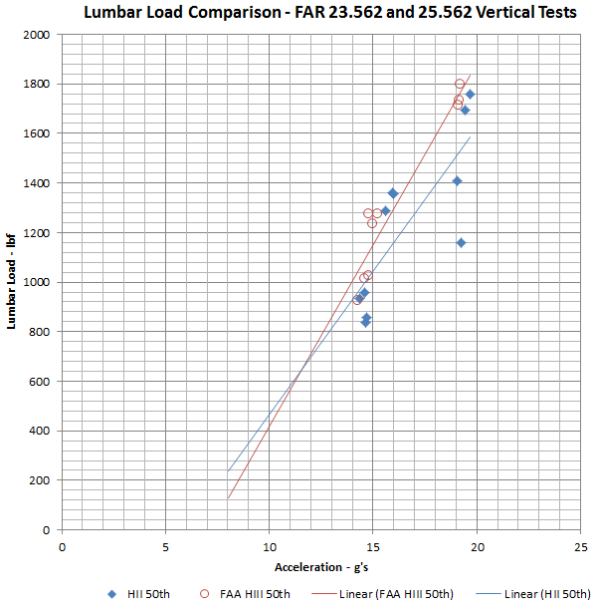

Figure 8. HII and FAA HII lumbar loads vs. sled acceleration

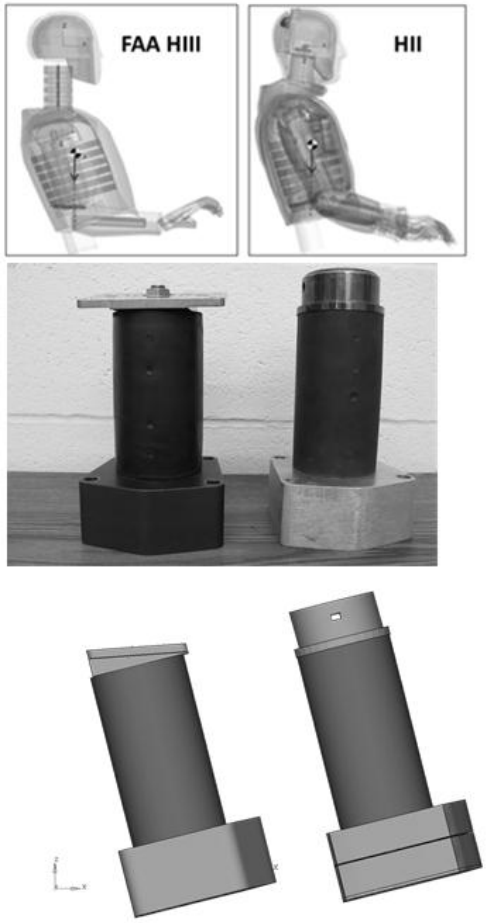

Figure 9. HII and FAA HII lumbar spines

DISCUSSION

At first glance it would appear that there is not much lumbar load variation, the USAF study had a Standard Deviation under 5%, the FAA Hybrid III development tests had less than 5% Standard Deviation, and even the 14G Part 25 tests at NIAR had Standard Deviations under 7%. Looking at each of these well controlled tests separately, does not tell the whole story. In the facility comparison study which all used the Hybrid II, the Standard Deviation increases to 14%. The highest variability observed corresponds to the NIAR test series with 19G Part 23 pulses with a standard deviation in excess of 20%. There are many factors which can affect the lumbar loads from these tests. They include different initial positions in setup, pulse variations between tests and between facilities, friction differences from the different setups, different ATDs used and condition of the ATDs used.

The first factor, different initial positions is something that can be controlled and documented with different test procedures. Research conducted at CAMI has shown that an ATD can be consistently placed in a seat and that by controlling the fore-aft and vertical position of the ATD, along with the pelvic orientation, good repeatability of lumbar load can be achieved. When seating the ATD per SAE AS 8049b procedures, apply a 20 lb force to the sternum while lowering the ATD into position. This procedure is similar to using a H-point machine, which is common in the automotive field. When using this procedure, researchers at CAMI found that the ATD's vertical position varied by no more than 0.05", the fore-aft position varied by less than 0.3" and the pelvic angle varied by less than 1.5° with a typical PAX seat cushion. During setup of a download test, an iterative process can be employed to position the ATD in the same pelvic location (X, Z, and angle) as during the 1-g measurement. It is recommended to control the Z position to within 0.15", the X position to 0.25", and the angle to 1.5°. When using the procedure across a range of cushions, the lumbar load typically varied by less than 10%. While these results are promising, the iterative nature of this procedure will increase the time required to setup a test. In most of the CAMI tests, the ATD was positioned and measured in 10-20 minutes. The researchers noted that there was a learning curve and that initially the procedure took longer to accomplish. It was also noted that the tolerance on the fore-aft position can depend on the particular seat being tested. On a rigid seat, this dimension is less critical than a flexible seat where the fore-aft location may be the difference between loading a tube and loading only a flexible (e.g. clothe) seat pan.

Each time a dynamic impact test is run, the resulting input from the test setup can vary slightly. For accelerator type systems, this pulse can be well controlled with only minimal differences. On decelerator sleds and drop towers, the pulse can vary slightly more, both between the tests and during a particular test the pulse may have some higher order frequency components that may be unintentional. The larger differences come in when trying to compare the results against different facilities. While the pulse obtained from a decelerator and an accelerator sled may meet the requirements of the FAR for 562 type testing, there are some differences in the rise time, peaks, and pulse widths which could contribute to variations in the resulting peak lumbar loads as was seen in the facility comparison tests. An interesting study would be to conduct a new facility comparison test program since many facilities have upgraded and replaced their impact systems.

Seat interface friction affected the lumbar response for both ATDs. For the case of the Hybrid II decreased friction increased the variation and for the FAA Hybrid III decreased friction decreased the variation. The change in friction may be a similar effect as slight changes in initial position. With the different amount of friction, the pelvis made slightly slide or rotate, changing the position and the response of the dummy. For practical applications, this generally would not be an issue as the ATD would be wearing standard garments and would typically be seated on a cushion, thereby setting what the frictional coefficients are for any particular test series. Since the variation increases dramatically for the Hybrid II when the friction is reduced, it is recommended to avoid testing in those configurations or to ensure that an adequate number of tests are conducted to avoid gathering data that might be at the boundary of acceptability. NIAR is currently conducting a series of sled tests and simulations to identify the source of the lumbar load variability due to surface friction.

The final two factors, different ATDs and their condition, are two that a particular test lab does not have any control over, however, they should know about them and have a way to assess their affects. During the manufacturing process of the ATDs, there are many tolerances on the various components. Because of these tolerances, each ATD can be slightly different. Care is taken to minimize any of these differences, and these natural variations can be measured by such things as checking the weights and

center of gravity of various parts, measuring the flesh thickness, checking the anthropometry of the as built dummy and conducting calibration tests. For the ATDs, there are several calibration tests that are performed to ensure that the ATDs are within accepted response corridors. These calibration tests serve two roles. The first is to certify that the as built dummy is suitable for testing and to quantify its natural variation from other dummies. The second is to ensure the continued suitability of the ATD for testing through the periodic calibration testing. This periodic testing will assess the ATDs current condition and determine if it can continue to be used. However, in the case of vertical compression of the lumbar spine, there currently is no calibration test to quantify the ATD variability or its changes over time. Because of this, there is no way to assess if a particular dummy is worn out and if any changes that are occurring are the result of the natural aging of the dummy materials.

The data does show small variability for repeated testing, but it should be noted that many of these tests were conducted in a short time from one another. For the USAF testing, each group of tests was run one right after another, as evidenced by the sequential test numbering. This is also true of the FAA Hybrid III development tests. In this case, the three Hybrid II tests were conducted sequentially and two of the three FAA Hybrid III tests were conducted sequentially. It can be noted here that the third test from this series which was run the following year also had the highest lumbar load and was the test that increased the test variability. This increased variability is also present in the facility comparison tests which spanned several years and the NIAR tests which also spanned some time. Apart from a visual inspection of the ATD, and calibration of the load cell and other instrumentation, no checks were done to assess the performance of the ATD to compressive lumbar loads.

To address this issue, a calibration test is needed to determine whether a particular ATD is suitable for vertical impact testing. The first requirement should be verification of the calibration of the lumbar load cell. This could be accomplished through a static 1 g measurement of the ATDs upper torso body weight with and without the abdominal insert. This measurement should then be compared with a separate standard scale measurement and the load cell measurement. In a previous Navy study [14] it was found that this measurement does not directly scale with body weight, so a standard tolerance band for both of these measurements would be needed for each ATD.

With the static torso weight verified, a test should be conducted to verify the dynamic behavior of the ATD. The dynamic test will be used to assess the condition of the pelvic flesh and lumbar spine. A couple of choices are possible and include a separate component test and a full scale dynamic sled test. A component test will have the advantage of the input being tightly controlled and repeatable. For example, if the test is conducted on a tensile test machine, the input parameters such as stroke and compressive force could be directly prescribed with tight conditions. Drawbacks would be that either a specialized test device or a specialized fixture would need to be developed. In addition, the component tests would have to be followed by full scale dynamic tests to verify the transfer function between the component and the full seat test. The second choice would be to just use a rigid seat fixture and use an input pulse similar to what the ATD would be expected to experience. This could be several dynamic impact tests conducted at different acceleration levels to ensure compliance with the different types of tests. Some drawbacks here are that an additional sled impact tests would have to be periodically run to ensure compliance of the ATD. Another drawback is this test itself may cause some degradation to the pelvis. To mitigate this issue, perhaps a well characterized cushion could be used. The advantage is that if the particular test lab is already involved in this type of testing, then they already have the facilities and expertise needed to run this test, this would only not be the case for those that support field type testing or testing with real world vehicles as opposed to within a test lab.

A new series of full scale dynamic tests can provide several benefits. The first would be to generate new data for facility comparisons as discussed previously. The second would be additional data collection on dummies for a detailed lumbar load comparison that can also now include several different test labs and different loading levels. The final benefit would be the development of the acceptable response corridors upon which to base the calibration acceptance criteria.

CONCLUSIONS

The aviation community has been using the lumbar load from the ATDs as both a regulatory requirement and as a research parameter for a number of years. Recently, lumbar loading has been proposed as an injury metric for other environments including under vehicle blast and possibly for vehicle rollover.

A limitation of the data presented here is that the tests were conducted with different purposes in mind, other than assessing lumbar load variation. While care was made in selecting tests that were similar, not all of the tests had the same configuration. For example, the facility comparison tests were conducted on a non-rigid seat. It is clear that the lumbar load in the current ATDs can vary, even in the environment for which it is widely used and may vary even more when it is used in different environments. Due to the high variability exhibited by the Hybrid II at higher deceleration pulses (19G Part 23); additional research will be conducted to identify the source of the problem. The first step that is necessary after appropriate injury criteria are adopted is to verify the performance of the ATD with a calibration test, similar to what is performed for the other body regions. This calibration test will allow test engineers to have confidence in the repeatability and usability of the generated test data.

While some options for this calibration test were discussed, the actual specifics were not presented. It is recommended that the proposed test methods be conducted on a variety of ATDs in several locations to develop the needed response corridors which can then become the calibration requirements. Dynamic and component tests should be conducted with the aim of determining if different calibration standards are required for part 23, 25, 27, and 29 requirements because of the differences in loading rates.

DISCLAIMER

The findings and conclusions in this paper are the opinions of the authors and should not be construed to represent any agency determination or policy.

REFERENCES

1. U.S. Code of Federal Regulations, Title 14, Parts 23.562, 25.562, 27.562, 29.562. Washington, DC: US Government Printing Office.

2. Eiband, A.M., "Human Tolerance to Rapidly Applied Accelerations, A Summary of the Literature," NASA Memorandum 5-16-59E, 1959

3. Stech, E. L. and Payne, P. R., "Dynamic Models of the Human Body," AAMRL-TR-66-157, Aerospace Medical Research Laboratory, Wright-Patterson Air Force Base, Ohio, 1969.

4. Crew Systems Crash Protection Handbook, Department of Defense, Joint Services Specification Guide, JSSG-2010-7, October 30, 1998.

5. Desjardins, S.P., "Establishing Lumbar Injury Tolerance for Energy Absorbing Seats," Proceedings of the American Helicopter Society Forum 64, Montreal, Canada, April 29-May 1, 2008.

6. Pellettiere, J.A., Crocco, J., and Jackson, K.E., "Rotorcraft Full Spectrum Crashworthiness and Occupant Injury Requirements," Proceedings of the American Helicopter Society, Forum 67, Virginia Beach, VA, May 3-5, 2011.

7. Van Gowdy, DeWeese, R., Beebe, M.S., Wade, B., Duncan, J., Kelly, R., Blaker, J.L., "A Lumbar Spine Modification to the Hybrid II ATD for Aircraft Seat Tests," SAE Paper No. 1999-01-1609.

8. http://www.humaneticsatd.com/crash-test-dummies/aerospace-military/aerospace, Accessed 10 February, 20111.

9. Cheng, H., Mosher, S.E., and Buhrman, J.E., "Development of the Biodynamics Data Bank and its Web Interface," AFRL-HE-TR-2004-0147, 2004.

10. Cheng, Z. and Pellettiere, J.A., "Evaluation of the Safety Performance of Ejection Seat Cushions," 2004 SAFE Symposium, Salt Lake City, UT.

11. Society of Automotive Engineering Aerospace Standard SAE AS8049 Rev B, "Performance Standard for Seats in Civil Rotorcraft, Transport Aircraft, and General Aviation Aircraft," 2005.

12. Soltis, S.J. and Forest, K.E., "Comparison of Results from Dynamic Tests of an Airplane Seat at Different Facilities," SAE Paper No 1999-01-1608.

13. Olivares, G., "Dynamic Seat Certification by Analysis: Hybrid II and FAA Hybrid III Anthropomorphic Test Dummies Validation and Verification Methodology," DOT/FAA/AR-TBD, 2011.

14. Rappaport, M. Forster, E., Schoenbeck, A., and Domzalski, L., "Establishing a Spinal Injury Criterion for Military Seats," 1997 SAFE Symposium, Reno, NV

A SLED TEST METHOD FOR SMALL OVERLAP CRASHES AND FATAL HEAD INJURIES

Ola Bostrom
Dion Kruse
Autoliv Research
Sweden
Paper Number 11-0369

ABSTRACT

A large portion of fatal crashes are characterized by passenger cars being hit at the front but without engaging the drive train or longitudinal structural beams. The objective of this paper was to describe a cost-effective sled test method developed to address the issue of small overlap crashes and fatal head injuries. A real-life small overlap crash and literature review revealed that, in most cases, fatal injuries were multiple and the dominating injury mechanisms were head impacts with the inboard side, A-pillar, or external objects. Full-scale crashes with the THOR dummy confirmed this. A sled test method was developed replicating the critical events in the full-scale crashes. In additional tests with the HIII dummy there was no indication of head contact with the inboard side.

In conclusion, sled tests with the THOR dummy may be used in the evaluation of restraints' ability to protect occupants in small overlap types of crashes.

INTRODUCTION

Passenger cars have probably had frontal crashes with other cars with a partial, narrow or small overlap since the beginning of car history. Nevertheless, to date, there is no standardized procedure of evaluating a car's ability to protect occupants from injury in these types of crashes. A first step towards such standardization is to clarify and define relevant crash circumstances. Examples of definitions used in the literature include frontal crashes with less than 1/3 overlap (O'Neill et al 1994), without drive train (Lindquist 2004) or longitudinal structural beam engagement (Scullion 2009).

In order to evaluate a car's ability to protect an occupant in a standardized test there is a need to understand injury distribution, mechanisms and causations. 1968 Mackay (1968), using UK data, noted that the benefit of a belt was greatly reduced in frontal corner impacts, presumably because the A-pillar and door structure played a greater role in generating injury compared with non-corner frontal impacts. According to Kullgren et al. (1998) 22% of all frontal impacts in Sweden and 42% of severely injured (MAIS3+) drivers had an overlap below 30%. Lindquist (2004) showed that a large part of Swedish fatal crashes were characterized by cars being hit at the front without engaging the drive train or longitudinal beams. Moreover, in this group of fatal crashes, occupants died of head and/or thorax injuries caused by interaction with the side interior (Lindquist 2006). Lindquist concluded in his thesis (2007) that the injury mechanism in this configuration was characterized by an oblique movement and interaction with the outboard side. Pintar et al (2008) analyzed narrow offset frontal crashes in NASS and CIREN databases and concluded that countermeasures designed with standard large overlap frontal crashes may not address the specific injuries associated with narrow overlap crashes. The authors continue: "Rotation of the vehicle and subsequent occupant movement lateral to the airbag could be a factor in less severe impacts". Based on NASS/CIREN analysis and modeling, NHTSA performed a series of small overlap, vehicle-to-vehicle, and vehicle-to-pole THOR crash tests. The research dummy THOR (Test device for Human Occupant Restraint) has been shown to be more biofidelic compared to the dummy HIII (Shaw et al. 2000). At the 2010 Government-Industry meeting Saunders (2010) noted that the THOR head was in contact with the A-pillar, door or instrument panel in all NHTSA tests in accordance with real-life case reviews. Hollowell (2011), in an overview of NHTSA's compatibility and frontal impact activities, noted, after analyzing the vehicle-to-vehicle (Taurus) small overlap tests, that the THOR dummy rolled off the bag resulting in head-door contact.

Planath et al (1993) developed a test method addressing severe partial overlap collisions (0-30 degrees frontal impacts, <50% overlap and extensive deformation) where a full-scale car impacts a fixed rigid barrier with a 20-40% overlap at speeds of up to

Figure 1 – To the right, post crash photos of the CCIS case chosen for vehicle-to-vehicle crash replication, to the left, the post crash photos of the vehicle-to-vehicle crash test. The photos of the CCIS car have been mirrored.

65 km/h. Recently, the Insurance Institute of Highway Safety (IIHS) presented arguments for and proposed a test concept that would make it possible to address fatal injuries in small overlap types of crashes (IIHS 2009, Sherwood 2009). In the IIHS research program the Institute has performed vehicle-to-vehicle and vehicle-to-pole/-barrier crash tests where the overlap was approximately 25%. In the 2011 Government-Industry meeting Sherwood (2011) presented research progress where the Institute started with a 10-inch diameter pole, continued with a flat barrier with a 2-inch radius and then went on to a 20-inch diameter pole. They have now started with a flat barrier with a 6-inch radius THOR and HIII tests for better understanding compromise of vehicle and occupant dynamics.

With standardized full-scale car tests at hand there is a need for cost-effective tests in order to understand potential benefits of traditional and new occupant restraints such as airbags and belts. Also, such a resource- and purpose-limited test could be used to evaluate the applicability of using dummies such as the HIII and THOR.

The objective of this paper was to describe the developed sled test method as a tool to evaluate differences between dummy kinematics as well as the ability of restraint systems to protect the head in a set of fatal small overlap or narrow offset types of crashes.

METHOD

A simple cost-effective sled test method needed to be developed with the complex reality of real-world crashes in mind. More specifically, simplicity should only be directed toward the purpose of the test. The purpose of the test method proposed and discussed in this paper was to evaluate the applicability of dummies and restraint systems regarding fatal head injuries. Therefore, as a first step, a real-life data analysis and literature review were performed to gain an understanding as to which type of small overlaps were both frequent in fatalities but capable of mitigating the consequences. Also, this review/analysis was meant to get an idea of the most frequent AIS3+ injury mechanisms. The data analysis was previously documented in an internal report by Kruse (2008). Thereafter, a test series of small overlap vehicle-to-vehicle and vehicle-to-barrier crashes with a THOR dummy were performed. Based on free flying mass trajectories and A-pillar/instrument panel intrusion a sled test method including a set of linkage arms was developed. The development was previously documented in an internal report by Kruse (2009). The sled test method was used in a series of THOR and HIII tests. The test specifications were similar for the two dummies which were restrained by a retractor-pretensioned load-limiting belt and a driver airbag. The pre-test nose-rim and chest-center hub distances were 470 and 310 mm for the HIII and for THOR (w/o nose) 490

and 370 mm. The THOR-NT was equipped with the second generation of shoulder modification developed by Tornvall et al (2006).

The real-life analyses were performed using fatal frontal crashes (direction of force 11-01), no roll, with belted occupants in CCIS (1998-2006) including 247 fatalities and NASS (1995-2005) with 390 fatalities. The inclusion criterion used in this study was drivers and 33% of overlap with accurate data.

RESULTS

Real-life analysis

The 247 and 390 frontal/no roll/belted CCIS and NASS fatal cases were reduced to 34 and 60 drivers respectively exposed for well documented small (<33%) overlap cases. Among the 60 NASS cases there were 327 AIS3+ injuries. The most common injury of the small overlap NASS cases were brain injuries (35%) followed by ribcage, femur, heart/aorta injuries (10% respectively) and lung injuries (7%). The most common injury cause was side structure (35%) followed by exterior object (25%) and A-pillar (12%) and steering wheel (7%). Among the CCIS and NASS small overlap cases most occurred on roads with a posted 60 and 45 mph limit, respectively. Of the 34 CCIS cases one representative case was chosen to be replicated in a vehicle-to-vehicle and a vehicle-to-barrier crash test. While negotiating a left hand bend the target vehicle (right hand side driven) in this case collided with a another car travelling in the opposite direction resulting in a 22% overlap, crash CDC code 12FREE4, and no longitudinal beam engagement. According to the report the driver sustained severe head and neck injuries in contact with the A-pillar, severe thorax injuries in contact with the steering wheel and severe lower extremity injuries in contact with the intruded door and instrument panel. See Figure 1 for post-crash photos of the car (right hand side).

a)

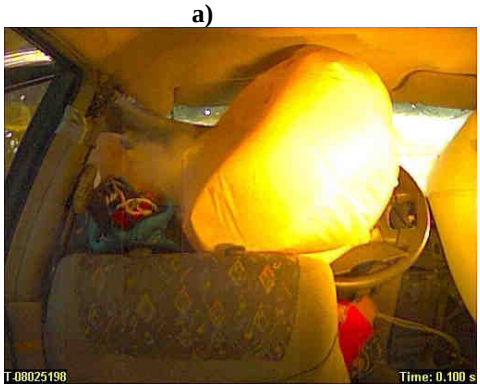

b)

Figure 2 – Interior rear-view snapshots 100 ms into the a) vehicle-vehicle test replicating the CCIS case and b) barrier tests. The tests showed two critical small overlap features, the lateral motion of the dummy and the intrusion of the steering wheel and instrument panel.

Full-scale car tests

The chosen circumstances for the vehicle-to-vehicle test were two identical cars (the same as the target vehicle in the chosen CCIS case) colliding collinearly with both cars traveling at a speed of 80 km/h. The circumstances for the first vehicle-to-barrier tests were chosen to be same type of car colliding at a speed of 80 km/h with a barrier at a 150 mm (approximately 6-inch) radius corner. Tests were carried out on an airfield with remote controls and the car engines as driving forces. The two tests resulted in 25 and 28% overlaps and both tests resulted in crash deformations typical for what the tests should replicate. In Figure 1 post crash photos of the vehicle-to-vehicle test and the chosen CCIS case are shown.

In both tests driver injury causations in the real-life case were more or less replicated. The head of the THOR dummy missed the driver airbag (see Figure 2) and the lower extremities interacted with the severely intruded toe-pan. Two critical events or features of this type of crash were identified, the intrusion of the instrument panel and the lateral motion of the occupant relative to the compartment during the crash.

The vehicle in the CCIS case and the full-scale tests were not available numerically (FE-code) to the authors. In order to vary crash circumstances in a cost-effective way two more vehicle-to-barrier crash tests were performed with a numerically available car model. Two Ford Taurus models from 2001 were crashed into a barrier with a 150 mm radius corner at

Figure 3 – Lateral view of the ΔV 50 km/h 26% overlap Taurus test 80 ms after contact with the flat barrier with the 150 mm radius corner.

a speed of approximately 80 km/h with resulting overlaps and ΔV of 19% and 32 km/h and 26% and 50 km/h respectively, (see Figure 3 for a lateral view 80 ms into the crash in the 26 % overlap Δv 50 km/h test).
For all crash tests the ratio of lateral and longitudinal displacements of the cars during the event were calculated. These calculations showed that a free flying mass in the car during the first tens of milliseconds would move less than 50 mm straight ahead in the car and thereafter stabilize to move at an specific angle ranging between 19 and 37 degrees in the four tests. This specific angle was used as a set-up angle in the sled test method. Also, the (resultant) crash pulse and change of velocity in this direction, was used as the ΔV in the sled test method.

Sled test development

According to the limited overlap literature, real-life analyses and the four full vehicle crash tests, the intrusion of the instrument panel/steering wheel and the lateral movement of the occupant with consequent injurious head contact with the side/A-pillar/exterior object were simulated in a sled test addressing protection of fatal head injuries. The sled test method was developed with a seat and door set-up at a specific angle to the track direction.

The angle should be equal to the set-up angle as defined above. The sled pulse, created by means of a combination of iron-bar bending and pneumatic brake is tuned to mimic the crash pulse of the full-scale test in this direction. Moreover, the toe-pan, instrument panel and steering wheel were guided by means of a set of linkage arms. After a specific time of the sled pulse, calculated from the full-scale crash to be replicated, the toe-pan, instrument panel and steering wheel is forced by means of a separate friction break system to rotate to a certain angle (see Figure 4). The range of rotation angle enabled intrusion-simulation of up to 300 mm of A-B pillar closure.

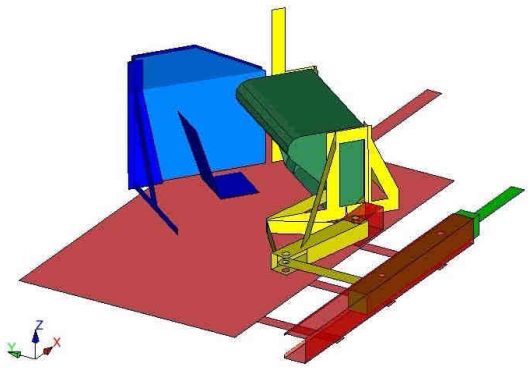

Figure 4- The seat and door (blue parts) are pre-set to a predetermined angle. The slewing bracket arrangement (yellow parts) allows rotation of the instrument panel (green) to a predetermined angle.

A series of sled tests were performed and results showed the method sufficiently robust to be used as a cost-effective method. Included in these tests was a validation test with the Taurus full-scale barrier test where the THOR dummy in the sled test was shown to move accordingly and hit the side structure with a resulting comparable HIC value (1707 compared to

1813). See Figure 5 for a snapshot at the moment of head contact with the door. In the sled test an inflatable curtain was added (in contrast to the Taurus tests) but the curtain had a negligible influence on the dummy head motion for this specific test condition.

Figure 5 – The THOR head 110 ms after start of the sled pulse. Accordingly, with real-life analysis and the full-scale tests, the head recorded a high HIC value.

THOR versus HIII

HIII and THOR comparison tests were also carried out for a test set-up simulating more conservative (less lateral motion) small car conditions. The tests were carried out with a set-up angle of 15 degrees (compared to 26 degrees in the previous sled tests). Even with less pronounced lateral motion the THOR reached about a head length farther than the HIII. The interaction with the driver airbag was also critically different. While the THOR head rolled off the bag with the face directed towards the bag the HIII head forward motion was obstructed and delayed by the bag. See also Figure 6 for lateral, front and top-views at 150 ms after impact and Appendix for shoulder, lap belt and femur force-time histories.

DISCUSSION

According to the literature and the executed real-life analyses, one of the injury mechanisms in small or narrow offset crashes is the head forced laterally outboards colliding with side or external structures. This paper presented a sled test method which simulated the lateral motion of the occupant in combination with the intrusion of instrument panel with the steering wheel and the frontal airbag. The HIII dummy was shown less flexible compared to the THOR dummy during this oblique loading. The THOR head moved a head-length's greater distance compared to the HIII in the comparison tests carried out at a moderate set-up angle. This was in accordance with HIII versus THUMS numerical simulations (Bostrom et al 2009, Mroz et al 2010) where the human body model in frontal collision conditions without lateral movement, moved a considerably greater distance compared to the HIII model (see Figure 7).

The sled test method, far more cost-effective compared to full-scale tests may be used in extensive development test series in order to develop, optimize or tune occupant restraints to be able to handle the situation when the occupant is forced outboards (actually, the car is forced) and the A-pillar, instrument panel and steering wheel intrude into the compartment. Examples of such occupant restraints are belts and frontal and side airbags.

As small overlap crashes include a high variety of circumstances both for the cars and occupants involved, the sled tests are still limited in incorporating all aspects of this important yet ill-defined crash type.

As the focus of the method was on fatal head injuries the method and the paper did not address important mechanisms such as thorax interaction with the side structure and lower extremity injuries due to extensive intrusion. Neither does the paper address the situation where the B-pillar is engaged in the striking car (one type of injury causation found by Lindquist (2006)).

If cars are designed to reduce the amount of intrusion in small overlap types of crashes the need for using the full performance capacity of the proposed method is reduced. On the other hand, when considering the laws of physics, avoiding intrusion will likely lead to higher lateral or longitudinal forces on the car. Thus, even with cars glancing off the collision partner, occupant restraints still need to be tested for their ability to protect an occupant from moving sideways and colliding with side structures.

Figure 6 – Lateral, top and front views 150 ms after impact of the tests with THOR (left) and HIII (right). The Δv was 60 km/h, the angle was set to 15 degrees and the amount of intrusion at the A-pillar base was almost 300 mm.

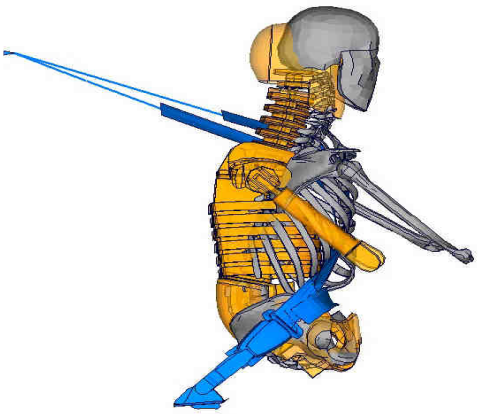

Figure 7 Lateral view of the HIII and THUMS models 100 ms after impact in a frontal collision (load limited belt and driver airbag) with no lateral movement. From Bostrom et al (2009).

CONCLUSIONS

The real-life small overlap crash and literature review revealed that in most fatal cases the AIS3+ injuries were multiple and the dominating injury mechanisms were head impacts with the inboard side, A-pillar or external objects. Full-scale crashes with the THOR dummy confirmed this. A sled test method was developed replicating critical events in the full-scale crashes. In additional tests with the HIII dummy there was no indication of head contact with the inboard side.

In order to protect the head in small overlap situations the structure of the car and the belt and airbag system may have to be enhanced. In conclusion, the paper offers an adjustable sled test method as a tool for understanding how to protect the head in a set of small overlap types of crashes.

REFERENCES

Bostrom O, Mroz K, Pipkorn B, Olsson J, "Influence of Belt Load-Limiting Force on Thorax Deflection, Rib Strain and Excursion in Frontal Impacts -A Numerical Evaluation using THUMS and HIII", Government/Industry Meeting, 2009.

Hollowell W T, "Overview of NHTSA´s compatibility and frontal impact activities", FIMCAR workshop, 2011.

IIHS Status report Vol 42, No 2, March 7, 2009.

Kullgren A., Ydenius A., Tingvall C."Frontal impacts with small partial overlap: Real-life data from crash recorders". ESV 1998, Paper No: 98-S1-O-13.

Lindquist M, "Fatal car crash configurations and injury panorama- with special emphasis on the function of restraint system", PhD Thesis, Umeå University, 2007.

Lindquist M., Hall A., Björnstig U. "Car structural characteristics of fatal frontal crashes in Sweden". IJCrash vol 9, 2004.

Lindquist M, Hall R, Björnstig U, "Kinematics of belted fatalities in frontal collisions: a new approach in deep studies of injury mechanisms", Journal of Trauma 61: 1506-16, 2006.

Kruse D, "Passenger cars in fatal small overlap frontal impacts, an in-depth study of injuries, injury causations and potential injury reductions for nearside impact positioned belted drivers", Autoliv internal report 2008.

Kruse D, "Test set-up documentation and function description based on confirmative tests for Off-set overlap frontal impact test method", Autoliv internal report 2009.

Mackay GM, "Injury and Collision severity". STAPP1968.

Mroz K, Bostrom O, Pipkorn B, Wisman J, Brolin K, "Comparison of Hybrid III and human body models in evaluating thoracic response for various seat belt and airbag loading conditions", Ircobi2010

O'Neill B., Lund A.K., Preuss C.A., Zuby D.S., "(IIHS/NASS 90-92): Offset Frontal Impacts – A Comparison of Real-World Crashes with Laboratory Tests". Paper No: 94-S4-O-19, ESV 1994.

Planath I, Norin H, Nilson S, "Severe frontal collisions with partial overlap – significance, test methods and car design". SAE Technical report 930636, 1993.

Pintar FA, Yoganandan N, Maiman DJ. "Injury mechanisms and severity in narrow offset frontal impacts". Ann Adv Automot Med 2008.

Saunders J, "Evaluation of Small Overlap / Oblique Test Procedures", 2010 Government/Industry Meeting, January, 2010.

Scullion P, Morgan RM, Mohan P, Kan CD, Shanks K, Jin W, Tangirala R, “A reexamination of the small overlap frontal crash”. Ann Adv Automot Med 2010

Sherwood C, Nolan J, Zuby D, “Characteristics of small overlap crashes”, paper number 09-0423, ESV2009.

Sheerwood C, “An Update on the IIHS Small Overlap Frontal Crash Research Program”, 2011 Government/Industry Meeting, January, 2011.

Shaw G, Lessley, D, Crandall J, Butcher J, “Biofidelity evaluation of the THOR advanced Frontal crash test dummy”. Ircobi2000.

Tornvall FV, Holmqvist K, Davidsson J, Svensson MY, Haland Y, Ohrn H, “A new THOR shoulder design: A comparison with volunteers, the Hybrid III and THOR NT”. Short paper Ircobi2006.

APPENDIX

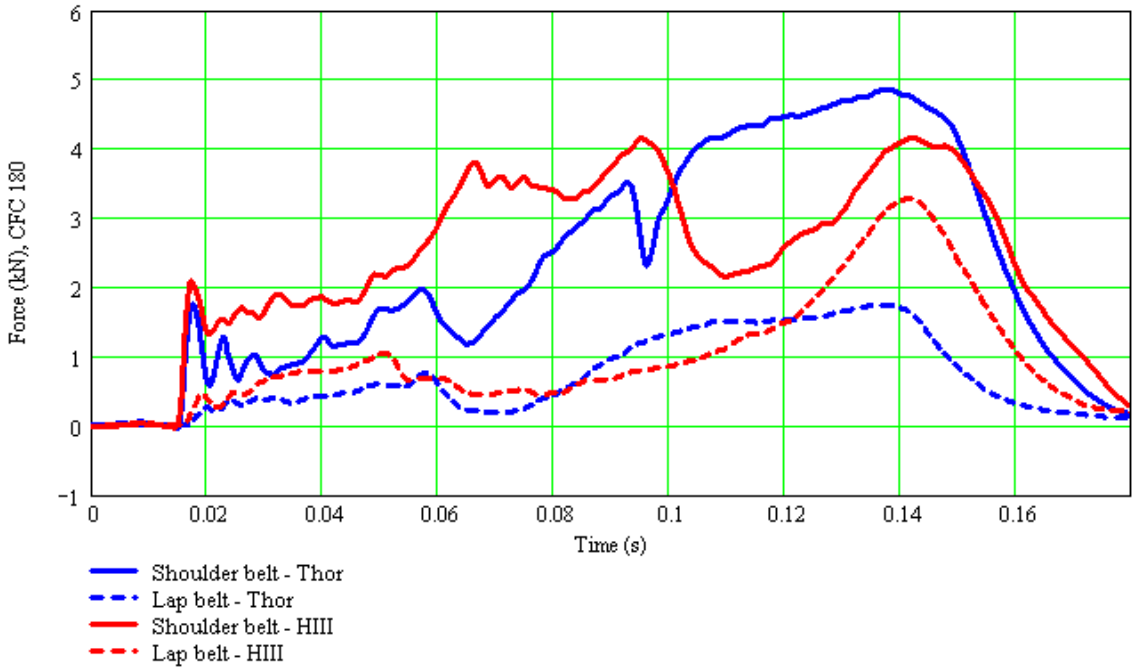
Force (kN), CFC 180
Time (s)
Shoulder belt - Thor
Lap belt - Thor
Shoulder belt - HIII
Lap belt - HIII

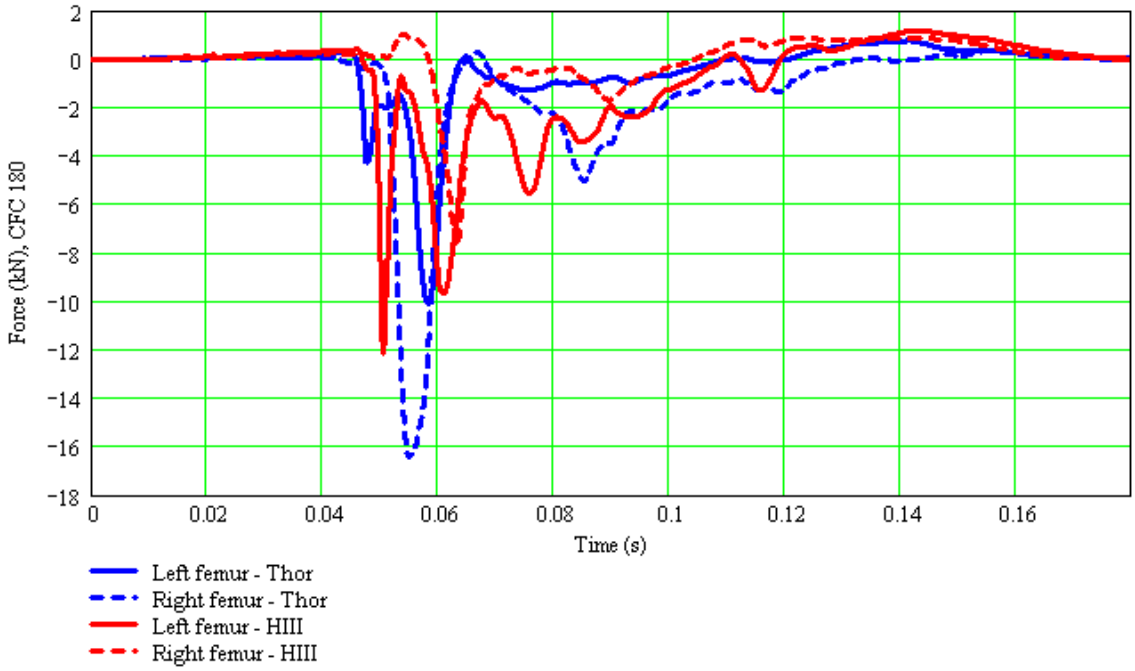
Force (kN), CFC 180
Time (s)
Left femur - Thor
Right femur - Thor
Left femur - HIII
Right femur - HIII

KINEMATIC ROTATIONAL BRAIN INJURY CRITERION (BRIC)

Erik G. Takhounts
National Highway Traffic Safety Administration
Vikas Hasija
Bowhead Systems Management, Inc
Stephen A. Ridella
National Highway Traffic Safety Administration
Steve Rowson
Stefan M. Duma
Virginia Tech
Paper Number: 11-0263

ABSTRACT

Head rotation as a mechanism for brain injury was proposed back in the 1940s. Since then a multitude of research studies by various institutions were conducted to confirm/reject this hypothesis. Most of the studies were conducted on animals and concluded that rotational acceleration sustained by the animal's head may cause axonal deformations large enough to induce their functional disruption. Other studies utilized mathematical models of human and animal heads to derive brain injury criteria based on deformation/pressure histories computed from the models. This study differs from the previous research in the following ways: first, it uses a detailed mathematical model of human head validated against various human brain response datasets; then establishes physical (strain and stress based) injury criteria for various types of brain injury based on scaled animal injury data; and finally, uses dummy (Hybrid III, ES-2re, WorldSID; all 50th percentile male) test data to establish kinematically (rotational accelerations and velocities) based brain injury criterion (BRIC) for each dummy. Similar procedures were applied to the college football data where thousands of head impacts were recorded using a six degrees of freedom (6 DOF) instrumented helmet system. Since animal injury data used in derivation of BRIC were predominantly for diffuse axonal injury (DAI) which is an AIS 4+ injury, cumulative strain damage measure (CSDM) was used to derive BRIC risk curve for AIS 4+ brain injuries. The AIS 1+, 2+, 3+, and 5+ risk curves for CSDM were then computed using the ratios between corresponding risk curves for head injury criterion (HIC) at a 50% risk. The risk curves for BRIC were then obtained by setting its value to 1 such that it corresponds to 30% probability of DAI (AIS4+). The newly developed brain injury criterion is a complement to the existing HIC which is based on translational accelerations. Together, the two criteria may be able to capture most brain injuries and skull fractures occurring in automotive or any other impact environment. One of the main limitations for any brain injury criteria, including BRIC, is the lack of human injury data to validate the criteria against, although some approximation for AIS 2+ injury is given based on the estimate of average injurious (concussion) angular velocities and accelerations for the college football players instrumented with 5 DOF helmet system. Despite the limitations, a new kinematic rotational brain injury criterion – BRIC – may offer additional protection to an automotive occupant in situations when using translational accelerations based HIC alone may not be sufficient.

INTRODUCTION

According to the Centers for Disease Control (CDC) traumatic brain injury (TBI) is an important public health problem in the United States. TBI is frequently referred to as the "silent epidemic" because the complications from TBI, such as changes affecting thinking, sensation, language, or emotions, may not be readily apparent. The most recent CDC report (Frieden et. al, 2010) estimates 1.7 million people sustain a TBI annually, of them 52,000 die. The report finds that among all age groups, motor vehicle-traffic (MVT) was the second leading cause of TBI (17.3%) and resulted in the largest percentage of TBI-related deaths (31.8%).

Based on NASS-CDS analyses of frontal crashes (Eigen and Martin, 2005) fatalities attributable to head injuries are second only to fatalities attributable

to thoracic region (Figure 1) with societal costs exceeding $6 Billion.

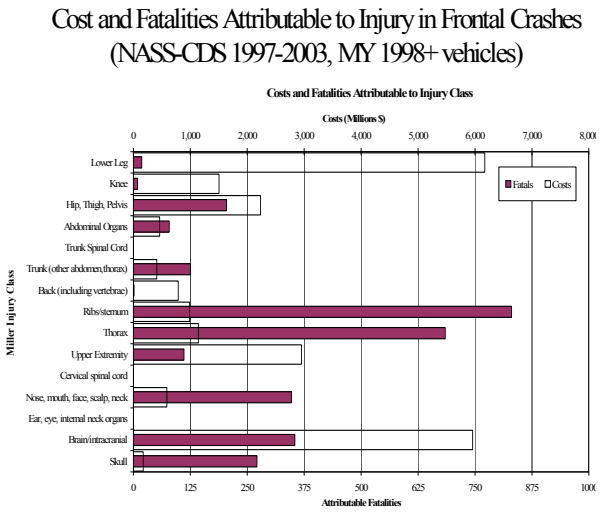

FIGURE 1. Cost and fatalities attributable to injuries in frontal crashes (Eigen and Martin 2005).

Many attempts have been made in the past to reduce the occurrence and severity of TBI as a result of automotive crashes. Among them are design and development of improved safety systems governed by various Federal Motor Vehicle Safety Standards (FMVSS), requirements of the New Car Assessment Program (NCAP), tests of Insurance Institute for Highway Safety (IIHS), and others. However, despite of all these requirements TBI is still one of the most frequent injury types in MVC (Figure 1). The reasons for this may be multiple: (1) the mandatory and voluntary requirements may not capture some real world crash scenarios leading to TBI, (2) the test dummies used in the tests are not interacting with vehicle environment in the way humans do, and (3) the interpretation of the dummies' measurements is not sufficient to capture all possible types of TBI.

It is reason 3 that is investigated in this paper with the focus on the most frequent type of TBI – diffuse axonal injury (DAI). First, we make use of the scaled animal data (Abel et al., 1978; Gennarelli et al., 1982; Stalnaker et al., 1977; Nusholtz et al., 1984; Meaney et al., 1993) along with the NHTSA developed finite element (FE) model of human brain, e.g. the simulated injury monitor (SIMon) and its biomechanical injury criterion for DAI – cumulative strain damage measure (CSDM) (Takhounts et al., 2003 and 2008). Then, assuming DAI and its biomechanical equivalent - CSDM to be an AIS 4+ injury (AAAM, 2005), the risk curves for CSDM are scaled to AIS 1+, 2+, 3+, and 5+ using ratios between the risk curves similar to those developed for HIC (FMVSS 208) at 50% risk. These scaled CSDM risk curves represent various severities of concussive injuries. For example, AIS 3+ risk curve is a risk of severe concussion with the loss of consciousness 1-6 hours (AAAM, 2005). Finally, kinematic brain injury criteria (BRIC) were developed for each tested dummy (Hybrid III, ES2-re, and WorldSID) as well as human volunteers based on college football data.

METHODS

The SIMon model was tested using available experimental animal injury data, including rhesus monkeys (Abel et al., 1978; Gennarelli et al., 1982; Stalnaker et al., 1977; Nusholtz et al., 1984), baboons (Stalnaker et al., 1977), and miniature pigs (Meaney et al., 1993). A total of 114 animal brain injury experiments were simulated in the development of the biomechanical injury metric - CSDM. The experimental kinematic loading conditions were scaled in amplitude and time to satisfy the equal stress/velocity scaling relationship, i.e., translational velocity scaled as 1, angular velocity as $1/\lambda$, and time scaled as λ, where λ is the scaling ratio (Takhounts et al., 2003). Once correctly scaled, these loading conditions were applied to the SIMon model. The SIMon FE model consists of 42,500 nodes and 45,875 elements, of which 5153 are shell elements (3790 rigid), 14 are beam elements, and 40,708 are solid elements (Takhounts et al., 2008). Major parts of the brain were represented: cerebrum, cerebellum, brainstem, ventricles, combined CSF and pia arachnoid complex (PAC) layer, falx, tentorium, and parasagittal blood vessels (Figure 2).

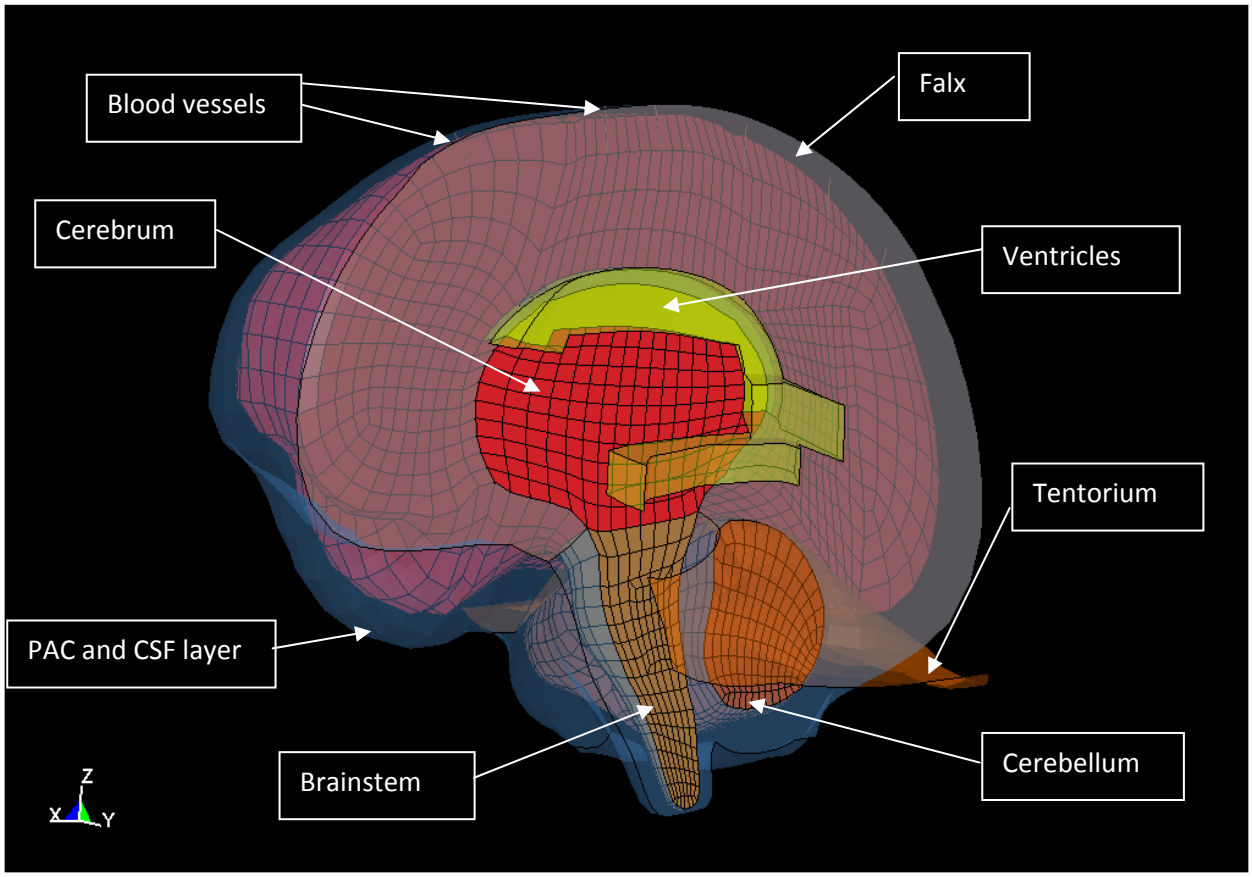

FIGURE 2. SIMon Finite Element Head Model

It was assumed that the injury results from animal subjects were the same as that which would be observed from a human under the equivalent impact input.

CSDM is based on the hypothesis that DAI is associated with the cumulative volume of brain tissue experiencing tensile strains over a predefined critical level. The CSDM metric predicts injury by monitoring the accumulation of strain damage. This is accomplished by calculating the volume fraction of the brain which sometime during the event is experiencing strain levels greater than various specified levels. This strain level is based on the maximum principal strain calculated from a strain tensor that is obtained by the integration of the rate of deformation tensor (Bandak and Eppinger, 1995). The cumulative nature of the CSDM means that the strain damage at the end state of a calculation may be related to the DAI associated with a particular loading regime. To select the critical values of strain and volume for the CSDM injury metric, data from animal experiments conducted by Abel et al. (1978), Stalnaker et al (1977), Nusholtz et al., (1984), and Meaney et al. (1993) was used to relate the CSDM levels to the observed occurrence of DAI.

The risk curve for CSDM was constructed using survival analysis (Weibull distribution, left/right censored data):

$$Injury\ Risk = 1 - e^{-(\frac{CSDM}{\lambda})^k}, \quad (1)$$

where λ is scale and k is shape parameter for Weibull distribution. In the case of CSDM, λ = 0.6162 (st. err. 0.0431), and k = 2.7667 (st. err. 1.0302), Max Loglikelihood = -31.7.

This injury risk curve (Eq. 1) would correspond to AIS 4+ brain injury according to the recently published AIS scale (AAAM, 2005) for DAI. To obtain other levels of the abbreviated injury scale, the risk curves for HIC were used (The U.S. Department

of Transportation's FMVSS No. 208 Final Economic Assessment), assuming equal severity ratios between corresponding risk curves for HIC and CSDM at 50% risks. For example, to obtain AIS3+ risk curve for CSDM, the ratio (β_{34}) of AIS3+/AIS4+ risk curves at 50% for HIC was found, and then AIS4+ risk curve for CSDM at 50% was multiplied by this ratio to find 50% risk point for the AIS3+ CSDM:

$$\text{CSDM AIS3+ (50\%)} = \beta_{34} * \text{CSDM AIS4+ (50\%)}. \quad (2)$$

Using Eqs. 1 and 2 together the CSDM risk curve for AIS3+ was found. Other risk curves for CSDM were found in the similar fashion.

Next, frontal impact tests with the Hybrid III dummy (43 NCAP tests - drivers and passengers - available from NHTSA database), 31 side impact tests with ES-2re test dummy, and eight side impact tests with WorldSID test dummy (all were 50th Percentile male sized) were used to develop BRIC for each dummy. To do that, first, CSDM values were calculated for each test. Then optimization was carried out to obtain the best linear fit between CSDM and BRIC (in the form of equation 3) using critical values of angular velocity and acceleration ω_{cr} and α_{cr} as design variables and subjected to the constraint that BRIC =1 when CSDM =0.425 (30% probability of DAI/AIS4+).

$$BRIC = \frac{\omega_{max}}{\omega_{cr}} + \frac{\alpha_{max}}{\alpha_{cr}}, \quad (3)$$

where ω_{max} and α_{max} are maximum angular velocities and accelerations for each test respectively. The linear relationship between CSDM and BRIC was then utilized to obtain risk curves for each dummy.

Similarly to the procedure above, BRIC was developed based on translational and rotational data obtained from the college football players. Between 2007 and 2008, the helmets of 19 Virginia Tech football players were instrumented with a custom 6 degree of freedom (6DOF) head acceleration measurement device (Rowson et al, 2009). The measurement device consists of 12 accelerometers and recorded linear and angular acceleration about each axis of the head using a novel algorithm (Chu et al, 2006). Any time an accelerometer exceeded 10 g during play, data acquisition was automatically triggered and data were collected for 40 ms (including 8 ms of pre-trigger data). Once data collection was complete, data were wirelessly transmitted to a computer on the sideline. Linear and angular head accelerations were recorded for a total of 4709 head impacts of which 362 had peak resultant linear accelerations greater than 40 g. To determine resultant angular velocity, angular acceleration about each individual axis of the head was numerically integrated throughout the entire acceleration trace. Resultant angular velocity was then calculated. Each impact was visually inspected so that the angular acceleration (and resulting angular velocity) pulse of interest could be examined and peak values identified. Once peak angular acceleration and peak angular velocity were determined for each impact, a linear regression analysis was performed using a least squares technique. The regression model was constrained so that an angular acceleration of 0 rad/s^2 resulted in an angular velocity of 0 rad/s. Although none of the 6 DOF impacts resulted in brain or other head injury, CSDM and BRIC curves were computed to assess the potential for TBI.

To evaluate BRIC for college football players, concussive data were generated using the commercially available 5 DOF HIT System (Simbex, Lebanon, NH). This head acceleration device consisted of 6 accelerometers and measure resultant linear acceleration of the head. This device is limited in that only peak angular acceleration can be estimated from an assumed pivot point in the neck. Resultant angular velocities for concussive data points were estimated from resultant angular accelerations using a regression model. Details of the methods used for data collection can be found in the literature (Duma et al, 2005, Duma et al, 2009). Using the HIT System, head acceleration data were recorded for 6 concussions between 2003 and 2008 (Duma et al, 2009). These 6 concussions were combined with concussive data collected from published studies that utilized identical data collection methods (Broglio et al, 2010, Guskiewicz et al, 2007). This resulted in a dataset of 32 concussions.

RESULTS

Figure 3 illustrates the probability of DAI as a function of CSDM along with the 95% confidence intervals.

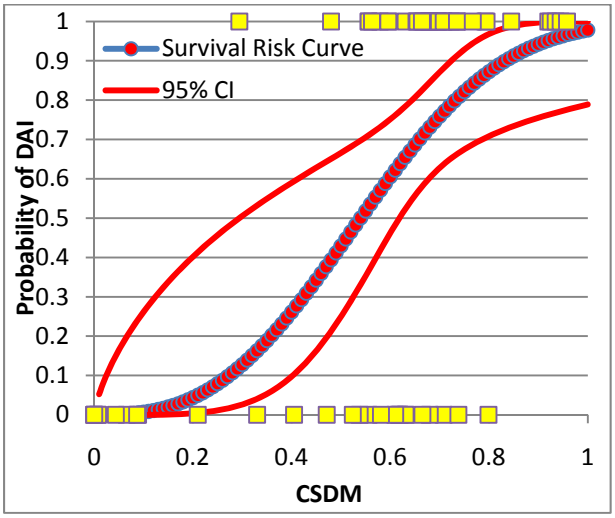

FIGURE 3. Risk of DAI (AIS 4+) as a function of CSDM based on animal injury data.

The ratios β_{i4}, where i is the level of AIS of interest, are given in Table 1.

Table 1. Ratios for computing risk curves for AIS 1, 2, 3, and 5 based on known risk curve for AIS 4.

β_{14}	β_{24}	β_{34}	β_{54}
0.1003	0.5003	0.8156	1.0411

Probability of brain injuries as functions of CSDM for various AIS levels are shown in Figure 4.

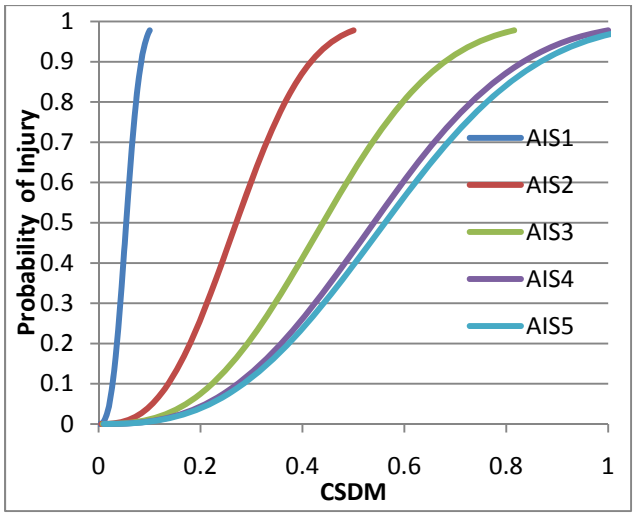

FIGURE 4. Risk of brain injuries as a function of CSDM for various AIS levels.

The following three charts show the probabilities of brain injury as functions of BRIC for each AIS level for Hybrid III (Figure 5), ES-2re (Figure 6), and WorldSID 50th percentile male dummies (Figure 7).

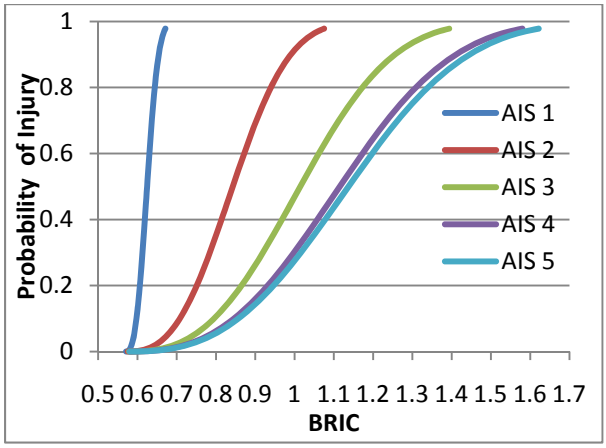

FIGURE 5. Risk of brain injuries as a function of BRIC for various AIS levels for Hybrid III.

The critical values of angular velocity and acceleration for the Hybrid III dummy were found to be ω_{cr} = 46.41 rad/s and α_{cr} = 39,774.87 rad/s^2, R^2 = 0.38.

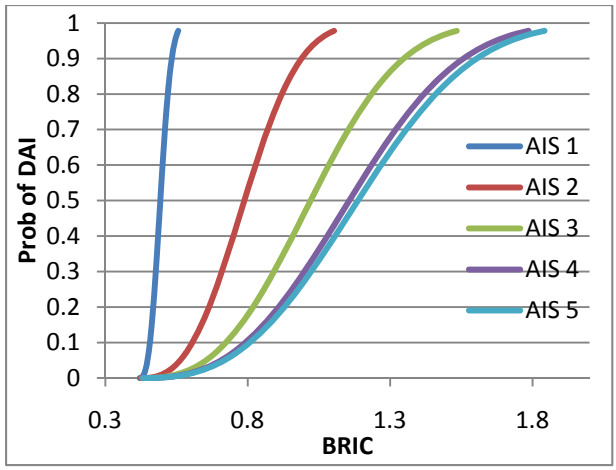

FIGURE 6. Risk of brain injuries as a function of BRIC for various AIS levels for ES-2re.

The critical values of angular velocity and acceleration for the ES-2re dummy were found to be ω_{cr} = 65.68 rad/s and α_{cr} = 23,063.90 rad/s^2, R^2 = 0.70.

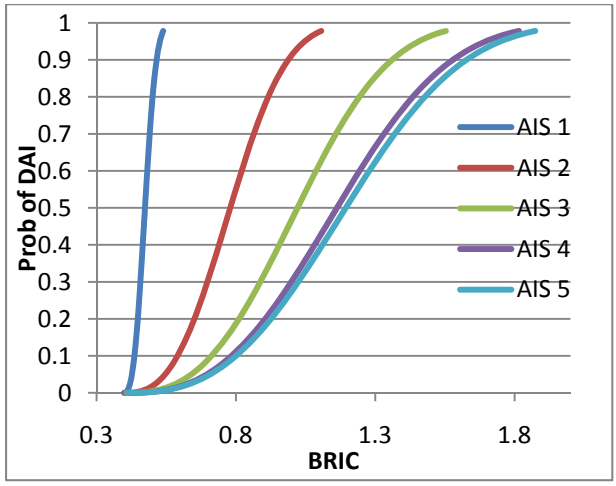

FIGURE 7. Risk of brain injuries as a function of BRIC for various AIS levels for WorldSID.

The critical values of angular velocity and acceleration for the WorldSID dummy were found to be ω_{cr} = 153.18 rad/s and α_{cr} = 11,527.92 rad/s^2, R^2 = 0.94.

For college football players, peak angular acceleration and peak angular velocity correlated strongly (R^2 = 0.96), proving to be a linear relationship. This suggests that most impact pulses in football are similar in duration and acceleration shape. For non-injury data points, the average angular acceleration was 2,404.00 rad/s^2 and the average angular velocity was 10.00 rad/s. The average concussive angular acceleration was 6,572.00 rad/s^2 and the average concussive angular velocity was 28.00 rad/s.

Figure 8 shows BRIC criterion for the college football players. The critical values of angular velocity and acceleration for the college football players were found to be ω_{cr} = 42.05 rad/s and α_{cr} = 363,268.91 rad/s^2, R^2 = 0.81.

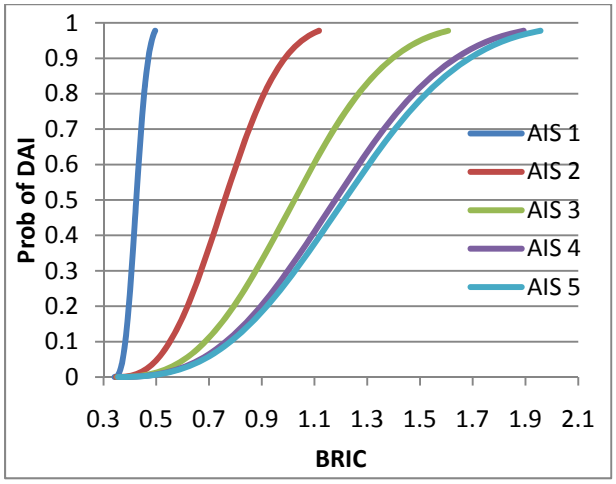

FIGURE 8. Risk of brain injuries as a function of BRIC for various AIS levels for college football players.

It should be noted that the high intercept value for angular velocity for WorldSID and high value of intercept for angular acceleration for human football data compared to those of Hybrid III and ES-2re, are due to high correlation between the angular velocities and angular accelerations for these two datasets. In these cases, the optimizer usually chooses one of the parameters in the optimization process and "makes" the other one irrelevant (very high value).

DISCUSSION

The importance of head rotational kinematics as a mechanism for brain injuries has been discussed in the scientific literature since the 1940s (Holbourn, 1943, Gennarelli et al. 1972, Ueno and Melvin 1995). More recently, Hardy et al, 2001 and 2007, in the experiments describing the motion of brain with respect to the overall motion of the skull, noted that

angular velocity was the most "convenient" measure in describing relationship between brain and skull kinematics. Takhounts et al (2008) described that one of the ways to deform/strain a soft, nearly incompressible material (brain) contained within an almost undeformable shell (skull) is to rotate the shell.

Despite the overwhelming evidence of the head rotational kinematics to be a mechanism for brain injuries, the difficulty was in relating animal injury data (Abel et al., 1978; Gennarelli et al., 1982; Stalnaker et al., 1977; Nusholtz et al., 1984; Stalnaker et al., 1977; Meaney et al., 1993, Ommaya, 1985) to the potential for brain injuries in humans. One possible way to accomplish this is to find injury criteria for animals and then scale it to humans using various scaling relationships (Ommaya, 1985). The advantage of this approach is in its simplicity – it is straightforward and a criterion is easily computed. The disadvantage of the approach is also in its simplicity as it doesn't necessarily address the equivalency of the brain deformations (believed to be the primary cause of TBI) inside the brains of animals and humans. Another approach for relating animal injury data to humans is to develop FE models of animals and humans, find a scaling relationship between the two (Takhounts et al, 2003), and then develop a deformation/strain based criterion (CSDM) that would be equally applicable for both animals and humans. The advantage of this approach is that it gives a link between deformation fields inside the brains of animals and humans and thus may be more physically/biomechanically justifiable. The disadvantage of the approach is that it requires a powerful computer and several hours of run time to calculate CSDM. Both approaches suffer, however, from the lack of knowledge of how the injury severity in animals would translate to the injury severity in humans given equivalent loading conditions.

A second approach was adapted in this paper where an already developed and validated finite element model of human head – SIMon – was employed along with its injury criterion for DAI – CSDM (Takhounts et al, 2008). Once CSDM was computed and scaled for various AIS levels (Eq. 2), BRIC was calculated for each tested dummy and college football players in the form of equation 3 where it was set to the value of 1 to correspond to 30% probability of DAI (AIS 4+ injury). There are many different ways of obtaining BRIC from CSDM, but the chosen value of 1 corresponding to 30% of DAI indicates that the closer the BRIC is to the value of 1 a worse outcome can be expected.

BRIC is a correlate, not a fundamental property of a system (like CSDM), hence it was anticipated that different dummies (and humans) will have different relationships of BRIC to CSDM (figures 5 – 8) even when they all are "forced" through the same point in the BRIC vs. CSDM relationship, e.g. point (0.425, 1), where CSDM = 0.425 corresponds to 30% probability of DAI (Fig. 3). This difference is due to different values of slopes and intercepts in the assumed linear relationship between CSDM and BRIC for different dummies and humans, which, in turn may be caused by the difference in impact conditions and properties of the neck.

If concussion is assumed to be a mild form of DAI, then figures 5 – 8 could be used in assessing concussion as an AIS 2+ injury (AAAM, 2005). For example, 30% probability of concussion in college football players will give BRIC equal to 0.67, which at the same time gives approximately 5% chances of DAI. Substituting the average values of angular acceleration and velocity for concussed players into BRIC for football players gives the concussed value of BRIC equal to 0.68. Referring to Figure 8 this value of BRIC gives about 33% probability of concussion (AIS 2+ risk curve) or 5% probability of DAI (AIS 4+ risk curve). From the same Figure 8, the risk of AIS 3+ TBI for BRIC = 0.68 is approximately 10%. This risk is probably the upper limit of what a regular human (not a trained athlete) should be allowed to experience when protecting against concussion. The risk of AIS 3+ TBI for BRIC = 0.68 when using the Hybrid III dummy as an assessment tool (Figure 5) is approximately 1%, when using ES-2re dummy it is approximately 7% (figure 6), and when using the WorldSID it is about 8% (figure 7). This illustrates that the values of BRIC should be used in conjunction with the injury assessment device (dummies or humans) it is measured with.

Ommaya (1985) gave an overview of the rotational injury tolerance values for the onset of concussion based on the research conducted on rhesus monkeys and chimpanzees. The human rotational tolerances were obtained using a mass scaling relationship for angular accelerations (inversely proportional to the two-thirds power of the brain mass) giving angular velocity and acceleration tolerances for human of 20 – 30 rad/s and 1,800 rad/s^2 respectively. Inserting these tolerance values into Eq. 3 and using critical values obtained from college football data for humans will give BRIC values between 0.48 (for angular velocity of 20 rad/s) and 0.72 (for angular velocity of 30 rad/s). Referring to the AIS2+ risk curve for humans (Figure 8) will give a risk of concussion ranging from 3% - 41% depending of the chosen tolerance value of angular velocity. Taking an average angular velocity of 25 rad/s will give BRIC equal to 0.60 and 17% risk of AIS2+ injury. The BRIC of 0.68 obtained from football data is within the range of those obtained from scaling animal data and is closer to the upper limit of 0.72.

Several approaches may be taken if BRIC is used in an automotive environment. One of them is to restrict BRIC for each injury assessment device to be no greater than the value at the respective 30% risks of AIS 3+ TBI (similar to HIC). This approach will give critical value of BRIC for the Hybrid III equal to 0.92, for ES-2re and WorldSID equal to 0.89.

The limitations of this study are multiple.

- First, all the limitations that were applicable in the development and validation of SIMon finite element head model (Takhounts et al, 2003, 2008) are applicable to this paper as well. In addition, correlation between CSDM and BRIC is not perfect that will add additional errors to the injury risk estimates. It should be noted, however, that similar limitations are applicable to any research – computational and/or experimental.
- Second, only DAI was investigated in this study. Inclusion of other types of TBI, such as focal lesions, contusions, or hematomas, may change the relationship for BRIC. However, BRIC is not an "ultimate" head injury criterion that captures all possible brain injuries and skull fractures, but rather a correlate to TBI with head rotation being a primary injury mechanism.
- Third, deriving CSDM and BRIC risk curves for various AIS levels based on ratios between 50% risks for different AIS levels for HIC assumes that rotationally induced injury severities change proportionally to those induced translationally. This assumption may or may not be correct, but due to lack of any data on rotational based changes in injury severity this assumption provides a "first approximation" of these changes.
- Fourth, although very valuable, the college football data has its own limitations: athletes are trained to sustain higher loads, the average concussed angular velocity and acceleration were calculated from the 5 DOF measuring system rather than measured directly by the 6 DOF system, thus the accuracy of these values may be questioned.
- Fifth, regarding scaling of the animal tolerances to those of humans, it is interesting to give a quote from Ommaya (1985): "It should be reemphasized that this information (rotational tolerances) is considered to be reliable for the Rhesus, sketchy for the chimpanzee, and completely speculative for man." He then suggests revising the human rotational tolerances when the data from accident reconstruction in humans become available. College football data may be considered as one of these "accident reconstruction" data.
- Finally, BRIC is a rotational injury criterion (see second limitation), while HIC is a translational injury criterion (calculated using translational accelerations only), and combining the two may offer better protection from head injuries. However, a human head is rarely experiencing just rotational or just translational motion. It usually is experiencing both. This paper does not address this combination of both modes of motion and corresponding injury mechanisms. This has been proposed by

others, but additional work to derive a relationship is required.

Despite the limitations that are inherent in any research, this paper provides valuable information on the importance on limiting rotational kinematics of the human head that may be beneficial to both – athletes and general driving population.

CONCLUSIONS

A kinematic rotational brain injury criterion – BRIC – was developed for three 50th percentile test dummies (HIII, ES-2re, and WorldSID) and human athletes. Following are the conclusions:

- BRIC is different for different dummies and human athletes.
- Concussive (AIS 2+) values of BRIC for humans varied from 0.60 when scaled directly from animal data (Ommaya, 1985) to 0.68 when obtained directly from the college football players.
- The risk of AIS 3+ TBI for BRIC = 0.68 when using the Hybrid III dummy as an assessment tool is approximately 1%, when using ES-2re dummy it is approximately 7%, and when using the WorldSID it is also about 8%.
- BRIC for the 30% risk of AIS 3+ TBI is 0.92 if measured with HIII dummy, 0.89 if measured with ES-2re and WorldSID dummies.
- BRIC should be used in combination with HIC. However, the risk of TBI for combination of rotational and translational loading modes should be investigated in the future.

REFERENCES

AAAM (2005) "Abbreviated Injury Scale 2005." Association for the Advancement of Automotive Medicine: 45-51.

Abel, J., Gennarelli, T.A., Seagawa, H. (1978) In cadence and severity of cerebral concussion in the rhesus monkey following sagittal plane angular acceleration. Proc. 22nd Stapp Car Crash Conference, pp. 33-53, Society of Automotive Engineers, Warrendale, PA.

Bandak, F.A., and Eppinger, R.H. (1995) A three-dimensional finite element analysis of the human brain under combined rotational and translational acceleration. Proc. 38th Stapp Car Crash Conference, pp. 145-163. Society of Automotive Engineers, Warrendale, PA.

Broglio, S.P., Schnebel, B., Sosnoff, J.J., Shin, S., Fend, X., He, X., and Zimmerman, J., *Biomechanical properties of concussions in high school football.* Med Sci Sports Exerc, 2010. **42**(11): p. 2064-71.

CDC, National Center for Injury Prevention and Control, 'Traumatic Brain Injury Facts', http://www.cdc.gov/ncipc/factsheets/tbi.htm, 2003.

Chu, J. J., Beckwith, J. G., Crisco, J. J., and Greenwald, R. (2006) A Novel Algorithm to Measure Linear and Rotational Head Acceleration Using Single-Axis Accelerometers. in World Congress of Biomechanics, Munich, Germany.

Duma, S.M., Manoogian, S.J., Bussone, W.R., Brolinson, P.G., Goforth, M.W., Donnenwerth, J.J., Greenwald, R.M., Chu, J.J., and Crisco, J.J., *Analysis of real-time head accelerations in collegiate football players.* Clin J Sport Med, 2005. **15**(1): p. 3-8.

Duma, S.M. and Rowson, S., *Every newton hertz: A macro to micro approach to investigating brain injury.* Conf Proc IEEE Eng Med Biol Soc, 2009. **1**: p. 1123-6.

Eigen, A. M. and Martin, P. G. (2005) Identification of real world injury patterns in aid of dummy development. 19th Enhanced Safety of Vehicles.

Frieden, T.R., Ikeda, R., Hunt, R.C., Faul, M., Xu, L., Wald, M.M., Coronado, V. (2010) Traumatic Brain Injury in The United States: Emergency Department Visits, Hospitalizations and Deaths 2002 – 2006. National Center for Injury Prevention and Control, Centers for Desease Control and Prevention, U.S. Department of Health and Human Services.

Gennarelli, T.A., Thibault, L.E., and Ommaya, A.K. (1972) Pathophysiologic Responses to Rotational and Translational Accelerations of the Head. Stapp Car Crash Journal 16: 296-308.

Gennarelli, T.A., Thibault, L.E., Adams, J.H., Graham, D.I., Thompson, C.J., and Marcincin, R.P. (1982) Diffuse axonal injury and traumatic coma in the primate. Annals of Neurology 12(6): 564-574.

Guskiewicz, K.M., Mihalik, J.P., Shankar, V., Marshall, S.W., Crowell, D.H., Oliaro, S.M., Ciocca, M.F., and Hooker, D.N., *Measurement of head impacts in collegiate football players: relationship between head impact biomechanics and acute clinical outcome after concussion.* Neurosurgery, 2007. **61**(6): p. 1244-53

Hardy, W.N., Foster, C., Mason, M., Yang, K., King, A., Tashman, S. (2001) Investigation of head injury mechanisms using neutral density technology and high-speed biplanar X-ray. Stapp Car Crash Journal 45: 337-368.

Hardy, W.N., Mason, M.J., Foster, C.D., Shah, C.S., Kopacz, J.M., Yang, K.H., King, A.L., Bishop, J., Bey, M., Anderst, W., Tashman, S. (2007) A Study of the Response of the Human Cadaver Head to Impact. Stapp Car Crash Journal, Vol. 51, pp. 17-80.

Holbourn, A.H.S. (1943) Mechanics of head injury. Lancet 2, October 9: 438-441.

Manoogian, S., McNeely, D., Duma, S., Brolinson, G., and Greenwald, R. (2006) Head acceleration is less than 10 percent of helmet acceleration in football impacts. Biomed Sci Instrum, vol. 42: 383-388.

Meaney, D.F, Smith, D., Ross, D.T., and Gennarelli, T.A. (1993) Diffuse axonal injury in the miniature pig: Biomechanical development and injury threshold. ASME Crashworthiness and occupant protection in transportation systems 25: 169-175.

Nusholtz, G.S., Lux, P., Kaiker, P., and Janicki, M.A., (1984) Head impact response skull deformation and angular accelerations. Proc. 28th Stapp Car Crash Conference, pp. 41-74, Society of Automotive Engineers, Warrendale, PA.

Ommaya A.K. (1985) Biomechanics of Head Injury: Experimental Aspects, in "The Biomechanics of Trauma" edited by Nahum A.M. and Melvin J.W., pp 245 – 269.

Rowson, S., Brolinson, G., Goforth, M., Dietter, D., and Duma, S.M., *Linear and angular head acceleration measurements in collegiate football.* J Biomech Eng, 2009. **131**(6): p. 061016.

Stalnaker, R.L., Alem, N.M., Benson, J.B., Melvin, J.W. (1977) Validation studies for head impact injury model. Final report DOT HS-802 566, National Highway Traffic Safety Administration, US, Department of Transportation, Washington, DC.

Takhounts, E.G., Eppinger, R.H., Campbell, J.Q., Tannous, R.E., Power, E.D., Shook, L.S. (2003) On the Development of the SIMon Finite Element Head Model. Stapp Car Crash Journal 47: 107-133.

Takhounts, E.G., Hasija, V., Ridella, S.A., Tannous, R.E., Campbell, J.Q., Malone, D., Danelson, K., Stitzel, J., Rowson, S., Duma, S, 2008, "Investigation of Traumatic Brain Injuries Using the Next Generation of Simulated Injury Monitor (SIMon) Finite Element Head Model." 52nd Stapp Car Crash Conference.

The U.S. Department of Transportation's FMVSS No. 208 Final Economic Assessment.

Ueno, K., and Melvin, J.W. (1995) Finite element model study of head impact based on hybrid III head acceleration: The effects of rotational and translational accelerations. J. Biomech Eng. 117(3): 319-328.

DEVELOPMENT OF A PROBABILISTIC SKULL FRACTURE MODEL FOR A 50TH PERCENTILE ADULT MALE MOTORCYCLIST ATD HEADFORM

R. M. Van Auken
T. A. Smith
J. W. Zellner
Dynamic Research, Inc.
United States of America
Paper Number 11-0035

ABSTRACT

The ability to measure and quantify the differences in injuries between helmeted and unhelmeted riders of motorcycles, quadricycles and other small open vehicles as well as injuries to other unhelmeted vulnerable road users such as pedestrians has led to the desire to extend motorcyclist injury assessment methods such as those in ISO 13232 (2005) to include the potential for skull fracture due to head contact forces (e.g., direct impact and crushing type injury mechanisms), in addition to the closed-skull brain injury probability calculations based on head accelerations which are currently in the ISO 13232 Standard (2005). A probabilistic injury model was developed for a 50th percentile adult male by correlating human biomechanical data on skull fractures with cranial vault and facial contact mechanical "work." This injury model was then transformed into an "equivalent work" model applicable to Motorcyclist Anthropometric Test Device (MATD) headform contact forces based on the series of assumptions listed. The biomechanical data comprised 64 cases involving temporoparietal region, maxilla and zygoma fractures as reported in Nahum et al. (1968) and Schneider and Nahum (1972). Laboratory tests were also conducted to measure the MATD contact forces during impact conditions that replicated those of the human cadaver tests reported in the scientific literature. The results demonstrated that the MATD headform contact forces can be measured and used to estimate the probabilities of an AIS 1, 2, 3, and 4 human cadaver face or vault fracture. The AIS probabilities generated from MATD testing were in substantial agreement with the scientific literature. Since the proposed skull fracture criteria are closely related to the forces acting on the skull that can result in bone fracture, rather than indirect measurements of these forces such as head acceleration, it is better suited for predicting skull fractures in some types of injury mechanisms (e.g., crushing type injury mechanisms) that may result in high contact forces but low resultant head accelerations. The resulting injury criteria for a 50th percentile adult male can be used to assess the probabilities of an AIS 2, 3, and 4 vault or AIS 1, 3, and 4 facial fracture resulting from unhelmeted head contact forces, using specialized test sensors and methods or calibrated ISO 13232 type computer simulations. The criteria are well suited for evaluating skull fracture injuries resulting from head contact forces and are complementary to existing head acceleration based injury criteria for closed skull brain injuries that are currently in the Standard. Limitations of the injury criteria are the relatively small number of available biomechanical data and the series of assumptions made. In addition, for potential use in crash tests, an ATD headform with specialized force sensors would also be needed to measure head contact forces in crash tests. The resulting probabilistic injury criteria provide a useful tool to assess the change in injury risks and benefits of potential protective devices for unhelmeted motorcycle and quadricycle riders, as well as pedestrians, using ISO 13232 type computer simulation methods.

INTRODUCTION

Background

ISO Standard 13232 (2005) [3] currently provides a method to assess the probability of injury and injury severity for specific types of injury to the head (closed skull brain), neck, chest (thorax), abdomen and lower extremities (femur, tibia and knee dislocation) based on objective measurements from a Motorcycle Anthropometric Test Device (MATD). These measurements may be based on either full-scale tests or calibrated computer simulation (e.g., [4]).

Research involving injuries to unhelmeted motorcycle, quadricycle, and all-terrain vehicle (ATV) riders has increased the need to extend the ISO 13232 type injury assessment methods to include the potential for skull fracture which can result from opposing contact forces, in addition to the closed-skull brain injury probability calculations based on

head accelerations which are currently in the Standard.

Objectives

The objective of this study was to develop probabilistic skull fracture injury criteria for skull fractures that are:

- consistent with the model forms for the other body regions in Part 5 of ISO 13232,
- based on contact deformation work time histories, which can be obtained either from computer simulations or specialized test devices and procedures (e.g.,[5]),
- suitable for predicting the AIS level [6] associated with skull fractures.

It is also recognized that skull fracture and injury severity depend on the fracture location. This is addressed by criteria specific to the face and vault.

METHODOLOGY

Probabilistic skull fracture injury criteria based on the maximum contact deformation work were developed by correlating injury severity with objective impact test data for 64 human cadaver tests reported in the scientific literature based on various assumptions listed below. The contact deformation work is given by the equation

$$W = \int_0^D F(x)dx \qquad (1).$$

where $F(x)$ is the contact force at deflection x, and D is the maximum deflection. The maximum contact deformation work was chosen because it tends to be less sensitive to variations in the contact force vs deflection (i.e., the biofidelity of the MATD headform) compared to other indices such as the peak contact force.

Assumptions

The skull fracture model is based on the following assumptions:

1. The skull fracture occurs as the result of contact with a blunt object (i.e., the object is not sharp).
2. The probability of skull fracture depends on whether the contact was to the vault (AIS-2005 body region 1) or face (AIS-2005 body region 2) and on the "mechanical work" to deform the skull resulting from the normal component of the contact force. For the purposes of this model,
   - The face comprises the zygoma and maxilla;
   - The vault comprises the entire head excluding the face.
3. Vault and facial fractures comprise AIS-2005 injuries listed in Tables 1 and 2. The vault fractures listed in Table 1 are AIS 2 though 6. The facial fractures listed in Table 2 are either AIS 1, 2, 3, or 4. However, since there were no AIS 2 facial fractures indicated in Nahum et al [1] and Schneider and Nahum [2] (see Table 12), it was further assumed that the probability of an AIS 2 facial fracture is small compared to the probability of AIS 1 or AIS 3 facial fracture in this analysis and can be assumed to be zero.
4. For each contact location, the probability of $AIS \geq i$ injury vs maximum contact deformation work $W_{\max}$ is assumed to have a Weibull distribution as follows:

$$P(AIS \geq i | W_{\max} = w) = 1 - \exp\left(-\left(\frac{w}{\eta_i}\right)^{\beta_i}\right) \qquad (2).$$

   where η_i and β_i are parameters to be determined. The Weibull distribution is descriptive of many types of mechanical failure, and is used to describe the probability of injury to other body regions in ISO 13232-5.
5. The probability of injury and injury severity is independent on the shape of the contacting blunt object (Note: these injury criteria do not estimate the probability of skull fracture due to contacts with sharp objects).
6. The AIS injury severity was assumed to correspond to the skull fracture severity reported in Nahum et al [1] and Schneider and Nahum [2] according to Table 3.
7. The force vs deflection characteristic of the human skull comprises linear-elastic, elastic, and plastic regions defined by the parameters D_l, D_e, and F_f as illustrated in Figure 1. This implies that the ultimate strength and yield strength are assumed to be the same. Figure 2 illustrates a measured force vs deflection characteristic from Allsop et al [7] that can be approximated by this characteristic. The linear-elastic deflection region is between 0 and D_l. The skull begins

to fracture when the contact force reaches F_f and the contact force remains constant at this level for larger deflections. Permanent deflection occurs if the maximum deflection is greater than the elastic limit D_e. This assumed force vs deflection characteristic is based on the results reported in [7][8] (e.g., Figure 5 in [7]).

8. The parameters D_l and D_e for the 50th percentile human male are deterministic and depend only on the whether the contact is to the vault or face. Assumed values are summarized in Table 4.
    a. Human vault - It was assumed that D_l =3.4 mm and D_e = 10.0 mm based on results in [7]. The value for D_l is based on the results in Table 8. The value for D_e is based on Figure 5 in [7], which indicates that a 12 mm maximum deflection rebounds by 10 mm after the load is released, resulting in a 2 mm permanent deflection. Therefore $\Delta_e = D_e - D_l$ =6.6 mm.
    b. Human face - It was assumed that D_l =10.9 mm and D_e = 17.5 mm based on results in [8]. The value for D_l is based on the results in Table 9. The value for $\Delta_e = D_e - D_l$ is assumed to be 6.6 mm based on the data for the human vault.
9. The amount of permanent deflection (Δ_p) is equal to the maximum deflection ($D_{\max}$) relative to the elastic limit (D_e), as illustrated in Figure 1.
10. The injury severity is dependent on the maximum deflection and permanent deflection of the human head according to Table 10. The rationale is also listed in this table. This assumed relationship between the contact force, deflection, deformation work, and injury is illustrated in Figure 3 where $\Delta_2 = \Delta_e$ and $\Delta_3 = 20$ mm.
11. The impactor shapes used in the Nahum and Schneider data [1][2] are representative of real-world impact conditions for unhelmeted motorcycle and quadricycle riders.
12. The impact conditions in the Nahum and Schneider data resulted in contact forces that were primarily normal to the skull surface (i.e., tangential movement and friction forces are small and can be neglected).
13. The total energy in the Nahum and Schneider tests were conserved. This energy comprised:
    a. Potential and kinetic energy of the impactor.
    b. Energy transferred to the head and supporting structure by the mechanical work of the impactor. This energy comprises:
        - Potential and kinetic energy of the head and supporting structure,
        - Work to "deform", fracture, and crush the skull.
        - Energy dissipated by the supporting structure (i.e. foam).
14. Changes in potential energy in the 5 ms time interval after initial impact are small and can be ignored.
15. The peak contact force in the Nahum and Schneider data is "uncensored" if fracture occurs (e.g., vault $AIS \geq 2$) (i.e., the fracture occurs at the measured force value). The peak contact force is "right censored" if the fracture does not occur (e.g., vault $AIS < 2$) because the fracture force would be greater than the measured value [9].
16. The deformation work done on the human skull during an impact is equivalent to the work done on a Hybrid III (e.g., MATD) headform when subjected to impacts similar to those reported in the scientific literature.
17. The mortality rate is dependent on the most severe head injury (brain, face or vault) and the mortality rate can be determined from the ISO 13232-5 mortality rate tables using the most severe head injury.
18. Medical and ancillary costs for a head injury are assumed to be related to the most severe brain or vault fracture injury; the same for brain, face or vault injuries; and that values in ISO 13232-5 [3] for the head injury are valid for all three.

Table 1.
AIS-2005 (Update 2008) Vault Fractures

Injury Severity	AIS-05 Code	Description
2	150000.2	Vault fracture NFS[a] (may involve frontal, occipital, parietal, sphenoid, or temporal bones)
	150402.2	Closed (simple; undisplaced; diastatic; linear)
3	116000.3	Penetrating injury NFS
	116002.3	Penetrating injury, superficial (≤2cm beneath entrance)
	150404.3	Comminuted (compound; depressed ≤ 2cm; displaced)
4	150406.4	Complex (open with loss of brain tissue)
	150408.4	Massively depressed (large areas of skull > 2cm)
5	116004.5	Penetrating injury, major (>2 cm penetration)
6	113000.6	Massive destruction of both cranium (skull), brain and intracranial contents (crush)

Source: AAAM (1998)
Notes:
a) "NFS" indicates "Not Further Specified"

Table 2.
AIS-2005 (Update 2008) Facial Fractures

Injury Severity	AIS-05 Code[a]	Description
1	25060x.1	Mandible fracture, closed or NFS[b]
	2510xx.1	Nose fracture, closed or NFS
	2514xx.1	Teeth
	2518xx.1	Zygoma fracture, non-displace, displaced
2	25061x.2	Mandible fracture, open
	25080x.2	Maxilla fracture, NFS, closed, LeFort I, or LeFort II
	251002.2	Nose fracture, open/displaced/comminuted
	2512xx.2	Orbit fracture, closed or NFS
	251814.2	Complex zygoma fracture[c]
	2512xx.2	Orbit fracture, open/displaced/comminuted
3	250808.3	Maxilla fracture, LeFort III
4	250810.4	Maxilla fracture, LeFort III, blood loss > 20%

Source: AAAM (2008)
Notes:
a) "x" indicates any number in this position
b) "NFS" indicates "Not Further Specified"
c) Zygoma fractures were reclassified as an AIS 1 or AIS 2 injury in AIS-2005, depending on the type of fracture.

Table 3.
Assumed Nahum and Schneider Data Fracture Severity Score

Nehum and Schneider Fracture Severity Scale		AIS-2005 Injury Severity
Code	Description	
0	"none"	0
1	"minimal detectable change, not clinically significant"	0
2	"readily detectable fracture, clinically significant"	2[a]
3	"comminuted, and/or depressed fractures"	3[a]

Note:
a) All Zygoma fractures were assumed to be AIS 1 because this represents all Zygoma fractures except complex fractures.

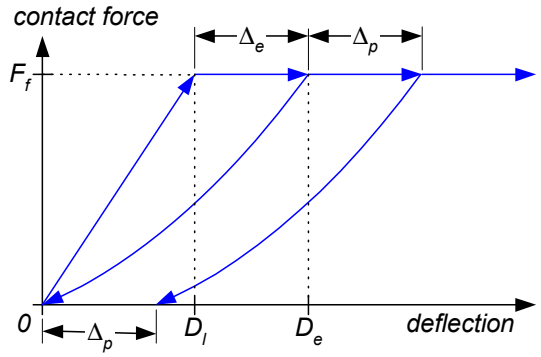

Figure 1. Assumed Human Skull Contact Force vs. Deflection Characteristic.

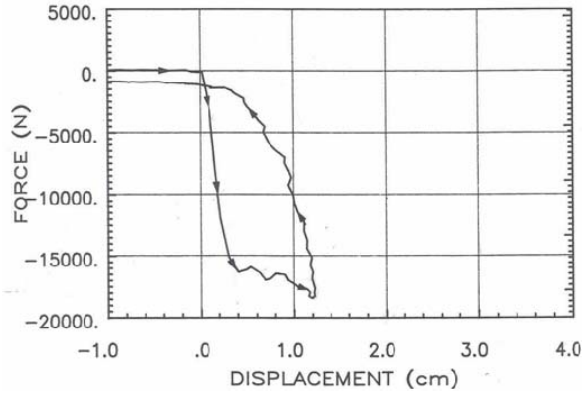

Figure 2. Example Human Skull Contact Force vs. Deflection (Allsop et al [7]).

Table 4.
Assumed Human Male Skull Force vs Deflection Characteristic Parameters

Characteristic Parameter		Assumed Value		Units
		Vault	Face	
D_l	Linear range	3.4 (0.5) [a]	10.9 (7.8) [b]	mm
$\Delta_e = D_e - D_l$		6.6 [d]	6.6 [e]	mm
D_e	Elastic limit	10.0 [c]	17.5 [f]	mm

Sources and Notes:

[a] Table 8 (derived from data in Allsop et al [7]).

[b] Table 9 (derived from data in Allsop et al [8]).

[c] Figure 5 in [7], which indicates that a 12 mm maximum deflection rebounds by approximately 10 mm after the load is released, resulting in a 2 mm permanent deflection

[d] Computed, $\Delta_e = D_e - D_l$

[e] Assumed equal to the Vault value

[f] Computed, $D_e = D_l + \Delta_e$

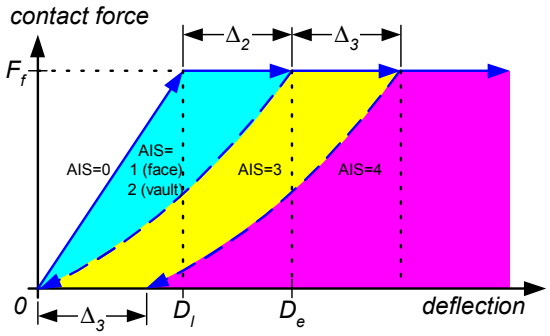

Figure 3. Assumed Relationship between Contact Force, Deflection, Work, and Skull Fracture Injury Severity.

Adult Human Male Cadaver Data

Data on skull fracture injuries and contact forces from over 200 human cadaver tests were compiled from results in [1][2][7][8] and [10]. These tests comprised various impactor shapes ranging in area from 302 mm² to 5200 mm². Of these, 128 tests using a flat circular plate with 645 mm² area were reported in the Nahum and Schneider studies. Therefore the Nahum and Schneider data were used because it represented the majority of the available data with a single medium-sized impactor shape. This eliminates the impactor shape and size as a potential confounding factor, yet the data are assumed to be representative of real-world impacts with blunt surfaces of this general area.

Of the Nahum and Schneider data, only the human male cadaver data were used. The frontal region tests were not used because they were a relatively small sample (8 cases), and tended to have larger peak forces than the temporo-parietal tests. Data for the remaining 64 tests are listed in Table 11 and Table 12. The tests comprised 45 embalmed and 19 unembalmed cadavers with 51 to 81 years age at time of death. The number tests by impact region are summarized in Table 5.

Table 5.
Number of Male Nahum and Schneider Tests Used

AIS-2005 Body Region	Impact Region	Number of Tests
Head (Vault)	Temporo-Parietal	27
Face	Zygoma	27
	Maxilla	10
Total		64

Estimation of Injury Probability Curves

Given the data in Table 11 and Table 12 the Weibull distribution parameters for the probability of fracture vs peak contact force can be estimated. Rank ordered data and estimated cumulative probability distribution curves are illustrated in Figure 4 and Figure 5. The symbol type indicates the data source. The open symbols are the tests that did not result in fracture and are assumed to be right censored. The filled symbols are the tests that resulted in a fracture, which was assumed to be force limiting and uncensored. The vertical axis of the data is plotted on a Kaplan-Meier empirical distribution, which accounts for data censoring.

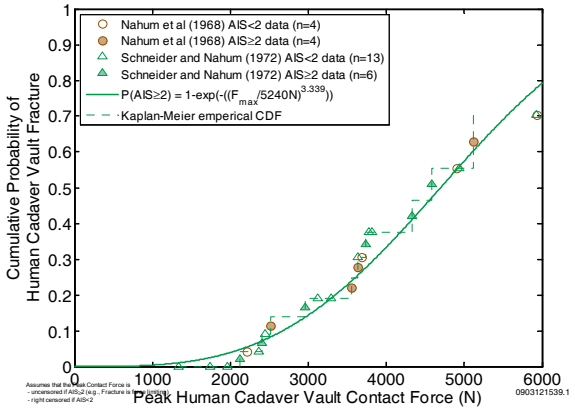

Figure 4. Probability of Human Cadaver $AIS \geq 2$ Vault Fracture vs Peak Contact Force.

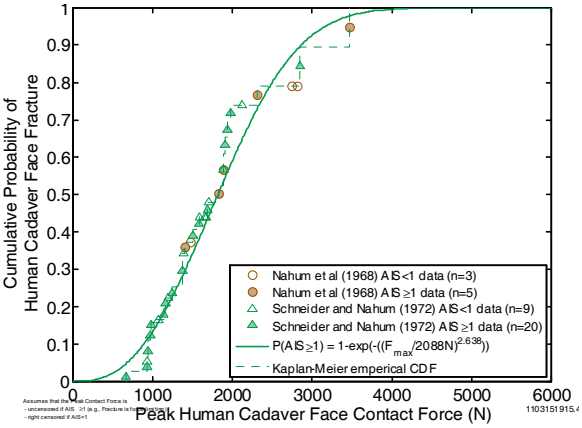

Figure 5. Probability of Human Cadaver $AIS \geq 1$ Facial Fracture vs Peak Contact Force.

Assuming the following Weibull distribution for the probability of an $AIS \geq 2$ vault fracture (or $AIS \geq 1$ facial fracture) vs the peak contact force,

$$P(AIS \geq 2 | F_{\max} = f) = 1 - \exp\left(-\left(\frac{f}{\eta'}\right)^{\beta'}\right) \quad (3).$$

Maximum likelihood estimates and 95% confidence intervals for η' and β' were estimated using the MATLAB Statistics Toolbox "WBLFIT" routine [11]. The MATLAB WBLFIT routine supports right-censored data using methods described in [9]. The results for the vault are η'=5240 (4302, 6384) N and β'=3.34 (2.09, 5.33); the results for the face are η'=2088 (1800, 2423) and β'=2.64 (1.98, 3.52) for the face. The values in parentheses "( )" are the lower and upper bounds for the 95% confidence interval for the estimated value.

Fracture Injury Risk - The probability of a vault or facial fracture can be expressed in terms of the equivalent contact deformation work based on the assumed force vs deflection characteristic illustrated in Figure 1. For example, the contact deformation work needed to fracture the skull, resulting in an $AIS \geq 2$ vault fracture is

$$W_2 = \int_0^{D_l} F(x)dx = \int_0^{D_l} \frac{F_f}{D_l} x \, dx = \frac{F_f D_l}{2} \quad (4).$$

where D_l is assumed to be a constant, depending on the contact location. Since W_2 is proportional to F_f (i.e., $W_2 = F_f D_l/2$), W_2 has the same statistical properties (e.g., censoring) as F_f. Therefore, equations (2) for $AIS \geq 2$ and (3) are equivalent provided that:

$$\eta_2 = \eta'\left(\frac{D_l}{2}\right) \qquad \beta_2 = \beta' \quad (5).$$

Scaled Nahum and Schneider data for W_2 and corresponding Weibull distribution curves are illustrated in Figure 6 and Figure 7, assuming D_l is 3.4 mm for the vault, and 10.9 mm for the face.

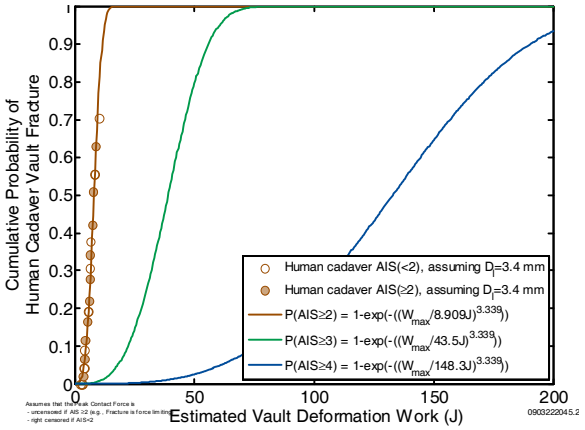

Figure 6. Probability of Vault Fracture vs Estimated Vault Deformation Work.

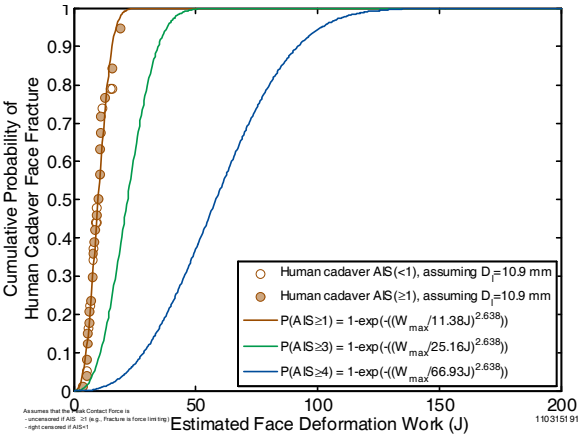

Figure 7. Probability of Facial Fracture vs Estimated Facial Deformation Work.

The estimated "deformation work" to fracture the skull tends to be a small portion of the initial kinetic energy of the impactor reported by Nahum and Schneider. This "deformation work" does not include:

- the kinetic energy that remains in the impactor,
- the energy transferred to the kinetic energy of the head,
- the energy absorbed by the skull after fracture, or
- the energy absorbed by the supporting foam.

$AIS \geq 3$ **Injury Risk -** The probability of an $AIS \geq 3$ skull fracture can also be expressed in terms of equivalent deformation work based on the assumed force vs deflection characteristic illustrated in Figure 1. The contact deformation work needed to fracture the skull and just begin permanent deformation is

$$W_3 = \int_0^{D_e} F(x)\,dx = \int_0^{D_l} \frac{F_f}{D_l} x\,dx + \int_{D_l}^{D_e} F_f\,dx = F_f\left(\frac{D_l}{2} + \Delta_2\right) \quad (6).$$

If an $AIS \geq 2$ fracture was observed in the Nahum and Schneider data for a given F_f and W_2, then we can assume that an additional $F_f \Delta_2$ amount of contact deformation work would have increased the maximum deflection by Δ_2, resulting in some permanent deflection and an $AIS \geq 3$ injury. Therefore the probability of an $AIS \geq 3$ fracture vs W_3 is the same as the probability of an $AIS \geq 2$ fracture vs W_2; and equations (2) for $AIS \geq 3$ and (3) are equivalent provided that:

$$\eta_3 = \eta'\left(\frac{D_l}{2} + \Delta_2\right) \qquad \beta_3 = \beta' \quad (7).$$

Scaled Nahum and Schneider data for W_3 and corresponding Weibull distribution curves are also illustrated in Figure 6 and Figure 7, assuming $\Delta_2 = \Delta_e$=6.6 mm.

$AIS \geq 4$ **Injury Risk -** In a similar manner, the probability of an $AIS \geq 4$ skull fracture can also be expressed in terms of equivalent work. The contact deformation work needed to fracture the skull and result in Δ_3 (20 mm) of permanent deformation is

$$W_4 = F_f\left(\frac{D_l}{2} + \Delta_2 + \Delta_3\right) \quad (8).$$

It follows that equations (2) for $AIS = 4$ and (3) are equivalent provided that:

$$\eta_4 = \eta'\left(\frac{D_l}{2} + \Delta_2 + \Delta_3\right) \qquad \beta_4 = \beta' \quad (9).$$

Scaled Nahum and Schneider data for W_4 and corresponding Weibull distribution curves are also illustrated in Figure 6 and Figure 7, assuming Δ_3 is 20 mm.

MATD INJURY CRITERIA

The probability of an $AIS \geq i$ skull fracture can be estimated based on the contact deformation work according to equation (2), where the values for parameters η_i and β_i depend on the contact

location. Maximum likelihood estimates and 95% confidence intervals of η_i and β_i are listed in Table 6 for contacts with the vault, and Table 7 for contacts with the face.

Table 6.
Estimated Vault Fracture Weibull Distribution vs Injury Severity Parameters

$P(AIS \geq i)$	η_i (J)	β_i
2	8.91 (7.31,10.9)	3.34 (2.09, 5.33)
3	43.5 (35.7,53.0)	3.34 (2.09, 5.33)
4	148. (122.,181.)	3.34 (2.09, 5.33)

Table 7.
Estimated Facial Fracture Weibull Distribution vs Injury Severity Parameters

$P(AIS \geq i)$	η_i (J)	β_i
1	11.4 (9.81,13.2)	2.64 (1.98, 3.52)
3	25.2 (21.7,29.2)	2.64 (1.98, 3.52)
4	66.9 (57.7,77.7)	2.64 (1.98, 3.52)

For comparison purposes the work to fracture the vault and face can also be computed from the Allsop data listed in Table 8 and Table 9. The mean work to fracture the vault from the data in Table 8 is 10.4 (3.5) J. The mean work to fracture the face from the data in Table 9 is 9.9 (8.0) J. These results are not statistically significantly different than the results for $AIS \geq 2$ in Table 6 and Table 7.

APPLICATION TO ISO 13232 MATD

The skull fracture injury criteria can be applied to the MATD (Hybrid III) headform provided the contact deformation work can be determined. The contact deformation work can be determined using computer simulation or special measurement of contact force (e.g., impactor force, pressure film, custom headform [5]).

Measured MATD Force-vs-Deflection

The force vs deflection characteristics of the MATD headform in the temporoparietal region were measured by a quasi-steady laboratory test illustrated in Figure 8. The headform was placed between two circular disks, each with 645 mm contact area. The contact force was measured by a load cell. The total displacement, which included deformation on both sides of the headform, was measured by a string potentiometer. The total displacement was divided by two to obtain the deflection for a single side.

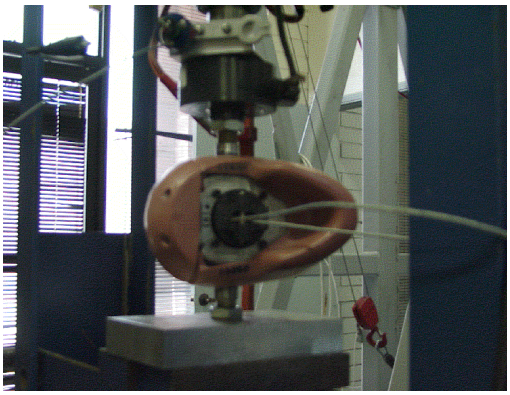

Figure 8. Quasi-Steady MATD Force vs Deflection Test Setup.

The force and displacement of the MATD headform was measured while slowly applying the contact force until the headform ultimate limit was reached at 23.8 kN. The test was done in two stages. The resulting force vs deflection characteristic of the MATD headform is illustrated in Figure 9.

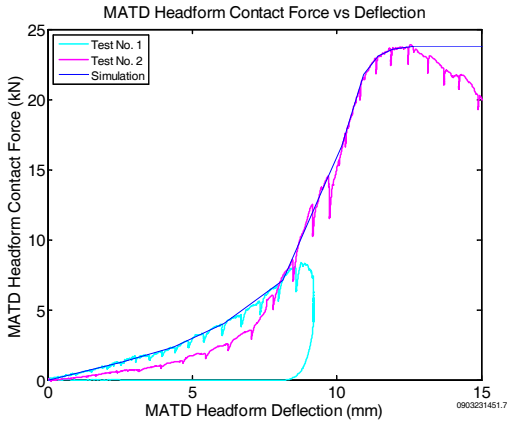

Figure 9. Measured MATD Headform Contact Force vs. Deflection.

MATD Injury Risk Curves

As previously indicated the probability of skull fracture can be estimated from the maximum contact deformation work according to equation (2) and the coefficients in Table 6 or Table 7, depending on the contact location. These probability curves were illustrated in Figure 6 and Figure 7.

The probability of skull fracture can be also estimated from the peak MATD headform contact force provided the contact deformation work can be uniquely and accurately determined from the peak contact force. This condition can be satisfied if the

contact force is a monotonically increasing function of the contact deformation.

Note that in order to address the ultimate limit of the MATD headform at 23.8 kN, the monotonically increasing "simulation" curve in Figure 9 was used in computer simulations. This curve was extrapolated with a small positive slope to obtain a monotonically increasing curve.

Provided the simulated MATD contact force is based on the force-deflection characteristic in Figure 9, the probability of injury versus peak MATD contact force ($F_{\max,MATD}$) can be determined as follows:

1. Refer to the MATD contact force vs deflection curve in Figure 9 to determine the contact deflection $D_{\max,MATD}$ from $F_{\max,MATD}$.
2. Integrate MATD contact force vs deflection curve from 0 to $D_{MATD,\max}$ to determine the maximum contact deformation work $W_{\max}$.
3. Estimate the probability of injury from the contact deformation work according the equation (2) and the coefficients in Table 6 or Table 7, depending on the contact location.

The resulting probability of injury versus the MATD contact force is illustrated in Figure 10 and Figure 11.

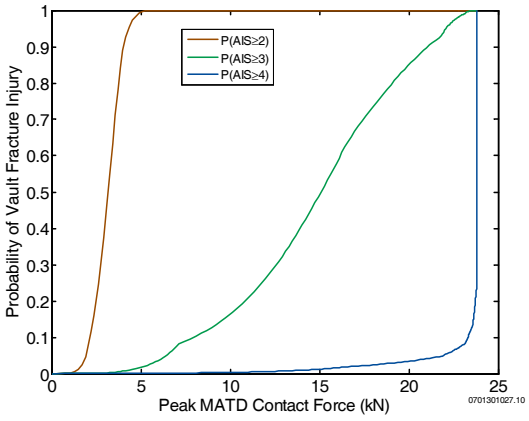

Figure 10. Estimated Probability of Vault Fracture Injury vs Peak Simulated MATD Contact Force.

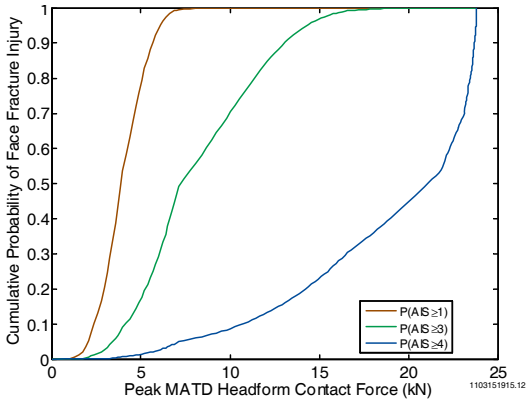

Figure 11. Estimated Probability of Facial Fracture Injury vs Peak Simulated MATD Contact Force.

Validation tests

Drop tests to replicate the conditions of the Nahum and Schneider human cadaver tests were accomplished in the Dynamic Research, Inc. Impact Test Laboratory. The test setup comprised a 3.275 kg impactor mounted on a vertical slide rail which was allowed to free-fall, impacting either in the vault (temporoparietal) or facial (zygoma) regions of the MATD headform, as illustrated in Figure 12. The MATD headform was supported by 100 mm of soft foam rubber as described in [1].

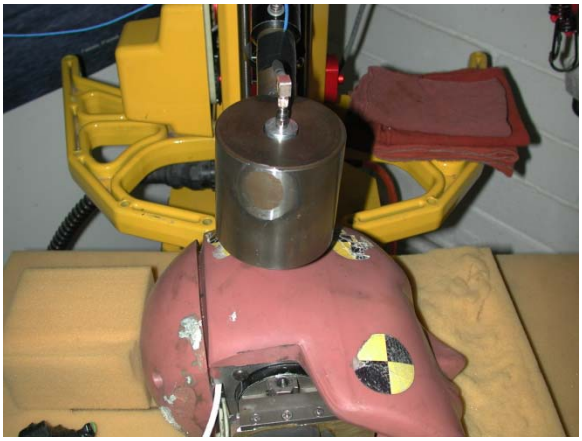

Figure 12. Impact Test Setup.

Results for a series of vault tests are summarized in Figure 13. The circle symbols represent the test data and the solid lines represent reconstructions of the tests using the US DOT and US Air Force Articulated Total Body (ATB) program [12]. The peak contact forces for the test data were derived from the peak measured impactor accelerations. The vault deflections were not measured in these tests, and were therefore estimated from time-domain reconstruction simulations. However these estimated

deformation data are considered reliable because of the close agreement between the test data and reconstructions.

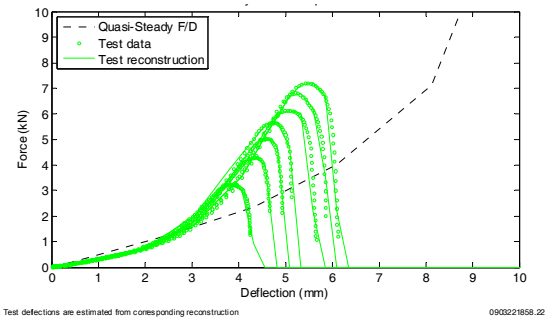

Figure 13. Measured and Reconstructed Vault Force vs Deflection in Impact Test Series.

The results in Figure 13 indicate that the force vs deflection characteristics for these tests are not monotonically increasing, and therefore the deformation work for these tests cannot be determined from the peak contact force. Instead the maximum deformation work for these tests was estimated by integrating the force vs deflection characteristic over the range of reconstructed deformation values. The non-monotonic characteristic observed in these tests is attributed to velocity-dependent characteristics of the elastomer MATD headform skin.

The green symbols and curves in Figure 14 and Figure 15 illustrate the measured and reconstructed time histories for an example vault test with 3.02 m/s impact speed. Figure 14 illustrates the acceleration vs time. Figure 15 illustrates the distribution of energy vs time. The test data impactor kinetic energy was computed from the impactor velocity, which was determined by integrating the acceleration. The test data "head energy" was computed by integrating the impactor force vs time. These figures illustrate that the reconstructed tests are in close agreement with the measured test data up until the point of maximum deflection and deformation work. Therefore the reconstructed test deformations are reliable estimates of the unknown actual values. The maximum vault contact deformation work was 8.9 J and the estimated probability of $AIS \geq 2$ fracture is 0.63.

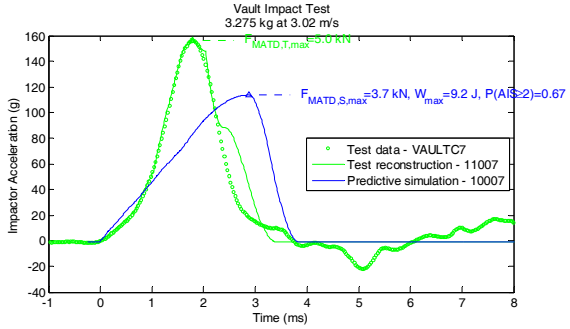

Figure 14. Measured and Simulated Acceleration Response of Vault Impact Test (3.02 m/s).

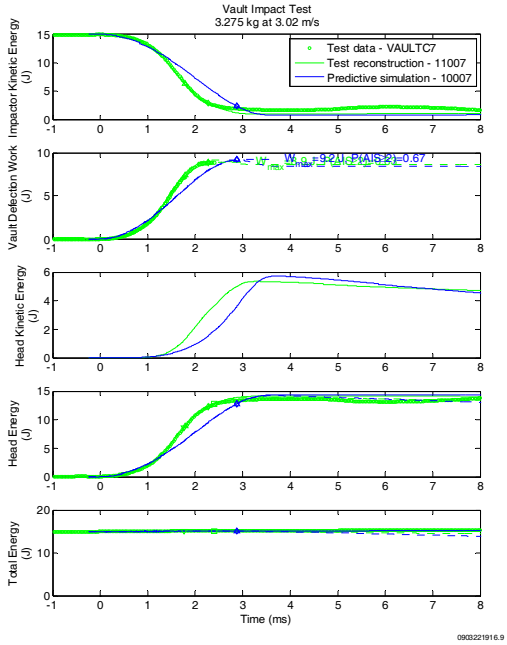

Figure 15. Measured and Simulated Energy Response of Vault Impact Test (3.02 m/s).

The blue curves in Figure 14 and Figure 15 illustrate the predicted responses for the same 3.02 m/s impact assuming a monotonically increasing force vs deflection function. These results indicate that whereas the predicted peak forces are different than the test values, the maximum vault contact deformation work was 9.2 J and the estimated probability of $AIS \geq 2$ fracture is 0.67, which is in close agreement with the test values.

Note the maximum vault contact deformation work can also be estimated according to the following equation

$$W_{\max} = \left(1 - \left(\frac{m_{\text{impactor}}}{m_{\text{impactor}} + m_{\text{headform}}}\right)\right) KE_0 \quad (10).$$

where m_{impactor} is the mass of the impactor (3.275 kg) and m_{headform} is the effective mass of the head (approximately 5 kg). Therefore $W_{\max} \cong 0.6 \times KE_0$ in these example tests.

Figure 16 illustrates the close overall agreement between the predicted and estimated vault deformation work for the vault test series. The estimated probabilities of injury for these test cases are also in close agreement since they are functions of the deformation work.

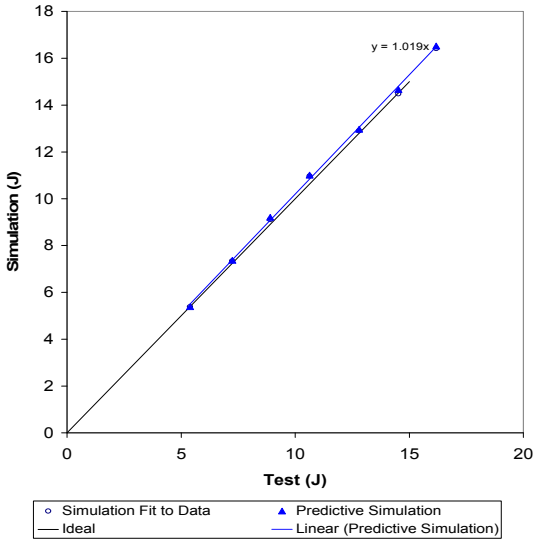

Figure 16. Comparson of Predicted and Estimated Vault Test Contact Deformation Work.

INJURY COST MODEL

The probabilistic skull fracture injury criteria can be incorporated into the ISO 13232 injury cost model in order to extend the ISO 13232 type injury assessment methods so as to include probability of skull fractures for unhelmeted riders of motorcycles and quadricycles. The changes to ISO 13232 that would be necessary are listed in Table 13 and Table 14.

CONCLUSIONS

A probabilistic skull fracture injury criteria has been developed for a 50th percentile adult male that is suitable for ISO 13232 type injury analysis for unhelmeted motorcycle and quadricycle (and ATV) riders. The skull fracture criteria are complementary to the existing closed skull brain injury criteria based on acceleration which is currently implemented in the Standard. This new skull fracture criteria address the injury potential due to crushing type injury mechanisms that have very low acceleration levels.

The skull fracture criteria estimate the probabilities of an AIS 2, 3, and 4 vault and AIS 1, 3 and 4 facial fractures based on the contact deformation work. The contact deformation work is assumed to be insensitive to the differences in the force vs deflection characteristics of the MATD headform compared to the adult male human head. It is assumed that the contact deformation work can be determined by ISO 12323 type computer simulations, or specialized laboratory and full scale test measurement methods.

ACKNOWLEDGMENTS

Dynamic Research, Inc. staff members Jeff Porter, Alex Ricardo, and others assisted in various aspects of this analysis, including compiling the data and conducting the laboratory tests.

REFERENCES

[1] Nahum, A.M., Gatts, J.D., Gadd, C.W., Danforth, J., “Impact Tolerance of the Skull and Face”, Paper No. 680785, Proc. of the 12th Stapp Car Crash Conference, Detroit, 1968, pp. 302-316.

[2] Schneider, D.C., Nahum, A.M., “Impact Studies of Facial Bones and Skull”, Paper No. 720965, Proc. of the 16th Stapp Car Crash Conference, Detroit, 1972, pp 186-203.

[3] ISO 13232-5, Motorcycles – Test and Analysis Procedures for Research Evaluation of Rider Crash Protective Devices Fitted to Motor Cycles – Part 5: Injury Indices and Risk/Benefit Analysis, ISO 13232-5, International Organization for Standardization, Geneva, 2005.

[4] Kebschull, S.A., Zellner, J.W., Van Auken, R.M., “Injury Risk/Benefit Analysis of Motorcycle Protective Devices Using Computer Simulation and ISO 13232”, Paper Number 98-S10-W-26, proceedings of the 16th International Technical Conference on the Enhanced Safety of Vehicles, Windsor, Canada, National Highway Traffic Safety Administration, Washington, 1998, pp. 2357-2374.

[5] Hatano, K., Kawai, H., Hatamura, Y., Uchimura, T., “An Application of Car Crash Test Technology to a Causal Investigation of a Revolving Door

Accident", Paper No. 2006-01-0717, Society of Automotive Engineers, Warrendale, PA, 2006.

[6] AAAM, The Abbreviated Injury Scale, 2005, Update 2008, Association for the Advancement of Automotive Medicine, Des Plaines, IL, 2008.

[7] Allsop, D.L., Perl, T.R., Warner, C.Y., "Force/Deflection and Fracture Characteristics of the Temporo-parietal Region of the Human Head", Paper No. 912907, Proc. of the 35th Stapp Car Crash Conference, San Diego, 1991, 269-278.

[8] Allsop, D.L., Warner, C.Y., Wille, M.G., Schneider, D.C., Nahum, A.M., "Facial Impact Response - A comparison of the Hybrid III Dummy and Human Cadaver", Paper 881719, Proc. of the 32nd Stapp Car Crash Conference, Atlanta, 1988, 139-155.

[9] Kent, R.W., and Funk, J.R., "Data Censoring and Parametric Distribution Assignment in the Development of Injury Risk Functions from Biomechanical Data", Paper No. 2004-01-317, Society of Automotive Engineers, Warrendale, PA., 2004.

[10] Yoganandan, N., et al, "Steering Wheel Induced Facial Trauma", Paper No. 881712, Proc. of the 32nd Stapp Car Crash Conference, Atlanta, 1988, 45-69.

[11] Mathworks, Statistics Toolbox for use with MATLAB®, Users Guide, Version 5, The Mathworks, Natick, MA, 2006.

[12] Fleck, J.T., and F. E. Butler, Validation of the Crash Victim Simulator, Vol. 1: Engineering Manual – Part 1: Analytical Formulation, DOT HS-806-279, Washington, 1981.

[13] Blincoe, L., et al, The Economic Impact of Motor Vehicle Crashes, DOT HS 809 446, National Highway Traffic Safety Administration, Washington, May 2002.

DEFINITIONS, ACRONYMS, ABBREVIATIONS

AIS	Abbreviated Injury Scale
NFS:	Not Further Specified
D:	Deflection
F:	Force
W:	Work
Δ:	Change in deflection

Subscripts

e	Elastic limit
l	Linear range limit
p	Plastic deformation

APPENDIX

Table 8.
Human Male Cadaver Temporo-parietal Force/Deflection and Fracture Characteristics for Circular Plate Impacts

Cadaver ID	Fracture Force (N)	Stiffness (N/mm)	Linear Range Deflection (mm)
M26329	4,800	1,480	3.24
M26350	6,400	1,470	4.35
M26368	7,700	2,570	3.00
M26372	7,300	1,800	4.06
M26373	10,000	3,140	3.18
M26383	5,000	1,540	3.25
M26903	3,100	830	3.73
M26922	4,000	1,440	2.78
Mean	6,038	1,784	3.45
Std. Deviation	1,801	881	0.54
95% confidence interval for the Mean			(0.46)

Source: Allsop et al [7] Tables 2 and 4.

Table 9.
Human Male Cadaver Facial Force/Deflection and Fracture Characteristics

Impact Location	ID	Fracture Force (N)	Stiffness (N/mm)	Linear Range Deflection (mm)
Zygoma	2278	1,700	110	15.45
	2201	2,300	230	10.00
	mean	1,738	148	12.73
Maxilla	2185	1,800	130	13.85
	2291	1,100	250	4.40
	mean	1,350	142	9.12
Mean		1,571	145	10.93
Std. Deviation		492	70	4.92
95% confidence interval for the Mean				(7.82)

Source: Allsop et al [8] Table 1.

Table 10.
Assumed Injury Severity vs Maximum Deflection and Permanent Deflection of the Human Skull

AIS Injury Severity	Maximum Deflection $D_{\max}$	Permanent Deflection $\Delta_p = D_{\max} - D_e$	Rationale
0	$D_{\max} \le D_l$	None	No fracture
1 (face) 2 (vault)	$D_l < D_{\max} \le D_e$	None	AIS 2 Vault fractures include: "fracture NFS"*; "closed (simple; undisplaced; diastatic; linear)". AIS 1 Zygoma fractures include "non-displaced" and "displaced"
3	$D_e < D_{\max}$	$0 < \Delta_p \le 20$ mm	AIS 3 fractures of the vault include: 116002.3 – superficial penetrating injury "(≤2 cm beneath entrance)" 150404.3 - "comminuted (compound; depressed ≤ 2 cm; displaced"
4	$D_e < D_{\max}$	$20 \text{ mm} < \Delta_p$	AIS 4 fractures of the vault include: 116004.5 – Major penetrating injury (> 2 cm) 150408.4 - "massively depressed (large areas of the skull depressed > 2 cm)"

Note: *"NFS" indicates "Not Further Specified"

Table 11.
TemporoParietal (Vault) Fracture Injury Data from Nahum and Schneider

Specimen	Force (N)	Fracture Severity	AIS-2005 Severity[a]
1	2518	3	3
1	2215	1	0
2	5115	2	2
2	3634	2	2
3	3683	1	0
3	3550	2	2
5	5934	1	0
5	4902	1	0
18 EM	3290	0	0
18 EM	5920	0	0
19 EM	2360	0	0
19 EM	4580	2	2
20 EM	4330	3	3
20 EM	1340	0	0
31 FM	4940	0	0
31 FM	2960	3	3
34 FM	3640	1	0
34 FM	2450	0	0
35 EM	3120	0	0
35 EM	3820	1	0
38 EM	1740	0	0
38 EM	2400	3	3
39 EM	3740	2	2
39 EM	2360	0	0
40 EM	3780	0	0
41 EM	2120	3	3
41 EM	1960	0	0

Sources: Nahum et al[1], Schneider and Nahum [2]
[a)] All fractures with Fracture Severity 2 were assumed to have AIS-2005 code 150402.2; All fractures with Fracture Severity 3 were assumed to have AIS-2005 code 150404.3.

Table 12.
Facial Fracture Injury Data from Nahum and Schneider

Impact Location	Specimen	Force (N)	Fracture Severity	AIS-05 Severity
Zygoma	1	1828	3	1
	1	1477	1	0
	2	2740	1	0
	2	2816	1	0
	3	1406	3	1
	3	1890	3	1
	5	3469	3	1
	5	2304	3	1
	18 EM	1580	3	1
	18 FM	1140	3	1
	19 EM	970	3	1
	19 EM	2850	2	1
	20 EM	930	0	0
	20 EM	1910	3	1
Zygomatic Arch	31 FM	930	3	1
	34 FM	1590	0	0
	34 FM	2120	0	0
	35 EM	1670	0	0
	35 EM	1940	2	1
	38 EM	1510	3	1
	38 EM	1390	0	0
	39 EM	1690	3	1
	39 EM	1250	3	1
	40 EM	1660	0	0
	40 EM	1710	0	0
	41 EM	1890	3	1
	41 EM	1370	3	1
Maxilla[b]	31 FM	1980	3	3
	34 FM	1370	3	3
	34 FM	940	3	3
	35 EM	980	3	3
	38 EM	1200	0	0
	38 EM	1160	3	3
	39 EM	940	3	3
	40 EM	1070	0	0
	40 EM	1370	3	3
	41 EM	660	3	3

Sources: Nahum et al [1], Schneider and Nahum [2]
[a)] All Zygoma and Zygomatic Arch fractures in these data are assumed to have AIS-2005 code 251800.1
[b)] All Maxilla fractures in these data are assumed to have AIS-2005 code 250808.3 (i.e., LeFort III).

Table 13.
Changes to ISO 13232-5 Injury Cost Model

Clause		Change
5.1	Injury variables	Add computation of vault and face contact deformation work
5.3	Injury severity probabilities	Compute the vault fracture injury severity probability ($ISP_{vault,H,j}$) for each $AIS \geq j$ injury severity level according to equation (2) using the coefficients in Table 6.[a] The head ISP, $ISP_{H,j}$, for each AIS injury severity level is redefined in clause 5.3.1 as the larger of either $ISP_{Gmax,H,j}$, $ISP_{HIC,H,j}$, or $ISP_{Vault,H,j}$.
		Compute the facial fracture injury severity probability ($ISP_{F,j}$) for each $AIS \geq j$ injury severity level according to equation (2) using the coefficients in Table 7.[b]
5.4	Probability of discrete AIS injury severity level	Add the Face body region as a separate region to subclause 5.4.1
5.5	Injury costs	Add the Face body region as a separate region
5.6	Probability of fatality	Add the Face body region as a separate region
5.7	Probable AIS	Add the Face body region as a separate region
Annex A		Add the Face injury costs listed in Table 14

Note:

a) The probability of an AIS 1, 5, and 6 vault fracture is assumed to be zero, therefore $ISP_1 = ISP_2$ and $ISP_j = 0$ for j=5 and 6.

b) The probability of an AIS 2, 5, and 6 face fracture is assumed to be zero, therefore $ISP_2 = ISP_3$ and $ISP_j = 0$ for j=5 and 6.

Table 14.
Facial Injury Cost

AIS Injury Severity Level	Costs (2000 US Dollars)[a]	
	Medical Costs	Ancillary Costs[b]
1	$ 1 183	$ 2 961
2	12 020	32 908
3	56 149	90 727
4	178 285	142 605
5	92 107	568 701

Source: Blincoe [13]

Notes:

a) Costs do not include emergency services, insurance administration and non-economic costs (e.g., pain and suffering)

b) Ancillary costs include lost market and household productivity (including wages), workplace, and legal/court costs

RESEARCH OF COLLISION SPEED DEPENDENCY OF PEDESTRIAN HEAD AND CHEST INJURIES USING HUMAN FE MODEL (THUMS VERSION 4)

Ryosuke Watanabe
Hiroshi Miyazaki
Yuichi Kitagawa
Tsuyoshi Yasuki
Toyota Motor Corporation
Japan
Paper Number 11-0043

ABSTRACT

In this research, the collision speed dependency of pedestrian head and chest injuries was investigated using the human FE model THUMS Version 4, independently developed by Toyota Motor Corporation and Toyota Central R&D Labs, Inc. to predict brain and internal organ injuries. In addition, this research also looked at the relationship between impact speed and fatality risk. The study first verified the biofidelity of the THUMS pedestrian model in terms of body region components, such as the head, chest, and lower extremities, and the whole body. The model closely simulated the impact response of each body region component described in the literature. As for the whole body kinematics, the calculated trajectories of each portion of the body during a collision with a vehicle were a good match with those of post mortem human subjects (PMHS) described in the literature. It was also determined that the model predicted injuries at the locations reported in the PMHS tests.
Using the validated THUMS model, this research then looked at the relationship of head and chest injuries with collision speed. Collisions between a pedestrian and an SUV were analyzed at three collision speeds of 30, 40, and 50 km/h. Head injuries did not occur at a collision speed of 30 km/h, but in collisions at 40 and 50 km/h the results suggested that a serious brain injury, known as diffuse axonal injury (DAI), occurred. Furthermore, in regard to the chest area, injuries did not occur at 30 km/h, but at 40 km/h bone fractures in the ribs occurred, and at 50 km/h, in addition to an increase in the number of bone fractures in the ribs, the results suggested that serious injuries to internal organs, such as damage to the heart, also occurred.
These results correspond with the trends in accident data that indicate that the fatality risk for pedestrians increases when the collision speed is 40 km/h or higher.

INTRODUCTION

According to the statistical research of the Traffic Bureau of the National Police Agency, the number of traffic fatalities in Japan in 2009 was 4,914. Pedestrians accounted for 1,717 of this total which is higher than the number of fatalities among vehicle occupants (1,600 people, Figure 1). Looking at the fatalities based on the region of the body that was injured, head injuries accounted for the largest proportion at approximately 54%, followed by chest injuries at approximately 16% (Figure 2) [1].
Anderson et al. (2005) investigated the relationship between collision speed and fatality risk for pedestrians [2]. When the collision speed exceeds 40 km/h, the pedestrian fatality risk increases (Figure 3), but the reason for this has not been determined.
Experimental studies have been conducted to investigate pedestrian injuries using post mortem human subjects (PMHS) and crash test dummies. Schroeder et al. (2008) [3] and Subit et al. (2008) [4] simulated collisions between compact cars, SUVs, and minivans with pedestrians in PMHS tests to analyze the behavior of a pedestrian body during a collision and what kinds of injuries are suffered as a result.
Kerrigan et al. (2008) conducted a series of PMHS tests to investigate the injuries to a pedestrian's lower extremities when impacted by the front end of a small sedan and a large SUV [5]. Kerrigan et al. (2005) also conducted collision tests between an SUV and both PMHS and test dummies to compare the behavior at the time of a collision [6].
In recent years, FE models have been used to simulate injuries to pedestrians in a collision. Yasuki (2005) [7] and Miyazaki et al. (2009) [8] analyzed the difference in impact response between a pedestrian lower extremity and a Transport Research Laboratory (TRL) lower leg impactor (used in assessment tests) in car impacts through FE simulations. Tamura et al. (2006) simulated the behavior of a pedestrian during a collision using a whole body pedestrian model containing a part simulating a brain, and then discussed the possible mechanism of head injuries [9]. As described above, research into pedestrian-to-vehicle collisions mostly focus on the behavior of the lower extremities and injuries such as ligament ruptures and bone fractures of the lower extremities, or on head injuries. However, few studies have been conducted on chest injuries and especially on internal organ injuries.
This paper analyzes the relationship of pedestrian head and chest injuries with the collision speed in vehicle collisions, and then discusses possible factors that increase the fatality risk at a collision speed of 40 km/h or higher. The research used a full-body FE

model called the Total Human Model for Safety (THUMS) Version 4 which includes both the brain and internal organ parts in detail. First, the biofidelity of the THUMS pedestrian model was verified. Impact tests on body region components and car-to-pedestrian impact tests described in the literature were simulated with the model. Impact responses of the model were compared to those in the tests. Next, the research analyzed the relationship between collision speed and head and chest injuries through pedestrian-to-SUV impact simulations at various collision speeds. The finite element analysis code, LS-DYNA^{TM} V971, was used for the simulations.

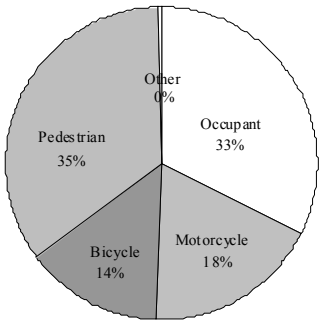

Figure 1. Proportions of traffic accident fatalities according to type.

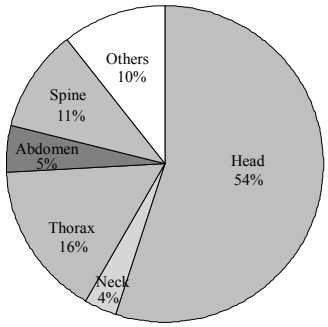

Figure 2. Proportions of injuries suffered by pedestrians in fatal accidents.

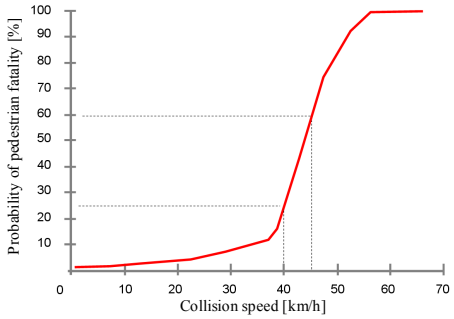

Figure 3. Relationship between collision speed and fatality risk in pedestrian impact.

MODEL VALIDATION

Outline of THUMS Version 4

THUMS is a human body FE model that was jointly developed by Toyota Central R&D Labs, Inc. and Toyota Motor Corporation. Figure 4 shows the physique of the THUMS model in a standing posture. This model simulates a 50th percentile American male with a height of 175 cm and a weight of 77 kg. THUMS Version 4 includes the internal organs of the body, the brain, and the skeleton, in great detail. The number of nodes in the model is approximately 650,000 and the number of elements is approximately 2 million [10]. The geometrical data of the internal organs was created based on high-precision CT scan data, and the positions within the human body and connections to each other were carefully duplicated. The anatomical features of each internal organ were reflected in the modeling, and the material property data was defined referring to recent literature[11-21]. The biofidelity of the body region components were verified by comparing their impact responses with those in the literature data [22-25].

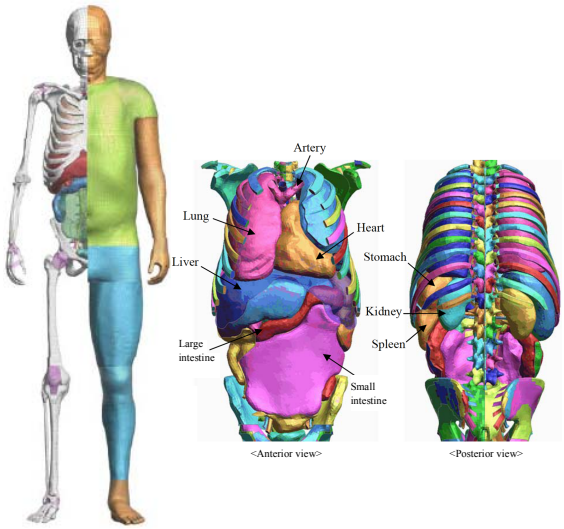

Figure 4. Outline of THUMS Version 4.

Validation of Body Region Component Models

This research assumed a condition in which a vehicle strikes a pedestrian from the side. The principal body region components that might sustain injuries are the head, chest, and knee. The mechanical response of these components against lateral impact was then verified.

<u>Impact Response of Head (Lateral Load)</u> - Figure 5 shows the model used by Yoganandan et al. (2004) to simulate a lateral impact test to the head [26]. In this test, the head was dropped with the side facing down so that it impacted on a pad set on top of a load cell at a speed of 3.5 to 6.0 m/s. This test was conducted on a total of ten PMHS and force response

corridors were then created for each impact speed. The force response corridors for the representative loading conditions (initial speed of 6.0 m/s) were then cited when verifying the force response of THUMS. Detailed descriptions of PMHS behavior immediately before the impact are not included in the literature, so it was assumed that the side of the head was perpendicular to the surface of the pad on impact. The force calculated at the surface of the load cell was then compared to the test results.

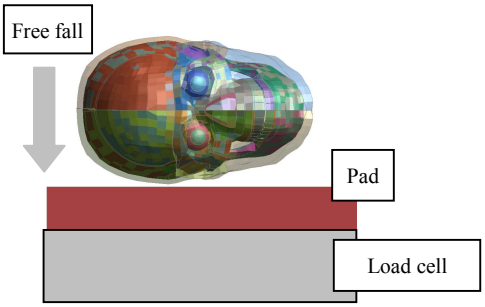

Figure 5. Lateral head impact test.

Figure 6 compares the time history curves of the forces measured and calculated at an impact speed of 6.0 m/s. The black lines are the test corridor and the red line is the force curve of THUMS. The results of THUMS are mostly within the test corridor. Figure 7 compares the peak force at impact speeds of 3.5, 4.9, and 6.0 m/s. The black line segments show the range of the force in the tests and the bar graphs show the peak force values of THUMS. The peak force values of THUMS are within the force ranges from the tests at all the impact speeds. With these comparison results, the research assumed that THUMS Version 4 closely simulated the impact response of the head against lateral impacts.

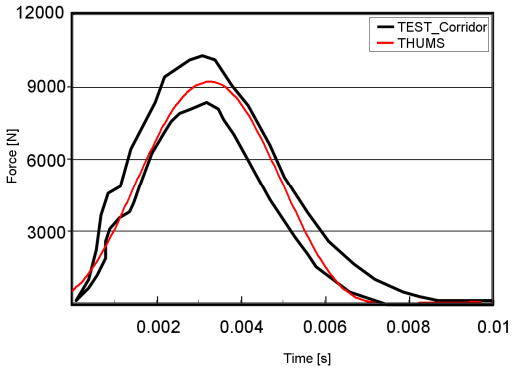

Figure 6. Force response curves of tests and THUMS (6.0 m/s).

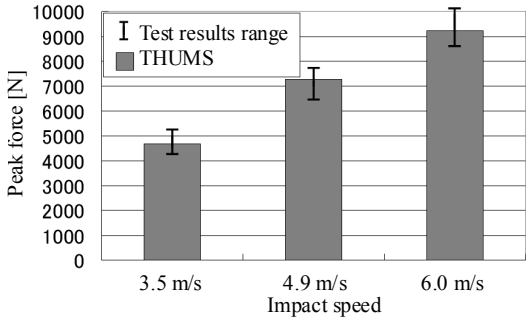

Figure 7. Peak force range of tests and THUMS.

<u>Impact Response of Chest (Lateral Load)</u> - Figure 8 shows a model simulating the lateral chest impact test performed by Viano et al. (1989) [27]. In this test, a cylindrically-shaped impactor with a mass of 23.4 kg is collided with the side of the chest of the PMHS at an initial speed of 3.6 to 10.2 m/s. The displacement of the impactor and the acceleration of the chest were measured during the test. This impact test was conducted on a total of 16 PMHS and force response corridors were created for each initial speed. The corridors for the representative loading conditions (initial speed of 4.5 m/s) were then cited when verifying the force responses of THUMS. The injuries sustained by each of the PMHS were described in the literature. The number of fractured ribs that occurred in a total of ten cases at initial speeds of 4.5 m/s and 6.5 m/s was referenced when verifying the results of THUMS. Detailed descriptions of the postures of the PMHS at the time of the tests are not included in the literature, so these postures were simulated based on the figures in the literature, and THUMS was arranged so that both arms were raised upwards. The impact force was calculated at the end of the impactor (the surface that makes contact with the side of the chest). The displacement of the impactor was obtained from the displacement of the nodes on the model and the deflection of the chest was found from the change in distance between the nodes on the surface of the side of the chest where the impact occurred, and the nodes on the opposite side of the chest from the impact.

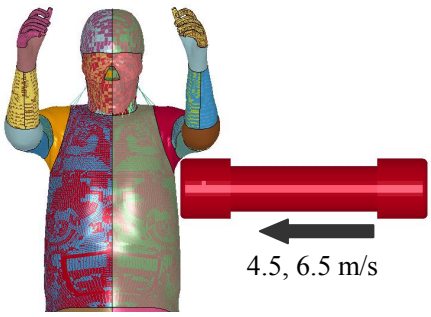

Figure 8. Lateral chest impact test.

Figure 9 compares the chest force response of the PMHS and THUMS with an initial speed of 4.5 m/s. The horizontal axis shows the chest deflection, and

the vertical axis shows the impact force. The force response of the PMHS is displayed by the grey corridor and the force response of the THUMS is shown by the red line. The upper limit of the test was a chest deflection of 50 mm at 3.2 kN, and the lower limit was a chest deflection of 60 mm at 1.5 kN. The result obtained from the THUMS was a chest deflection of 60 mm at 2.8 kN, so the result fell within the range of the upper and lower limits of the test.

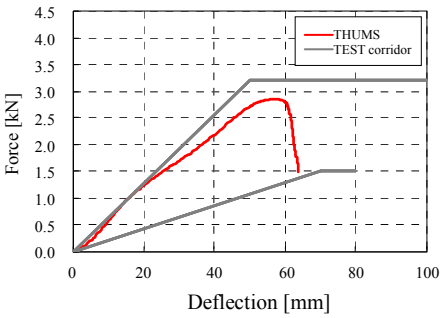

Figure 9. Comparison of chest load – chest deflection response.

Figure 10 compares the number of bone fractures in the ribs of the chest area in PMHS and THUMS. The vertical axis shows the number of rib fractures and the horizontal axis shows the initial speed. It was reported that, of the ten ribs in the PMHS used to verify THUMS in this research, eight were fractured in the tests performed by Viano et al[27]. The number of bone fractures ranged from 0 to 2 when the initial speed was 4.5 m/s, to a range of 2 to 7 fractures when the initial speed was 6.5 m/s. At 4.5 m/s, the number of fractured ribs with THUMS was 0, while at 6.5 m/s, the number of fractured ribs was 3. In both cases theses results were within the ranges established for the number of fractured bones in the tests. Furthermore, in this research it was assumed that a bone fracture occurred when the strain value calculated from the cortical bone shell elements exceeded 3%.
Based on the results described above, the research assumed that THUMS Version 4 closely simulated the impact response of the chest against lateral loading.

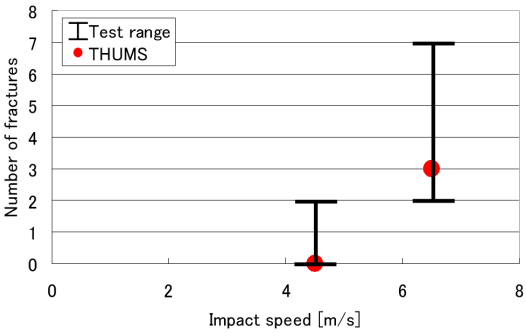

Figure 10. Number of rib fractures.

<u>Four-Point Bending Response of Knee</u> -
Figure 11 shows a model that simulates the knee joint bending test that was conducted by Bose et al. (2004) [28]. In this test, both ends of a PMHS knee (distal femur and proximal tibia) were fixed in place on a 4-point bending test device and the knee joint was moved and bent at an input velocity of 1.5 m/s. This test was conducted on a total of eight PMHS knee joints and a force response corridor was created. The force response corridor created from these PMHS tests was then compared to the FEM response. It was assumed that the ligaments in the knee ruptured when 16% elongation occurred.

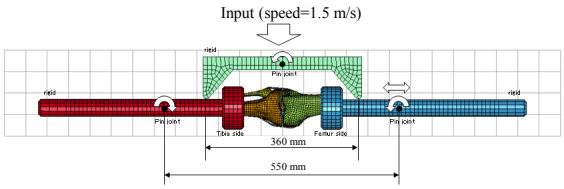

Figure 11. 4-point bending of knee joint.

Figure 12 compares the moment-bending angle corridor lines obtained from the test and the moment-bending angle line calculated using THUMS. The results obtained from THUMS (red line) indicate that up to a bending angle of 12.5 degrees the results stayed almost within the center of the test corridor (black dotted lines) and therefore were very consistent with the test results. It is estimated that when the bending angle of the knee joint in THUMS exceeded 12.5 degrees the ligaments ruptured. This is equivalent to a 40% risk of ligament rupture according to the results obtained from experimentation.
With these comparison results, the research assumed that THUMS Version 4 closely simulated the bending response of the knee joint in four-point bending.

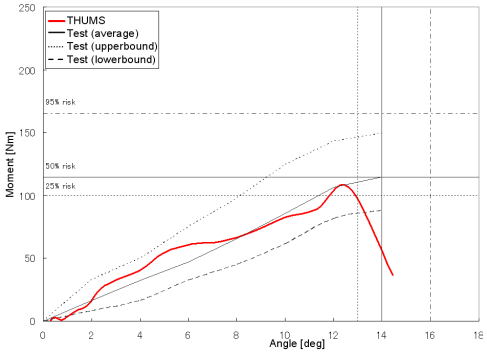

Figure 12. Relationship between moment and bending angle.

Verification of Pedestrian Behavior during Collision with SUV

Figure 13 shows a model that simulates a collision test between a PMHS and an SUV that was conducted by Schroeder et al. (2008) [3]. In this test, an SUV traveling at 40 km/h collided with a PMHS

that was being kept in a standing posture. Table 1 shows an outline of the test conditions. Scaling was performed on each portion of the body to make the physique of THUMS more closely match the proportions of the PMHS. The test conditions, such as the standing posture, were also simulated by referring to the descriptions in the literature. Figure 4 shows an outline of the PMHS and THUMS after it was modified. In this test, target markers were affixed to each portion of the PMHS and then the position of these markers was captured with a high speed camera to measure the trajectories during the collision. In the case of THUMS, the change in the node coordinates at each of the same positions as the target markers was outputted. In the test, the locations of the fractured ribs caused by the collision were recorded. Therefore, THUMS was used to predict rib fractures presuming that a fracture occurs when the strain of the cortical bones reached 3%.

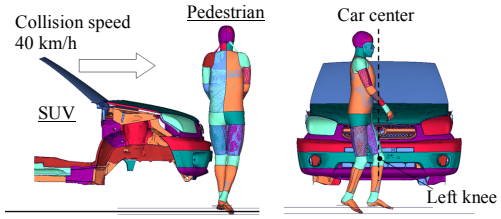

Figure 13. Simulation model of collision between pedestrian and SUV.

Table 1.
Pedestrian collision test conditions

	Test	THUMS
Vehicle type	SUV	SUV
Collision speed [km/h]	40	40
PMHS-height [cm]	185	185
Weight [kg]	85	84
Gender	Male	Male

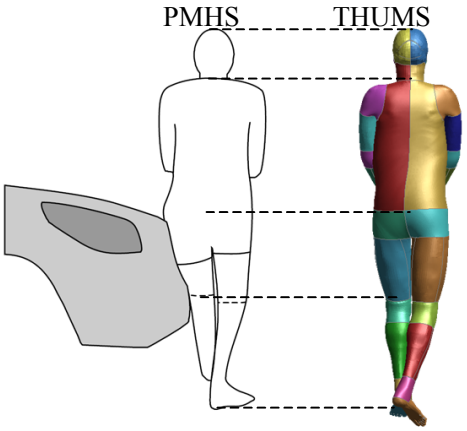

Figure 14. Pedestrian physique and posture .

Figure 15 shows the collision behavior of the PMHS from a posterior view, and Figure 16 shows the trajectories of each portion of the pedestrian's body according to the vehicle datum points. The gray lines in the figure are the trajectories of each portion obtained from the test and the red lines are the results calculated using THUMS. The full-body behavior of the pedestrian measured in the test and the results calculated using THUMS were mostly the same.

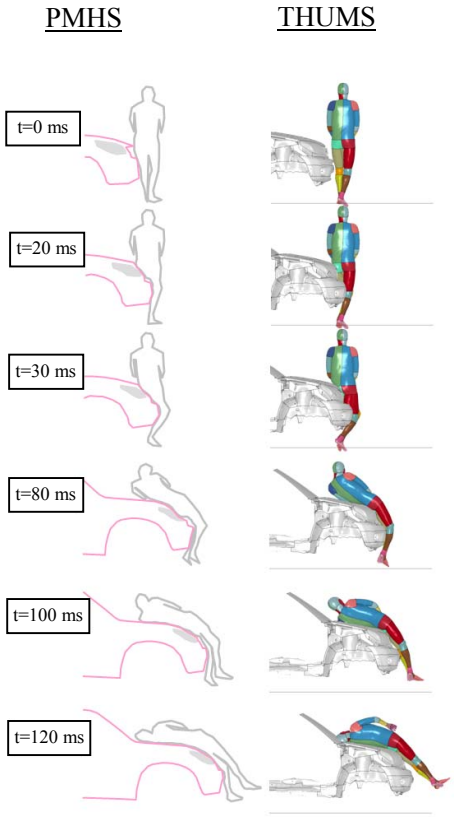

Figure 15. Pedestrian collision behavior .

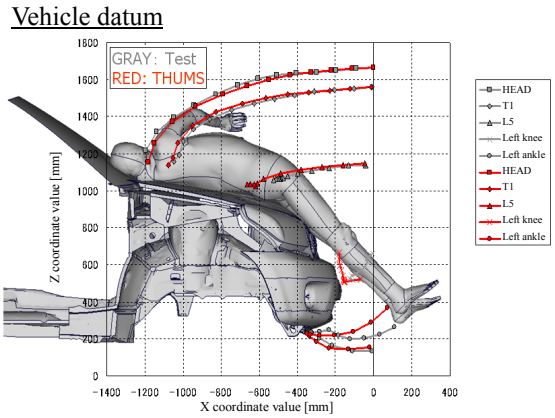

Figure 16. Comparison of pedestrian full-body behavior histories.

Figure 17 compares the PMHS autopsy results and the results predicted by THUMS for bone fractures in the chest region. From both the test and the THUMS simulation, two rib fractures were reported. However, a difference was seen in the locations where these fractures occurred. In the test, the injury was concentrated in the area where the pedestrian's arm was caught between the vehicle and the body, resulting in bone fractures (ribs #5 and #6). In the

case of THUMS, one rib was fractured in the same location (#6) and another rib fracture occurred where the vehicle hood and stomach collided (#10). This difference in the results was inferred to have resulted from differences in the shape of the skeleton in the PMHS and THUMS. The shape of the thorax in the THUMS model has large left and right dimensions in the lower region. It is conjectured that if the horizontal dimension of the inferior portion of the thorax cage of the PMHS is smaller, as shown in the diagram on the left side of Figure 17, then fractures of the lower ribs would not be as likely to occur. Further research is necessary to look into the relationship between the shape of the thorax cage and rib fractures.

PMHS THUMS

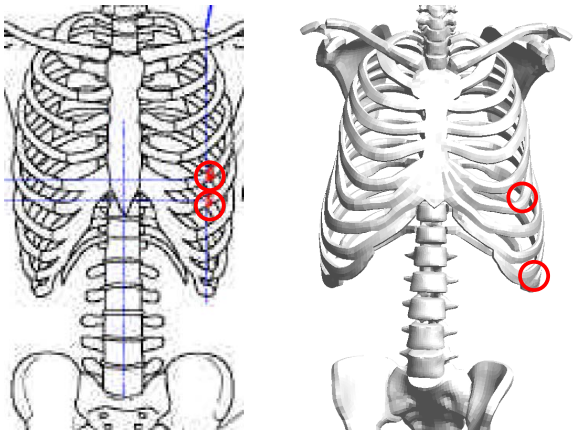

Figure 17. Comparison of rib fracture locations.

Figure 18 compares the locations of ligament ruptures in the knee. In both the test and THUMS, the ACL, PCL, and MCL were all ruptured on the side of the collision (left leg). Furthermore, the areas in the knee where these ligament ruptures occurred were very consistent in both the test and in THUMS. Consequently, after using THUMS Version 4 to predict pedestrian behavior and injuries in the event of a collision with an SUV, the results indicated that THUMS was able to largely reproduce the same results as in tests using PMHS. Therefore, the research assumed that THUMS Version 4 is capable of investigating the dependency of pedestrian injuries on the collision speed.

PMHS THUMS

ACL: detached ACL: detached

PCL: detached PCL: ruptured

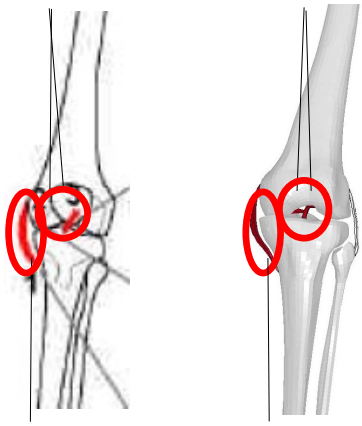

MCL: ruptured MCL: ruptured

Figure 18. Comparison of ligament rupture conditions.

METHODOLOGY

The validated THUMS Version 4 was used to analyze collisions between an SUV and a pedestrian at different collision speeds. Table 2 shows the colliding conditions.

Injury reference criteria values were defined for each body region referring to the literature (Table 3).

For estimating head injuries, the head injury criterion (HIC) and the principal strain on the brain (white matter) were evaluated [29-30]. It was assumed that a skull fracture would occur if the HIC value was 700 or higher. It was also assumed that brain tissue damage and cerebral contusion would occur when the principal strain on the brain white matter exceeded 30%.

For estimating chest injuries, the research monitored rib fractures and the human body tolerance thresholds of the principal internal organs [31-32]. It was assumed that a heart laceration would occur when the principal strain exceeded 30%, while a liver laceration would occur when the strain was 40% or higher.

Table 2.
Colliding conditions

	A	B	C	D	E	F
Collision speed [km/h]	20	30	40	50	60	65

Table 3.
Assumed threshold values

Region	Evaluation index	Reference criteria values
Head (skull)	HIC	700 or more
Brain	Principal strain	30% or higher
Rib (cortical bone)	Plastic strain	3% or higher
Heart	Principal strain	30% or higher
Liver	Principal strain	40% or higher

RESULTS

Of the analysis results obtained under all six colliding conditions (20 to 65 km/h), a significant difference in the injury prediction results was found in the three cases where the collision speed was 30, 40, and 50 km/h (Table 4). This paper compares the full-body behavior and occurrence of injury with an emphasis on these three conditions.

Table 4.
Injury prediction results

Region	Injury	Collision speed					
		20	30	40	50	60	65
Head	Skull fracture	-	-	-	-	-	-
	Cerebral contusion	-	-	Occurred	Occurred	Occurred	Occurred
Chest	Rib fracture	-	-	Occurred	Occurred	Occurred	Occurred
	Heart damage	-	-	-	Occurred	Occurred	Occurred
	Liver damage	-	-	-	-	-	-

Full-Body Behavior

Figures 19 to 21 show the pedestrian behavior during the collisions. At a collision speed of 30 km/h, the knee and vehicle bumper make contact first, and then the hip, side of the stomach, and chest (shoulder) collide with the hood of the vehicle in that order. Finally, the head collides with the windshield glass. When the collision speed is 40 km/h or more, the collision from the knee to the hip with the vehicle is the same as at 30 km/h. However, the chest (shoulder) collides with the cowl portion at the back end of the hood. The head collides with the windshield in the same way as it does at a collision speed of 30 km/h.

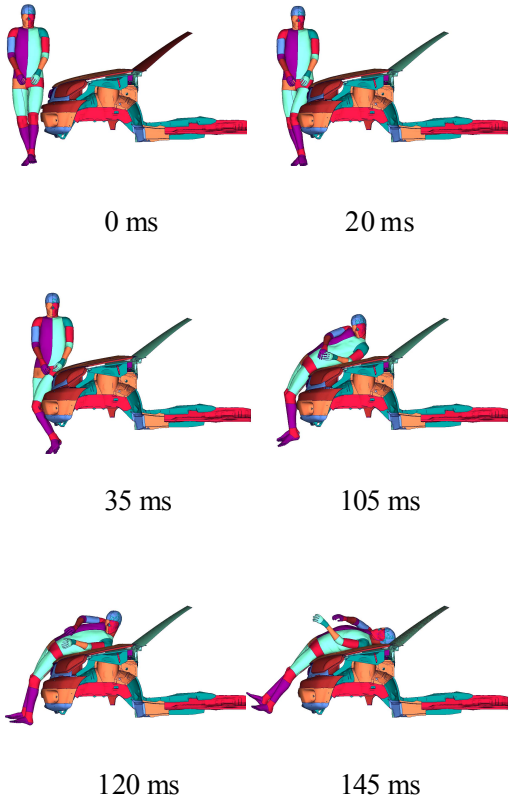

Figure 19. Pedestrian behavior at collision speed of 30 km/h.

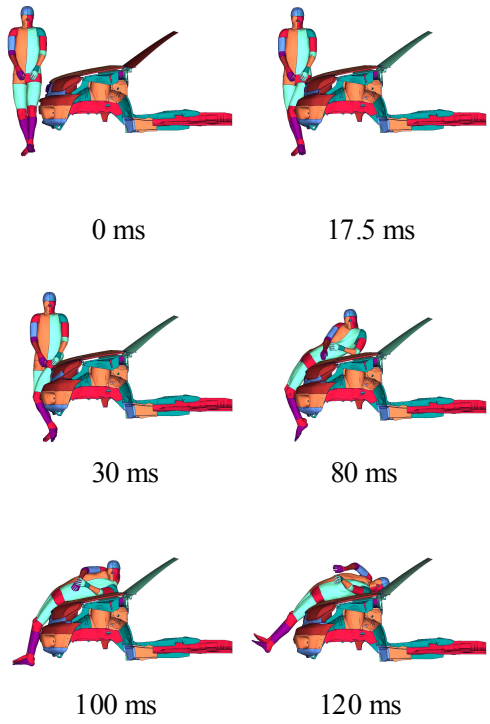

Figure 20. Pedestrian behavior at collision speed of 40 km/h.

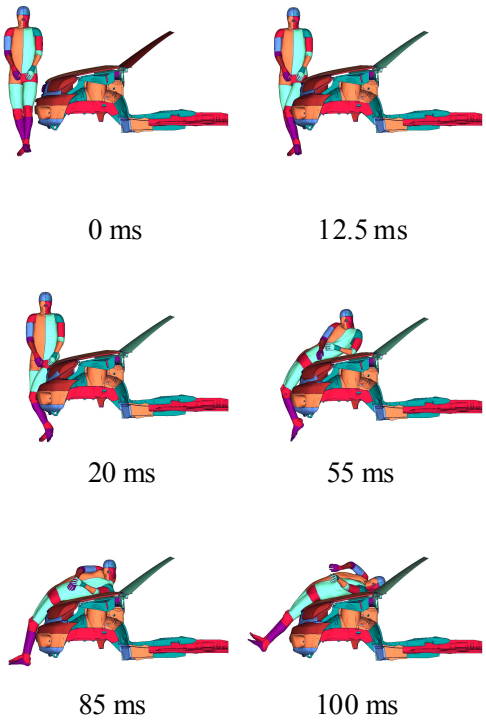

Figure 21. Pedestrian behavior at collision speed of 50 km/h.

Contact Reaction Force during Collision

Figure 22 shows the time history curves of the contact reaction force that the pedestrian receives from the vehicle. The force rises when the bumper collides with the knee and a substantial increase occurs when the hip collides with the edge of the hood. After this, the force reaches its first peak when the side of the stomach collides with the hood and the third force peak appears when the shoulder collides with the hood. The peaks of these forces increase in accordance with the increase in the collision speed.

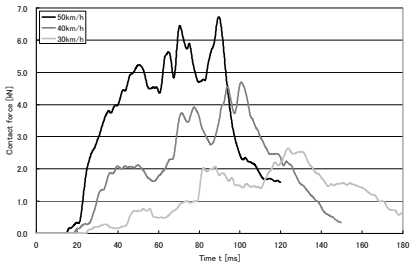

Figure 22. Contact reaction force of pedestrian and vehicle at different collision speeds.

Head Injuries

Table 5 shows the HIC values calculated at each collision speed. All the HIC values were less than the reference criterion value of 700, at which injuries occur, and were generally low values. Figure 23 shows contour maps of the principal strain observed in a central cross section of the brain. It was estimated that at a collision speed of 40 km/h or higher, principal strain exceeded 30%, which is assumed to be the reference criterion value of brain injury.

Table 5.
Head impact responses

		20 km/h	30 km/h	40 km/h	50 km/h	60 km/h	65 km/h
Head	HIC	271	39	214	280	512	512
	Angular velocity [rad/s]	104	64.8	90.7	99.7	207.6	208.5
	Angular acceleration [rad/s^2]	4484	6840	12300	12000	13080	13283

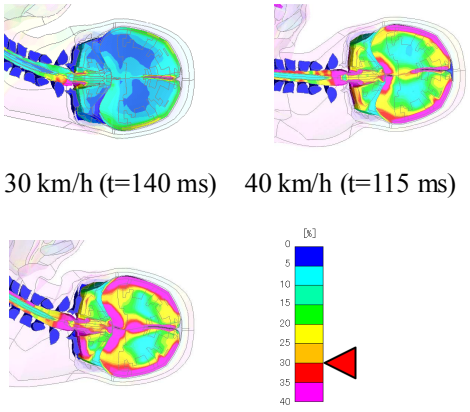

Figure 23. Contour map of principal strain in brain.

Chest Injuries

Table 6 shows the locations on the vehicle hood where the chest collided, the number of fractured ribs, and the compression rate of the chest. Furthermore, Figure 24 shows the locations of fractured ribs depending on the collision speed. At a collision speed of 30 km/h there were no fractured ribs, but at a collision speed of 40 km/h, two ribs were fractured on the side of the body that collided with the hood of the vehicle. At a collision speed of 50 km/h a total of seven ribs were fractured, including ribs on the opposite side of the body from the collision.

Table 6.
Chest impact responses

		20 km/h	30 km/h	40 km/h	50 km/h	60 km/h	65 km/h
Chest	Location of shoulder impact	Hood	Hood	Cowl	Cowl	Cowl – windshield-glass	Cowl – windshield-glass
	Bone fractures	None	None	2	7	14	12
	Chest compression rate (Cmax)	15	16.1	20.1	30.2	42.3	40.5

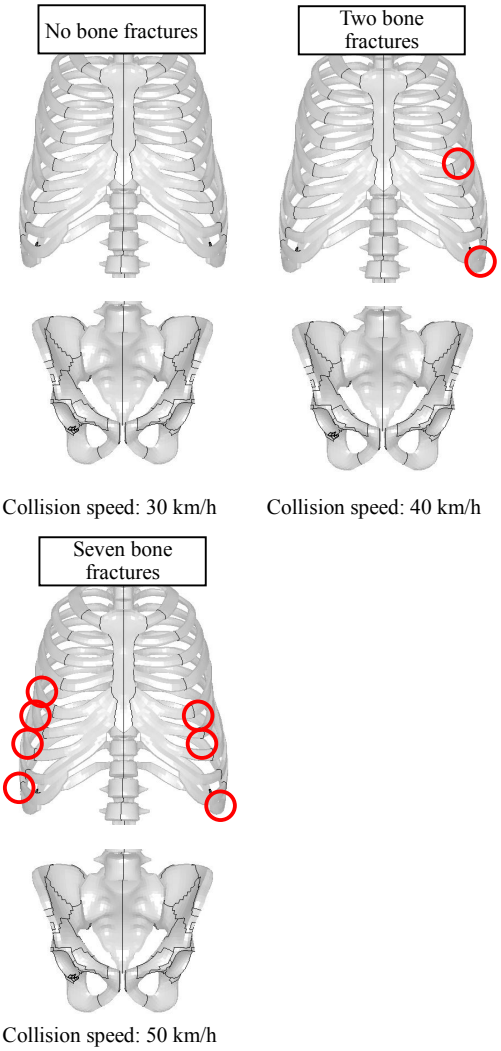

Figure 24. Locations of rib fractures.

Figures 25 and 26 show contour maps of the principal strain observed in a central cross section of the heart and liver. The calculated strain in the heart exceeded 30% at a collision speed of 40 km/h, while the area in which strain exceeded 30% expanded to cover the entire area of the heart at a collision speed of 50 km/h. On the other hand, the range of principal strain that exceeded 40% in the liver at a collision speed of 50 km/h was localized (an area of less than 3% of the total area of the liver).

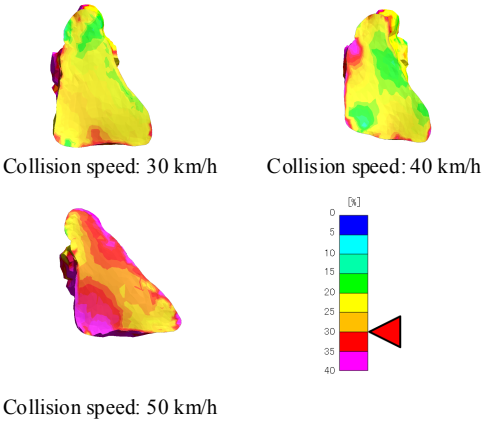

Figure 25. Contour map of principal strain in heart.

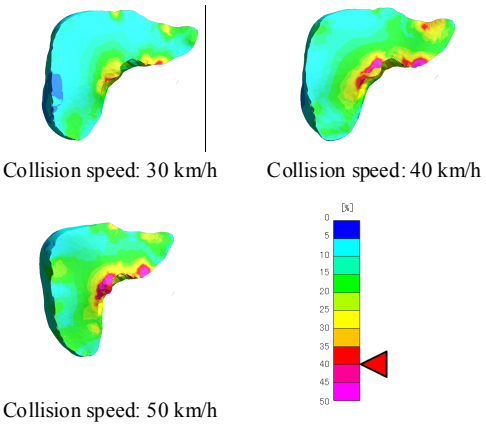

Figure 26. Contour map of principal strain in liver.

DISCUSSION

Relationship between Collision Speed and Brain Injury

The risk of incurring the serious DAI brain injury has been proposed by Margulies et al. (1992) [32]. Figure 27 shows the relationship between the risk of DAI and the angular velocity and angular acceleration of the head. Margulies et al. proposed that the risk of DAI increases when the angular acceleration of the head is 8,000 rad/s^2 or more, or the change in the angular velocity of the head is in the range of 80 rad/s or more (area A in Figure 27). The results of the investigation under the three conditions (collision speeds of 30, 40, and 50 km/h) were inserted into this figure. It was found that the results fell outside at a collision speed of 30 km/h, but that the results fell within area A at collision speeds of 40 km/h or more. Therefore, there is a high risk of DAI occurring at these speeds.

For reference, an evaluation using the cumulative strain damage measure (CSDM) proposed by Thakhounts et al. (2003) [33] was also performed. CSDM is an evaluation index for the occurrence of DAI that uses the amount of strain placed on the

brain. It assumes that DAI occurs when a principal strain that exceeds 25% is present in an area that exceeds 54% of the entire brain area. Figure 28 shows the relationship between the collision speed and CSDM. As shown in Figure 23, when the distribution of principal strain in the brain at a collision speed of 40 km/h or more is considered, the scope of the area where the principal strain exceeds 25% expands significantly. The CSDM (0.25) values also confirm a major increase (35%) between collision speeds of 30 and 40 km/h. CSDM exceeds 54%, which is said to be the criterion value at which brain injuries occur, at a collision speed of 40 km/h or more.

Based on the results described above, the results of the evaluations using angular acceleration and strain-based CSDM at three collision speeds showed that the risk of receiving a brain or other head injury increased when the collision speed was 40 km/h or more.

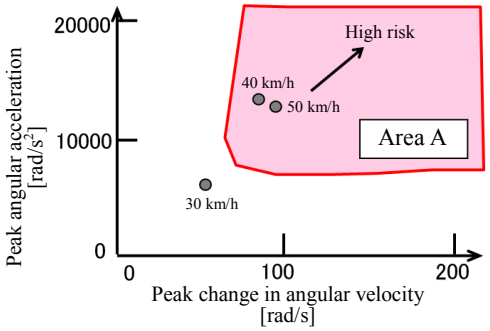

Figure 27. Relationship between angular velocity and angular acceleration of head and DAI risk.

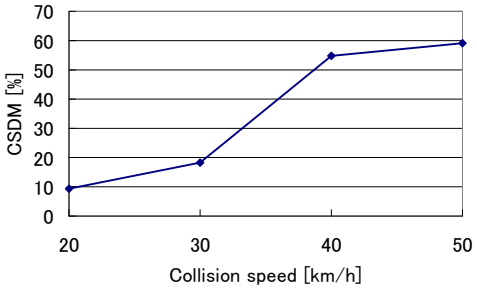

Figure 28. Relationship between collision speed and CSDM.

Mechanism Linking Angular Velocity of Head to Increase in Brain Strain

This research investigated a collision between an SUV and a pedestrian. When the collision speed exceeded 40 km/h, the shoulder of the pedestrian collided with the hard cowl portion located at the rear end of the vehicle's hood and the movement of the chest was greatly decelerated, which produced a large difference in the velocities of the head and the chest (Figure 29). As a result, the angular velocity of the head increased greatly. Furthermore, it is thought that when the translational movement of the head changes into angular motion, a tensile force is generated near to the spinal cord (Figure 30). It is presumed that this increase in the angular velocity of the head and the tensile force generated near to the spinal cord are the causes of the principal strain that is generated near the surface of the brain and near the spinal cord (Figure 31). Therefore, it can be inferred that if the impact of the collision between the shoulder and the hood is lessened, then it may be possible to reduce the angular velocity of the head. In addition, because the head collided with the windshield glass under the conditions in this investigation, the strain on the head due to direct impact was small and the HIC values were also all less than 700.

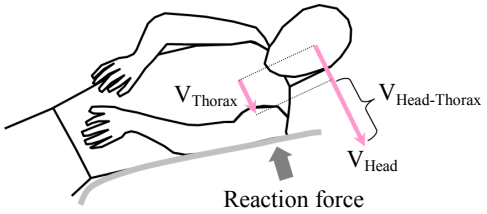

Figure 29. Head and chest velocity pattern diagram at time of shoulder impact.

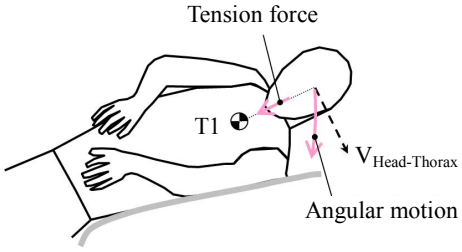

Figure 30. Generation of tensile force and angular motion of head due to difference in velocity between head and chest.

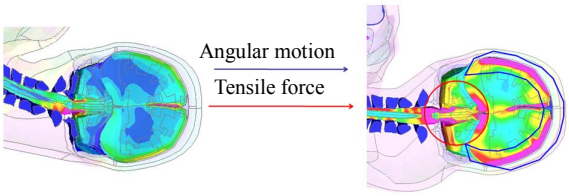

30 km/h 40 km/h

Figure 31. Principal strain generated in brain due to angular motion and tensile force.

Relationship between Collision Speed and Internal Organ Injuries

As shown in Figure 22, when the collision speed of the vehicle increases, the force that acts on the chest of the pedestrian also increases greatly. At a collision speed of 50 km/h the collision force on the side of the stomach is approximately 5 kN and rib fractures occur on both sides of the body. Deformation of the

thorax increases due to this expansion of the area where rib fractures occur and it is assumed that this leads to an increase in the force on the internal organs. Figure 32 shows the amount of deformation of the thorax depending on the collision speed, while Figure 33 shows the human body tolerance threshold excess ratio of the heart (principal strain is 30% or more) depending on the collision speed. It was found that at a collision speed of 50 km/h, there was a significant increase in the deformation of the thorax and also an expansion of the scope of the strain that was generated on the heart.
Based on the fact that serious brain injuries are predicted to occur when the collision speed is 40 km/h or more and that heart damage is predicted to occur when the collision speed is 50 km/h or more, it was inferred that the fatality risk for pedestrians involved in a collision with a vehicle increases when the collision speed is 40 km/h or more.

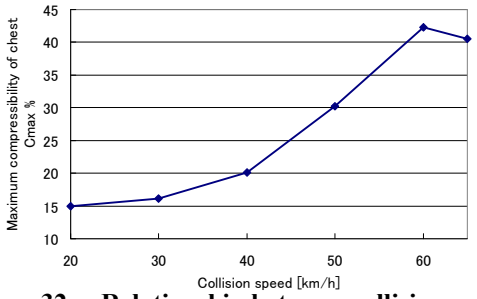

Figure 32. Relationship between collision speed and thorax deformation ratio.

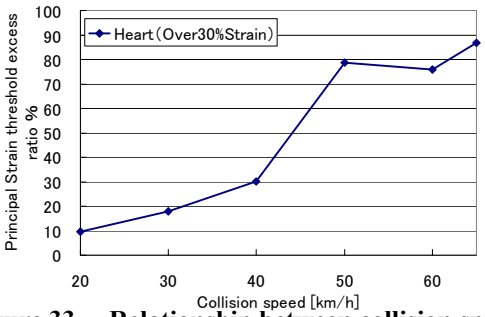

Figure 33. Relationship between collision speed and heart strain.

Limitations

In the calculations conducted in this research it was assumed that an SUV impacts a pedestrian from the side and that the collision is centered in the middle of the vehicle's front end. In an actual accident the pedestrian's physique and posture at the time of the collision, and the shape of the vehicle will all likely vary greatly from these conditions. The results of this research are not intended to explain all accidents involving pedestrians. Furthermore, this research used what was considered to be mean values for the human body tolerance thresholds, which were determined after consulting a wide variety of literature on the topic, in consideration of the great differences that exist among individuals. In the future more research that takes these differences among individuals into account, such as the decrease in the tolerance thresholds due to aging, will be necessary.

CONCLUSION

1. The THUMS Version 4 pedestrian model was used to simulate a collision between a pedestrian and an SUV as described in the literature. It was estimated that THUMS Version 4 successfully simulates the full-body behavior of the pedestrian (PMHS) reported in the literature.

2. Using the validated THUMS Version 4 pedestrian model, the research investigated the relationship of pedestrian head and chest injuries with collision speed.
- It was predicted that the risk of head and chest injuries is lower up to a collision speed of 30 km/h, but that this risk increases at collision speeds of 40 km/h or more.
- When the collision speed exceeds 40 km/h, the pedestrian shoulder collided with the back end of the vehicle's hood and the translational movement of the chest was stopped violently. As a result, the angular acceleration of the head increased greatly and the risk of DAI also increased.
- Moreover, at collision speeds of 50 km/h or more, rib fractures were predicted on both the left and right sides of the body, the deformation of the thorax increased greatly and the risk of sustaining a heart injury was also higher.
The research findings described above were consistent with the trends cited in accident data that the fatality risk for pedestrians increases when the collision speed is 40 km/h or more.

ACKNOWLEDGMENTS

The authors would like to thank Toyota Technical Development Corporation for its assistance with the modeling and simulation work.

REFERENCES

[1] Traffic accident statistics annual report. 2009. Institute for Traffic Accident Research and Data Analysis.

[2] R. W. G. Anderson, A. J. McLean, M. J. B. Farmer, and B. H. Lee. 1995. "Vehicle Travel Speeds and the Incidence of Fatal Pedestrian Crashes." International Research Council on the Biomechanics of Impacts (IRCOBI), 107-117.

[3] G. Schroeder, K. Fukuyama, K. Yamazaki, K. Kamiji, and T. Yasuki. 2008. "Injury Mechanism of Pedestrians Impact test with a Sport-utility Vehicle and Mini-van." IRCOBI, 259-273.

[4] D. Subit, J. Kerrigan, J. Crandall, K. Fukuyama, K. Yamazaki, K. Kamiji, and T. Yasuki. 2008. “Pedestrian-Vehicle Interaction: Kinematics and Injury Analysis of Four Full-Scale Tests.” IRCOBI, 275-294.

[5] J. Kerrigan, D. Subit, C. Untaroiu, and J. Crandall. 2008. “Pedestrian Lower Extremity Response and Injury: A Small Sedan vs A Large Sport Utility Vehicle.” SAE, SAE2008-01-1245.

[6] J. Kerrigan, C. Kam, C. Drinkwater, D. Murphy, D. Bose, J. Ivarsson, and J. Crandall. 2005. “Kinematic Comparison of the POLAR- and PMHS in Pedestrian Impact Test with a Sport-Utility Vehicle.” IRCOBI, 159-174.

[7] T. Yasuki. 2005. “A Survey on the Biofidelity of the Knee Bending Angle of the TRL Lower Leg Impactor.” 19thESV, 05-0101.

[8] H. Miyazaki, F. Matsuoka, M. Kuwahara, Y. Kitagawa, and T. Yasuki. 2009. “Development of Flexible Pedestrian Legform Impactor FE model and Comparative study with Leg Behavior of Human FE Model THUMS.” 21st ESV, 09-0112.

[9] A. Tamura, Y. Nakahira, M. Iwamoto, I. Watanabe., K. Miki, S. Hayashi, and T. Yasuki. 2006. “The Influence of the Traction Force Due to Inertia of the Brain Mass on Traumatic Brain Injury during SUV-to-Pedestrian Impact.” IRCOBI.

[10] THUMS Users Manual. (2010).

[11] J. A. W. van Dommelen, B. J. Ivarsson, M. M. Jolandan, S. A. Millington, M. Raut, J. R. Kerrigan, J. R. Crandall, and D. R. Diduch. 2005. “Characterization of Rate-Dependent Mechanical Properties and Failure of Human Knee Ligaments.” SAE, SAE2005-01-0293.

[12] H. Yamada. 1970. “Strength of Biological Materials.” F. G. Evean, Ed., The Williams & Wilkins Company, Baltimore.

[13] H. Abe, K. Hayashi, and M. Sato. 1996. “Data Book on Mechanical Properties of Living Cells, Tissues and Organs.” Springer-Verlag. Tokyo.

[14] C. S. Shah, K. H. Yang, W. Hardy, H. K. Wang, and A. I. King. 2001. “Development of a Computer Model to Predict Aortic Rupture due to Impact Loading.” Stapp Car Crash Journal, Vol. 45, 161-182.

[15] J. B. Lee and K. H. Yang. 2001. “Development of a Finite Element Model of the Human Abdomen.” Stapp Car Crash Journal, Vol. 45, 79-100.

[16] D. Cesari and R. Bouquet. 1990. “Behaviour of Human Surrogates Thorax under Belt Loading.” SAE902310.

[17] J. Cavanaugh, G. Nyquist, S. Goldberg, and A. King. 1986. “Lower Abdominal Tolerance and Response.” SAE861978.

[18] C. Foster, W. Hardy, K. Yang, A. King, and S. Hashimoto. 2006. “High-Speed Seatbelt Pretensioner Loading of the Abdomen.” Stapp Car Crash Journal, Vol. 50, 27-51.

[19] A. Kemper, S. Duma, F. Matsuoka, and M. Masuda. 2005. “Biofidelity of the SID-ⅡsandaModified SID-IIs Upper Extremity: Biomechanical Properties of the Human Humerus.” Proc. 19th ESV Conference, 05-0123.

[20] A. Kemper, C. McNally, E. Kennedy, A. Rath, S. Manoogian, J. Stitzel, and S. Duma. 2005. “Material Properties of Human Rib Cortical Bone from Dynamic Tension Coupon Testing.” Stapp Car Crash Journal, Vol. 49, 199-230.

[21] E. S. Karl, P. M. Wilbur, C. C. Chales, and A. L. Averill. 1958. “Mechanisms in Development of Interstitial Emphysema and Air Embolism on Decompression from Depth.” Journal of Applied Physiology, Vol. 13, 15-29.

[22] R. W. Nightingale, J. H. McElhaney, D. L. Camacho, M. Kleinbberger, B. A. Winkelstein, and B. S. Myers. 1997. “The Dynamic Responses of the Cervical Spine: Buckling, End Conditions, and Tolerance in Compressive Impacts.” Proceedings of 42nd Stapp Car Crash Conference.

[23] C. K. Kroell, D. C. Schneider, and A. M. Nahum. 1971. “Impact Tolerance and Response of the Human Thorax.” Proc. 15th Stapp Car Crash Conference, 84-134.

[24] C. K. Kroell, D. C. Schneider, and A. M. Nahum. 1971. “Impact Tolerance and Response of the Human Thorax II.” Proc. 18th Stapp Car Crash Conference, 383-457.

[25] K. Shigeta, Y. Kitagawa, and T. Yasuki. 2009. “Development of Next Generation Human FE Model Capable of Organ Injury Prediction.” 21st ESV, 09-0111.

[26] N. Yoganandan, J. Zhang, and F. A. Pintar. 2004 “Force and Acceleration Corridors from Lateral Head Impact.” Traffic Injury Prevention, 368-373.

[27] D. C. Viano. 1989. “Biomechanical Responses and Injuries in Blunt Lateral Impact.” 33rd Stapp Car Crash Conference, SAE892432.

[28] D. Bose, K. Bhalla, L. Rooji, S. Millington, A. Studley, and J. Crandall. 2004. “Response of the Knee Joint to the Pedestrian Impact Loading Environment.” SAE2004-01-1608.

[29] J. M. Abel, T. A. Gennarelli, and H. Segawa. 1978. “Incidence and Severity of Cerebral Concussion in the Rhesus Monkey Following Sagittal Plane Angular Acceleration.” STAPP, 780886.

[30] S. S. Margulies, L. E. Thibault, and T. A. Gennarelli. 1985. “A Study of Scaling and Head Injury Criteria Using Physical Model Experiments.” IRCOBI, SAE1985-13-0015.

[31] J. W. Melvin, R. L. Stalnaker, and V. L. Roberts. 1973. “Impact Injury Mechanisms in Abdominal Organs.” 17th Stapp Car Crash Conference, SAE730968.

[32] S. S. Margulies and L. E. Thibault. 1992. “A Proposed Tolerance Criterion for Diffuse Axonal Injury in Man.” Journal of Biomechanics, Vol. 25 No. 8 917-923.

[33] E. G. Thakhounts. 2003. “On the Development of the SIMon Finite Element Head Model.” Stapp Car Crash Journal, Vol. 47.

DEVELOPMENT OF INJURY CRITERIA FOR FRONTAL IMPACT USING A HUMAN BODY FE MODEL

Eric Song
Erwan Lecuyer
Xavier Trosseille
LAB Peugeot Citroën Renault
France
Paper Number 11-0330

ABSTRACT

Sternal deflection is an injury criterion used in current regulatory and consumer tests worldwide to assess thoracic injury risk. However, this criterion has some serious limits when applied to the Hybrid-III dummy: the risk curve based on the criterion is restraint dependent, and it does not allow discrimination between some advanced restraint systems. The THOR dummy, despite its better biofidelity, is confronted with similar limits. This paper presents a study aiming at identification of more robust injury criteria. A human body FE model-based approach was used to achieve this objective. First, an existing human model was updated and validated for frontal impact simulation, not only in terms of its gross motion response, but also in terms of its capability to predict rib fractures. It was then submitted to a wide range of loading types: impactor, static airbag, belt only restraint, airbag only restraint and combined belt and airbag restraint. For each loading type, different loading severities were applied to generate different levels of rib fracture: from the absence of fractures to numerous fractured ribs. Based on these simulations, bending was identified as the main loading pattern for rib fracture, and two injury criteria were formulated: the Combined Deflection (Dc) and the Number of Fractured Ribs (NFR). The Dc is a deflection-based criterion which takes into account not only sternal deflection, but also the effect of asymmetrical loading. This effect can be characterized by L-R differential deflection (difference of thoracic deflections measured on the left side and the right side of the thorax). The NFR is a rib strain-based criterion which intrinsically reflects the injury level of ribs. The simulations showed that the maximum peak strain of all ribs does not correlate with the number of fractured ribs. The NFR can be calculated by measuring dummy rib strain and by fixing a strain threshold beyond which a dummy rib is considered fractured. A possible approach to apply the NFR to mechanical dummies was proposed. However, based entirely on numerical simulations, the findings of this study need to be evaluated by physical testing. A preliminary study on THOR rib strain measurement showed positive signs for implementation of the NFR on the THOR dummy.

INTRODUCTION

Sternal deflection is an injury criterion used in current regulatory and consumer tests (such as US-NCAP, EURO-NCAP …) worldwide to assess thoracic injury risk. However, this criterion has some serious limits regarding its applications.

Kent et al. (2003) showed that the risk curve in terms of sternal deflection is restraint dependent when measured with the Hybrid-III (H-III) dummy. The risk curve relative to belt loading is completely different from that of airbag loading and that of combined belt and airbag loading. This dependency on the restraint type raises a question as to the relevance of the criterion for its use with the H-III dummy. It means that it is not relevant to construct injury risk curve by mixing data relative to different loading types. It means also that it is incorrect to compare injury risk between these loading types using an injury risk curve constructed in this way.

A more elaborated injury criterion, Cmax (maximum chest compression), was evaluated by Kent et al. (2003) based on 93 cadaver tests. They found that the Cmax is not sensitive to loading types when measured on cadavers. Bose et al. (2009) studied the application of the Cmax on the THOR dummy and found that the risk curve is also restraint-dependent with the dummy.

This study aimed to investigate the relationship between the number of rib fractures and the thoracic deformation in frontal impact, and in particular its variability with respect to various loading types. A finite element thorax model was used to perform this study. It is difficult to use existing biomechanical data for such a study due to: 1) the limited number of PMHS tests available, 2) the important individual variation among PMHS subjects in anthropometry and in mechanical resistance, 3) the lack of the thoracic deflection measurement, or the difficulty to compare them between different methods of measurement when they are available, 4) the uncertainty in the measurements obtained, 5) the different methods used to identify rib fractures. By using a human body model to deal with this issue, one can examine effects of various loading types on a unique subject, with a uniform and accurate

measurement of the thoracic deflection. However, such an approach should be conducted with a thorax model validated not only in terms of global responses but also in terms of injury occurrence, and this for a large range of loading configurations.

Different finite elements thorax models were reported in the literature (Plank and Eppinger 1989, Huang et al. 1994, Lizée et al. 1998, Ruan et al. 2003, Kimpara et al. 2005). These models focused mainly on the validation in terms of global responses, such as the global thorax deflection and the global impact force. Few were dedicated to the validation in terms of injury outcome.

In the current study, an existing human body model (Song et al. 2009) was first updated and validated for frontal impact simulation, not only in terms of its gross motion response, but also in terms of its capability to predict rib fractures. This model was then submitted to a wide range of loading types: impactor, static airbag, belt only restraint, airbag only restraint and combined belt and airbag restraint. For each loading type, different loading severities were applied to generate different levels of rib fracture: from the absence of any fractures to numerous fractured ribs. Based on these simulations, the injury mechanism of rib fractures was investigated, and two candidates are presented respectively as global injury criteria: one based on global thoracic deflection measurement, and the other based on rib strain measurement along the ribs.

EVALUATION OF HUMOS2LAB HUMAN BODY MODEL

The thorax model used in this study was an improved version of the HUMOS model. The HUMOS model is a full human body finite elements model developed by a consortium of universities, research institutes and car manufacturers (Robin 2001). Its mesh was constructed based on the geometry of a single subject who's mass, stature and seated height were close to the mean for a European male. However, the subject presented a more massive torso and less massive lower extremities, typical for an aged person. LAB (Laboratory of Accidentology and Biomechanics) was in charge of the shoulder and the thorax modeling in the first phase of the HUMOS model development in the Radioss^{TM} FE code. The HUMOS model was scaled to other body sizes, and was further updated with respect to new biomechanical data available in the following phases of its development (Vezin et al. 2005). The HUMOS 50th percentile male model in the Radioss^{TM} code was used in this study. Regarding the thorax part of the HUMOS model, the cortical bone of the ribs and the sternum was represented by shell elements, and the trabecular bone by solid elements. The cartilage between the sternum and the ribs was also represented by solid elements. The muscles and internal organs, such as the heart, lungs, stomach and liver were represented by solid elements. An elasto-plastic material law was used to model the cortical bone, an elastic material law for the trabecular bone and cartilage, and a Boltzman material law for the organs and muscles. The vertebrae were considered as rigid bodies, the connections between them were modeled with general springs. The same was done for the connections between the ribs and the vertebrae. Figure 1 provides an overall view of the HUMOS 50th male model, and Figure 2 shows the thorax part of the model.

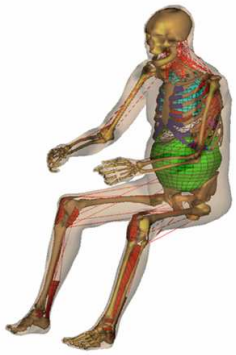

Figure 1. Overall view of the RadiossTM HUMOS 50th male model.

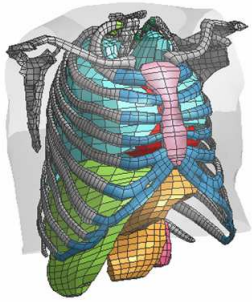

Figure 2. Thorax part of the HUMOS model.

A number of modifications were made to the HUMOS model at the LAB to make the model representative of the behavior of a human thorax, not only in terms of global responses, but also in terms of local responses, such as the strain profiles and rib fractures (Song et al. 2009). To facilitate the expression, the modified model will be referred as the HUMOS2LAB model in the following sections.

In the current study, the HUMOS2LAB model was slightly modified: the cortical bone thickness of first ring of ribs was increased from 0.5 mm to 3 mm; the stiffness of the joint between these ribs and the first dorsal vertebrae was also increased. These modifications were introduced to offer a

more resistant support to the clavicle when the model was subjected to high shoulder belt loading in sled test configuration. They did not change the general validation level of the HUMOS2LAB model. Some examples of validation results of the modified HUMOS2LAB model are provided in Appendix A:

Figure A1 compares the global responses of the HUMOS2LAB model to those of cadaver tests performed by Shaw et al. 2009. Compared responses include: upper and lower shoulder belt forces, sternal deflection, upper left and right thoracic deflection, lower left and right thoracic deflection. A good agreement was observed between model responses and PMHS responses. In particular, the asymmetric deflection pattern of the lower ribcage - characterized by compression on belted side of the ribcage and bulging-out on unbelted side – was well produced.

Figure A2 compares the local strain profile of the 5th rib ring between the thorax model and the cadaver tests under static airbag loading performed by Trosseille et al. 2009. A positive strain corresponds to tension and a negative strain to compression. It can be observed that the model is appropriate to represent the state of deformation for this loading type: the regions of tension and compression, as well as the relative magnitude of strain match the experimental data well.

Figures A3 compares rib fracture regions given by the thorax model to those given by a cadaver test for the frontal sled test with 6kN belt load limiter (Petitjean et al. 2002). In the model, a fracture was established when a shell element of the ribs was deleted. Similar fracture regions were observed.

Figure A4 compares the model responses to those of the experiments (Kroell et al. 1974, Bouquet et al. 1998, Trosseille et al. 2009) in terms of the number of separated fractured ribs (NSFR) versus the impact velocity for the impactor loading type. In the model, a 'separated' fracture was established when a pair of face to face shell elements in the external and internal side of rib were deleted. A reasonable agreement between the model responses and the experiments were observed.

In summary, the validation approach used to validate the HUMOS2LAB model represents a significant advance with respect to the classic approach, which is focused mainly on the validation in terms of global responses. It allowed evaluation of the relevance of a thorax model at deeper layers: the interaction between the ribcage and the surrounding tissues, the ribcage deformation, the occurrence and the variation in location of rib fractures versus loading type and severity. Overall, the thorax model was shown to be consistent with the main features of current cadaver test data available at the LAB, and can be considered as representative of the thoracic behavior.

INJURY MECHANISM OF RIB FRACTURES

It is generally agreed that an excessive strain leads to failure. It is reasonable to extend this general principle to ribs. However, it is not clear how an excessive rib strain is generated in a crash event. In others words, we do not know what type of loading is responsible for excessive strain of ribs. Is it traction, compression, bending, torsion, or a combination of two or more loading modes?

In the HUMOS2LAB model, plastic strain was used as a failure criterion of shell elements representing cortical bones of ribs. A rib fracture occurs when equivalent strain reaches the specified threshold of plastic strain. Consistence of rib fracture regions between the HUMOS2LAB model and PMHS tests observed in the model validation phase supports that excessive strain explains rib fracture well.

Using the HUMOS2LAB model, longitudinal rib strain (along the rib curvilinear axis) and transverse rib strain (along the rib cross section circumference) were compared. Figure 3 is an example of this type of comparison. It shows that the longitudinal strain is the main component compared to the transverse strain. Extensive examination of this type of comparison confirms the generality of this observation. It implies that measurement of strain along the rib axis is a good descriptor of strain state.

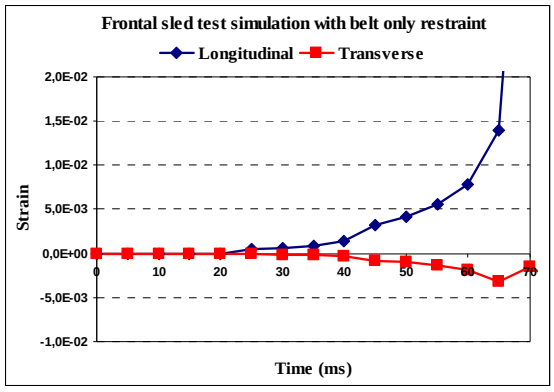

Figure 3. Comparison of the longitudinal rib strain to the transverse rib strain in the same shell element representing rib cortical bone.

In order to determine the loading modes responsible for excessive rib strain, the longitudinal strain field was examined for different HUMOS2LAB model simulations. Bending was identified as an injury mechanism in rib fractures.

Figure 4 is an example for belt loading in a frontal sled test simulation, where high longitudinal strain (≥ 2%) locations are indicated in red (for traction) and in blue (for compression). One can observe that red elements and blue elements are in the opposite sides for each rib. Figure 5 plots stress in face to face shell elements at one of the rib fracture locations. It shows that the traction stress level in the external side of rib is close to the compression stress level in the internal side of rib. These characteristics were also observed for airbag only loading and for combined belt and airbag loading. Based on theses observations, it can be concluded that excessive rib strain (or rib fracture) is mainly generated by bending.

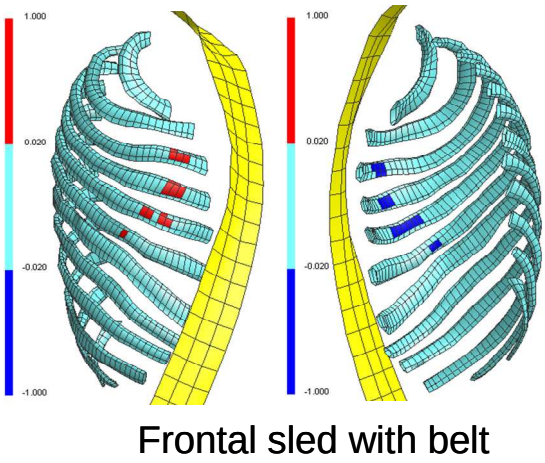

Figure 4. Longitudinal strain field of ribs showing that bending is the main loading mode leading to rib fracture: external side of ribs (left figure), internal side of ribs (right figure).

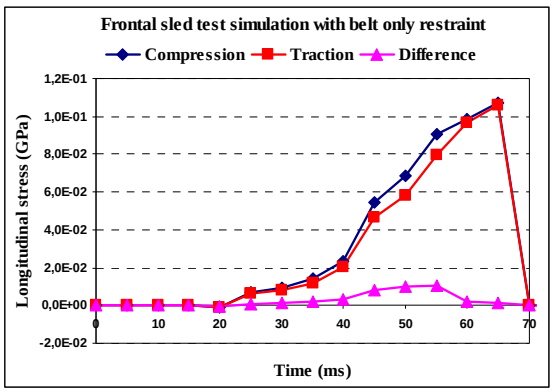

Figure 5. Stress recorded in face to face shell elements at one of the rib fracture locations for belt loading in a frontal sled test simulation.

IDENTIFICATION OF A DEFLECTION-BASED INJURY CRITERION

Simulation matrix

The HUMOS2LAB model was used to identify a global injury criterion correlated to rib fractures but independent to loading types. That means: the relationship between the number of fractured ribs and the injury criterion candidate should be relatively stable. In other words, it should not depend on loading type. For this purpose, the HUMOS2LAB model was submitted to different loading types:

- Static impactor
- Static airbag
- Belt only restraint in dynamic sled environment
- Airbag only restraint in dynamic sled environment
- Combined belt and airbag restraint dynamic sled environment

These loading types cover the main loading configurations used for PMHS tests in literature, but also current restraint systems used for frontal impact protection. For each loading type, different loading severities were applied in order to generate different levels of ribcage damage: from the absence of any fractures to numerous fractured ribs.

Two series of simulations were carried out. One series corresponds to a plastic strain threshold of 1.3%, another to a plastic strain threshold of 2.4%. The reason of varying the plastic strain threshold is to examine the influence of body resistance level on the injury criterion. The plastic strain threshold of 1.3% is the value used by the HUMOS2LAB model resulting from its validation. It reflects the threshold for fragile subjects since all PMHS tests used to validate the model were carried out with aged subjects. The plastic strain threshold of 2.4% corresponds to an ultimate failure strain of 3.1%, which is in line with experimental data on bones (Burstein et al. 1976) for a middle age subject (around 45 year old). Tables A1 summarizes the simulations performed with plastic strain threshold of 1.3% and corresponding injury outcome. Table A2 gives similar results with the plastic strain threshold of 2.4%. The injury outcome is expressed by the number of fractured ribs. A rib is considered as fractured when a separated fracture occurs on it. A separated fracture was established when a pair of inside and outside face to face shell elements were deleted.

Thoracic deflection measurement

Springs with null stiffness were defined over the ribcage to measure its global deflection at different locations. Each spring records the relative displacement of the node, on which the spring is connected, with respect to the corresponding vertebra, but also with respect to its posterior extremity in order to exclude the rigid body

movement of the rib relative to the vertebra. For example, the springs of the 5th rib measure the relative motion of the nodes relative to the 5th vertebra and the posterior extremity of the 5th rib. The floating ribs were not assessed for this study. The thoracic deflection was measured at 4 different locations for each rib, apart from the first ribs where it was measured only at two locations. To facilitate presentation and discussion, the deflections measured for each rib were noted as D1, D2, D3 and D4, respectively. Figure 6 is an example for the 5th rib ring. For the first ribs, the deflections were noted as D1 and D2 in a similar way.

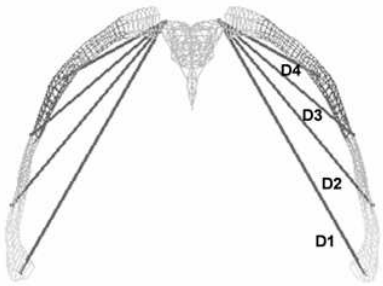

Figure 6. Position of springs measuring the global deformation of the ribcage at the 5th rib level.

More springs were defined over the ribcage to measure its global deflection in its anterior-posterior direction. They are:

- Deflection between the extremity rib 1 and the vertebrae T1
- Deflection between the extremity rib 3 and the vertebrae T4
- Deflection between the extremity rib 5 and the vertebrae T8
- Deflection between the extremity rib 7 and the vertebrae L1
- Deflection between the extremity rib 9 and the vertebrae L2

Three springs were also defined to measure thoracic deflection at levels of the upper sternum, the mid-sternum and the lower sternum.

Based on these measurements, different indicators characterizing thoracic deflection can be defined and calculated.

Injury curve and injury risk curve

In order to examine whether an injury criterion is loading type-dependent, we are going to use a concept named "injury curve". An injury curve is defined as the relationship between injury outcome and injury predictor. Regarding rib fractures, it is the number of fractured ribs that is used to express injury outcome. Figure 7 is an example of an injury curve for airbag only restraint in a dynamic sled environment.

The traditional injury risk curve was also used to evaluate loading dependency of an injury predictor. Since a human body model represents a single subject (there is no individual dispersion), the resulting risk curve always presents a vertical slope which separates injury area from non-injury area. The injury risk is either 0% or 100%, and there is no intermediate risk level. Figure 8 is an example of such a risk curve.

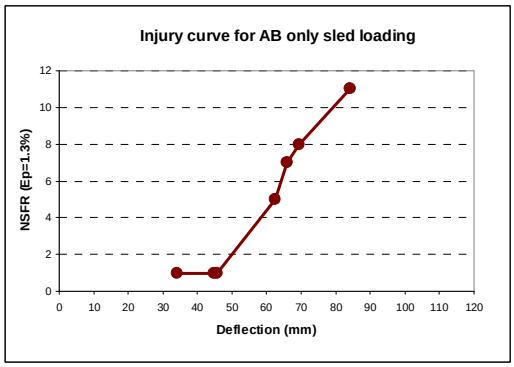

Figure 7. Example of injury curve for airbag only restraint in a dynamic sled environment.

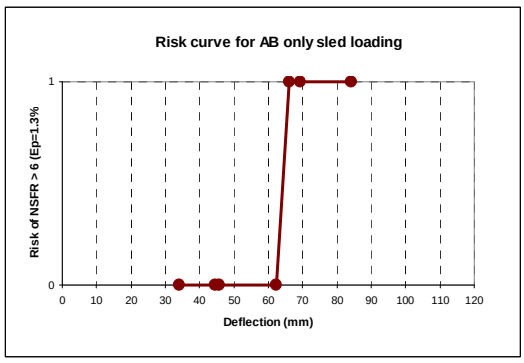

Figure 8. Example of risk curve for airbag only restraint in a dynamic sled environment.

Sternal deflection

Figure 9 shows injury curves and risk curves established based on these simulations in terms of sternal deflection (X-component of the mid-sternum displacement relative to the spine in anterior-posterior direction) for a fragile subject. It can be observed that the injury curve and the risk curve vary from one loading type to another, the 6kN belt loading presenting the most notable difference. The same observation can be made for a stronger subject in Figure 10. Based on these observations, it can be concluded that the sternal

deflection presents, to some extent, signs of loading-type dependent metric. Considering the limits of the criterion when used on H-III and THOR dummies, a loading-type independent criterion needs to be identified.

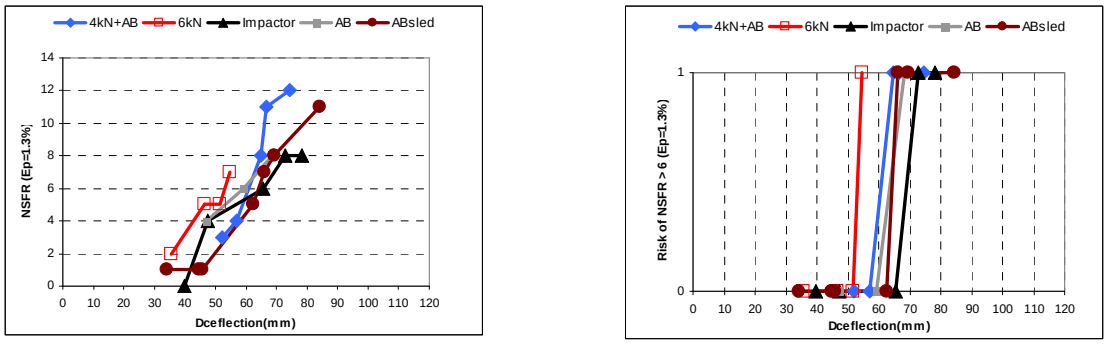

(a) (b)

Figure 9. Injury curves (a) and risk curves of NSFR>6 (b) with sternal deflection as injury criterion. The plastic strain failure threshold was fixed at 1.3%, representing a fragile subject.

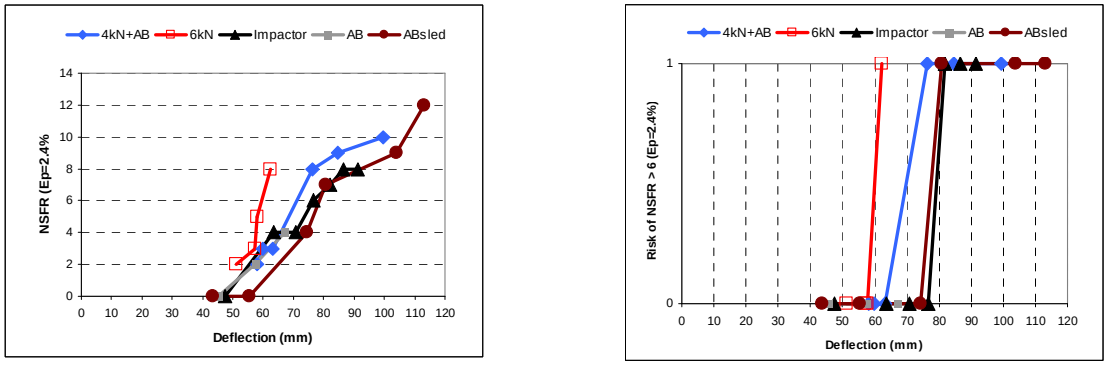

(a) (b)

Figure 10. Injury curves (a) and risk curves of NSFR>6 (b) with sternal deflection as injury criterion. The plastic strain failure threshold was fixed at 2.4%, representing a stronger subject.

Combined deflection - a new injury criterion candidate

Simulations with HUMOS2LAB model allow examination of the ribcage deformation shape under different loading types. Figure 11 compares these deformation shapes. It can be observed that important asymmetric deformation was associated with restraints containing a belt, and in particular with a belt only restraint. Tests with cadavers also showed this type of thorax deformation shape under belt loading (Shaw et al. 2009).

Based on these observations, a new injury criterion candidate, named the Combined Deflection and noted as Dc, was defined as below:

$$Dc = Ds + Cf \times \left[(dD - Lc) + \left|(dD - Lc)\right|\right]$$

Where:
Ds represents the sternal deflection (i.e. the X-component of the mid-sternum displacement relative to the vertebrae T8). This deflection reflects the amplitude of the symmetric part of the ribcage deflection.

dD, named the differential deflection, is the difference between right and left deflections of lower ribcage measured at the junction between the 7th ribs and the cartilage (i.e. the X-components relative to the vertebrae L1). This deflection reflects the amplitude of the asymmetric part of the ribcage deflection.

The X-axis of the coordinate systems for Ds and dD are oriented to be perpendicular to the sternum at the beginning of a test.

Lc, named the characteristic length, serves to amplify the differentiation effect of the term "dD-LC" between different types of asymmetric loadings.

Cf, named the contribution factor, is a coefficient to weight the contribution of the differential deflection to the Dc.

The Dc was calculated for each simulation performed with HUMOS2LAB model, Lc being fixed at 24 mm, and Cf at 0.15. These values were chosen to give the best result in terms of independency for the various loading types. Figure 12 shows injury curves and risk curves corresponding to different loading types for a fragile subject, and Figure 13 shows similar results for a stronger subject.

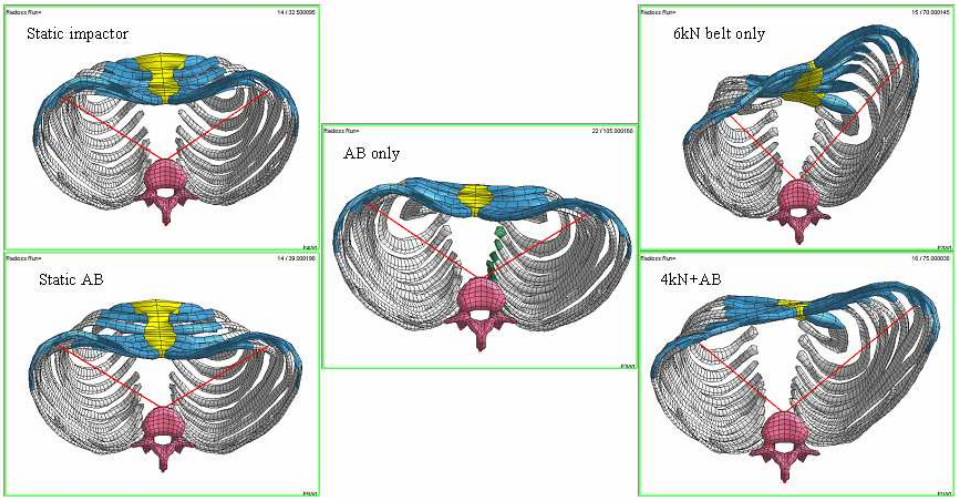

Figure 11. Ribcage deformation shape under different loading types based on the HUMOS2LAB simulations.

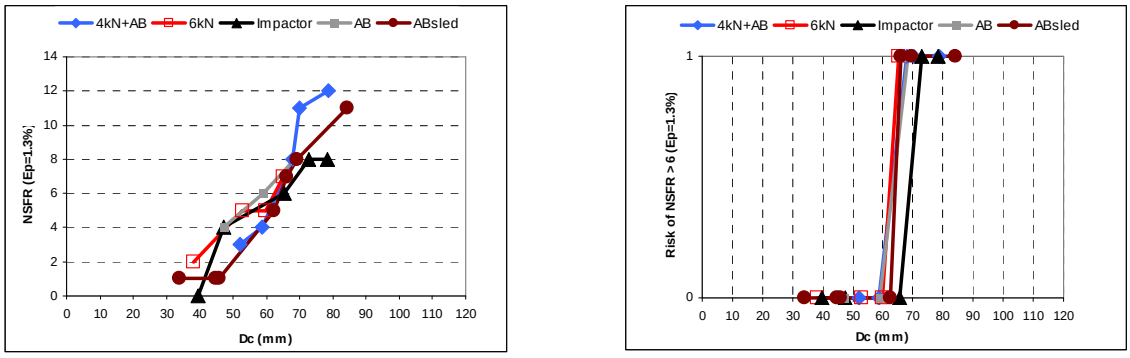

(a) (b)

Figure 12. Injury curves (a) and risk curves of NSFR > 6 (b) with Dc as injury criterion. The plastic strain failure threshold was fixed at 1.3%, representing a fragile subject.

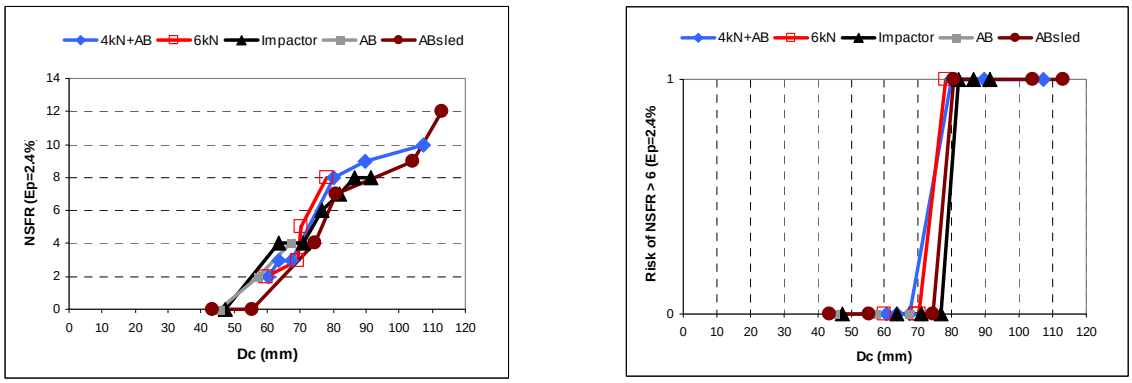

(a) (b)

Figure 13. Injury curves (a) and risk curves of NSFR > 6 (b) with Dc as injury criterion. The plastic strain failure threshold was fixed at 2.4%, representing a stronger subject.

It can be observed that:

- The injury curve does not change significantly from one loading type to another.
- Risk curves of NSFR > 6 are reasonably close, especially when only sled tests are considered.
- The closeness between injury curves, but also between risk curves is much better with combined deflection than with sternal deflection.
- These observations are true both for a fragile subject (strain threshold at 1.3%) and also for a stronger subject (strain threshold at 2.4%).

A STRAIN-BASED INJURY CRITERION

In the section related to injury mechanism, it was concluded that rib fractures can be explained by excessive strain level and that bending is the main component leading to high strain levels. This mechanism of rib fractures suggests that a strain (curvature)-based injury criterion could be used to evaluate rib fracture risk.

A first idea may be to use the maximum peak strain within the ribcage to predict rib fracture risk and severity. However, based on our simulations, we found that the maximum peak strain of ribs does not correlate with the number of fractured ribs. An example is provided below to illustrate this phenomenon.

First, let's compare two simulations of sled tests, performed under identical crash conditions (a 50km/h, 0° frontal sled test): Simulation A corresponding to a 6kN shoulder load limiting belt only restraint, and Simulation B corresponding to a combined restraint with a 4 kN shoulder load limiting belt plus a driver airbag. Figure 14 shows predicted rib fractures for Simulation A and Simulation B. Elements in blue colour are those whose plastic strain went beyond the failure threshold fixed at 3%. The maximum peak strain is higher in Simulation A than in Simulation B. We can observe that there are five fractured ribs in Simulation A and one fractured rib in Simulation B. So, for the subject with a 3% plastic strain as the failure threshold, higher peak strain means also more fractured ribs.

Now let's examine the same simulations but with a more fragile subject (the failure strain fixed at 1.8%). The maximum peak strain is higher in Simulation A than in Simulation B. We can observe that there are eight fractured ribs in Simulation A and twelve fractured ribs in Simulation B (Figure 15). So, for the subject with a 1.8% plastic strain as failure threshold, higher peak strain does not mean more fractured ribs.

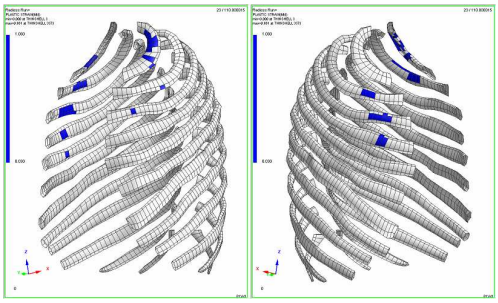

(a) Simulation A: LL6kN belt only

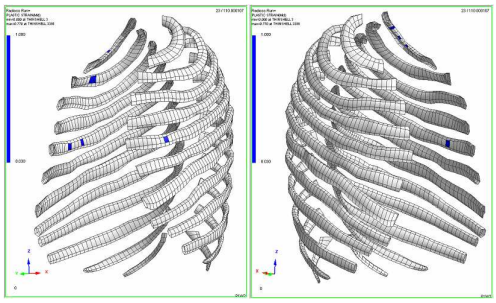

(b) Simulation B: LL4kN+AB

Figure 14. Rib fractures (blue elements) with plastic failure strain at 3%: (a) corresponding to a 6kN shoulder load limiter belt only restraint, and (b) corresponding to a 4kN shoulder load limiter belt plus airbag restraint.

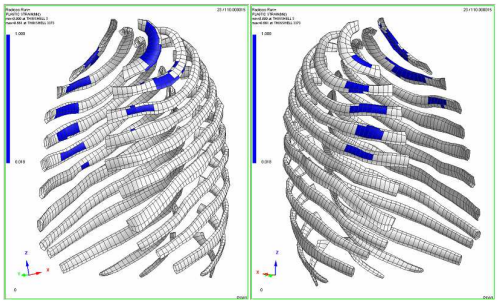

(a) Simulation A: LL6kN belt only

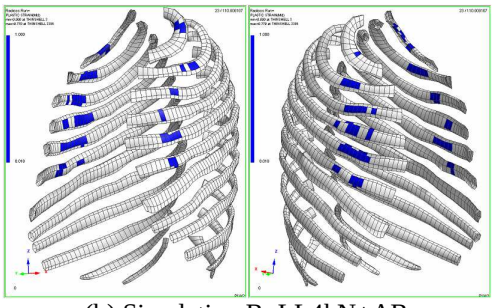

(b) Simulation B: LL4kN+AB

Figure 15. Rib fractures (blue elements) with plastic failure strain at 1.8%: (a) corresponding to a 6kN shoulder load limiting belt only restraint, and (b) corresponding to a 4kN shoulder load limiting belt plus airbag restraint.

Based on the elements above, we propose to use the number of fractured ribs (NFR) as a global injury criterion. On the one hand, this number intrinsically reflects the injury level for the ribs, and on the other hand, it can be determined by strain measurement of each rib. However, a mechanical dummy does not mimic rib fractures. Besides, a mechanical dummy, such as the THOR or H-III, do not have the same number of ribs as the human. So, one may wonder how it is possible to apply such a criterion on a dummy.

Figure 16 illustrates a possible approach to use this criterion. The key point is to determine, for a given dummy, a strain threshold. For each rib of the dummy, once its maximal peak strain reaches the threshold, the rib will be considered as fractured. In this way, we can determine the number of fractured ribs for the dummy in question for each test. But what is the best way to determine the strain threshold? To do this, a three-step approach can be used. First, PMHS-dummy matched tests should be gathered, where we know rib fracture outcome of all PMHS tests, and where the strain distribution of each rib is measured. Then, the NFR-PMHS should be plotted versus the NFR-dummy determined by supposing a strain failure threshold. Finally, we should vary this strain failure threshold until the best correlation is identified. This strain threshold will be the threshold for this specific dummy. For another dummy, we can apply the same method to identify its proper strain threshold.

Once the strain threshold has been determined, the NFR can be derived easily and be used as an injury criterion in the same way as a traditional one, such as the sternal deflection: either to discriminate two restraints as showed in
Figure 17-a, or to evaluate the injury risk by constructing risk curves (
Figure 17-b). For example, a NFR of 1 may indicate that the risk of AIS≥ 3 is 20%. A NFR of 4 may indicate that the risk of AIS≥ 3 is 50%. However, it is important to keep in mind that NFR(dummy) is equivalent to the number of ribs exceeding the strain threshold, which will be lower for the dummy than for PMHS because the dummy ribs will not fail and cause other ribs to be subjected to greater strain. Furthermore, it should be remembered that the THOR dummy has 14 ribs while human has 24. So, NFR(dummy) should be considered as a global indicator reflecting the severity of ribcage deformation.

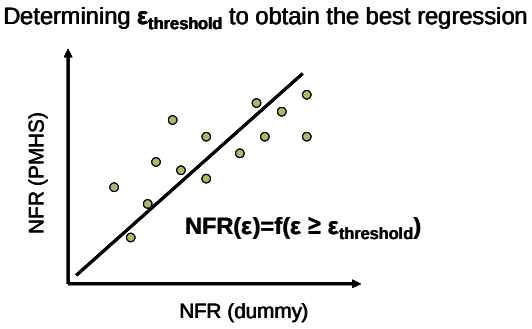

Figure 16. Scheme of a possible approach to apply the NFR as an injury criterion to dummies.

In order for the NFR to work on a mechanical dummy, a reasonable correlation between the NFR-PMHS and the NFR-Dummy should exist. This requirement implies that the dummy should be sensitive to ribcage strain distribution in a similar way to human bodies, and this similitude should be true for different types of loading and its tendency should follow the same trend as in human bodies versus impact severity. To prove this, a large amount of PMHS tests may need to be duplicated with the dummy equipped with strain gauges. But for a feasibility study, a demonstrator with a dummy model may be considered. For this purpose the simulation matrix, presented above for the HUMOS2LAB model, needs to be duplicated with the dummy model.

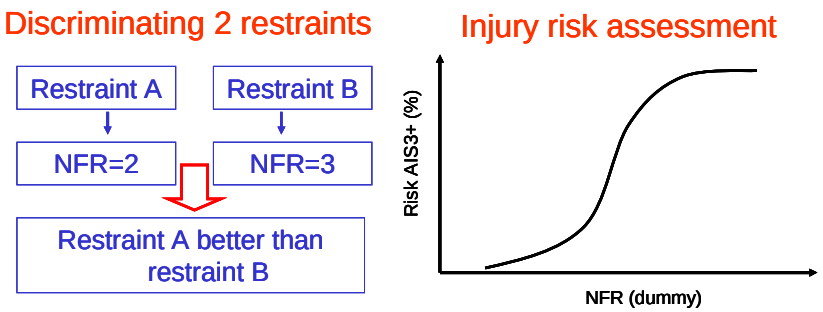

(a) (b)

Figure 17. Scheme illustrating how the NFR can be used to discriminate different restraints and to assess injury risk.

DISCUSSION

Effects of rib fracture modeling mode

In the HUMOS2LAB model, rib fractures are simulated by deleting shell elements representing cortical bone of ribs, once their plastic failure thresholds are reached. With a mechanical dummy, it is unrealistic to imagine, for the time being, a frangible ribcage. So, it is natural to ask if the Dc would work on a mechanical dummy. To investigate this question, simulations were run without deleting shell elements that reached the failure threshold. It is easy to understand that such an approach is more dummy-like but neglects in some extent the domino effects of rib fractures.

Injury curves and risk curves in terms of Dc are given in Figure 18 for a fragile subject and in Figure 19 for a stronger subject. It can be observed that restraint-dependency is considerable for the fragile subject, but is not significant for the stronger subject, especially when only restraints in a dynamic sled environment are taken into account. Although a more significant restraint-dependency was observed based on simulations without shell element deletion, the Dc remains globally better than the sternal deflection, and presents only a moderate restraint-dependency when considering the overview of injury curves corresponding to sled-related loading types.

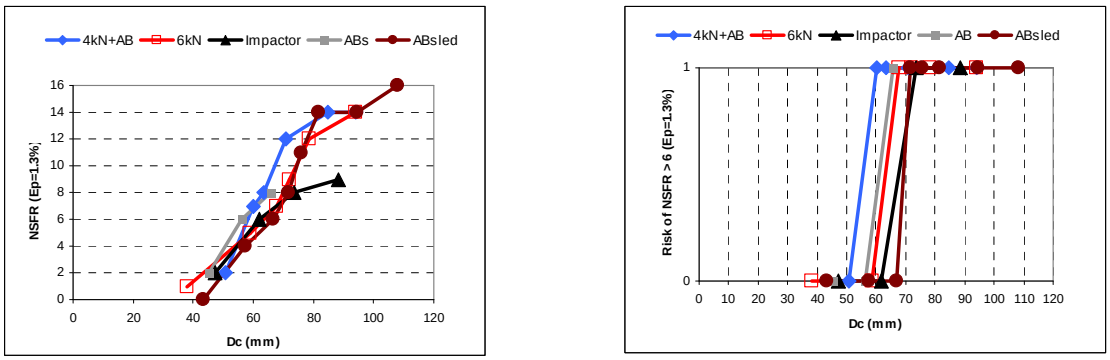

(a) (b)

Figure 18. Injury curves (a) and risk curves of NSFR>6 (b) with Dc as injury criterion, based on simulations without element deletion. The plastic strain failure threshold was fixed at 1.3%, representing a fragile subject.

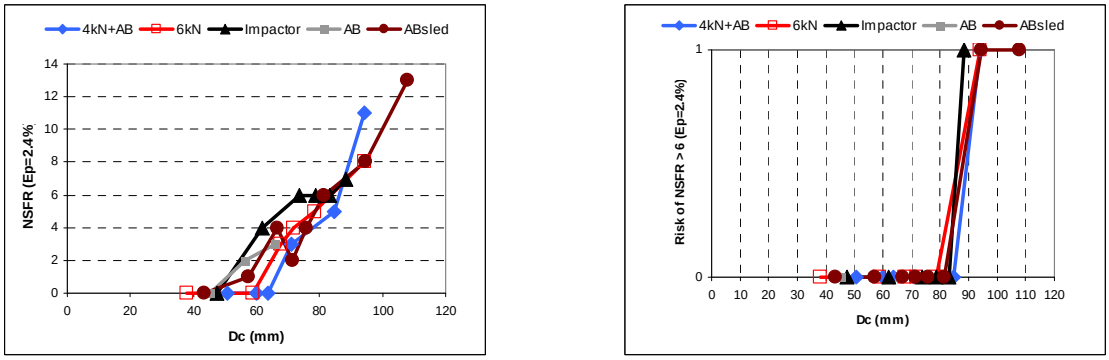

(a) (b)

Figure 19. Injury curves (a) and risk curves of NSFR>6 (b) with Dc as injury criterion, based on simulations without element deletion. The plastic strain failure threshold was fixed at 2.4%, representing a stronger subject

Applicability of Dc to dummies

One important question is whether the Dc can be applied to mechanical dummies.

In Figure 20, THOR geometry and HUMOS2LAB geometry are compared. It can be noted that the two lower thoracic deflection measurements correspond, in some extent, to the deflection measured at Ribs 7 of HUMOS2LAB model. The two upper deflection measurements can be used to approximate the mid-sternum deflection.

Petitjean et al. (2002) performed THOR and H-III sled tests. For the THOR dummy, they found a 47 mm differential deflection for the 6 kN belt only

restraint and a 37 mm differential deflection for the 4kN+AB restraint. Even for the H-III dummy, they found also the existence of differential deflection: 15 mm with the 6kN restraint and 8 mm with the 4kN+AB restraint.

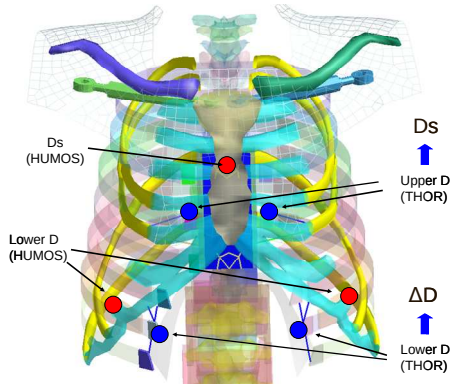

Figure 20. Comparison of the THOR dummy (NHTSA THOR FE model) geometry to the HUMOS2LAB model.

So, in principle, the combined deflection can be calculated with current THOR dummy. However, it is unknown if the criterion measured with the dummy remains valid, i.e. keeps its insensitivity to loading types, as it is the case with HUMOS2LAB model.

To verify this, the most direct method is to gather matched PMHS-THOR test data and to construct risk curves for different types of loading.

Again, an alternative is to use a model of THOR dummy to duplicate simulations performed with HUMOS2LAB.

Choices of Lc and Cf

Lc and Cf are two parameters which determine how the differential deflection of the lower thorax should contribute to the combined deflection. In the results and discussions above, Lc was fixed at 24 mm and Cf at 0.15 for both fragile and resistant subjects. However, there is no reason that these parameters should be the same between fragile and resistant subjects. By using population-oriented Lc and Cf, the restraint-independency of the Dc can be further improved. Regarding the application of Dc on a mechanical dummy, it is obvious that specific Lc and Cf should be determined.

Applicability of NFR to dummies

In order to give a first indication as to whether the criterion NFR may be applied to a dummy, a preliminary study was carried out on THOR dummy. The THOR dummy was instrumented with strain gauges: 20 gauges for each rib ring. It was loaded from the front with the conventional 23.4 kg cylinder impactor at 4.3 m/s. Strain measurements were then used to calculate the strain profile for each rib ring. These strains profiles were compared to strain profiles derived from PMHS tests in the same loading conditions. Figure 21 shows an example of the comparisons: the blue curve represents strain distribution in THOR test, and the two other curves represent the strain distribution in two PMHS tests. The strain measured on the THOR being much lower than the strain measured in PMHS tests, the original THOR strain was tripled in the blue curve in Figure 21 to enable the comparison. First positive signs for implementing the NFR on THOR dummy can be observed in the figure: the strain distribution on the THOR rib was correctly measured by using strain gauges; and the distribution has the potential to be transformed to reflect PMHS rib strain profile.

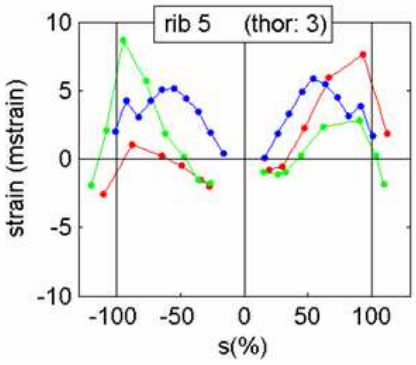

Figure 21. Strain distribution along the 3rd THOR ribs (blue) compared to corresponding 5th ribs on PMHS. Original THOR strain measurement was tripled to enable the comparison.

Limitations of the study

Findings and recommendations in the study were based on human body model simulations. They are results of a series of exploration activities, which were made possible by exploiting advantages of human body model approach. Results are more indicative than confirmative. They should be checked in particular with respect to experimental data when they become available.

CONCLUSIONS

An existing human model was updated and validated for frontal impact simulation, not only in terms of its gross motion response, but also in terms of its capability to predict rib fractures. A series of simulations using the model were performed, forming a "virtual" PMHS test database. Five loading types were covered by this database: three point shoulder-lap belt restraint, combined three point shoulder-lap belt and airbag restraint, and airbag only restraint in a dynamic sled test

environment, and airbag and cylindrical impactor loading in a static environment. For each simulation, the rib fracture outcome was established and different metrics of ribcage deflection were recorded.

Based on these "virtual" PMHS tests, excessive strain, mainly generated by bending, was identified as a primary mechanism of rib fractures.

It was found that maximum peak strain of ribs does not predict the number of fractured ribs correctly. It was suggested to use the NFR (Number of Fractured Ribs) directly as a global injury criterion. A scheme to use the NFR on a mechanical dummy, where ribs always remain in the elastic state, is proposed. The NFR offers the potential to be a universal injury criterion – restraint-independent, impact direction-independent and suitable for evaluating different levels of injuries.

A more usual metric, named as Combined Deflection and noted as Dc, is also proposed. This metric is a global deflection-based predictor for serious injury (more than six fractured ribs). Injury curves and risk curves constructed with this criterion do not vary significantly from one loading type to another. It has potential as a candidate for a restraint-independent injury predictor.

ACKNOWLEGEMENTS

This work was performed in the framework of the EU funded FP7 THORAX project. The authors would like to think the EU-Commission for the funding and the project partners for their collaboration.

REFERENCES

Bose, D., Pipkorn, B., Crandall, J., Lessley, D., Trowbridge, M. (2009) Multi-point thoracic deflection measurement as a predictor of rib injury in frontal collision. Proc. 30th International Workshop on Human Subjects for Biomechanical Research, Savannah, GA.

Bouquet, R., Ramet, M., Bermond, F., Caire, Y., Talantikite, Y., Robin, S. and Voiglio, E. (1998) Pelvis human responses to lateral impact. Proc. ESV1998.

Burstein, A.H. et al. (1976) Aging of bone tissue : mechanical properties. Jouranl of Bone and Joint Surgery 58(A): 82.

Kent, R., Lessley, D., Shaw, G., and Crandall, J. (2003) The utility of H-III and THOR chest deflection for discriminating between standard and force-limiting belt systems. Stapp Car Crash Journal 47: 267-297.

Kent R., Patrie J., Poteau F., Matsuoka F., Mullen C., 'Development Of An Age-Dependent Thoracic Injury Criterion For Frontal Impact Restraint Loading' Paper No. 72, ESV Conference, Nagoya, Japan 2003.

Kimpara, H., Lee, J.B., Yang, K.H., King, A.I., Iwamoto, M., Watanabe, I., and Miki, K. (2005) Development of a three-dimensional finite element chest model for the 5th percentile female. Stapp Car Crash Journal 49: 251-269.

Kroell, C., Schneider, D., Nahum, A. (1974) Impact Tolerance Of The Human Thorax II. . Proc. 18th Stapp Car Crash Conference, pp. 84-134. Society of Automotive Engineers, Warrendale, PA.

Lizee, E., Robin, S., Song, E., Bertholon, N., Le Coz, J.Y., Besnault, B. and Lavaste, F. (1998) Development of a 3D finite element model of the human body. Proc. 42nd Stapp Car Crash Conference, pp.115-138. Society of Automotive Engineers, Warrendale, PA.

Petitjean, A., Lebarbé, M., Potier, P., Trosseille, X., Lassau, J-P. (2002) Laboratory reconstructions of real world frontal crash configurations using the H-III and THOR dummies and PMHS. Stapp Car Crash Journal 46: 27-54.

Robin (2001). HUMOS: Human model for safety - A joint effort towards the development of refined human-like car occupant models. Proc. of the 17th Int. Tech. Conf. on the Enhanced Safety of Vehicles, Paper Number 297.

Shaw, G. et al. (2009) Rib Impact response of Restrained PMHS in frontal sled tests: Skeletal deformation patterns under seat belt loading. Stapp Car Crash Journal 53: 1-48.

Song, E., Trosseille, X., Baudrit, P. (2009) Evaluation of thoracic deflection as an injury criterion for side impact using a finite elements thorax model. Stapp Car Crash Journal 53: 155-191.

Trosseille, X., Baudrit, P., Leport, T., Petitjean, A., Potier, P., Vallancien, G. (2009) The effect of angle on the chest injury outcome in side loading. Stapp Car Crash Journal 53: 403-419.

Vezin, P., Verriest, J.P. (2005) Development of a set of numerical human model for safety. Proc. of the 19th Int. Tech. Conf. on the Enhanced Safety of Vehicles, Paper Number (05-0163).

APPENDIX A

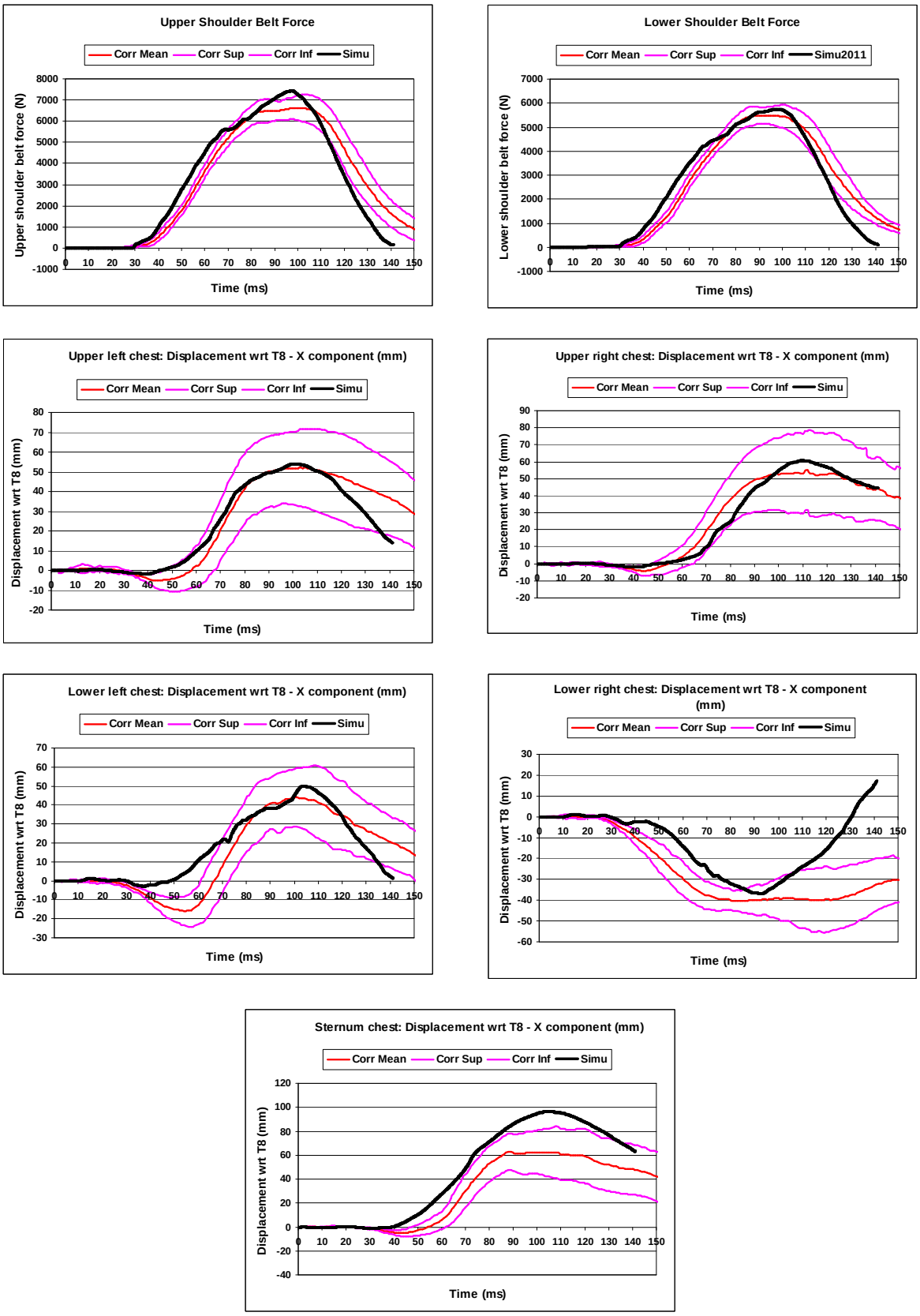

Figure A1. Comparison of HUMOS2LAB model responses to corridors based on sled tests with belt only restrained cadavers performed by Shaw et al. 2009. The corridors were derived by Lebarbé et al. in the framework of ISO WG5.

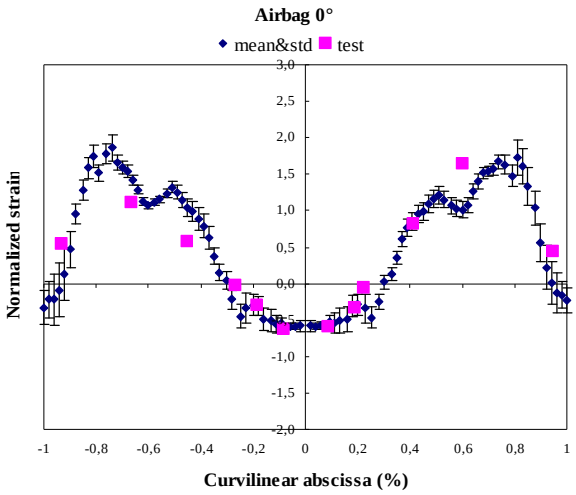

Figure A2. Comparison of the strain profile for the 5th rib between the HUMOS2LAB model and the cadaver tests under static airbag loading performed by Trosseille et al. 2009.

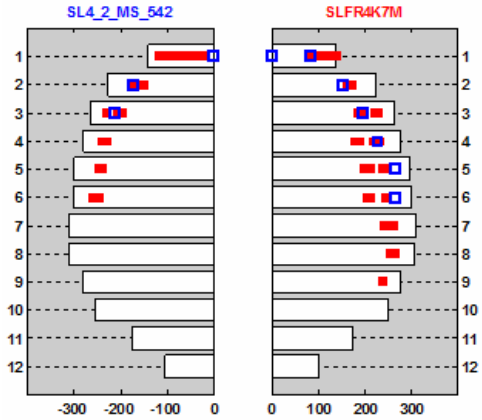

FIGURE A3. Comparison of the fracture regions between the HUMOS2LAB model (red) and the cadaver sled test MS_542 (blue) under combined 4kN belt load limiter and airbag restraint performed by Petitjean et al. 2002.

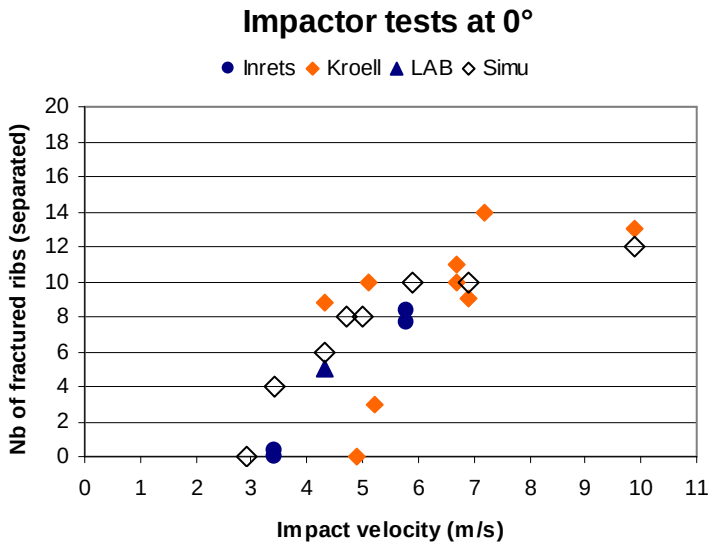

FIGURE A4. Number of fractured ribs versus loading severity for impactor tests: comparison between the HUMOS2LAB model and the experimental data (Kroell et al. 1974, Bouquet et al. 1998, Trosseille et al. 2009).

Table A1.

Simulation matrix performed with plastic strain threshold of 1.3%

Plastic strain = 1.3%				
Model name	Test config	Severity	Loading type	NFR
20AB4R8R	Sled test	ΔV=20km/h	4kN belt+AB	3
22AB4R8R	Sled test	ΔV=22km/h	4kN belt+AB	4
23AB4R8R	Sled test	ΔV=23km/h	4kN belt+AB	8
25AB4R8R	Sled test	ΔV=25km/h	4kN belt+AB	11
30AB4R8R	Sled test	ΔV=30km/h	4kN belt+AB	12
20FD6R8R	Sled test	ΔV=20km/h	6kN belt only	2
25FD6R8R	Sled test	ΔV=25km/h	6kN belt only	5
28FD6R8R	Sled test	ΔV=28km/h	6kN belt only	5
30FD6R8R	Sled test	ΔV=30km/h	6kN belt only	7
30AB0R8R	Sled test	ΔV=30km/h	AB only, Δp*, m(t)**	1
40AB0R8R	Sled test	ΔV=40km/h	AB only, Δp, m(t)	1
40AB488R	Sled test	ΔV=40km/h	AB only, 1.07Δp, m(t)	1
40AB508R	Sled test	ΔV=40km/h	AB only, 1.11Δp, m(t)	5
40AB528R	Sled test	ΔV=40km/h	AB only, 1.15Δp, m(t)	7
40AB3R8R	Sled test	ΔV=40km/h	AB only, 1.22 Δp, m(t)	8
40AB1R8R	Sled test	ΔV=40km/h	AB only, 1.44Δp, m(t)	11
F29STR8R	Impactor	Vimpact=2.9m/s	15cm&23.4kg disc	0
F34STR8R	Impactor	Vimpact=3.4m/s	15cm&23.4kg disc	4
F43STR8R	Impactor	Vimpact=4.3m/s	15cm&23.4kg disc	6
F47STR8R	Impactor	Vimpact=4.7m/s	15cm&23.4kg disc	8
F50STR8R	Impactor	Vimpact=5.0m/s	15cm&23.4kg disc	8
OPM12R8R	Static airbag	D AB/PMHS=128mm	Unfolded AB	8
OPM15R8R	Static airbag	D AB/PMHS=158mm	Unfolded AB	6
OPM17R8R	Static airbag	D AB/PMHS=178mm	Unfolded AB	4
* Δp=differential pressure for venting; ** m(t)=mass flow law				

Table A2.
Simulation matrix performed with plastic strain threshold of 2.4%

Plastic strain = 2.4%				
Model name	Test config	Severity	Loading type	NFR
30AB4R8Q	Sled test	ΔV=30km/h	4kN belt+AB	2
40AB4R8Q	Sled test	ΔV=40km/h	4kN belt+AB	3
45AB4R8Q	Sled test	ΔV=45km/h	4kN belt+AB	3
47AB4R8Q	Sled test	ΔV=47km/h	4kN belt+AB	8
50AB4R8Q	Sled test	ΔV=50km/h	4kN belt+AB	9
60AB4R8Q	Sled test	ΔV=60km/h	4kN belt+AB	10
30FD6R8Q	Sled test	ΔV=30km/h	6kN belt only	2
40FD6R8Q	Sled test	ΔV=40km/h	6kN belt only	3
45FD6R8Q	Sled test	ΔV=45km/h	6kN belt only	5
50FD6R8Q	Sled test	ΔV=50km/h	6kN belt only	8
40AB0R8Q	Sled test	ΔV=40km/h	AB only, Δp*, m(t)**	0
40AB3R8Q	Sled test	ΔV=40km/h	AB only, 1.44Δp, m(t)	0
43AB3R8Q	Sled test	ΔV=43km/h	AB only, 1.44Δp, m(t)	4
45AB3R8Q	Sled test	ΔV=45km/h	AB only, 1.44Δp, m(t)	7
50AB1R8Q	Sled test	ΔV=50km/h	AB only, 1.44Δp, 1.3m(t)	9
50AB2R8Q	Sled test	ΔV=50km/h	AB only, 1.89Δp, 1.6m(t)	12
F34STR8Q	Impactor	Vimpact=3.4m/s	15cm&23.4kg disc	0
F43STR8Q	Impactor	Vimpact=4.3m/s	15cm&23.4kg disc	4
F47STR8Q	Impactor	Vimpact=4.7m/s	15cm&23.4kg disc	4
F50STR8Q	Impactor	Vimpact=5.0m/s	15cm&23.4kg disc	6
F53STR8Q	Impactor	Vimpact=5.3m/s	15cm&23.4kg disc	7
F56STR8Q	Impactor	Vimpact=5.6m/s	15cm&23.4kg disc	8
F59STR8Q	Impactor	Vimpact=5.9m/s	15cm&23.4kg disc	8
OPM12R8Q	Static airbag	D AB/PMHS=128mm	Unfolded AB	4
OPM15R8Q	Static airbag	D AB/PMHS=158mm	Unfolded AB	2
OPM17R8Q	Static airbag	D AB/PMHS=178mm	Unfolded AB	0
* Δp=differential pressure for venting; ** m(t)=mass flow law				

ANALYTICAL AND EXPERIMENTAL DATA OF CHEST DEFLECTIONS AND INJURIES IN SIDE IMPACTS

Narayan Yoganandan, Frank A. Pintar, John R. Humm, Jason J. Hallman, Dennis J. Maiman
Medical College of Wisconsin
Milwaukee, WI USA
Paper number 11-0256

ABSTRACT

Studies using post mortem human subjects (PMHS) are conducted for the design and evaluation of dummies. Biomechanical variables such as forces, accelerations, and deflections are used to characterize responses under simulated environments including frontal, rear, nearside and far-side impacts. The present paper is focused on the nearside occupant. Chest and abdominal deflections are important variables in this mode because real-world injuries to these regions of the human body are shown to correlate with occupant kinematics during the loading event. Consequently, this paper focuses on kinematic data from PMHS tests. Specifically, deflections obtained from chestbands placed on the outer periphery of the thorax and abdomen, and injury data from simulated pure lateral, anterior oblique, and posterior oblique impacts are presented.

INTRODUCTION

Sled tests are often conducted to compare responses of different surrogates (PMHS and dummies) under predetermined initial and boundary conditions in a laboratory environment. Such tests are essential during dummy design and development as it is critical to mimic the human response during impact [1-6]. In crashworthiness research, PMHS responses are commonly used as a benchmark [7-10]. This process, in vogue for more than half a century, has been a major tool for regulators around the world, component suppliers, and other agencies such as the Insurance Institute for Highway Safety in the evaluation of the safety of motor vehicles [11-13]. The present paper focuses on side impacts.

Side impact-induced injuries have been categorized based on the direction of the impact force. From a historical perspective, pure lateral, that is, clock positions of nine for the driver and three for the passenger in the United States, are commonly used as the direction of the loading vector for the evaluation of biomechanics and motor vehicle crashworthiness [10, 14-17]. Analyses using the United States National Automotive Sampling System (NASS-CDS) and Crash Injury Research and Engineering Network (CIREN) have identified anterior-directed oblique, in addition to pure lateral, as another vector associated with trauma to the chest, abdomen, and pelvis in real world side impacts [18]. Because the impact vector is oblique, deflection patterns imparted to the human torso differ from those induced by the pure lateral vector. Recognition of this vector and quantification of biomechanical data requires tests with PMHS in simulated sled environments. These tests produce peak deflections in the anterior oblique directions due to orientation of the impact.

Recent epidemiological and case-specific analyses from NASS and CIREN databases have shown the importance of posterior–directed oblique loading of the thorax in lateral impacts in modern motor vehicle environments. In 2010, Hallman et al. advanced a theory wherein side airbags deployed during impact, may act as a source for spleen and kidney traumas [19]. Mathematical models incorporating side airbag in the simulation of occupant kinematics have delineated the role of posterior-directed thoracic and abdominal deflection in the injury process [20]. In order to better understand the role of this loading vector on injury biomechanics, tests are necessary with PMHS in simulated sled environments.

Consequently, the aim of this paper is to provide side impact data from PMHS sled tests conducted under the above discussed load vectors. Chest and abdomen deflections and injury-related data are given under pure lateral, anterior oblique, and posterior oblique impacts.

METHODS

Pure Lateral Impacts

Specimen Preparation: Unembalmed PMHS were procured, medical records evaluated, and screened for HIV, and Hepatitis A, B, and C before specimen preparation for sled tests. Anthropomorphic data and pretest x-rays were obtained according to established procedures [17]. All specimens were dressed in tight-fitting leotards, and a mask covered the head/face. Prepared subjects were placed on a Teflon-coated bench seat fixed to the platform of a

deceleration sled, configured with an impacting load wall to simulate side impact. The bench seat was 1.3 m long. Four plates (upper plate for measuring contact forces with the mid-thorax, middle plate for the abdomen, lower plate for the pelvis, and extremity plate for the lower extremities) were used in the load wall design. Figure 1 shows the schematic of the load wall and buck.

The configuration of the load wall was such that specimens impacted the wall with the force vector perpendicular to the path of travel of the specimen or with no anterior or posterior obliquity, i.e., pure lateral impact. While the mode was pure lateral, the wall had a flat, pelvic or thoracic offset achieved by moving the lower or upper plate closer to the specimen. The offset was set at 100 mm. The vertical height of the upper edge of the thoracic plate was set at 400 mm to prevent shoulder contact. Figure 2 shows a schematic of the specimen and the targeted impact locations along with the load wall, based on mid-size male anthropometry. Tests were done at 6.7 and 8.9 m/s (low and high) velocities.

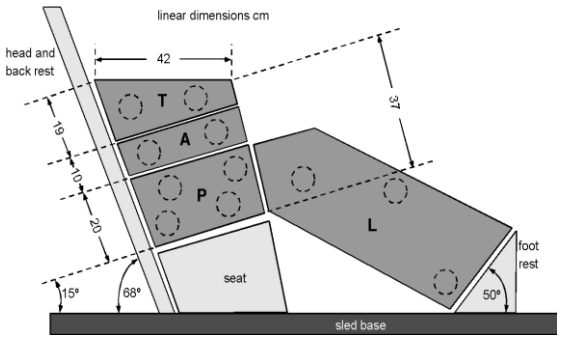

Figure 1: Schematic of the buck showing the load plates (T: thorax, A: abdomen, P: pelvis, and L: lower leg).

Initial Positioning

The initial positioning was such that the Frankfort plane was horizontal, legs were stretched parallel to the mid-sagittal plane, and curvature and alignment of the dorsal spinal column were maintained without any pre-torso rotation in the axial plane. The right-handed Cartesian coordinate system of reference was followed according to the Society of Automotive Engineers (SAE) specifications, i.e., the positive x-acceleration was along the posterior-anterior direction, positive y-axis acceleration was along the left-right axis, and positive z-axis acceleration was along the superior-inferior direction.

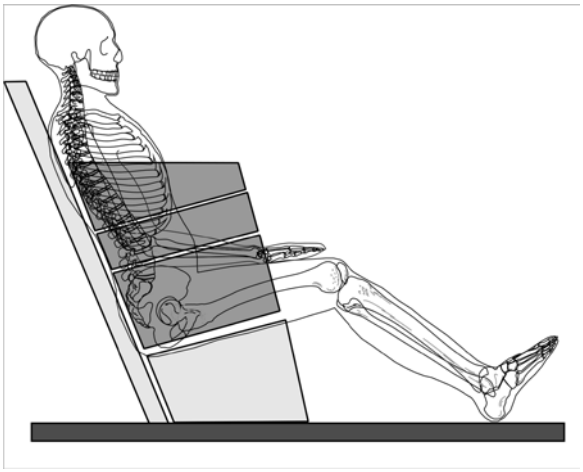

Figure 2: Schematic of targeted impact locations from the four plates onto the specimen, assuming mid-size anthropometry.

The specimen contacted the initially configured flat load wall (padded or rigid) without changes in the anatomical interrelationships between the various body segments. The entire pelvis up to the level of the iliac crest contacted the pelvic load plate. The abdominal load plate was exposed to lower regions of the ribcage while the thoracic load plate engaged the section of the middle ribcage. Tests included rigid and padded impacts. The padding was 10-cm thick, LC200 type. The compressive stiffness was 103 kPa.

Instrumentation

A uniaxial accelerometer was used on the sled to record the input velocity; and tri-axial accelerometers were fixed to the upper thoracic spine (T1), lower thoracic spine (T12), and sacrum (Figure 3). To record medial-lateral accelerations of the struck-side ribcage, uni-axial accelerometers were fixed to the left side of ribs four and eight and sternum. Eleven load cells (two each in the thorax and abdomen, four in the pelvis, and three in the extremity) were used to record the dynamic forces. Chestbands were fixed at the axilla (upper), xyphoid process (middle), and tenth rib (lower) to measure deformation-time histories. Chestband signals were filtered at class 600, and deformation contours were computed at 250 one-millisecond intervals. Starting at the spine and following the contour clockwise path, locations were identified at 20, 25, and 30% of the circumference (Figure 4). A line was drawn between the sternum (one-half of contour circumferences) and spine on each contour, and the three identified locations were projected onto the sternum-spine line. The distance

was measured between each point on the contour of the left side of the thorax and the projected sternum-spine line. The resulting three measurements (0, 25 and 30 percent circumference) were averaged to obtain the mean deflection. The process was repeated at all time intervals to obtain left-half chest deflection-time plot. Normalized chest deflections were obtained by dividing this deflection by the one-half depth of the PMHS chest.

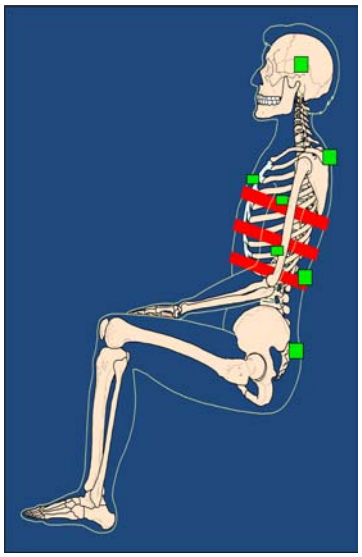

Figure 3: Instrumentation showing chestbands and accelerometers on the spine and head.

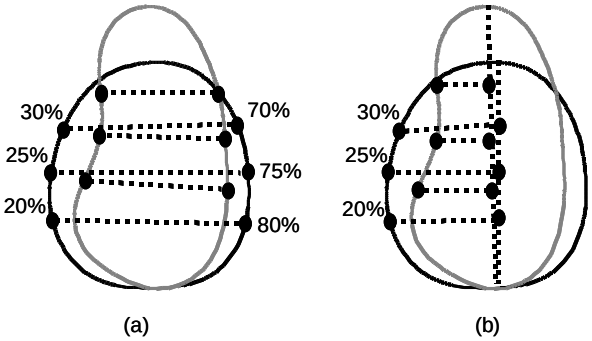

Figure 4: Schematic to determine full (a) and half (b) deflections from chestband contours.

Following the test, specimens were palpated, a clinical-type examination for stability was performed by the clinical personnel, x-rays were obtained, an autopsy was conducted, and traumas were graded based on the Abbreviated Injury Scale [21].

Anterior Oblique Impacts

The experimental protocol used for anterior oblique impacts were based on pure lateral impacts. The setup was configured, as before, for left side impacts. The specimens were seated upright with the Frankfort plane horizontal, legs stretched parallel to the mid-sagittal plane, and normal curvature and alignment of the dorsal spine was maintained without any initial torso rotation. Frontal and overhead schematic views of the test setup are shown in figures 5 and 6. To simulate an oblique lateral impact, the abdominal and thoracic plates of the wall were angled 20- or 30-degrees.

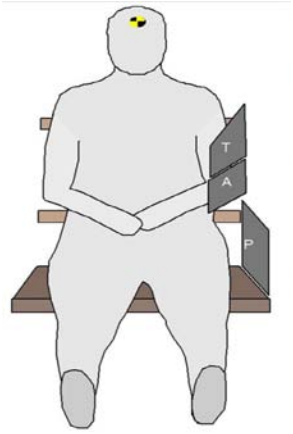

Figure 5: Frontal view showing the positioning for anterior oblique impact tests. The same four load wall plates used in pure lateral impacts were used in this series. Figure 1 shows plate details and dimensions, and figure 6 shows the overhead view of the setup.

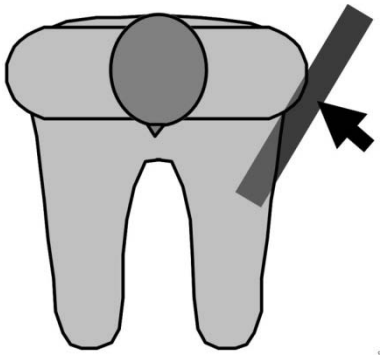

Figure 6: Overhead view showing positioning for anterior oblique impact tests. The arrow indicates the direction of the impacting load vector. Figure 5 shows the frontal view, albeit to a different scale.

Contours of chest deflections at the three thoracic levels were computed at every millisecond. Using palpation, the spine location corresponding to PMHS spinous process was identified and two closest gages bilateral to the anatomy were located. The center of the line joining the two gages defined the origin and the "spine" on the contour. The sternum location on the contour was identified as the point diametrically opposite to the "spine". These sternum and spine locations defined the reference line for determining one-half chest deflections on the struck side. After defining the spine and sternum locations on the undeformed contour, or on the contours before time-zero, these locations were used to define half deflection values throughout the event. On the undeformed contour, the midpoint of the line segment joining the spine and sternum was located and the distance from the spine point to midpoint was recorded. This distance was used to continue to define the reference point from which the half deflection measures were obtained throughout the deforming contour time history. Temporal deflection at any specific location on the chest was defined as the change in the distance between the line joining the location and the reference point in the initial undeformed chest contour and the deformed contour at any instant. Peak deflection was determined from these time histories (Figure 7).

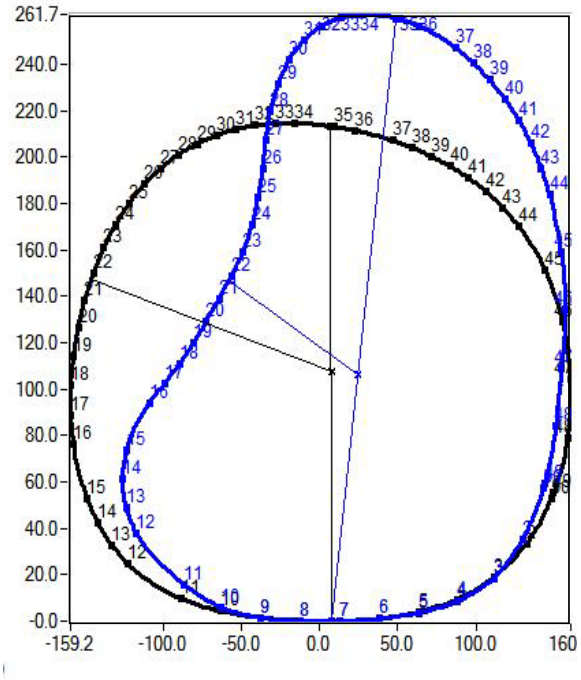

Figure 7: Contours showing the method used to define maximum deflections from the chestband.

Posterior Oblique Impacts

Although the loading patterns for posterior oblique impacts were different, as in the case of the previous load vectors, specimens were seated upright with the Frankfort plane horizontal, legs stretched parallel to the mid-sagittal plane, and the normal curvature and alignment of the dorsal spine maintained without any initial torso rotation. Loading was induced by attaching a side airbag to the load wall, shown in figure 8 [19]. Static and dynamic deployments tests were conducted. In the former, the airbag was deployed to the stationary PMHS, and in the latter, the airbag was deployed using the sled load wall with the PMHS moving towards the wall, similar to the previous two vectors. In static tests, the airbag was mounted approximately 130 mm away from the wall, subjects were positioned approximately 100 mm from the T6-L1 posterolateral thorax to contact the airbag, and sequential bilateral deployment tests were conducted. In dynamic tests, the airbag was mounted approximately 150 mm away from the wall, subjects were positioned 400 mm from the wall, and the airbag was activated when the outboard edges of the module and torso were coincident in the frontal plane to ensure airbag interaction with the posterolateral region of the thorax and abdomen. In static tests, one 59-channel chestband was placed at the xyphoid level, and in dynamic tests, two chestbands were used at the xyphoid and tenth rib levels.

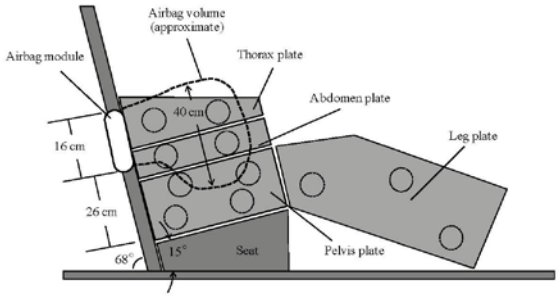

Figure 8: Schematic of the buck showing the four plates (see figure 1 for details) and the side airbag used in static and dynamics tests for posterior oblique loading.

Chestband contours were processed by shifting the contour-based spine and sternum to the right side (10% of circumference) of the subject-specific spine and sternum. The origin was defined as the midpoint between the spine and sternum contour locations at

time zero. As deformation progressed, the origin remained coincident with the spine-sternum axis and maintained a fixed distance from the spine. Net deflections at discrete locations were quantified, normalized to the initial chest breadth, and processed using CFC 180 filter (Figure 9). Similar to the earlier modes of loading, injuries were identified using x-rays and autopsy, and were graded based on the Abbreviated Injury Scale [21].

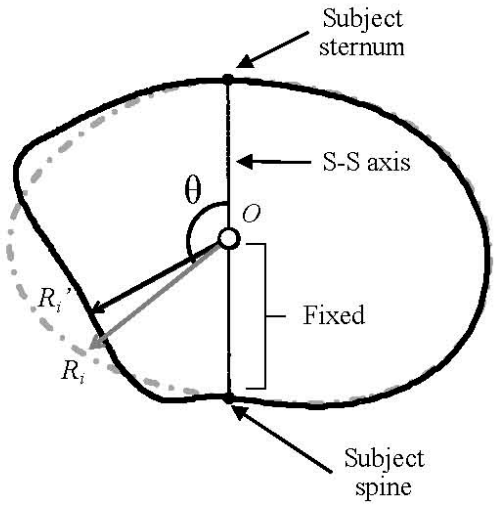

Figure 9: Schematic of the chestband contour for left side posterior oblique loading. S-S refers to the spine-sternum axis. The difference between the two vectors represents the chest deflection.

RESULTS

Figure 10 shows a typical, square wave shape sled pulse used in all tests. Deflection data are described followed by injury results.

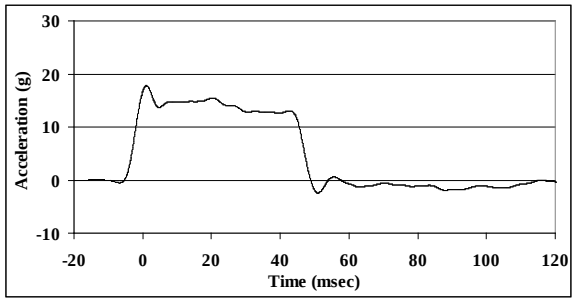

Figure 10: Typical sled pulse.

Pure lateral Impacts

Anthropometric data from 26 PMHS were such that the average age was 62 years, stature was 173 cm, and body mass was 71 kg. Deflection-time signals were unimodal. Corridor data are given [16]. Table 1 summarizes peak deflections of the upper thorax, lower thorax, and abdomen as a function of initial conditions. The upper and lower thoracic deflections were not significantly influenced by the change in test conditions. The time of maximum upper thorax deflection was dependent upon test condition and peaked earliest in the rigid high-speed condition, followed by the padded high-speed, rigid low-speed, and padded low-speed. Similar trends occurred in the lower thoracic deflection; however, discrimination between time of peak was not as pronounced since the rigid low-speed and padded high-speed test results overlapped. Abdominal deflections in the high-speed condition were greater than those in the low-speed condition. The reader is referred to the original paper for deflection-time histores under each conditon.

Table 1: Summary of peak deflections from pure lateral impacts. R and P refer to rigid and padded, H and L refer to high and low speed, and F refers to flat wall, respectively.

Test Condition		Deflection (mm)			
Measurement Location		RHF	PHF	RLF	PLF
Upper thorax	Full	95	89	110	85
	Half	58	60	72	56
	Half/Full	61%	67%	66%	66%
Lower thorax	Full	93	100	82	82
	Half	58	55	51	52
	Half/Full	62.40%	55.00%	62.20%	63.40%
Abdomen	Full	n/a	118	86	98
	Half	n/a	78	52	58
	% Half/Full	n/a	66.10%	60.50%	59.20%

While the upper and lower thoracic deflections were not considerably influenced by test conditions, their times of occurrence depended on test condition and peaked earliest in the rigid high-speed condition, followed by the padded high-speed, rigid low-speed, and padded low-speed. Abdominal deflections were greater in the high-speed than the low-speed test condition.

Anterior Oblique Impacts

Anthropometric data from four specimens were such that the mean age, stature, and total body mass were 55 years, 173 cm, and 59 kg. Peak deflections at the upper, middle, and lower levels of the chest, from the

three temporal chestband contours, on a test-by-test basis, are given in table 2. The mean maximum deflections at the upper, middle and lower levels of the chest for the 30-degree tests were 96.2, 78.5, and 76.8 mm, and for the 20-degree tests, the peak deflection magnitudes were 77.5, 89.9, and 73.6 mm, respectively.

A comparison of deflections from pure lateral and anterior oblique loadings is shown in figure 11. Peak deflections at the upper level were similar between the two groups of tests; at the mid and lower levels, peak deflections were greater in both oblique loadings compared to pure lateral tests, indicating the effect of the obliqueness of the load vector. Although the magnitudes of deflections are the same for the upper band, if deflections are at different locations, the injury tolerance might be less at that thoracic region. While peak deflections at the upper chest level were not different between oblique and pure lateral tests ($p > 0.05$), at the mid and lower thoracic levels peak deflections were significantly greater ($p < 0.05$) in oblique than pure lateral tests.

Table 2: Summary of specimen-specific peak deflections (mm) from anterior-oblique impacts from four specimens.

Test Description	Upper	Middle	Lower
20-degree PMHS test 1	69.6	69.4	69.5
20-degree PMHS test 2	85.3	110.4	77.6
30-degree PMHS test 1	90.5	75.1	86.3
30-degree PMHS test 2	101.9	81.9	67.3

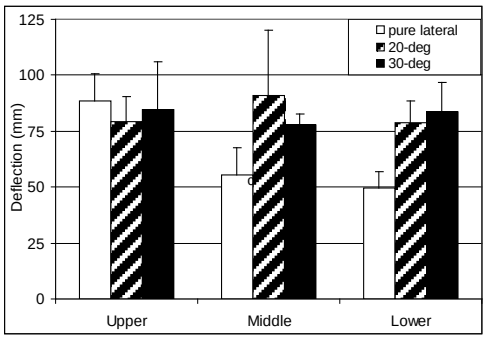

Figure 11: Comparison of the peak deflections at the three thoracic levels between pure lateral and anterior oblique impact tests. Error bars indicate standard deviations.

Posterior Oblique Impacts

Anthropometric data of seven PMHS (three static and four dynamic tests) were such that the mean age, stature, and total body mass were 61 years, 170 cm, and 92 kg. Deformations ensued from the posterior-lateral region of the thorax and abdomen due to airbag interaction in both tests. Table 3 shows a summary of peak deflections along with the angle and time of occurrence on a specimen-by-specimen basis. Maximum deflections occurred between 100 and 110 deg in dynamic and 115 and 135 deg in static tests. A comparison of the mean deflection angles from pure lateral, and anterior and posterior oblique loadings is shown (Figure 12). Deflection angles were in-line with the impact vector in the former two types of tests. At the onset of deflection, mean deflection angle was significantly greater (t-test; $p < 0.001$; 35 deg) in dynamic than pure lateral and anterior oblique tests. Further, both posterior oblique tests showed transient deflection loci ranging from 20 to 30 deg during the first 60 ms of impact; deflection angles resulting from pure lateral and anterior oblique impacts did not vary by more than five deg. Further details along with deflection corridors are given [19].

Table 3: Peak chest deflections at different levels in static (S) and dynamic (D) tests.

PMHS	Location	Peak	Time	Angle
		mm	(ms)	(deg)
S-1	Xyphoid	39.84	14.6	135
S-2	Xyphoid	29.56	21.4	99
S-3	Xyphoid	58.26	22.0	132
S-4	Xyphoid	41.88	12.8	128
S-5	Xyphoid	23.88	23.2	116
S-6	Xyphoid	53.27	16.9	128
D-1	Axilla	69.58	31.2	112
	Xyphoid	64.36	27.3	103
D-2	Xyphoid	113.52	26.7	99
	Rib 10	74.34	36.0	102
D-3	Xyphoid	56.36	18.1	110
	Rib 10	41.32	33.4	98
D-4	Xyphoid	52.10	21.5	108
	Rib 10	66.42	25.4	125

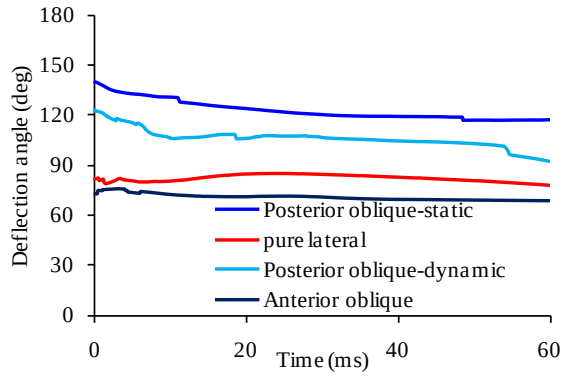

Figure 12: Comparison of the peak deflections between pure lateral, and anterior and posterior oblique impact tests.

Injuries

In general, skeletal injuries in the form of rib fractures were most prevalent in pure lateral and anterior oblique loadings. In pure lateral impact loading, skeletal traumas ranged from AIS 0 to 4 [21]. However, at the high velocity loading of 8.9 m/s, internal organ trauma occurred.

Anterior oblique impacts also showed similar skeletal injury predominance: in the 30- and 20-degree series, one specimen sustained AIS 3 and the other sustained AIS 4 trauma. In both specimens with AIS 3 trauma, unilateral fractures and single fracture to any specific rib were identified. Thirty-degree tests produced fractures to the ribcage including fracture to the first rib; and in the 20 deg tests, while inducing rib fractures, the first rib was not involved, and soft tissue injuries were identified as lung contusions and diaphragm laceration along with a flail chest in the specimen that sustained the greatest injury severity. The pleural tear attributed to the fracture of the seventh rib occurred at its lateral end. In contrast, the diaphragm laceration was not in the vicinity of the rib fracture. Traumas were not produced to renal or spleen structures.

In contrast, in posterior oblique impacts under static testing, out of the three specimens, one had no injury, another had AIS 3 level rib fractures, and the third specimen sustained AIS 3 skeletal and AIS 2 spleen laceration. In dynamic tests, all specimens sustained skeletal or visceral injuries: three sustained rib fractures (AIS 3 in two and 4 in one); and three sustained visceral (renal and spleen laceration; AIS 2 in two specimens), and left inferior labrum (AIS 3) lacerations.

DISCUSSION

Differences were found in the pattern regarding the peak and attainment of peak deflections between the three modes of impacts. This finding may assist in evaluating side impact dummies, from deflection-related metrics, an approach used in pure lateral impact biofidelity evaluations [22].

An anterior oblique impact, of the same severity and to the same level of the chest as the pure lateral impact, engages the same internal organ differently. At the upper thoracic region, the pure lateral vector directly loads regions dorsal to the subclavian artery while an oblique vector at 30 deg applies forces to the ventral arterial regions engaging the common carotid artery and brachio-cephalic vein. The former force vector introduces posteroanterior load transfer, in contrast to antero-posterior load transfer by the oblique vector. The ribcage is loaded in direct compression at its most lateral region under pure lateral loading in contrast to the angulated compression at the antero-lateral region by the oblique vector. The anterior regions of the thoracic vertebral body sustains lateral shear in the pure loading case. It resists antero-lateral shear in the oblique case. Spine is weaker antero-posteriorly. At an inferior level, while the aorta is protected by the stomach in the pure lateral loading, in the oblique case, the major vessel is protected by the relatively smaller liver lobe and its articulations [23].

Similar regional load transfer mechanisms are apparent as the impact vector traverses caudally. Pure anatomical considerations with respect to the impact vector, in addition to the functional and constitutive differences, may contribute to the mechanism of load transfer and injury. Deflections being a hallmark for these injuries, it is important to delineate this metric. Results in this paper serve as a first step in the process.

While deflection angles remained essentially aligned with the impact vector over the entire loading event in pure lateral and anterior oblique cases, data were different in the posterior oblique loading. This is due to the interaction of the PMHS with the airbag. The area of contact from the deploying airbag with the PMHS torso is more transient than in the rigid wall case regardless of the impacting vector. From this perspective, the deflection magnitude and the time of occurrence may have been influenced by the chosen airbag system. Parametric studies may be needed to examine the role of variables such as the volume, venting pattern, and pressure on the deflection variable. Mean peak deflections occurring at 130 and

108 deg for the static and dynamic posterior oblique loading cases may have also been influenced by the type of the airbag system used in the present study.

Regarding the potential role of these posterior-lateral directed deflections due to airbag interaction on injuries, an analogy similar to the anterior oblique loading can be applied. The posterior oblique vector induces focal loading to the local upper abdominal organs such as spleen. Rib fractures correlated to peak local deflection may also be an outcome, as documented in literature [19]. The role of deflection and its associated secondary variables, such as rate of deflection and viscous criterion, may be important in the analyses of real-world internal injuries.

Regarding injuries and their potential mechanisms, skeletal trauma has been associated with deflections while internal organ trauma is associated with metrics such as rate of compression [10]. The relatively infrequent or absence of visceral trauma in pure lateral and anterior oblique tests, and the more commonly observed spleen and renal traumas in the posterior oblique impacts, may suggest that skeletal trauma is a direct consequence of impact loading to the rib cage while internal organ injury may be modulated by the initial absorption and transmission of the energy by the skeletal structure. From this perspective, internal organ injuries may be more complex, and need further research.

In summary, the present paper provides information on deflections and injuries in side impacts under pure lateral, anterior and posterior oblique vectors. These data are valuable to assess the biofidelity of anthropomorphic test devices such as the ES-2re and WorldSID, and assist in improving occupant safety in these environments.

ACKNOWLEDGMENTS

This study was supported in part by DTNH22-07-H-00173, and VA Medical Research. The assistance of Neuroscience research staff is acknowledged.

REFERENCES

1. Backaitis, S.H. and H.J. Mertz, eds. *Hybrid III: The First Human-Like Crash Test Dummy*. 1994, Society of Automotive Engineers: Warrendale, PA. 830.
2. Backaitis, S.H. and D.C. Viano, *Side Impact: Injury Causation & Occupant Protection*, ed. I.l.C.a. Exposition. Vol. SP769. 1989. 191 pp.
3. Yoganandan, N., F. Pintar, and T. Gennarelli. *Evaluation of side impact injuries in vehicles equipped with side airbags*. in *IRCOBI*. 2005. Prague, Czech Republic.
4. Yoganandan, N., F. Pintar, T. Gennarelli, and M. Maltese. *Patterns of abdominal injuries in frontal and side impact*. in *AAAM*. 2000. Chicago, IL.
5. Yoganandan, N. and F.A. Pintar, *Biomechanics of human thoracic ribs.* J Biomech Engr, 1998. **120**: p. 100-104.
6. Yoganandan, N. and F.A. Pintar, *Acceleration, deflection, and force corridors for small females in side impacts.* Traf Inj Prevention, 2005. **6**: p. 1-8.
7. Tarriere, C., G. Walfisch, A. Fayon, C. Got, and F. Guillon. *Synthesis of human impact tolerance obtained from lateral impact simulations*. in *7th Int'l Tech Conf on Experimental Safety Vehicles*. 1979. Washington, DC.
8. Viano, D., I. Lau, C. Asbury, A. King, and P. Begeman, *Biomechanics of the human chest, abdomen, and pelvis in lateral impact.* Accid Anal & Prev, 1989. **21**(6): p. 553-574.
9. Viano, D.C., I.V. Lau, D.V. Andrzejak, and C. Asbury, *Biomechanics of injury in lateral impacts.* Accid Anal Prev, 1989. **21**(6): p. 535-51.
10. Yoganandan, N., F.A. Pintar, B.D. Stemper, T.A. Gennarelli, and J.A. Weigelt, *Biomechanics of side impact: injury criteria, aging occupants, and airbag technology*. J Biomech, 2007. **40**(2): p. 227-43.
11. Yoganandan, N., R.M. Morgan, R.H. Eppinger, F.A. Pintar, A. Sances, Jr, et al., *Mechanism of thoracic injury in a frontal impact.* J Biomech Engr, 1996. **118**: p. 595-597.
12. Yoganandan, N., R.M. Morgan, R.H. Eppinger, F.A. Pintar, D.A. Skrade, et al., *Thoracic deformation and velocity analysis in frontal impact.* J Biomech Engr, 1995. **117**: p. 48-52.
13. Yoganandan, N., F. Pintar, and T. Gennarelli, *Field data on head injuries in side airbag vehicles in lateral impact.* AAAM, 2005. **49**: p. 171-184.
14. Cavanaugh, J.M., Y. Zhu, Y. Huang, and A.I. King, *Injury and response of the thorax in side impact cadaveric tests*, in *Biomechanics of Impact Injury and Injury Tolerances of the Thorax-Shoulder Complex*, S. Backaitis, Editor. 1994, SAE, Inc.: Warrendale, PA. p. 949-972.
15. Kallieris, D., R. Mattern, G. Schmidt, and R.H. Eppinger. *Quantification of side impact responses and injuries*. in *Stapp Car Crash Conf*. 1981. San Francisco, CA.
16. Maltese, M.R., R.H. Eppinger, H.H. Rhule, B.R. Donnelly, F.A. Pintar, et al., *Response corridors of human surrogates in lateral impacts.* Stapp Car Crash J, 2002. **46**: p. 321-51.

17. Pintar, F.A., N. Yoganandan, M.H. Hines, M.R. Maltese, J. McFadden, et al. *Chestband analysis of human tolerance to side impact*. in *Stapp Car Crash Conf*. 1997. Lake Buena Vista, FL.
18. Pintar, F.A., D.J. Maiman, and N. Yoganandan. *Occupant dynamics and injuries in narrow-object side impact*. in *Experimental Safety of Vehicles*. 2007. Lyon, France.
19. Hallman, J.J., N. Yoganandan, and F.A. Pintar, *Biomechanical and injury response to posterolateral loading from torso side airbags.* Stapp Car Crash Journal, 2010: p. 227-257.
20. Hallman, J.J., N. Yoganandan, and F.A. Pintar, *Thoracic injury metrics with side air bag: stationary and dynamic occupants.* Traffic Inj Prev, 2010. **11**(4): p. 433-42.
21. AIS, *The Abbreviated Injury Scale*, AAAM, Editor. 1990, American Association for Automotive Medicine: Arlington Heights, IL. p. 74.
22. Rhule, H.H., M.R. Maltese, B.R. Donnelly, R.H. Eppinger, J.K. Brunner, et al., *Development of a new biofidelity ranking system for anthropomorphic test devices.* Stapp Car Crash J, 2002. **46**: p. 477-512.
23. Yoganandan, N., F.A. Pintar, and M.R. Maltese, *Biomechanics of abdominal injuries.* Crit Rev Biomed Eng, 2001. **29**(2): p. 173-246.

IMAGE SEGMENTATION AND REGISTRATION ALGORITHM TO COLLECT HOMOLOGOUS LANDMARKS FOR AGE-RELATED THORACIC MORPHOMETRIC ANALYSIS

Ashley A. Weaver
Elizabeth G. Armstrong
Elizabeth A. Moody
Joel D. Stitzel
Virginia Tech – Wake Forest University Center for Injury Biomechanics
Wake Forest University School of Medicine
Medical Center Boulevard, Winston Salem, NC, 27157
USA
Paper Number 11-0317

ABSTRACT

Skeletal and physiological resilience are known to decline with age, resulting in a decreased ability for the body to withstand traumatic insults. Adults 65 years of age and older currently constitute more than 12% of the total population and the elderly population is projected to reach nearly 20% by 2030. The objective of the current study is to quantify age and gender-specific variations in the thoracic skeletal morphology for use in generating a parametric thoracic model for injury prediction. This goal will be accomplished using the image segmentation and registration algorithm developed in this study to collect homologous (or comparable) landmarks from the ribs. A minimum of 10 normal chest CT scans for each gender were collected from a radiological database for the following age groups: newborns, 3 month, 6 month, 9 month, 1 year, 3 year, and 6 year olds. Beginning with 10 year olds, a minimum of 10 CT scans for each gender were collected by decade up to age 100. Image segmentation and subsequent image registration of the collected scans was used to collect homologous rib landmarks. A semi-automated method was used to segment each rib and create a mask and three-dimensional (3D) model. Thresholding and region growing operations were applied and manual editing was used to ensure selection of the entire rib and exclusion of surrounding soft tissue. An atlas was created from segmentation of a normal chest CT scan of an average male with over 1,000 landmark points placed on each rib. Each segmented rib is registered to the atlas. Rigid, affine, and non-rigid, nonlinear transformations are used to morph the atlas to the subject rib. The transformation matrices are used to map the landmarks in the atlas coordinate system to the subject-specific coordinate system. Effectively, this allows for collection of homologous rib landmarks across subjects of all ages. Geometric morphometrics, particulary the Procrustes superimposition method can then be used to analyze the landmark data to formulate age and gender-specific shape and size variation functions. Shape and size functions computed from the landmark data can be used to create a scalable finite element model of the thorax that will allow vehicle crashworthiness to be evaluated for all ages and genders and will lead to improvements in restraint systems to better protect children and elderly in a crash.

INTRODUCTION

In motor vehicle crashes, thoracic injury ranks second only to head injury in terms of the number of fatalities and serious injuries, the body region most often injured, and the overall economic cost (Cavanaugh 2002; Ruan, El-Jawahri et al. 2003). Thoracic injuries account for 13% of all minor to moderate injuries, 29% of all serious to fatal injuries, and are attributed to up to 25% of traumatic deaths (Dougall, Paul et al. 1977; Galan, Penalver et al. 1992; Allen and Coates 1996; Ruan, El-Jawahri et al. 2003). While motor vehicle crashes are associated with 60-70% of blunt chest trauma, 20% is attributed to falls that are more commonly seen in the elderly (Galan, Penalver et al. 1992; Allen and Coates 1996).

Adults 65 years of age and older currently constitute more than 12% of the total population and with increases in life expectancy, the elderly population is projected to reach nearly 20% by 2030 (U.S. Census Bureau 2008). Motor vehicle crash is a common source of trauma among the elderly population, with the elderly having the second highest crash-related death rate compared to all age groups (National Center for Health Statistics 2003). The incidence of thoracic injury increases with age for both belted and unbelted occupants (Hanna 2009). Skeletal and physiological resilience are known to decline with age, resulting in a decreased ability for the body to withstand traumatic insults (Burstein, Reilly et al. 1976; Zioupos and Currey 1998). Thoracic injury tolerance in the elderly has been shown to decrease by 20% for blunt loading and up to 70% for concentrated belt-loading (Zhou 1996).

Thoracic morbidity and mortality also increase with age. Older patients sustaining a thoracic injury present with more comorbidities, develop more complications, remain on a ventilator longer, and require longer stays in the intensive care unit and hospital (Finelli, Jonsson et al. 1989; Shorr, Rodriguez et al. 1989; Perdue, Watts et al. 1998; Holcomb, McMullin et al. 2003; Hanna 2009). Complications from thoracic injury include pneumonia, atelectasis, acute respiratory distress syndrome, and respiratory failure. Elderly patients with rib fractures have two to five times the risk of mortality of younger patients with increases in risk observed as the number of rib fractures increase (Bergeron, Lavoie et al. 2003; Stawicki, Grossman et al. 2004). Each additional rib fracture results in a 19% increase in mortality and 27% increase in pneumonia (Bulger, Arneson et al. 2000). A recent study used a receiver-operator characteristic analysis to identify the age thresholds associated with increased mortality in 12 leading thoracic injuries (Stitzel, Kilgo et al. 2010). Although many thresholds were near the traditional age threshold of 55 years commonly used to identify patients of increased mortality risk, the study found age thresholds that were injury-specific. For instance, the age threshold for bilateral pulmonary contusion indicates patients older than 46 years with this injury have an increased mortality risk compared to patients younger than 46.

Age and gender-specific variations in the geometry and mechanics of the thoracic skeleton are expected to relate to thoracic injury. Previous studies have found statistically significant changes in the rib cage geometry with age (Kent, Lee et al. 2005; Gayzik, Yu et al. 2008). However, these studies had several limitations. Geometrical changes such as the shape, size, and angle of the ribs were quantified using a limited number of landmarks or measurements that were collected manually from two-dimensional (2D) images of a computed tomography (CT) scan. Also, the pediatric population was not analyzed in either of these studies and some other age groups were under-represented. The objective of the current study is to quantify age and gender-specific variations in the thoracic skeletal morphology for both genders and across the entire age spectrum (ages 0-100). This goal will be accomplished using a semi-automated image segmentation and registration algorithm to collect homologous landmarks from the ribs.

METHODS

An algorithm was developed to collect landmark data from the ribs for the purpose of quantifying age and gender-specific variations. The main steps of the algorithm are: 1) Scan Collection, 2) Image Segmentation, and 3) Image Registration.

Scan Collection

Normal chest CT scans of males and females ages 0-100 were collected from the radiological database at Wake Forest University Baptist Medical Center. To identify exclusion criteria and ensure normal scans were collected, a musculoskeletal radiologist was consulted. Exclusion criteria included, but were not limited to: congenital abnormalities, infections, fractures, and cancers of the ribs, scoliosis, kyphosis, sternotomy, thoracotomy, and osteopenia or osteoporosis in individuals younger than 50. Radiology reports and other patient medical records were reviewed and scans were visually inspected. A minimum of 10 male and 10 female scans were collected for the following age groups: newborns, 3, 6, and 9 month, 1, 3, and 6 year olds. Beginning with 10 year olds, 10 scans for each gender were collected by decade up to age 100 (Figure 1, Figure 2).

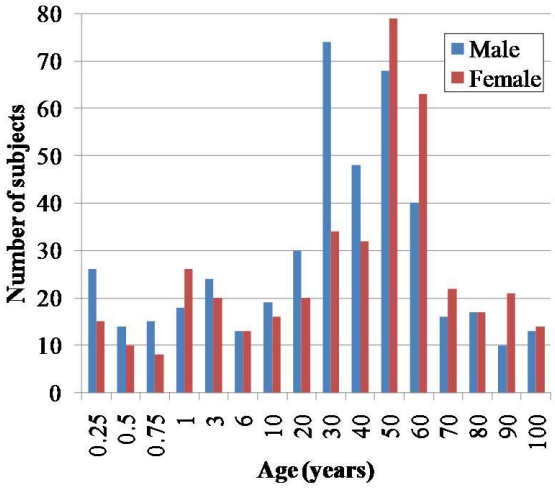

Figure 1. Histogram of CT scans collected with age values representing the upper bin limit.

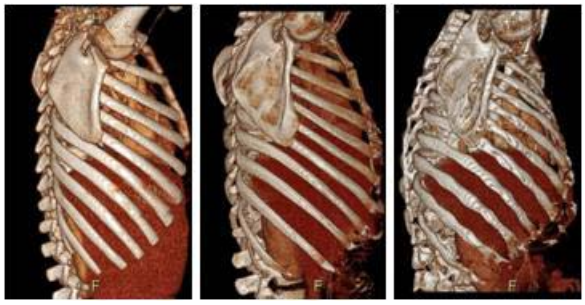

Figure 2. 3D CT reconstructions (left to right): 6, 29, and 73 year old subjects. Morphological thoracic skeletal differences of the pediatric, young adult, and elderly subjects are evident.

Image Segmentation

A semi-automated method was used to segment the 24 ribs on each subject. A bone threshold was applied, followed by a region growing operation. Minimal manual editing was used to ensure the entire rib was selected and the surrounding soft tissue was excluded. Calcified costal cartilage was excluded when present. A hole filling operation was used to enclose the rib interior. Each rib cage segmentation takes one to five hours depending on the subject size, bone density, and other factors. Results of the segmentation include a mask and a three-dimensional (3D) model for each rib (Figure 3).

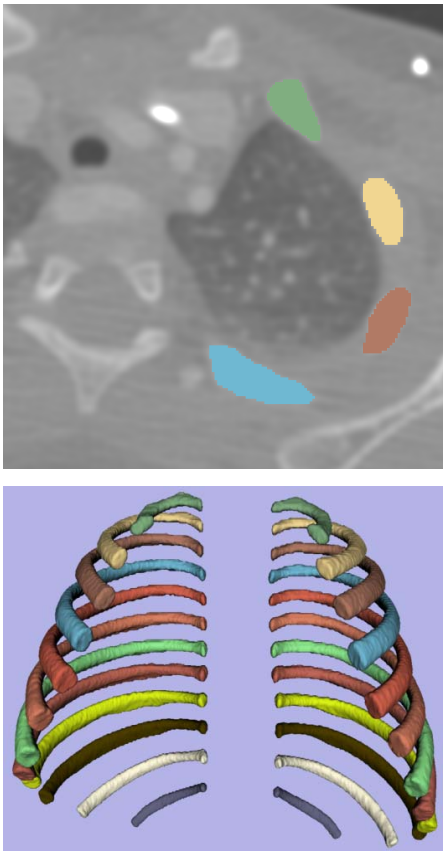

Figure 3. Rib segmentation results. Top photo: Masks of the segmented left ribs 1-4 overlaid on an axial chest CT image. Bottom photo: 3D models of the 24 segmented ribs of a pediatric subject.

Image Registration

An image registration algorithm was developed for the purpose of collecting homologous landmarks from the ribs for all subjects in the study. The image registration algorithm requires minimal user interaction and takes approximately five to ten minutes per rib. An atlas was created from segmentation of a normal chest CT scan of an average male. The atlas contained the 24 ribs with over 1,000 landmark points placed on each rib as illustrated in Figure 4. For every subject in the study, each segmented rib was registered with the corresponding rib in the atlas (i.e. the left first rib in each subject is registered with the left first rib in the atlas). Rigid, affine, and non-rigid, non-linear transformations were used in the registration algorithm to morph the atlas and it's landmarks to the rib of each subject (Figure 5, Steps 1 and 2). Following the registration, the 1,000+ landmark points on each rib have been transformed to the subject-specific coordinate system of the CT scan (Figure 5, Step 3). Effectively, this allows for collection of homologous rib landmarks across subjects of all ages.

Figure 4. Right third rib from the atlas with 1,000 landmarks placed.

RESULTS

An example of the results of the registration algorithm is provided in Figure 6. In this example the left fourth rib from a 16 year old male (termed "subject rib") was registered with the left fourth rib of the average male (termed "atlas rib"). The rigid transformation (Figure 6, Step 1) translates and rotates the atlas rib to align three landmarks on the atlas rib with three landmarks on the subject rib. The affine transformation (Figure 6, Step 2) applies

translation, rotation, scaling, and shearing operations to morph the atlas rib to the subject rib. In the final step of the registration algorithm, a non-rigid, non-linear transformation is applied to morph the atlas rib to the subject rib (Figure 6, Step 3).

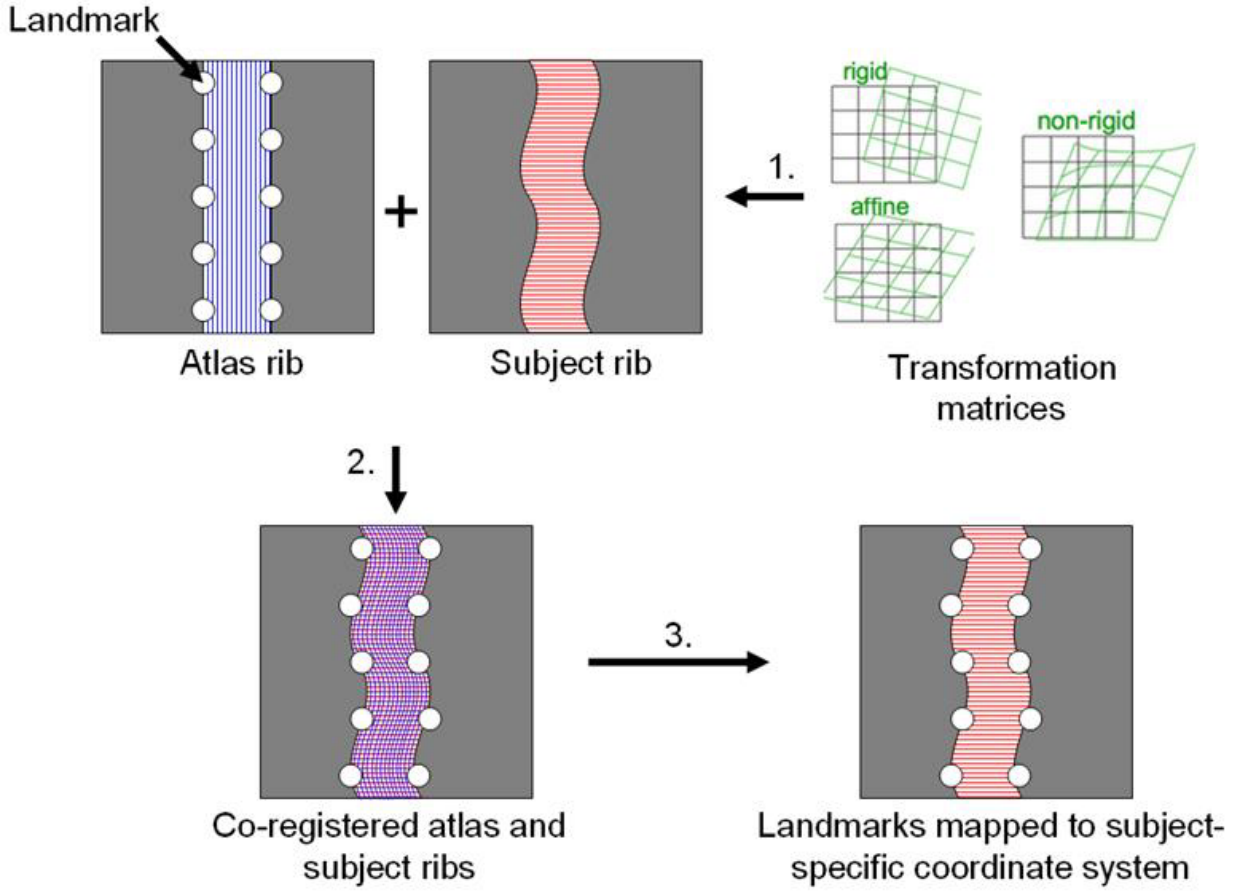

Figure 5. Image registration process. 1) Rigid, affine, and non-rigid, non-linear transformations are applied to register a subject's rib with the atlas. The atlas rib is depicted with only 10 landmarks for simplification. 2) The co-registered atlas rib and subject rib in the subject-specific coordinate system with 10 landmarks shown. 3) Depiction of 10 landmarks mapped to the subject-specific coordinate system.

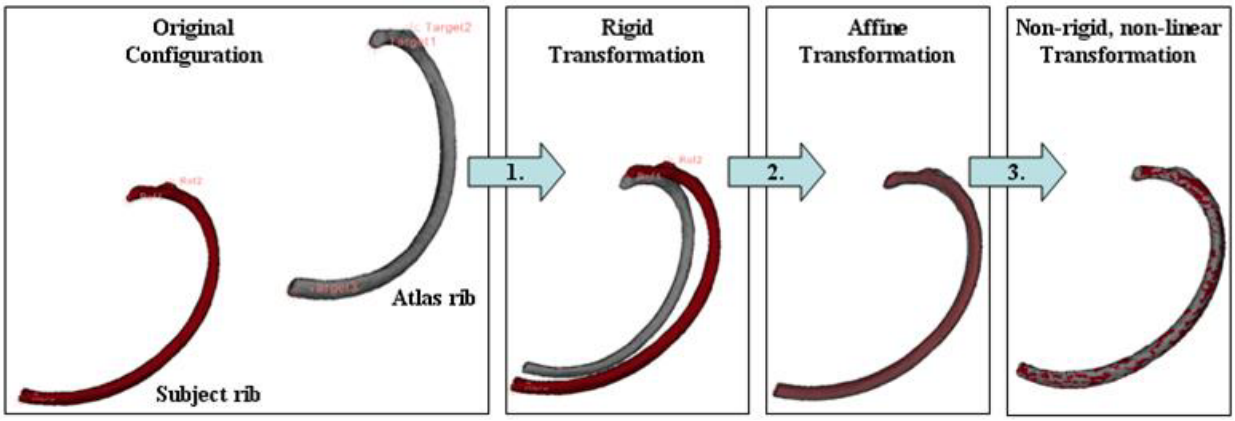

Figure 6. Image registration example. 1) Rigid transformation is applied to rigidly align three landmarks on the atlas rib with three landmarks on the subject rib. 2) Affine transformation is applied. 3) Non-rigid, non-linear transformation is applied.

Differences in the 3D models of the registered atlas rib and subject rib were compared with a deviation analysis within Geomagic Studio version 12.1.0 (Geomagic, Research Triangle Park, NC) to quantify the robustness of the image registration. The acceptable ranges of deviation were set based on the scan resolution (pixel spacing: 0.74 mm by 0.74 mm; slice thickness: 0.625 mm). Acceptable ranges corresponded to the maximum voxel length of the scan, 0.74 mm. Results are presented in Figure 7 with the color bar illustrating the deviations in millimeters between the two 3D models. Over 99% of the deviations fell within the acceptable range of -0.74 to 0.74 mm. The average deviations in the positive and negative directions were 0.194 and -0.138 mm, respectively with a standard deviation of 0.222 mm. The maximum deviations in the positive and negative directions were 1.208 and -3.109 mm, respectively. However, these deviations occurred in very localized regions on the rib and accounted for less than 1% of the overall deviations.

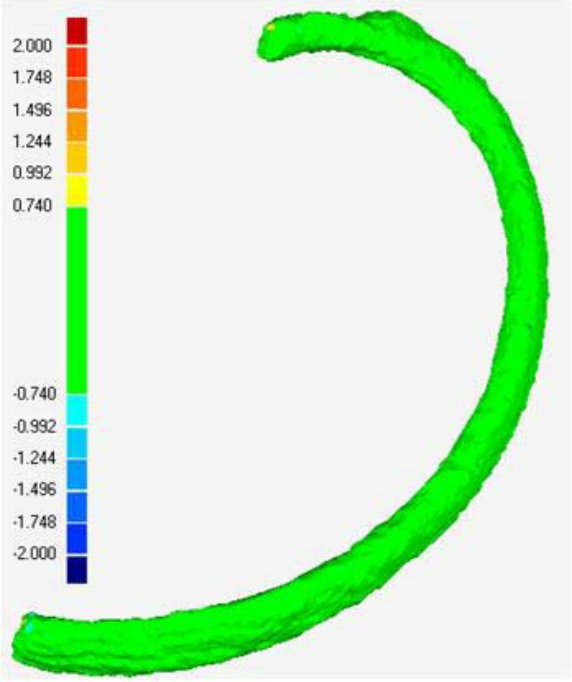

Figure 7. Deviation analysis with color bar indicating over 99% of the deviations fall in the acceptable range (+/- 0.74 mm).

DISCUSSION

The image segmentation and registration algorithm developed in the study provides a method for collecting extensive homologous landmark data from the ribs. The algorithm improves on the previous methods of measuring rib geometry by utilizing the full 3D information in the scan to collect landmarks (Kent, Lee et al. 2005; Gayzik, Yu et al. 2008). The algorithm requires little user interaction, allowing landmarks to be collected in an automated fashion for a large number of subjects and reducing intra-observer and inter-observer error. Landmarks on the ribs can be classified as: true anatomical landmarks representing a homologous structure, pseudolandmarks defined by relative locations such as the most lateral point, or semilandmarks defined relative to other landmarks. Previous methods have relied on the manual landmark identification and this method may not result in selection of homologous landmarks, particularly for pseudolandmarks or semilandmarks (Gayzik, Yu et al. 2008). Automatic selection of landmarks through image registration eliminates error in landmark identification and improves the ability to select a large number of homologous landmarks on the ribs.

Limitations include the possible introduction of error since some manual interaction was required to segment the ribs. The CT scan resolution presents a limiting factor on the rib cage variation that can be detected as differences less than the maximum voxel length cannot be accurately measured. Efforts were made to select higher resolution CT scans with a slice thickness ranging from 0.625 mm to 1.25 mm to address this limitation.

Image registration has been widely used to study injuries, disease, and cancers of the brain (Maldjian, Chalela et al. 2001; Lee, Wen et al. 2010; Long and Wyatt 2010). The image segmentation and registration algorithm developed in the current study could be modified and used in subsequent research studies to collect landmark data from other bony and soft tissue anatomy. Similar to the current study, geometrical variation in the anatomy could be characterized for different ages or genders. The algorithm could also be used to study pathology and volumetrically characterize the extent and location of injured or diseased tissue.

The homologous landmark data collected with the image segmentation and registration algorithm will be input into a geometric morphometrics analysis, particularly the Procrustes superimposition method, to formulate age and gender-specific shape and size variation functions of the rib cage. Additional research will be conducted to quantify changes in bone mineral density and cortex thickness and generate functions describing variation with age and gender.

Previous studies have altered geometrical and structural characteristics of thoracic finite element

(FE) models to represent subjects of different ages (Kent, Lee et al. 2005; Ito 2009; El-Jawahri 2010). Kent et al. (2005) modified an existing FE thorax model to create three models: 1) An "up" model where the ribs were rotated upward until the ninth rib was rotated seven degrees, 2) An "old" model where the bone material properties were reduced by 30%, and 3) A "thin" model where the rib cortical shell thickness was reduced by 40% (Kent, Lee et al. 2005). Ito et al. (2009) and El-Jawahri et al. (2010) used age-specific geometry and material criteria from the literature and modified existing FE models to represent 35 year, 55 year, and 75 year old mid-size males (Ito 2009; El-Jawahri 2010).

The extensive amount of data collected in the current study will supplement existing data in the literature and more fully characterize rib morphology across ages and genders. The efficiency and efficacy of the semi-automated image segmentation and registration algorithm allows for collection of rib landmarks at a high resolution from hundreds of subjects over a wide range of ages (0-100 years) and across genders. The morphological functions developed from this landmark data will be used to create a parametric FE model of the thorax that can be scaled to represent a subject of a particular age and gender. This model will allow vehicle crashworthiness to be evaluated for all ages and genders and will lead to improvements in restraint systems to better protect children and elderly in a crash.

CONCLUSIONS

A semi-automated image segmentation and registration algorithm was developed to collect homologous rib landmarks from normal CT scans of males and females ages 0-100. The algorithm uses rigid, affine, and non-rigid, non-linear transformations to morph segmented ribs from different subjects to a rib atlas. The collected landmarks will be analyzed to formulate age and gender-specific shape and size variation functions. Results of this study will lead to an improved understanding of the complex relationship between thoracic geometry, age, gender, and injury risk.

ACKNOWLEDGEMENTS

Funding was provided by the National Highway Traffic Safety Administration and the National Science Foundation Graduate Research Fellowship Program. The authors would like to thank Dr. Leon Lenchik for providing assistance with exclusion criteria and CT scan normality. Hannah Kim, Callistus Nguyen, Hannah Reynolds, and Colby White assisted with data collection. Dr. Chris Wyatt and Haiyong Xu provided technical assistance on the image segmentation and registration algorithm development.

REFERENCES

Allen, G. S. and N. E. Coates (1996). "Pulmonary contusion: a collective review." Am Surg **62**(11): 895-900.

Bergeron, E., A. Lavoie, et al. (2003). "Elderly Trauma Patients with Rib Fractures Are at Greater Risk of Death and Pneumonia." J Trauma **54**(3): 478-485.

Bulger, E. M. M. D., M. A. M. D. Arneson, et al. (2000). "Rib Fractures in the Elderly." Journal of Trauma-Injury Infection & Critical Care **48**(6): 1040-1047.

U.S. Census Bureau (2008). An Older and More Diverse Nation by Midcentury. P. Division, Public Information Office.

Burstein, A. H., D. T. Reilly, et al. (1976). "Aging of bone tissue: mechanical properties." J Bone Joint Surg Am **58**(1): 82-86.

Cavanaugh, J. M. (2002). Biomechanics of Thoracic Trauma. Accidental Injury: Biomechanics and Prevention. J. M. Alan M. Nahum. New York, Springer-Verlag**:** 374-404.

Dougall, A. M., M. E. Paul, et al. (1977). "Chest Trauma-Current Morbidity and Mortality." J Trauma **17**(7): 547-553.

El-Jawahri, R. E., Laituri, T.R., Ruan, J.S., Rouhana, S.W., Barbat, S.D. (2010). "Development and Validation of Age-Dependent FE Human Models of a Mid-Sized Male Thorax." Stapp Car Crash Journal **54**: 407-430.

Finelli, F. C., J. Jonsson, et al. (1989). "A Case Control Study for Major Trauma in Geriatric Patients." J Trauma **29**(5): 541-548.

Galan, G., J. C. Penalver, et al. (1992). "Blunt chest injuries in 1696 patients." Eur J Cardiothorac Surg **6**(6): 284-287.

Gayzik, F. S., M. M. Yu, et al. (2008). "Quantification of age-related shape change of the

human rib cage through geometric morphometrics." J Biomech **41**(7): 1545-1554.

Hanna, R., Hershman, Lawrence (2009). Evaluation of Thoracic Injuries Among Older Motor Vehicle Occupants. Washington, DC, National Highway Traffic Safety Administration.

Holcomb, J. B., N. R. McMullin, et al. (2003). "Morbidity from rib fractures increases after age 45." J Am Coll Surg **196**(4): 549-555.

Ito, O., Dokko, Y., Ohashi, K. (2009). Development of adult and elderly FE thorax skeletal models. Society of Automotive Engineers. **Paper number 2009-01-0381**.

Kent, R., S. H. Lee, et al. (2005). "Structural and material changes in the aging thorax and their role in crash protection for older occupants." Stapp Car Crash J **49**: 231-249.

Lee, J. W., P. Y. Wen, et al. (2010). "Morphological characteristics of brain tumors causing seizures." Arch Neurol **67**(3): 336-342.

Long, X. and C. Wyatt (2010). An Automatic Unsupervised Classification of MR Images in Alzheimer's Disease. 23rd IEEE Conference on Computer Vision and Pattern Recognition, San Francisco, USA.

Maldjian, J. A., J. Chalela, et al. (2001). "Automated CT segmentation and analysis for acute middle cerebral artery stroke." AJNR Am J Neuroradiol **22**(6): 1050-1055.

National Center for Health Statistics, N. (2003). Health, United States, 2002, Special Excerpt: Trend Tables on 65 and Older Population, Centers for Disease Control and Prevention/National Center for Health Statistics, Department of Health and Human Services.

Perdue, P. W., D. D. Watts, et al. (1998). "Differences in Mortality between Elderly and Younger Adult Trauma Patients: Geriatric Status Increases Risk of Delayed Death." J Trauma **45**(4): 805-810.

Ruan, J., R. El-Jawahri, et al. (2003). "Prediction and analysis of human thoracic impact responses and injuries in cadaver impacts using a full human body finite element model." Stapp Car Crash J **47**: 299-321.

Shorr, R. M., A. Rodriguez, et al. (1989). "Blunt Chest Trauma in the Elderly." J Trauma **29**(2): 234-237.

Stawicki, S. P., M. D. Grossman, et al. (2004). "Rib fractures in the elderly: a marker of injury severity." J Am Geriatr Soc **52**(5): 805-808.

Stitzel, J. D., P. D. Kilgo, et al. (2010). "Age thresholds for increased mortality of predominant crash induced thoracic injuries." Ann Adv Automot Med **54**: 41-50.

Zhou, Q., Rouhana, Stephen W., Melvin, John W. (1996). "Age Effects on Thoracic Injury Tolerance." Stapp Car Crash J **Paper 962421**.

Zioupos, P. and J. D. Currey (1998). "Changes in the stiffness, strength, and toughness of human cortical bone with age." Bone **22**(1): 57-66.

Multi-Scale Biomechanical Characterization of Human Liver and Spleen

Andrew Kemper, Anthony Santago, Jessica Sparks, Craig Thor,
H. Clay Gabler, Joel Stitzel, and Stefan Duma
Virginia Tech – Wake Forest, Center for Injury Biomechanics
United States of America
Paper Number 11-0195

ABSTRACT

The purpose of this study is to present a multi-scale approach for the biomechanical characterization of the human liver and spleen. A four step approach was taken to quantify the injury mechanism, biomechanical response, and rate dependent constitutive material models for each organ. First, the CIREN and NASS-CDS databases were examined to determine the crash characteristics which result in liver and spleen injuries. From this data, the injury mechanism relative to loading directions and loading rates could be approximated. Second, whole fresh human organs were tested with in 48 hours of death using indenter-style compression tests. Sub-failure tests, up to 20% compression, were performed at multiple loading rates, followed by a failure test. Third, fresh human organs were processed into either dog-bone tension coupons or cylindrical compression coupons and tested within 48 hours of death at multiple strain rates to the point of failure. Fourth, an optimization routine and FEM of the coupons tests was developed to determine the best constitutive model for each organ. The data from this study shows that the response of human liver and spleen is both non-linear and rate dependant. It is anticipated that the data from this research will enhance the understanding of internal organ injuries and provide a foundation for future human internal organs finite element models.

INTRODUCTION

Motor vehicle collisions (MVCs) commonly result in serious blunt abdominal injuries [Mackenzie et al., 2003]. Although abdominal injuries account for only 3-5% of all injuries observed in MVCs, they comprise 8% of AIS 3+ injuries, 16.5% of AIS 4+ injuries and 20.5% of AIS 5+ injuries [Bondy, 1980; Rouhana and Foster, 1985; Elhagediab and Rouhana, 1998; Augenstein et al., 2000]. Although it has been demonstrated that internal organ injuries account for a considerable portion of injuries in automotive crashes, previous studies pre-date the implementation of advanced safety restraint technologies such as: depowered airbags, seatbelt load limiters, and seatbelt pretensioners.

Currently, no crash test dummies used to assess injury risk in MVCs are equipped to represent individual solid abdominal organs located asymmetrically in the human abdomen [Tamura et al., 2002]. Consequently, finite element models (FEMs) are becoming an integral tool in the reduction of automotive related abdominal injuries. However, the response of these models must be locally and globally validated based on appropriate biomechanical data in order to accurately assess injury risk. Furthermore, since FEMs allow for the prediction of injury based on the calculation of physical variables mechanically related to injury, such as stress and strain, the establishment of tissue level tolerance values is critical for the accurate prediction of injuries [Moorcroft et al., 2003; Stitzel et al., 2005a; Stitzel et al., 2005b; Takhounts et al., 2008].

Several biomechanical studies have evaluated the mechanical response and injury tolerance of the internal organs by conducting compression tests on intact animal or human cadaver organs [Melvin et al., 1973; Trollope et al., 1973; Wang et al., 1992; Kerdok et al., 2006; Sparks et al., 2007]. Although these studies provide significant contributions to the literature and valuable organ level validation data, they are limited in their ability to accurately quantify localized stress and strain essential for local FEM validation.

In order to directly quantify the material properties of biological tissue, tension and compression testing must be conducted on isolated tissue coupons. There have only been a few studies which have investigated the compressive material properties of liver or spleen by performing compression tests on isolated samples [Tamura et al., 2002; Nasseri et al., 2003; Roan and Vemaganti, 2007; Mazza et al., 2007]. A number of studies have investigated the failure properties of liver by performing tension tests on isolated samples of

liver or spleen tissue [Yamada, 1970; Uehara, 1995; Stingl et al., 2002; Hollenstein et al., 2006; Santago et al. 2009a; Santago et al., 2009b] Although these studies have provided considerable insight into the factors that affect the material response of the liver and spleen parenchyma, these studies have been limited to testing of animal tissue, sub-failure loading, or a single loading rate.

The purpose of the paper is to present a multi-scale approach to characterize injuries and material properties of the human liver and spleen. This approach consists of four parts: determine the crash characteristics which result in liver and spleen injuries, perform indenter-style compressive impacts to intact whole human organs, conduct tension and compression material tests on isolated specimens of human liver and spleen parenchyma at multiple loading rates, and develop a method to obtain accurate FEMs from the tissue level tests.

METHODS AND PRELIMINARY RESULTS

Whole Body Data Analysis

Multiple resources were utilized to perform data-driven analyses of injuries to the heart and great vessels, lungs, liver, and spleen. The National Automotive Sampling System - Crashworthiness Data System (NASS-CDS) was utilized to determine the distribution and mechanisms of thoracic organ injury. The liver and spleen were included as thoracic organs because they are partially protected by the rib cage and they are among the most frequently injured internal organs. For this analysis, only buckled, front seat occupants in vehicles of model year 1998 or later were included. Crash modes were limited to frontal crashes and rollovers were excluded. The distributions in Figures 1, 2, and 3 were published in Thor (2008).

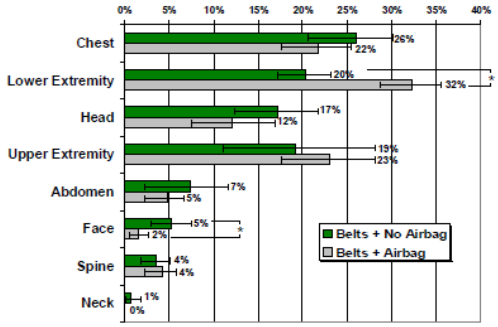

Figure 1: Distribution of MAIS 3+ injuries by body regions (weighted).

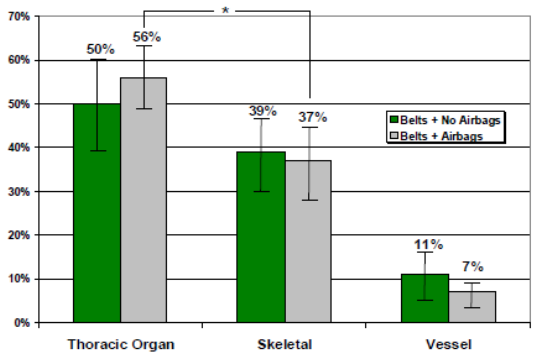

Figure 2: Distribution of AIS 3+ thoracic injuries by tissue type (weighted).

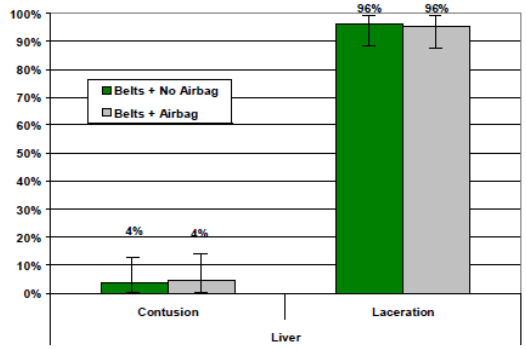

Figure 3: Distribution of AIS3+ liver injuries by lesion type (weighted).

The Virginia Tech – Wake Forest University CIREN database was utilized to determine the crash characteristics and involved physical components for cases which resulted in a liver or spleen injury. It was found that 12.5% (10 of 80 patients) of CIREN study patients experienced liver injuries and 20% (16 of 80 patients) experienced spleen injuries.

For each of the aforementioned injury groups, the crash characteristics were determined (Figures 4 and 5). Often, case occupants sustained injuries in several anatomical categories so each injury listing is not exclusive. The involved physical components assigned to each bio-tabbed injury were also determined. The majority of bio-tabbed liver injuries were attributed to seatbelt loading. The majority of bio-tabbed spleen injuries were attributed to loading from the door.

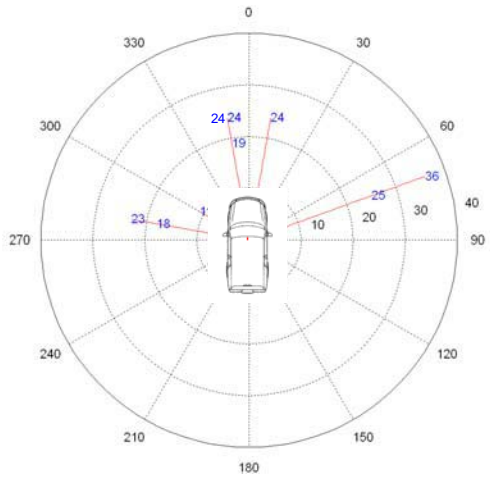

Figure 4: Radial plot of crash Delta-V and PDOF for CIREN cases with liver injuries.

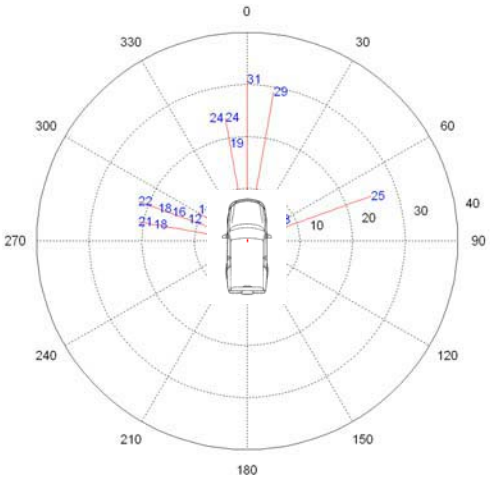

Figure 5: Radial plot of crash Delta-V and PDOF for CIREN cases with spleen injuries.

Organ and Tissue Testing

Organ Procurement and Preservation- In order to obtain accurate material properties it is imperative to test the organs as quickly as possible after subject death. A procurement protocol was developed in order to limit degradation of the organs (Figure 6). Each organ was obtained within 36 hours of death and tested within 48 hours of death to minimize the adverse effects of tissue degradation. An age limit of 80 was set for each subject. All donors were screened to avoid any medical issues that might affect the mechanical properties of the liver or spleen, such as hepatitis and abdominal cancer. It should be noted that the organs were not frozen at any point between the time of death and testing since it has been shown that freezing significantly affects the tensile material properties of the liver parenchyma [Santago et al., 2009b]. In order to preserve the tissue between the time of procurement and specimen preparation, the organs were immersed in Dulbecco's Modified Eagle Medium (DMEM), which is a tissue culture medium, and chilled with wet ice.

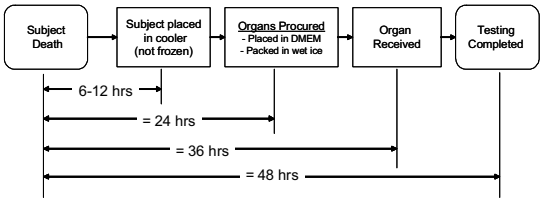

Figure 6: Organ procurement testing time-line.

Whole Organ Testing- The primary component of the indenter-style whole organ compression experimental setup was a high rate servo-hydraulic material testing system (MTS Systems Corporation, MTS-810, Eden Prairie, MN) (Figures 6 and 7). A load cell (Interface 1210-AF-500lbf, Scottsdale, AZ) was attached into the MTS piston. An accelerometer (Endevco 7264B, 2000 g, San Juan Capistrano, CA) was attached to the load cell, and was used to inertially compensate the force. The piston displacement was measured with the MTS internal linear variable differential transformer (LVDT) and a potentiometer (Space Age Control, 160-1705, 540mm, Palmdale, CA) attached to the MTS piston. A cylindrical polypropylene impactor (Dia.=3.81 cm) attached to the load cell was used to load the organs. It should be noted that the edge of the impactor tip was chamfered (r =10 mm).

Each organ was placed on a rigid flat plate, covered with a Teflon© sheet, and aligned underneath the impactor (Figures 7 and 8). A gravity-fed perfusion system was used to pressurize the arterial and venous systems of the organ to simulate physiological conditions [Kerdok et al., 2006; Sparks et al., 2007]. A static pressure of 100 mmHg was utilized for the hepatic artery and splenic artery, while a static pressure of 9 mmHg was utilized for the hepatic vein and splenic vein [Sparks et al., 2007]. The perfusion fluid was heated to approximately 98°F to simulate physiological conditions. A contact switch, consisting of copper tape on the impactor tip and a thin wire placed on the organ, was used to determine the time of initial contact.

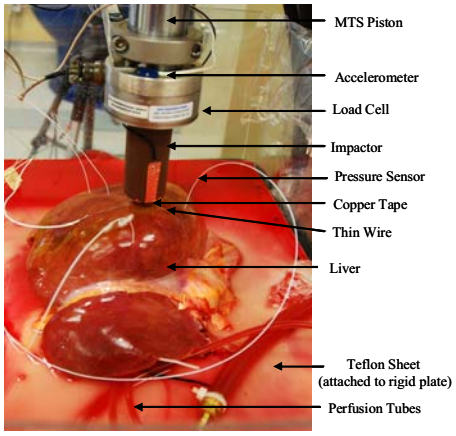

Figure 7: Whole liver on test apparatus.

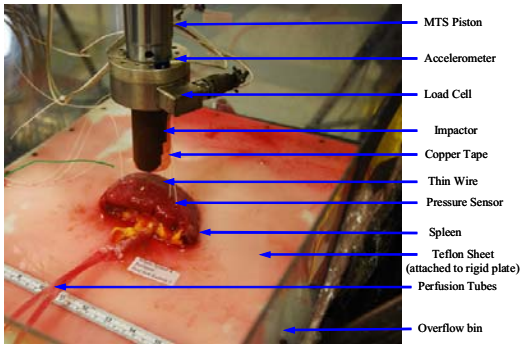

Figure 8: Whole spleen on test apparatus.

Once the perfused organ was positioned on the test setup, the organ and impactor were scanned using a FaroArm (FARO, Platinum 8Ft Arm and P1 Scanner, Switzerland) to obtain the three dimensional surface geometry (Figures 9 and 10). It should be noted that the organ was perfused with heated fluid for approximately one hour prior to scanning. Obtaining the three dimensional surface geometry of each organ allows for the development and validation of organ specific FEMs.

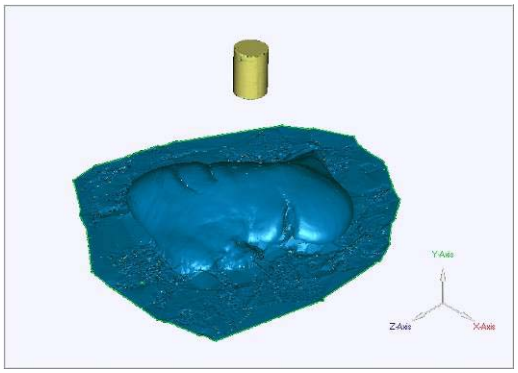

Figure 9: 3D surface geometry of a liver (blue) and impactor (gold).

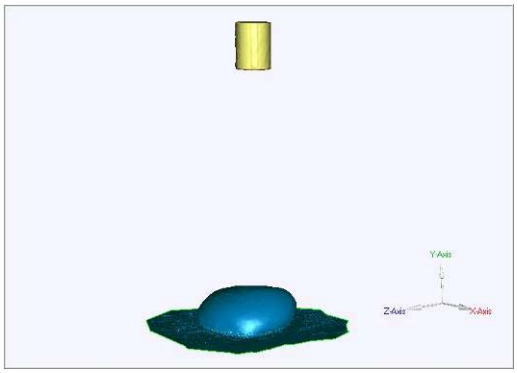

Figure 10: 3D surface geometry of a spleen (blue) and impactor (gold).

A series of impacts were performed on each organ. Each organ was allowed to sit for approximately 10 minutes between each test to allow time for the organ to recover after the impacts. First, 15 preconditioning cycles were performed using a maximum deflection of 20% of the organ height at a loading rate of 0.2Hz, which is the rate of normal breathing. It should be noted that the height of the organ at the point of impact decreased after preconditioning. A series of three impacts were then performed at 2mm/sec, 20mm/sec, and 200mm/sec to a depth of 20% of the organ height measured prior to preconditioning. The sub-failure loading performed on 3 perfused livers is provided as an example (Figure 11). Finally, a failure impact was performed at 2000mm/sec. However, the failure tests are not presented in this paper. The whole liver force versus deflection curves show that the compressive response was non-linear and rate dependent.

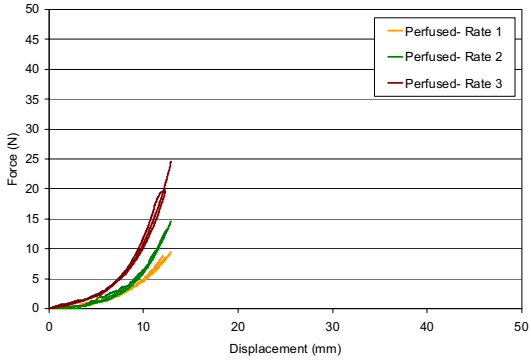

Figure 11: Liver sub-failure loading at multiple loading rates. (Note: Data cut at 14% compression)

Tissue Level Tension Testing- Uniaxial tension tests were conducted using "dog-bone" shaped tension samples of constant thickness. A custom blade assembly and slicing jig were used to obtain constant thickness slices of liver and spleen parenchyma (Figure 12). The blade assembly consisted of multiple 48.3 cm long razor blades spaced such that the tips of the blades were 5 mm apart. The slicing jig was an aluminum fixture, designed to securely hold a block of tissue, with vertical slots spaced 5 mm apart to act as guides for the blades. To generate tissue slices, a square block of tissue was first cut from the parenchyma of the liver or spleen and placed in the slicing jig. The blades were then aligned in the blade guides on the slicing jig. The slicing was performed in one smooth slow pass through the tissue while minimizing downward force in order to avoid damaging or deforming the tissue. The tissue slices were then immersed in a bath of DMEM to maintain specimen hydration.

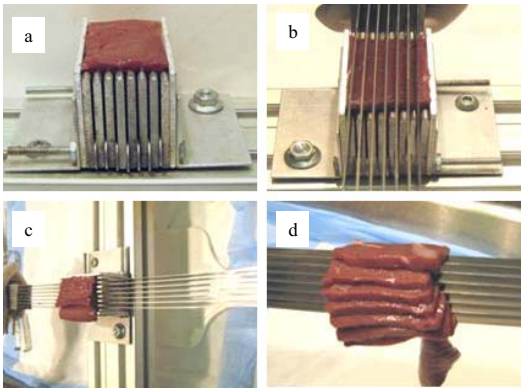

Figure 12: Specimen slicing methodology.

A custom stamp and stamping base were used to obtain "dog-bone" shaped specimens commonly used for uniaxial tension testing. The geometry of the dog-bone was designed to ensure that the specimen would fail in the gage length, which had a constant width and thickness. Prior to stamping, a template was used to position the tissue slice on the stamping base in order to obtain a specimen devoid of any visible vasculature or defects (Figure 13). The stamp was then placed over the tissue slice and lightly struck several times in order to cut the tissue into the desired shape (Figure 13). After stamping, the dog-bone samples were then immersed in a bath of DMEM to maintain specimen hydration.

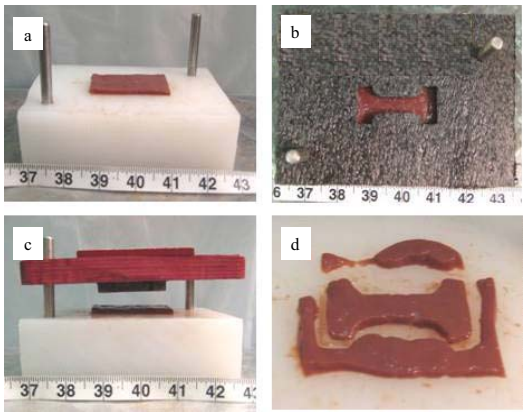

Figure 13: Tension specimen stamping methodology.

The primary component of the tension experimental setup was a custom designed uniaxial dynamic tensile testing system (Figure 14). The entire experimental setup was contained in an environmental test chamber heated to 37°C. The testing system consisted of two motor driven linear stages (Parker Daedal MX80S, Irwin, PA) mounted to a vertically oriented aluminum plate. Each of the linear stages was instrumented with a single-axis load cell (Interface, WMC Miniature-22.24N**,** Scottsdale, AZ) and accelerometer (Endevco 7264B, 2000 G, San Juan Capistrano, CA). The system was operated with a multi-axis controller (Parker ACR9000, Irwin, PA), which provided synchronized motion of both linear stages, and a motor driver (Parker ViX, Irwin, PA). The testing system placed a tensile load on the test specimen by simultaneously moving the top and bottom grips away from one another at a constant velocity.

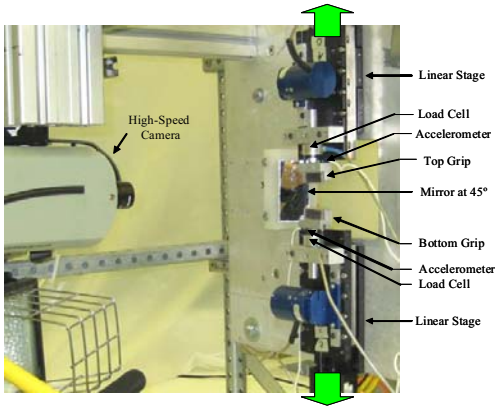

Figure 14: Uniaxial tension experimental setup**.**

For tension testing, a detailed mounting procedure was developed in order to minimize variations in initial specimen preload and the adverse affects of shear due to improper specimen alignment. Immediately prior to mounting the specimens on the experimental setup, the specimens were immersed in a bath of DMEM heated to 37°C. To mount the specimens the top grip assembly was first removed from the experimental setup and laid flat on a table top. The specimen was aligned on the top grip so that the main axis of the specimen coincided with the centerline of the load train and then clamped in place. Sandpaper was placed on the clamping surfaces to ensure that the specimens would not slip during loading. After clamping, the top grip assembly was then attached to the experimental setup and the specimen was allowed to hang in 1 g of tension and then clamped into the bottom grip. By allowing the specimens to hang under their own weight during the clamping process, all specimens had a minimal but consistent preload.

Once the coupons were mounted, side view and back view pre-test pictures were taken with high resolution digital cameras in order to obtain initial width and thickness measurements at the failure locations (Figures 15). Finally, equally spaced optical markers were placed on the gage length in view of the high-speed camera. In order to investigate rate dependence, each specimen was pulled to failure at one of four desired strain rates: 0.01 s^{-1}, 0.1 s^{-1}, 1.0 s^{-1}, or 10.0 s^{-1}.

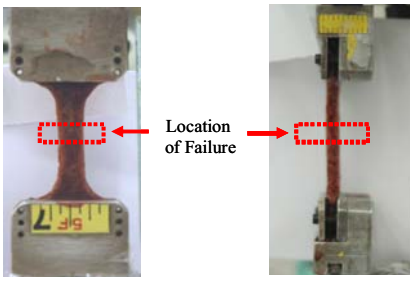

Figure 15: Pre test width and thickness images for the tension tests.

For a tension test to be deemed acceptable, the location of the failure must have occurred in the gage length of the specimen. Therefore, specimens which tore next to the grip or pulled out of either grip were not included in the data set. Failure was defined as the point at which the failure tear initiated in the high-speed video. If the initiation of the failure tear could not be observed in the video, then failure was defined as the point of peak load preceding a significant decrease in the load. Local stress was calculated from the measured displacement between the closest optical markers surrounding the location of the failure tear, which was quantified using motion analysis software. Local stress was calculated based on the inertially compensated force and the original cross-sectional area at the location of the failure. Characteristic averages were developed for each loading rate (Lessley et al. 2004).

The stress versus strain curves for specimens tested at approximately 0.1 s^{-1} are provided as examples, along with the corresponding characteristic average and standard deviations (Figures 16 and 17). The stress versus strain curves show that the tensile response was non-linear for both liver and spleen tensile specimens. Although the 1 g initial condition used in the current study provided a consistent initial state of strain for all specimens, the effect of this condition on the toe region of the stress versus strain curves should be addressed and quantified in future studies.

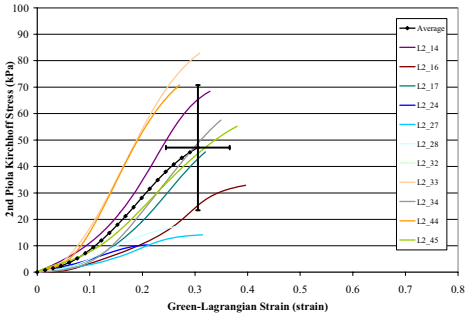

Figure 16: Human liver parenchyma response in uniaxial tension at ~0.1 s^{-1}.

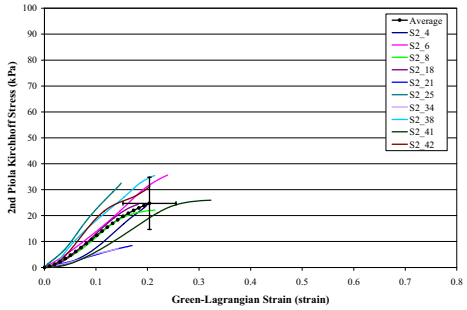

Figure 17: Human spleen parenchyma response in uniaxial tension at ~0.1 s^{-1}.

The results from the liver and spleen tension tests demonstrate rate dependence, with strain decreasing and stress increasing with each increasing strain rate (Figures 18 and 19). The results also show that the tensile failure stress and strain were considerably higher for the liver parenchyma compared to that of the spleen.

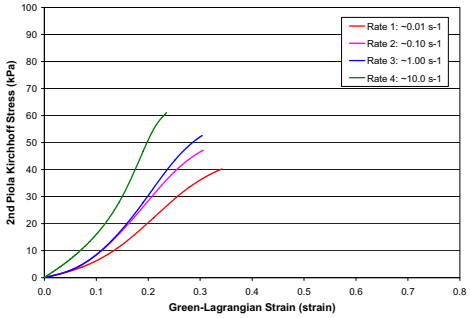

Figure 18: Characteristic averages for human liver parenchyma in uniaxial tension.

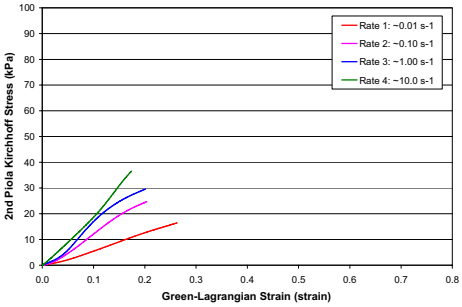

Figure 19: Characteristic averages for human spleen parenchyma in uniaxial tension.

Tissue Level Compression Testing- Uniaxial compression tests were performed on cylindrical compression samples of constant thickness. As with the tension testing, the same custom blade assembly and slicing jig were used to obtain constant thickness slices of liver and spleen parenchyma. However, the 48.3 cm long razor blades were spaced such that the tips of the blades were 10 mm apart for compression samples. After slicing, the samples were immersed in a bath of DMEM to maintain specimen hydration.

A custom cylindrical cutting tool and stamping base were used to obtain cylindrical shaped specimens commonly used for uniaxial compression testing (Figure 20). The custom cylindrical cutting tool was a sharpened, hollow, metal tube (I.D. = 25.4 mm). Prior to cutting, a template was used to position the tissue slice on the stamping base in order to obtain a specimen devoid of any visible vasculature or defects. The cutting was performed by slowly rotating cutting tool about the long axis, while applying minimal downward force in order to avoid tearing and deformation. After cutting, the samples were immersed in a bath of DMEM to maintain specimen hydration.

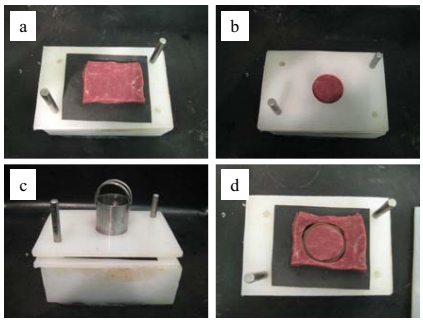

Figure 20: Compression specimen cutting methodology.

The primary component of the compression experimental setup was a high rate servo-hydraulic material testing system (MTS Systems Corporation, MTS-810, Eden Prairie, MN) (Figure 21). A load cell (Interface 1210-AF-500lbf, Scottsdale, AZ) was attached to a base plate, and the testing basin was attached to the top of the load cell. A load cell (Interface 1210-AF-500lbf, Scottsdale, AZ) was attached between the MTS piston, and the impacting surface. Both the reaction and impacting surfaces were constructed of polypropylene. An accelerometer (Endevco 7264B, 2000 g, San Juan Capistrano CA) was attached to the impacting surface, and was used to inertially compensate the impactor force. The piston displacement was measured with the MTS internal LVDT and a potentiometer (Space Age Control, 160-1705, 540mm, Palmdale, CA) attached to the MTS piston.

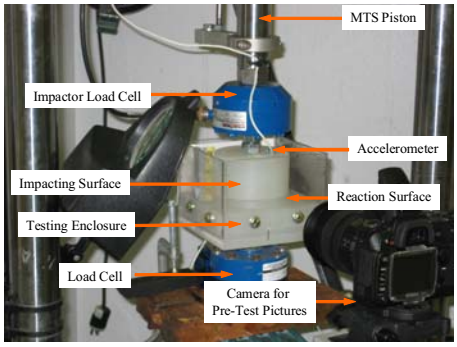

Figure 21: Uniaxial compression experimental setup.

Immediately prior to placing the specimens on the experimental setup, the specimens were immersed in a bath of DMEM heated to 37°C. A silicon spray lubricant was applied to each loading surface before each specimen was placed on the test setup to minimize friction between the specimen and each loading surface. After allowing the specimen to soak in the heated DMEM bath for several minutes, the specimen was removed and placed in the center of the reaction surface. Side view and top view pre-test pictures were taken to determine initial specimen area and initial specimen height (Figure 22). The impacting surface was then moved into position 13 mm above the maximum stroke to give the impactor time to accelerate to the desired velocity before contacting the sample (Figure 28).

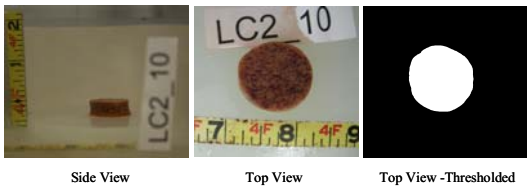

Figure 22: Pre-test area and thickness images for the compression tests.

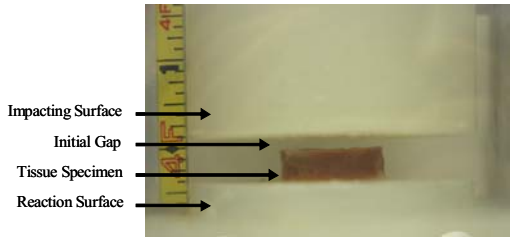

Figure 23: Pre-test image showing initial gap.

In order to investigate rate dependence, each specimen was compressed to failure at one of four desired strain rates: 0.01 s^{-1}, 0.1 s^{-1}, 1.0 s^{-1}, or 10.0 s^{-1}. Failure was defined as the fist major inflection point in the force time history (Figure 24). Strain was calculated based on the displacement of the MTS piston and initial specimen height. Stress was calculated based on the inertially compensated force and the original cross-sectional area, which was calculated using a custom Matlab code to analyze the thresholded top view image. Characteristic averages were developed for each loading rate in tension and compression (Lessley et al. 2004).

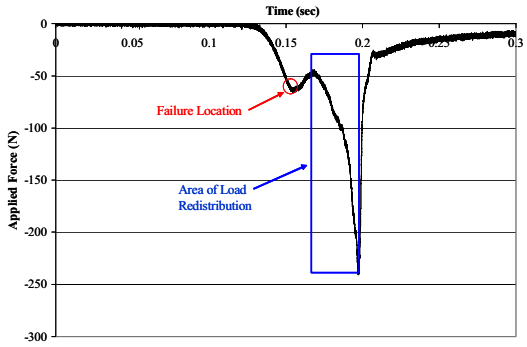

Figure 24: Typical force curve for compression specimens.

The stress versus strain curves for specimens tested at the approximately 1.0 s^{-1} are provided as examples, along with the corresponding characteristic average and standard deviations (Figures 25 and 26). The stress versus strain curves show that the compressive response was non-linear for both liver and spleen compressive specimens.

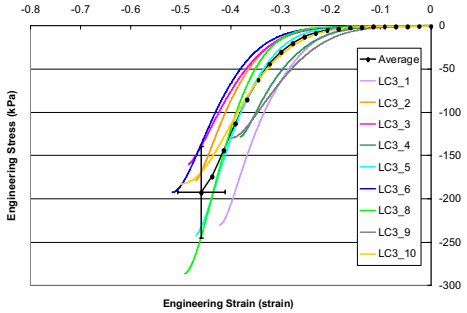

Figure 25: Human liver parenchyma response in uniaxial compression at ~1.0 s^{-1}.

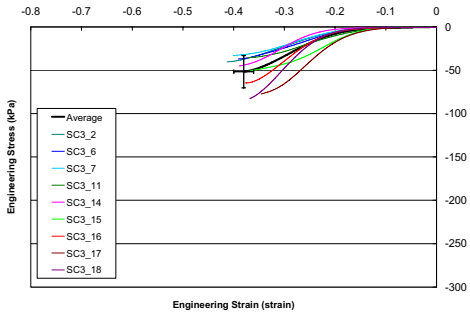

Figure 26: Human spleen parenchyma response in uniaxial compression at ~1.0 s^{-1}.

The results from the liver and spleen compression tests demonstrate rate dependence, with strain decreasing and stress increasing with each increasing strain rate (Figures 27 and 28). The results also show that the compressive failure stress was considerably higher for the liver parenchyma compared to that of the spleen.

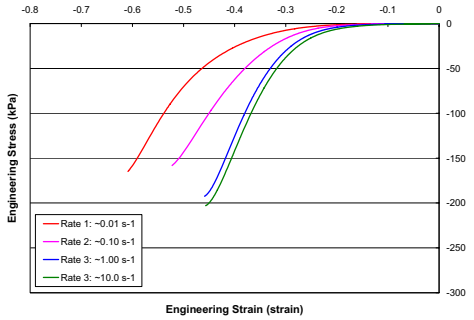

Figure 27: Characteristic averages for human liver parenchyma in uniaxial compression.

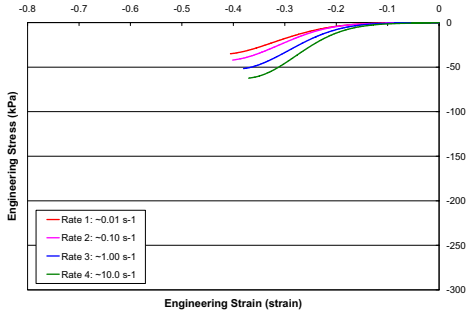

Figure 28: Characteristic averages for human spleen parenchyma in uniaxial compression.

Material Model Optimization Method

The overall approach to model development and optimization is shown in Figure 29. It involves experimental data interpretation and conditioning, simulation, and optimization steps outlined here.

Raw data processing: Raw data from the tensile tests are loaded and separated into different strain rate categories. Each strain rate has multiple series that consist of data from individual tests. Two graphs are produced for each series: displacement versus time and force versus time. Data before t=0 is truncated, and then normalization of the data is performed. The displacements are normalized by initial gauge length into stretches and the forces are normalized by initial cross-sectional area into stress. The initial cross sectional area for each series is calculated by multiplying the thickness by the gauge width. By normalizing both the displacement and the force, the series can then be combined to get a characteristic average for each strain rate. In addition to a characteristic average for each strain rate, a global characteristic average can be acquired to estimate initial material parameters.

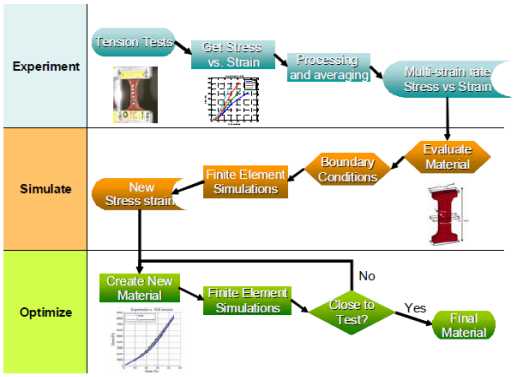

Figure 29: Optimization for finite element material constants.

Stretch averaging: To get an average stretch versus time characteristic knowing that the tests are done at a constant displacement rate, the stretch versus time data is differentiated to get the stretch rate versus time for each series. This plot can then be compared to a constant displacement rate to identify deviations from the defined displacement rate. The time for each series is scaled by the maximum time so that all of the data have x-values between 0 and 1. Then y-values can be averaged to get a characteristic curve that is the combined average for the full range of the data. The final average for each strain rate can then be scaled by the average end time to add back the temporal aspect. After the average for each strain rate is computed, the global average is computed for all strain rates.

Stress averaging: The stretch versus time defines the displacement of the top grip with respect to the bottom; in addition, the stress versus strain characteristic must be defined for the material model. The method used here is similar to the method used for the stretch versus time averaging, in which the strains are normalized by the maximum strain for each series, and the stresses are normalized by the maximum stress for each series. The averaged stress versus strain curves for each strain rate can then be regressed to a polynomial (order depends on fit) enabling them to be scaled by the average end strain and end stress. In addition, the global stress versus

strain curve can be calculated similarly by a regression of the series. The average can then be scaled back by the average end strain and average end stress.

Material selection: After the global stretch versus time and global stress versus strain relationships are found, the curves are inputt into a standard FE coupon model with varying material models to find the material model that best matches the shape of the global averages. Any material model that is deemed a possibility for this model is run with the input curves. All hyperelastic material models in LS-Dyna are considered as candidates. The different material models are compared with the target stress versus strain curve to find one that best matches the behavior of the experiments (Figure 30).

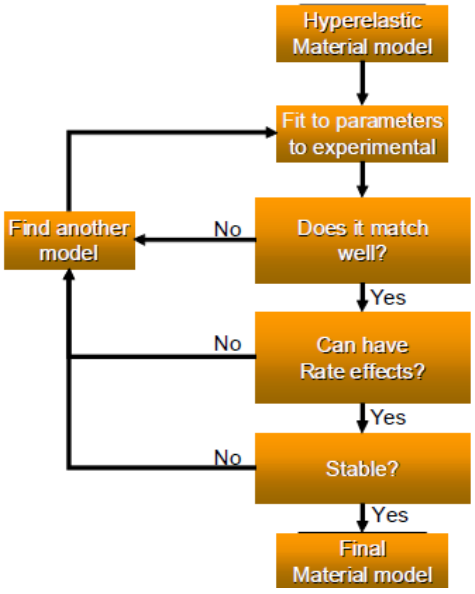

Figure 30: Methodology for selecting the appropriate material model.

Material parameter optimization: One best shape describing a material model is formulated using a polynomial from stretch and stress normalized data. Scaling parameters are defined to modify the input curve. The scaling factor approach is needed because of the need to optimize three separate loading rates, one for each strain rate, and the factors are optimized with a multi-island genetic algorithm to minimize the least square error between the model output and the target stress versus strain curve for all 3 rates (Figure 31).

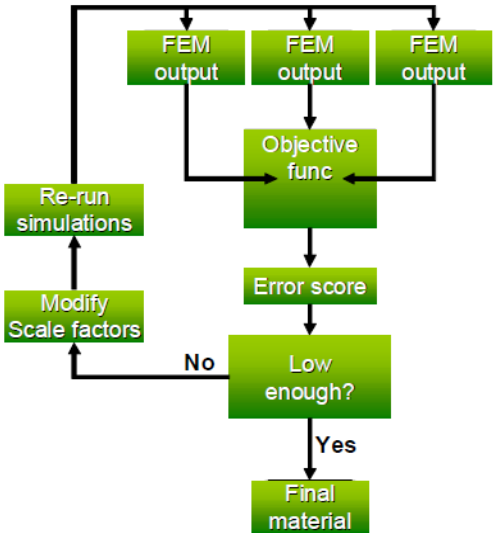

Figure 31: Methodology for optimizing the final material model.

SUMMARY

A multi-scale four step approach was utilized to characterize human liver and spleen tissue. Whole body injury analysis was performed by using the CIREN and NASS/CDS databases. Whole organ impacts were then performed. Sub-failure tests, at multiple rates, and failure tests were performed on each whole organ. Tissue level tension and compression failure tests were then performed on each organ at four different loading rates. Finally, finite element modeling was utilized to obtain an optimum model of the different tissue level tests. It is anticipated that the data from this research will enhance the understanding of internal organ injuries and provide a foundation for future human internal organs finite element models.

ACKNOWLEDGEMENTS

The authors would like to acknowledge the Toyota Motor Corporation for their funding and support.

REFERENCES

Augenstein J, Bowen J, Perdeck E, Singer M, Stratton J, Horton T, Rao A, Digges KH, Malliaris AC, Steps J. Injury Patterns in Near-Side Collisions. SAE 2000 World Congress: SAE International. 2000.

Bondy N. Abdominal Injuries in the National Crash Severity Study. National Center for Statistics and Analysis. 59-80, 1980.

Elhagediab A, Rouhana S. Patterns of Abdominal Injury in Frontal Automotive Crashes. The 16th International Technical Conference on the Enhanced Safety of Vehicles. 1998.

Hollenstein M, Nava A, Valtorta D, Snedeker JG, Mazza E. Mechanical Characterization of the Liver Capsule and Parenchyma. In: Szekely MHG, editor. Biomedical Simulation. Berlin/Heidelberg: Springer-Verlag. 150-158, 2006.

Hurtuk M, Reed R, Esposito T, Davis K, Luchette F. Trauma Surgeons Practice what the Preach: The NTDB Story on Solid Organ Injury Management. Journal of Trauma. 61(2): 243-255, 2006.

Kerdok A, Ottensmeyer M, Howe R. Effects of Perfusion on the Viscoelastic Characteristics of Liver. Journal of Biomechanics. (39): 2221-2231, 2006.

Lessley D, Crandall J, Shaw G, Funk J, Kent R. A Normalization Technique for Developing Corridors from Individual Subject Responses. SAE Technial Paper Series. Detriot, MI, 2004.

Mackenzie E, Fowler C. Epidemiology. In: Moore EE, Feliciano DV, Mattox KL, eds. Trauma. 5th ed. New York: McGraw- Hill; 21–39, 2003.

Matthews J and Martin J. Atlas of Human Histology and Ultrastructure. Philadelphia: Lea & Febiger, 1971.

Mazza E, Nava A, Hahnloser D, Jochum W, and Bajka M. The Mechanical Response of Human Liver and its Relation to Histology: An In Vivo Study. Medical Image Analysis. 11: 633-672, 2007.

Melvin J, Stalnaker R, Roberts V, Trollope M. Impact Injury Mechanisms in Abdominal Organs. Proceedings of the 17th Stapp Car Crash Conference. Society of Automotive Engineers, Warrendale, PA: 115-126, 1973.

Moorcroft D, Duma S, Stitzel J, Duma G. Computational Model of the Pregnant Occupant: Predicting the Risk of Injury in Automobile Crashes. American Journal of Obstetrics and Gynecology. 189 (2): 540-544, 2003.

Nasseri S, Bilston L, and Tanner R. Lubricated Squeezing Flow: A Useful Method for Measuring the Viscoelastic Properties of Soft Tissue. Biorheology. 40: 545-551, 2003.

Roan E, and Vemaganti K. The Non-Linear Material Properties of Liver Tissue Determined from No-Slip Uniaxial Compression Experiments. Transactions of ASME. 129: 450-456, 2007.

Santago A, Kemper A, McNally C, Sparks J, Duma S. The effect of Temperature on the Mechanical Properties of Bovine Liver. Biomed. Sci. Instrum. 45: 376-381, 2009a.

Santago A, Kemper A, McNally C, Sparks J, Duma S. Freezing Affects the Mechanical Properties of Bovine Liver. Biomed. Sci. Instrum. 45: 24-29, 2009b.

Sparks J, Bolte J, Dupaix R, Jones K, Steinberg S, Herriott R, Stammen J, Donnelly B. Using Pressure to Predict Liver Injury Risk from Blunt Impact. Stapp Car Crash Journal. 51: 401-432, 2007.

Stingl J, Baca V, Cech P, Kovanda J, Kovandova H, Mandys V, Rejmontova J, Sosna B. Morphology and some biomechanical properties of human liver and spleen. Surgical and Radiological Anatomy. 24(5): 285-289, 2002.

Stitzel J, Gayzik F, Joth J, Mercier J, Gage D, Morton K, Duma S, Payne R. Development of a Finite Element-Based Injury Metric for Pulmonary Contusion Part I: Model Development and Validation. Stapp Car Crash Journal. 49: 271-289, 2005a.

Stitzel J, Hansen G, Herring I, Duma S. Blunt Trauma of the Aging Eye: Injury Mechanisms and Increasing Lens Stiffness. Archives of Ophthalmology. 123: 789-794, 2005b.

Takhounts E, Ridella S, Tannous R, Campbell J, Malone D, Danelson K, Stitzel J, Rowson S, Duma S. Investigation of Traumatic Brain Injuries Using the Next Generation of Simulated Injury Monitor (SIMon) Finite Element Head Model. Stapp Car Crash Journal. 52: 1-31, 2008.

Tamura A., Omori K, Miki K, Lee J, Yang K, King A. Mechanical Characterization of Porcine Abdominal Organs. Stapp Car Crash Journal. 46: 55-69, 2002.

Thor, C. “Characteristics of Thoracic Organ Injuries in Frontal Crashes.” MS Thesis

Virginia Polytechnic Institute and State University, 2008.

Uehara H. A Study on the Mechanical Properties of the Kidney, Liver, and Spleen, by Means of Tensile Stress Test with Variable Strain Velocity. Journal of Kyoto Prefectural University of Medicine. 104(1): 439-451, 1995.

Wang B, Wang G, Yan D, Liu Y. An Experimental Study on Biomechanical Properties of Hepatic Tissue Using a New Measuring Method. Bio-Medical Materials and Engineering. 2: 133-138, 1992.

Yamada H. Strength of Biological Materials. Baltimore: Williams and Wilkins, 1970.

Effects of Pre-Impact Bracing on Chest Compression of Human Occupants in Low-Speed Frontal Sled Tests

Andrew R. Kemper, Stephanie Beeman, and Stefan M. Duma
Virginia Tech – Wake Forest, Center for Injury Biomechanics
United States of America
Paper Number 11-0193

ABSTRACT

Continued development of computational models and biofidelic anthropomorphic test devices (ATDs) necessitates further analysis of the effects of muscle activation on the biomechanical response of human occupants in automotive collisions. The purpose of this study was to investigate the effects of pre-impact bracing on human occupant chest compression during low-speed frontal sled tests. In this study, a total of 10 low-speed frontal sled tests (5.0g, Δv=9.7kph) were performed with 5 male human volunteers. The height and weight of the human volunteers were approximately that of the 50th percentile male. Each volunteer was exposed to 2 impulses, one relaxed and the other braced prior to the impulse. A 59 channel chestband, aligned at the nipple line, was used to measure anterior-posterior sternum deflection for all test subjects. Subject head accelerations, spine accelerations, and forces at each interface between the subject and test buck were recorded for all tests. A Vicon motion analysis system, consisting of 12 MX-T20 2 megapixel cameras, was used to quantify subject 3D kinematics (±1 mm) at a sampling rate of 1 kHz. The chestband data showed that bracing prior to the initiation of the sled pulse essentially eliminated thoracic compression due to belt loading for all subjects except one. The load cell data indicate that forces were distributed through the feet, seatpan, and steering column as opposed to the seatbelt for the bracing condition. In addition, the forward excursion of the elbows and shoulders were significantly reduced during the braced condition compared to the relaxed condition. The data from this study illustrates that muscle activation has a significant effect on the biomechanical response of human occupants in frontal impacts and can be used to refine and validate computational models and ATDs used to assess injury risk in automotive collisions.

INTRODUCTION

Nearly 30,000 passenger vehicle occupant deaths occur annually in the United States. Approximately 50% of these fatalities are due to frontal crashes (NHTSA Traffic Safety Facts, 2008). In addition, the number of occupants sustaining injuries greatly exceeds the number of fatalities.

Computational models and anthropomorphic test devices (ATDs) are commonly used to predict and evaluate human occupant responses and injuries in motor vehicle collisions. These research tools are primarily validated against post mortem human surrogate (PMHS) data, which do not include the effects of muscle activation. However, studies have shown that tensing muscles prior to a crash event can change the kinetics and kinematics during the crash (Armstrong et al., 1968; Hendler et al., 1974; Begeman 1980; Sugiyama 2007; Ejima 2008). There have been no studies to the authors' knowledge that have quantified the chest deflection of human volunteers in a relaxed and braced state. Therefore, the purpose of this study was to investigate the effects of pre-impact bracing on human occupant chest compression during low-speed frontal sled tests.

METHODS

A total of 10 low-speed frontal sled tests (5.0g, Δv=9.7kph) were performed with 5 male human volunteers. Selected volunteers were approximately 50th percentile male height and weight (175cm; 76.7kg) (Schneider et al., 1983). Approval to conduct the human subject testing presented in the current study was granted by the Virginia Tech Internal Review Board (IRB). In addition, all volunteers signed an informed consent form prior to participating in the study.

Experimental Setup

Dynamic frontal sled tests were performed using a custom mini-sled and test buck (Figure 1). The mini-sled was accelerated with the use of a pneumatic piston, which was used to generate a 5.0 g (Δv=9.7kph) frontal sled pulse (Figure 2). The sled pulse severity was determined based on previous research which has shown that a frontal

sled pulse of this severity does not result in injury (Arbogast et al., 2009).

The test buck was instrumented with 5 multi-axis load cells and 18 single-axis accelerometers. A six-axis load cell was installed on both the seatpan and seatback (Robert A. Denton, Inc., 44 kN-Model 2513, Rochester Hills, MI). A six-axis load cell was installed on the right foot support (Robert A. Denton, Inc., 13.3 kN-Model 1794A, Rochester Hills, MI) and left foot support (Robert A. Denton, Inc., 13.3 kN-Model 1716A, Rochester Hills, MI). A five-axis load cell was installed on the steering column (Robert A. Denton, Inc., 22.2 kN-Model 1968, Rochester Hills, MI). Three-axis accelerometer cubes (Endevco 7264B, 2000 g, San Juan Capistrano, CA) were rigidly mounted to each load cell plate for inertial compensation. The test buck acceleration was measured with a three-axis accelerometer cube (Endevco 7264B, 2000 g, San Juan Capistrano, CA) rigidly mounted to the frame under the seatpan. Belt load sensors were added to the retractor, shoulder, and lap belts (Robert A. Denton, Inc., 13.3 kN-Model 3255, Rochester Hills, MI). Seatbelt spool out at the retractor was measured with a potentiometer (Space Age Control Inc. 160-1705, 539.75mm, Palmdale, CA) attached to a custom seatbelt clamp.

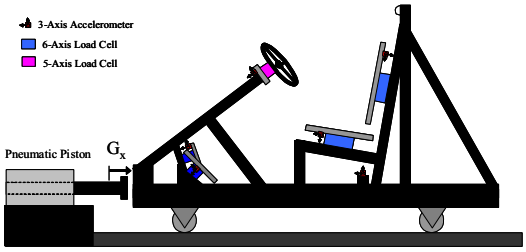

Figure 1: Test buck schematic.

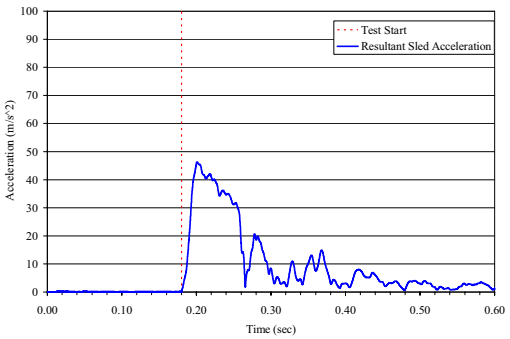

Figure 2: Resultant sled acceleration.

Subject Instrumentation

A 59 channel chestband (Denton, Inc., Model 8641, Rochester Hills, MI) was used to quantify thoracic displacement and contours. Gage 1 was positioned at the spine and the band was wrapped around the chest so that gage number ascended in the clockwise direction. The chestband was aligned with the nipple line (Figure 3). Heavy duty double sided adhesive tape was used to securely attach the chestband to each subject. The chestband was subsequently wrapped with co-flex, a self-adherent compression wrap, to ensure a tight connection and protect the chestband wires throughout each trial. The closest gage to both the sternum and the spine were noted as well as their respective distances.

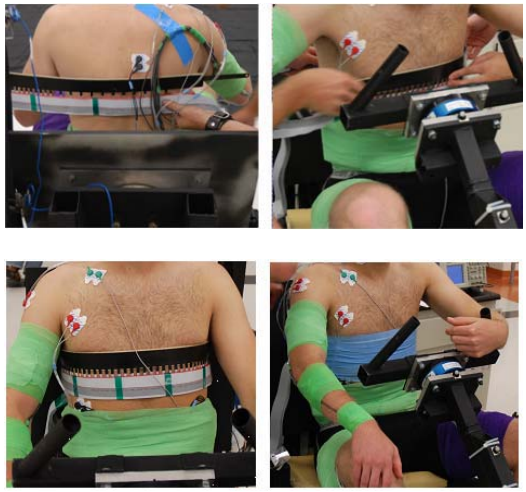

Figure 3: Chestband aligned with the nipple line of the chest.

For each subject, accelerations were measured at the sternum, spine, and head. In order to obtain linear acceleration and angular velocity of the head, three orthogonal accelerometers (Endevco 7264B, 2000 g, San Juan Capistrano, CA) and a three-axis angular rate sensor (IES 3103, 4800 deg/s, Braunschweig, Germany) were mounted to a metal mouthpiece fixture. A “boil and bite” mouth guard of thermoplastic material was created for each subject to ensure proper, repeatable positioning as well as a tight junction with the subject. In addition, each subject wore a chin strap to ensure that the jaw remained tightly clamped on the mouthpiece during the trials. Three-axis accelerometer cubes (Endevco 7264B, 2000 g, San Juan Capistrano, CA) were attached to the sternum (at the suprasternal notch), the 7th cervical vertebrae (C7), and the

sacrum of each subject. The three-axis accelerometer cubes were individually attached to the skin with adhesive patches glued to the cubes. However, since the focus of the current study is chest compression, the results of subject acceleration data are not presented.

Surface electromyography (EMG) was obtained from a total of 20 muscles during each test event (Table 1). Several preparation steps were taken prior to attaching the electrodes to the skin. To ensure a strong bond with the skin, hair was removed at the location of electrode attachment. The skin was lightly abraded to remove dead epithelial cells and then wiped with isopropyl alcohol to remove oils and surface residue. The skin was allowed to dry before the electrodes were adhered. After connecting the wires to the electrodes, the electrodes were wrapped with co-flex, a self-adherent compression wrap, to ensure a tight connection. However, since the focus of the current study is chest compression, the results of EMG data are not presented.

Table 1: Target muscles for EMG.

Body Region	EMG Location
Arm	Right Biceps Brachii
	Right Triceps Brachii
Forearm	Right Flexor Carpi Radialis
	Right Extensor Digitorum
Neck & Shoulder	Right Sternoceidomastoid
	Right Trapezius
	Right Deltoid
Chest	Right Pectoralis Major
Abdomen	Right Rectus Abdominis
	Right External Abdominal Oblique
Spine	Right Upper Erector Spinae
	Right Lower Erector Spinae
Thigh	Right/Left Rectus Femoris
	Right/Left Biceps Femoris
Shank	Right/Left Tibialis Anterior
	Right/Left Gastrocnemius

Test Conditions

Each volunteer was exposed to two 5.0 g (Δv=9.7kph) frontal sled impulses, one relaxed and the other braced prior to the impulse. For all tests, a load limiting driver side seatbelt was placed around the test subject, and the slack was removed. Volunteers were informed before each test as to whether they were to remain relaxed or brace themselves for the sled impulse. For the relaxed tests, a television monitor was used as a distraction mechanism and the trigger was out of sight so that the volunteers were unaware of when the test would occur. Prior to the relaxed tests, subjects were instructed to relax and continue to watch the monitor while facing forward. Then, the sled pulse was randomly initiated after several minutes of quiet sitting. For the tensed tests, subjects were asked to brace themselves with both their arms and legs. A guided countdown was used to instruct the volunteers when to brace with their arms and legs prior to the initiation of the sled pulse. Each subject had a waiting time of approximately 30 minutes between subsequent test conditions.

Data Acquisition and Processing

An onboard data acquisition system was used to record 148 channels of data at a sampling rate of 20kHz. For relaxed tests, data was collected during the relaxed state and test event. For braced tests, data was collected during the relaxed state, braced state, and test event. Data included subject accelerations, test buck accelerations, chest contour, surface electromyography of 20 muscles (legs, arms, abdomen, back, and neck), and forces at each interface between the subject and test buck. All reaction load cell data were compensated for crosstalk. The forces measured by each reaction load cell were inertially compensated with the use of three single-axis accelerometers mounted to each reaction plate. The reaction load cell data and test buck accelerometer data were filtered using SAE Channel Filter Class (CFC) 60 [SAE J211, 1995]. The seatbelt load cell data were filtered using SAE Channel Filter Class (CFC) 180. The unfiltered chestband data was processed using a software package called RBandPC. This software was used to generate 2D chest contours in 10 ms increments as well as the deflection between the spine and sternum.

A Vicon motion analysis system, consisting of 12 MX-T20 2 megapixel cameras, was used to quantify the 3D kinematics (±1mm) of photo-reflective markers placed on both the test subject and the test buck at a sampling rate of 1kHz (Figure 4). Marker trajectories were converted to the reference frame of the test buck and then to the SAE J211 sign convention [SAE J211, 1995]. The displacements of selected anatomical regions of interest relative to the buck were categorized as global trajectories. Regions of interest included the upper extremities (elbows and shoulders), lower extremities (knees), pelvis (hips), and the head. The excursions of these regions were normalized to their respective

initial positions and compared by test condition across subjects. A paired Student's t-test was used to assess significance between relaxed and braced conditions for each volunteer.

High-speed video was obtained from the lateral side of the volunteer at a sampling rate of 1,000 Hz with the use of a high resolution, high light sensitivity camera (Vision Research, Phantom V-9, Wayne, NJ).

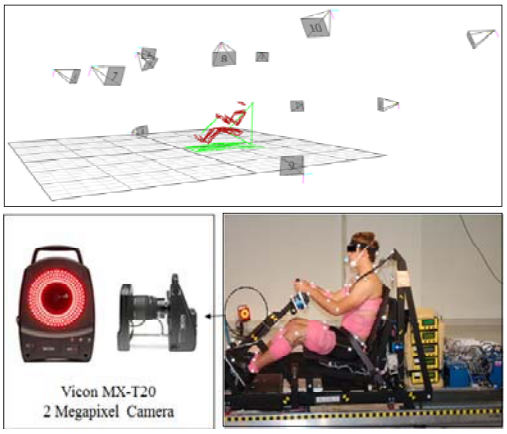

Figure 4: Vicon System and markers.

RESULTS

The time histories of the resultant sled accelerations were calculated and plotted for each subject and test condition (Figures 5 and 6). The consistency in the resultant sled acceleration between subjects for a given test condition shows that the custom mini-sled was extremely repeatable. Exemplar high-speed video stills for each condition are provided for qualitative kinematics (Figure 7). The sled pulse started at t=180ms for all tests.

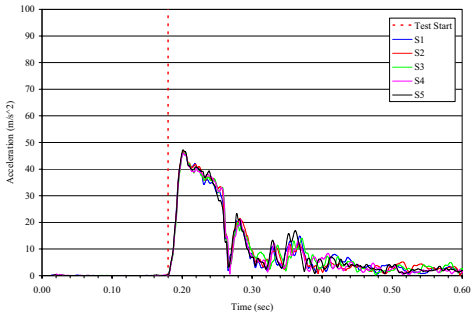

Figure 5: Resultant sled accelerations for relaxed tests.

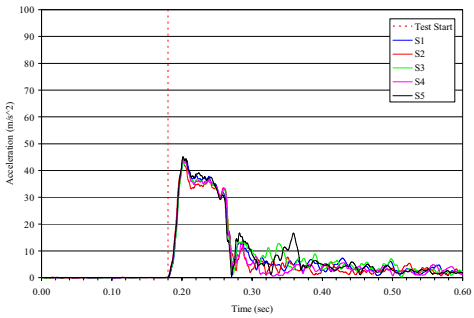

Figure 6: Resultant sled accelerations for braced tests.

Qualitative examination of the global trajectories of each test subject revealed marked differences between the relaxed and braced conditions in both initial position and forward excursions of the volunteer occupants (Figure 8). The normalized data highlighted pronounced differences in forward excursions due to bracing. It was found that bracing significantly reduced the forward excursion of the elbows ($p<0.01$), shoulders ($p<0.01$), and head ($p<0.01$). Although not significant, bracing considerably reduced the forward excursion of the lower extremities and pelvis.

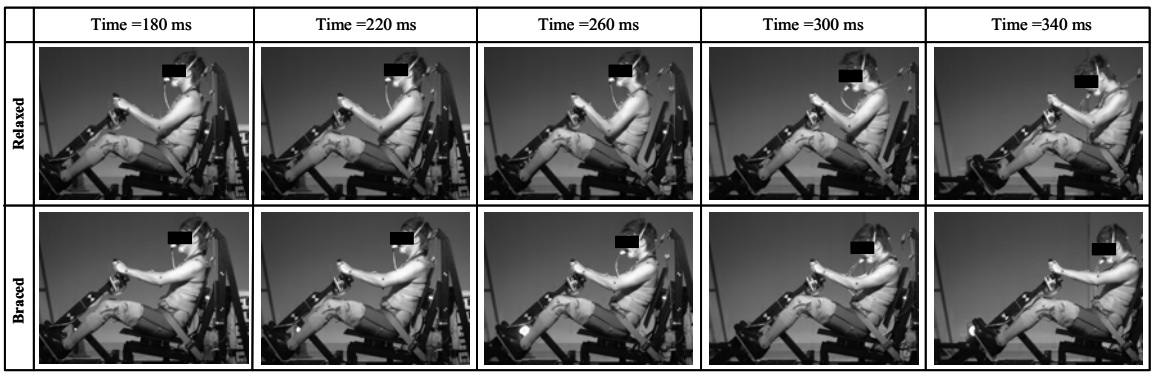

Figure 7: Exemplar high-speed video stills for relaxed and braced conditions.

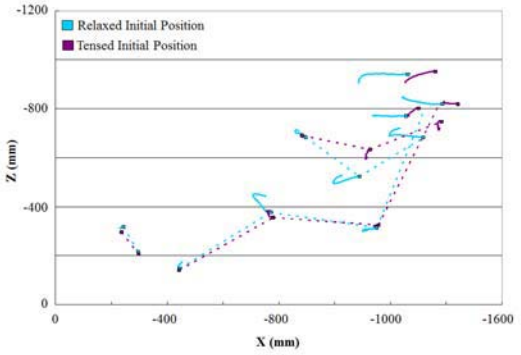

Figure 8: Example global trajectory of a relaxed vs. braced volunteer test.

Example 2D chestband contours were plotted for each test condition (Figures 9 and 10). In each figure, the red line represents the subject's chest contour 10 ms before the start of the trial and the blue line represents the subject's chest contour at the time of peak sternum deflection. For the braced trial, the red line represents the subject's chest contour while in a braced state, while the green line represents the subject's chest contour prior to bracing, i.e. relaxed state.

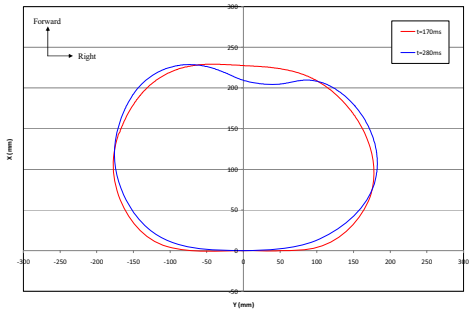

Figure 9: Example chestband contours during relaxed condition.

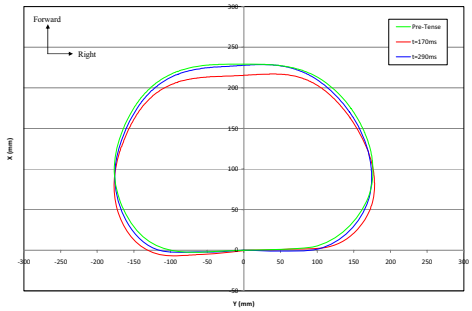

Figure 10: Example chestband contours during braced condition.

The chest compression for each subject was plotted for each test condition (Figures 11 and 12). Chest compression was defined as the ratio of the instantaneous chest depth at the sternum to the chest depth at the sternum measured during the relaxed state prior to the test. Positive chest compression indicates a decrease in chest depth at the sternum, while negative chest compression indicates an increase in chest depth at the sternum.

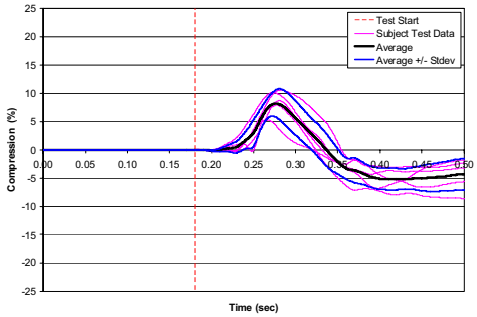

Figure 11: Chest compression during relaxed condition.

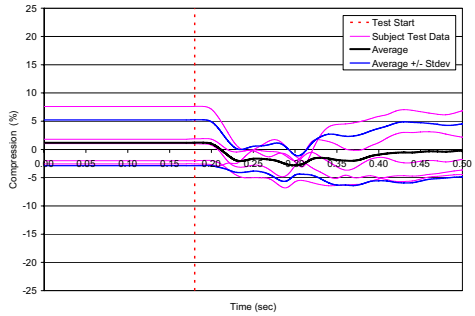

Figure 12: Chest compression during braced condition.

DISCUSSION

The chestband data show that the chest was compressed due to thoracic belt loading for all subjects during the relaxed condition. For the braced condition, the chestband data show that the act of bracing prior to the test resulted in a reduction in sternum depth, relative to the relaxed state, for three subjects due to compression against the seatback. For two of the subjects, the act of bracing prior to the test resulted in an increase in sternum depth, relative to the relaxed state, due to either lateral thoracic compression from the upper extremities or expansion of the pectoralis major muscles. During the test event for the braced condition, the chest depth at the sternum returned to a depth close to that recorded during the relaxed state for two of the subjects due to the decreased force applied to the seatback during the frontal sled pulse. For two subjects the chest depth at the

sternum increased slightly due to lateral thoracic compression from the upper extremities. Regardless, chest compression due to thoracic belt loading was essentially eliminated during the braced condition for all but one subject. The reaction load cell data showed that the one subject who sustained minor chest compression due to belt loading (1.7% compression), exerted considerably lower bracing forces on the steering column and foot rests than all other subjects.

SUMMARY

In the current study, a total of 10 low-speed frontal sled tests (5.0g, Δv=9.7kph) were performed with 5 male human volunteers. The height and weight of the human volunteers were approximately that of the 50th percentile male. Each volunteer was exposed to 2 impulses, one relaxed and the other braced prior to the impulse. A 59 channel chestband, aligned at the nipple line, was used to measure anterior-posterior sternum deflection for all test subjects. The chestband data showed that bracing prior to the initiation of the sled pulse eliminated thoracic compression due to belt loading for all subjects except one. The load cell data indicate that forces were distributed through the feet, seatpan, and steering column as opposed to the seatbelt for the bracing condition. In addition, the forward excursion of the elbows and shoulders were significantly reduced during the braced condition compared to the relaxed condition. The data from this study illustrates that muscle activation has a significant effect on the biomechanical response of human occupants in frontal impacts and can be used to refine and validate computational models and ATDs used to assess injury risk in automotive collisions.

ACKNOWLEDGEMENTS

The authors would like to thank Toyota Motor Engineering & Manufacturing (TEMA) and Toyota Central Research and Development Laboratories (TCRDL) for sponsoring this research.

REFERENCES

[1] Arbogast, K. B., S. Balasubramanian, T. Seacrist, M. R. Maltese, J. F. García-España, T. Hopely, E. Constans, F. J. Lopez-Valdes, R. W. Kent, H. Tanji and K. Higuchi; Comparison of kinematic responses of the head and spine for children and adults in low-speed frontal sled tests; Stapp Car Crash J.; 53, 329-372, 2009.

[2] Armstrong, R. W., H. P. Waters and J. P. Stapp; Human muscular restraint during sled deceleration; Stapp Car Crash J.; 12, 440-462, 1968.

[3] Begeman, P. C., King, A.I., Levine, R.S., Viano, D.C. Biodynamic response of the musculoskeletal system to impact acceleration. SAE Paper 801312: 479-509, 1980.

[4] Ejima, S., Ono, Koshiro, Holcombe, Sven, Kaneoka, Koji, Fukushima, Makoto. Prediction of the physical motion of the human body based onmuscle activity during pre-impact bracing. IRCOBI Conference: 163-175, 2008.

[5] Hendler, E., J. O'Rourke, M. Schulman, M. Katzeff, L. Domzalski and S. Rodgers; Effect of head and body position and muscular tensing on response to impact; SAE Technical Paper Series; SAE 741184, 1974.

[6] NHTSA Traffic Safety Facts 2008. Washington, DC, National Highway Traffic Safety Administration.

[7] SAE J211 "Instrumentation for Impact Test," SAE J211/1 MAR 1995, 1995 SAE Handbook Volume 4 - On-Highway Vehicles & Off-Highway Machinery, Society of Automotive Engineers, Warrendale, PA. 1995.

[8] Sugiyama, T., Kimpara, Hideyuki, Iwamoto, Masami, Yamada, Daisuke. Effects of muscle tense on impact responses of lower extremity. IRCOBI Conference. Maastricht, Netherlands: 127-139, 2007.

INVESTIGATION OF PRE-IMPACT BRACING EFFECTS FOR INJURY OUTCOME USING AN ACTIVE HUMAN FE MODEL WITH 3D GEOMETRY OF MUSCLES

Masami Iwamoto
Yuko Nakahira
Takahiko Sugiyama
Toyota Central R&D Labs. Inc.
Japan
Paper Number 11-0150

ABSTRACT

Accident data analyses conducted at the Institute for Traffic Accident Research and Data Analysis (ITARDA) in Japan reported that over 60% of drivers who faced unavoidable crash situations made evasive maneuvers on braking and steering in 2007. In such emergency cases, drivers also might brace their body with their muscle activity to prepare the upcoming impacts. Their muscle activity would not only generate muscular forces but also change muscular stiffness and mechanical properties of their articulated joints. Therefore, occupant behaviors during impacts could be different from those observed in dummy tests and cadaver tests.

In this study, we developed an active human finite element (FE) model with 3D geometry of muscles. The muscle was modeled as a hybrid model by combination of bar elements with active muscle properties and solid elements with passive muscle properties. The bar elements were modeled with a Hill type muscle model to generate muscular force according to inputted activation levels. The solid elements were modeled with a rubber-like material model to simulate 3D geometry of individual muscles and non-linear passive properties. This combined muscle model was validated against human volunteer test data and reproduced increase of muscular stiffness with increase of muscle activation level as observed in the tests.

A volunteer test with one healthy male subject was conducted to obtain physiological information in a bracing situation with braking under his informed consent based on the Helsinki Declaration. In this test, the subject was asked to push his right foot on a brake pedal and his hands on a steering with his maximal voluntary force in the test apparatus fixed on the laboratory. Besides three reaction forces of a brake pedal, a steering, and rigid flat seats, the posture, pressure distribution on the seats, and 24 surface EMG (Electromyography) signals during his braking motion were measured in this test. His maximal braking force was reached to 750N and was well matched to previously reported values for emergency braking situation.

We performed simulations using the active human model to reproduce the bracing condition. In the simulations, the activation levels of 24 muscles obtained from the EMG data were directly inputted to the corresponding muscles of the active human model and those of the other muscles were estimated to reproduce the reaction forces. After reconstructing the reaction forces for the braced volunteer, we performed frontal impact simulations to compare occupant behavior and injury outcome in an active human body with those in a cadaveric human body. The simulation results showed significant differences between both human bodies. Different from the cadaveric human body, the active human body could have less injury risks in the thorax and more in extremities. These injury outcomes correspond to those previously reported in comparison between real-world accidents and laboratory cadaver sled tests. Although the active human model has some limitations on accuracy of estimation of muscular activation levels due to lack of consideration for muscular reflex and posture stabilization, it could have possibility to evaluate injury outcome in real-world accidents.

INTRODUCTION

Recent accident data analyses indicate that thorax injuries and lower extremity injuries are still important to mitigate occupant injuries in frontal crashes. Carroll et al. (2010)[10] conducted accident data analyses using the UK Cooperative Crash Injury Study (CCIS), the German In-Depth Accident data Survey (GIDAS), and the French GIE RE PR (Renault, and PSA Peugeot Citroen) database. They reported that older occupants are likely to sustain more torso injury. They also reported that occupants seated in the front passenger seat tended to sustain more torso injuries compared with the driver's seat. Brumbelow et al. (2009)[8] investigated impact and injury patterns in frontal crashes of vehicles based on the NASS-CDS crash data. They showed that occupants 60 or older more often received at least one serious chest injury than a serious head injury and the opposite was true for occupants younger than 30. Simamura et al. (2003)[35] conducted accident data analyses of a total 246 vehicle occupants using ITARDA data. They reported that elderly occupants frequently experienced rib fractures near the seatbelt

line even under lower impact severity while younger occupants appeared not to sustain rib fractures even in higher impact collisions. Their accident data analyses on thoracic injury indicate that occupant injury outcomes are different between the driver's seat and the front passenger seat as well as occupant injury outcomes are different between younger occupants and older occupants. However, the injury mechanisms are not well known.

As for the lower extremity injuries, Rudd (2009)[32] investigated lower limb injury risk and causation in the NASS-CDS crash database with mean age of about 38-year-old. They reported that foot and ankle injury prevalence has not decreased in newer model-year vehicles, and that injury risk to the foot and ankle has actually increased despite structural improvements aimed at reduced footwell deformation. They also reported that the majority of the foot and ankle injuries occur at lower crash severities with delta-V of less than 30km/h. This study show that the foot and ankle injuries occurred for even younger occupants and lower speed of impacts. However, the injury mechanisms are also not well known. Therefore, it is critical to elucidate the mechanisms for the thoracic injury and the lower extremity injury in order to mitigate occupant injuries in frontal impacts.

In addition, accident data analyses on frontal crashes conducted at ITARDA[1] in Japan reported that over 60% of drivers who faced unavoidable crash situations made evasive maneuvers on braking and steering in 2007. In such emergency cases, drivers also might brace their body with their muscle activity to prepare the upcoming impacts. Their muscle activity would not only generate muscular forces but also change muscular stiffness and mechanical properties of their articulated joints. Therefore, occupant behaviors with their muscle activity during impacts could be different from those observed in dummy tests and cadaver tests.

Several experimental studies have been performed to investigate the effect of muscle activity on injuries under the assumed impact situations. Tennyson and King (1976)[37] conducted a series of neck loading cadaveric tests and reported that muscle tense increased the neck injury in higher acceleration, while muscle tense contributed to the decrease in neck injury probability in low acceleration. This study suggested inherent performance tradeoffs in the role of muscle tense on the injury severities in impact loadings. Begeman et al. (1980)[6] conducted a series of sled test using human volunteers and cadaveric subjects and investigated the effects of muscle tense on kinematics of the lower extremities. As the results, they revealed that muscle tense stiffened up the human body rigidly and alter the overall kinematics of the human body during whole impact events. Funk et al. (2001)[17] performed cadaveric axial impact tests for the foot and ankle complex under a condition to simulate entrapped knee. In their tests, a foot plate hit the foot axially with an initial velocity of 5 m/s while muscular tension forces of 0 kN, 1.7 kN or 2.6 kN were applied to the Achilles tendon for investigation of muscular effect to skeletal injuries of the lower leg. They found that the muscular tension force can increase axial compressive force and the possibility of bone fractures at the distal tibia. On the other hand, some benefit effects of muscle tense were also reported. Levine et al. (1978)[27] conducted frontal impact tests using cadavers restrained by a three-point belt system equipped with and without a knee brace which simulated muscular tense of quadriceps in thigh. They found that the knee brace played a role in the prevention of submarining in frontal collisions. Therefore, the muscle tense appears to have both aspects of advantage and disadvantage for occupant injuries. However, it is not fully understood how muscle tense affects the impact responses and injury severities.

Computational human models are effective tools to understand the injury mechanisms in automotive crashes. Several researchers developed human whole body FE models of which size is AM50 (American adult male 50%ile) and validated the models against impact responses obtained from existing cadaver test data (Iwamoto et al., 2002[21], Vezin et al., 2005[40], Ruan et al., 2005[31]). Recently, Shigeta et al. (2009)[33] developed much more detailed human FE model including internal organs whose total number of elements is 1.8 million and validated the model against impact responses obtained from several cadaver test data. These human FE model represented mechanical responses of human body during impacts and contributed to elucidate some injury mechanisms in automotive crashes. Since the purposes of developing these models were not to investigate effects of muscle activity on occupant injuries, these models did not include active muscles.

Recently, some human FE models have been developed with active muscles to investigate the muscular effects for human body kinematics. Choi et al. (2005)[12] conducted both sled tests using eight volunteer subjects and computational analysis using a human FE model in bracing during frontal impacts. They used the EMG as an indicator of muscle activation levels and normalized it against that of maximal voluntary contraction. Reaction forces on steering wheel and brake pedal predicted by using their FE model with 16 muscles in the upper and lower extremities agreed with those of experimental data. However, muscles in deep layers were not considered in the impact analysis of the human body. Chang et al. (2008)[11] also developed a MADYMO FE model with 35 Hill-type muscles including muscles in deep layers for each lower extremity and

simulated knee-to-knee-bolster impact response in bracing during frontal impacts. Their simulation results with and without different levels of lower-extremity muscle activation for bracing suggested that muscle tension had the potential to decrease the externally applied force required to cause knee-thigh-hip fracture, and had the potential to increase the likelihood of femoral shaft fracture. Since their muscle models were developed using bar elements, their model did not represent the interaction forces between adjacent two muscles and the interaction forces between muscles and the adjacent bones. Behr et al. (2006)[7] developed a FE model of the lower limb with 20 independent muscle bundles in the superficial and deep layers and used to investigate the effect of muscle tense on the skeletal injuries of the lower limb. Each muscle was modeled using coupling of solid elements and actions of fiber elements. The interaction forces between muscles and bones were represented in the model. They validated the model for isolated muscle contribution in the direction of fibers and bracing conditions under an emergency braking. Their simulation results indicated that muscle activation in bracing during frontal impacts significantly increased the stress level on the tibial shaft. Hedenstierna et al. (2007[19], 2008[20]) represented a muscle using a combination of passive non-linear, viscoelastic solid elements and active Hill-type truss elements. They applied the muscle model to 22 separate pair of human neck muscles and conducted kinematical validation against volunteer experiments. They showed strain distribution in each neck muscle in frontal impact and rear-end impact for injury analysis. However, these two models were not validated for muscle stiffness change according to the activity, which is one of the essential characteristic features of muscles in considering muscular responses for impacts.

In this study, we developed a human body FE model with 3-D geometry of individual muscles to represent the interaction between two adjacent muscles and between muscles and the adjacent bones. We also provided the model with capability of muscle contraction to reproduce muscular stiffness change according to the activity. The developed human body FE model was validated against cadaver test data on thoracic and lower extremity responses in frontal impacts. The model was also validated against cadaveric frontal impact sled test data with 50km/h. A bracing situation was selected to investigate effect of muscle activity on injury outcome in frontal impacts. A volunteer test was conducted to obtain EMG data of muscles in the upper and lower extremity in the bracing situation. The developed human body FE model with muscles reproduced the bracing situation in pre-impact and then sustained frontal impacts with 50km/h. Simulation results of the human body model with muscle activity were compared with those of the human body model without muscle activity. We discussed effects of muscle activity in pre-impact on injury outcomes. We also discussed if muscle activity can explain the unknown mechanisms for thoracic and lower extremity injury. All simulations in this paper were performed using an explicit finite element code LS-DYNA (LSTC, USA).

MODEL DEVELOPMENT AND VALIDATIONS

A human whole body FE model with muscles

Muscular FE models of a human whole body were developed and integrated with a human body FE model called THUMS (Total HUman Model for Safety, Iwamoto et al.,2002[21]) whose size was similar to that of AM50 with a height of 175cm and a weight of 77kg. Figure 1 shows a developed human body FE model in a standing posture. In this figure, the skin was removed to see muscles clearly. The model includes 266 muscles of lower extremities, upper extremities, trunk, and neck such as the Sternocleidmastoid, Trapezius, Rectus Abdominis, Erector Spinae, Pectoralis Major, Deltoid, Biceps Brachii, Triceps, Extensor Digitorum, Flexor Carpi Radialis, Rectus Femoris, Gluteus Maximus, Vastus Medialis, Biceps Femoris, Vastus Lateralis, Tibialis Anterior, Gastrocnemius and so on. Total number of elements in the whole body model is about 250,000. Three dimensional surface geometry of each muscle was created based on MRI image data of a human male cadaver with a height of 180 cm and a weight of 90 kg (Visible Human Project Data; NIH, USA). Since the size of the cadaver was larger than that of THUMS, the geometry of each muscle was resized to fit THUMS by referring to configuration and individual size of muscles and bones depicted in cross-sectional image data obtained from anatomical tests such as (Agur et al., 2005[2]). Then each muscle was modeled with hexahedron meshes by using HyperMesh ver.8 (Altair Engineering, USA). The maximum aspect ratio and jacobian of solid elements for muscles were 8.95 and 0.41, respectively. The physiological cross section area (PCSA) of each muscle model was determined based on Winters (1990)[41].

Each muscle FE model was represented as a hybrid model by combination of solid elements with passive muscle properties and bar elements with active muscle properties. The solid elements were modeled with a rubber-like material model (LS-DYNA: #181, MAT_SIMPLIFIED_RUBBER) to simulate 3D geometry of individual muscles and non-linear passive properties. This material model is based on Ogden model and users can use the model by inputting a single uniaxial non-linear stress-strain curve. Poisson's ratio is automatically set to 0.495 (Du Bois, 2003)[14]. The non-linear passive properties were given using tensile properties of muscles obtained from Yamada (1970)[42]. The bar elements were modeled with a Hill type muscle model (LS-DYNA: #156, MAT_MUSCLE) to generate muscular force according to inputted activation levels which are in range from 0 to 1. Some material properties are needed for the Hill type muscle model. A maximum contraction force per unit cross-sectional area of 5.5 kgf/cm^2 and the PCSA of each muscle were obtained from Gans (1982)[18] and Winters (1990)[41], respectively. The active force-length and active force-velocity were obtained from Thelen et al. (2003)[38]. Although the passive force-length relations are needed in the Hill type model, they were not assigned to bar elements because the solid elements have the passive properties.

This hybrid muscle FE model was applied for a single muscle such as Biceps Brachii and was used to validate the mechanical responses against fundamental characteristic features of a single muscle, that is, the force-length curve and force-velocity curve shown by Thelen et al.(2003)[38]. In addition, the hybrid muscle model was also validated against human volunteer test data and reproduced increase of muscular stiffness with increase of muscle activation level as observed in the tests. Figure 2 shows an experimental setup of the human volunteer tests. One healthy male volunteer of 33 years old with a weight of 75kg and a height of 176cm who was close to AM50 without any history of neurological or musculoskeletal disorders participated in this test. He gave his informed consent. All procedures were approved by the institutional ethics committee and conducted in accordance with the Declaration of Helsinki. The subject held his posture on supine body position and kept his elbow angle as 90 degrees with his muscular power while a load was given to his right wrist. Then, the subject pushed the circular head of the indentation machine with a diameter of 7mm

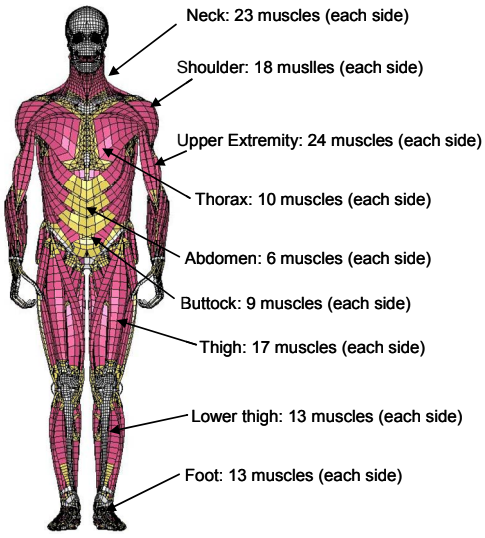

Figure 1. A human whole body FE model with muscles

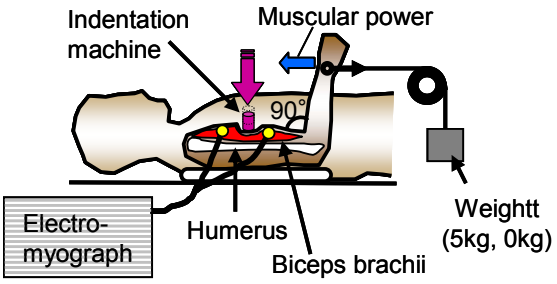

Figure 2. Experimental setup for measuring muscle stiffness and activation level

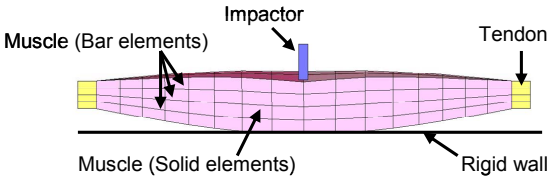

Figure 3. Simulation setup for validation of muscle stiffness.

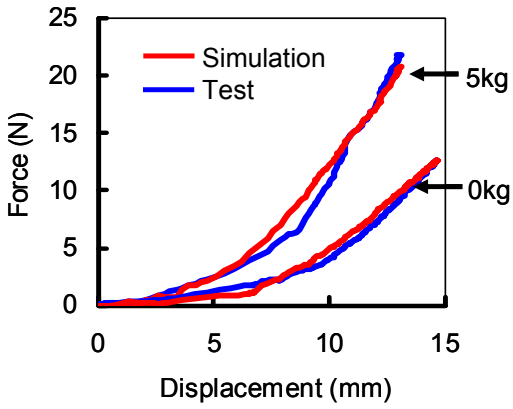

Figure 4. Comparison of muscle stiffness between experimental data and simulation results

into the most bulgy part of his biceps brachii in two cases with and without a weight of 5kg by himself. The EMG activity of the biceps brachii was measured. Figure 3 shows a simulation setup. In this simulation, the biceps brachii muscle was simplified and was pushed in the middle of the whole muscle while both ends of the muscle were fixed with a rigid wall. The rigid wall represented a bone to simulate the muscle pinched between the indentation head and the bone. Because the elbow joint angle little changed, we assumed the muscle length did not change and then we fixed tendons in both ends of the muscle. Displacement time history curves obtained from the tests with and without the weight were used for translating the head for the muscle. Muscle activation levels with and without the weight was assumed as constant values of 5% and 0.16%, respectively. These activation levels were the average values of the test data. Figure 4 shows a comparison between the model prediction and test data. The predicted force-displacement curves well agreed with test data for both cases with and without the weight. The detail descriptions of these validations are found in authors' publication (Iwamoto et al., 2009[22]).

According to anatomical text (Agur et al., 2005)[2], each muscle model was connected to the corresponding bone model through tendon models. The tendons were modeled by using shell and solid elements at both ends of muscles. Material properties of the tendons were obtained from the literature (Pioletti et al., 1998[30], Carlson et al., 1993[9]). Some sliding contacts were defined to produce the interaction between adjacent two muscles and the interaction between muscles and bones close to the muscles. The skin was modeled using shell elements with elastic material properties obtained from Yamada (1970)[42] while the fat was modeled using solid elements with the rubber-like material model. Sliding interfaces were also defined to produce interaction between the muscles and the skins.

To perform occupant injury analyses in frontal impacts, the human whole body FE model shown in Figure 1 must be changed to a sitting posture. The human model allows each joint angle of whole body to change by inputting a time history curve of activation level from 0 to 1 into each muscle. Although the model has possibility to change postures by activating each muscle, currently we do not have any enough muscle controllers for posture changes. Therefore, we determined activation level time history of each muscle based on EMG activity measured in volunteer tests. In this study, we conducted a series of volunteer tests on arm flexion from 165 to 90 degrees around right elbow joint while standing and obtained EMG activity of fourteen muscles of the right arm; the biceps brachii, brachialis, long head and medial head of triceps, extensor digitorum, flexor carpi ulnaris and so on

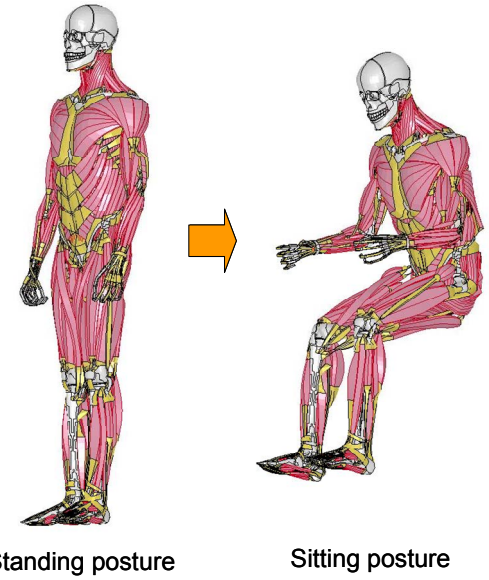

Figure 5. Posture change simulation results

(Iwamoto et al., 2009[22]). The activation curves obtained from the EMG data were used to estimate activation levels of whole body muscles for posture change from the standing posture to a sitting posture. According anatomical tests such as Agur et al.(2005)[2], we classified a role of each muscle for a unique motion, for example, flexion and extension of arm, leg, trunk, and neck as the agonists, synergists, and antagonists. Then, we hypothesized that the activation curves of agonists, synergists, and antagonists in whole body were similar to those of agonists, synergists, and antagonists in arm flexion obtained in the volunteer tests. Then, the absolute values of the activation levels were adjusted to achieve each target position for each motion. Consequently, a sitting posture was developed as shown in Figure 5. The detailed description of the posture change can be found in the authors' publication (Iwamoto et al., 2009[22]).

Model validation

The developed human whole FE model with muscles was validated against two series of cadaver tests on thoracic responses and occupant behaviors in frontal impacts. In addition, the model was also validated against foot impact cadaver tests.

Thoracic responses in frontal impacts Kent et al. (2004)[25] presented thoracic response corridors developed using fifteen post-mortem human subjects (PMHS) subjected to single and double diagonal belt, distributed, and hub loading on the anterior thorax. Subjects were positioned supine on a table and a hydraulic master-slave cylinder arrangement was used with a high speed materials testing machine to provide controlled chest deflection

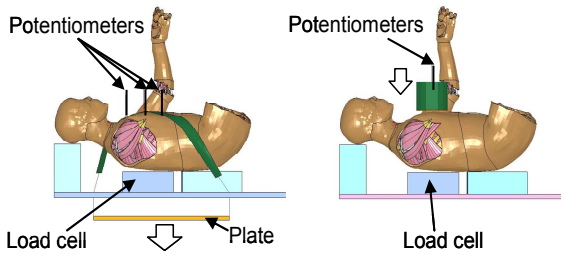

(a) Single shoulder belt (b) Hub impactor

Figure 6. Simulation setups for thoracic impact

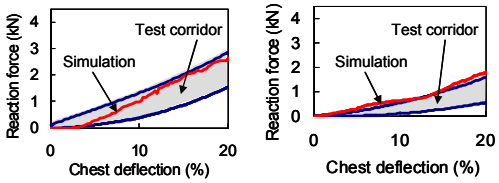

(a) Single shoulder belt (b) Hub impactor

Figure 7. Comparison of force-deflection responses between simulation results and test data

at a rate similar to that experienced by restrained PMHS in a 48-km/h sled test. Thoracic response was characterized using the deflection at the midline of the sternum and a load cell mounted between the subject and the loading table. Simulation setups using the human FE model carefully reproduced the abovementioned experimental setups. In this paper, only two simulation results with the single diagonal belt and hub loading were depicted. Figure 6 shows simulation setups for the two cases. Figure 7 shows simulation results of the posterior reaction forces and chest deflection compared with test corridors. Simulation results almost fell within test corridors in both single diagonal belt and hub loading.

Occupant behaviors in frontal impacts Vezin et al. (2001)[39] conducted a series of sled tests using four unembalmed cadavers to see head and thorax responses of occupants in frontal impact. The rigid flat seats with geometry close to that of a standard mid-size car were used in the tests. The feet of the

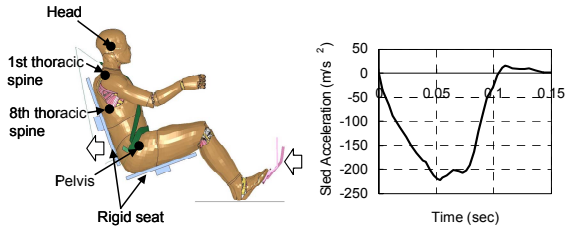

(a) Simulation model (b) Sled acceleration

Figure 8. A simulation setup for frontal impacts

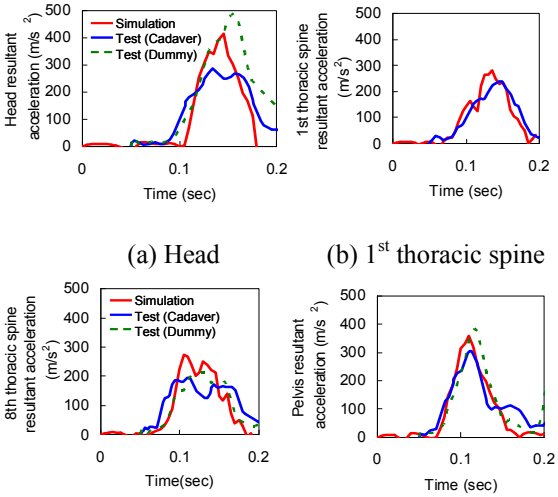

(a) Head (b) 1st thoracic spine

(c) 8th thoracic spine (d) pelvis

Figure 9. Resultant acceleration of pelvis, 1st and 8th thoracic spine, and head

cadavers were fixed on the footrest while the hands were maintained in the natural driver posture in the 10:10 o'clock position**,** with two nylon wires, which were released at the impact. The same device was used to maintain the head in a natural position just before the impact. The seat back was tilted at 20 degrees angle. The subjects were restrained by separate shoulder and static pelvis belts. The shoulder belt was equipped with a force-limiting system. Energy absorption by the retractor assembly was controlled through a torsion bar and the belt restraint was a standard production retractor system without a pre-tensioning device. The pre-tension was made manually before the crash. The nominal force limit was 4kN for the two first pairs of tests.

Simulation setups with force limit of 4kN using the human FE model carefully reproduced abovementioned experimental setups. Figure 8 shows a simulation setup for frontal impact simulations. Figure 9 shows comparison of resultant accelerations of the pelvis, 1st and 8th thoracic spine, and head between simulation results and test data. Simulation results show good agreement with test data.

Lower leg responses in frontal impacts Impact response of right lower leg was also validated against cadaveric test data with a preload simulating occupant bracing before foot impacts. Kitagawa et al. (2001)[26] conducted a series of impactor tests using four human cadaveric legs. All specimens were allowed to be sectioned above the knee at mid-femur to preserve the functional anatomy of the knee joint and leg musculature. Specimens were instrumented with an implanted tibia load cell to measure the tibial forces and moments. The specimen was mounted in a position simulating driver geometry. A rigid bar was attached to the femur and connected at the hip joint.

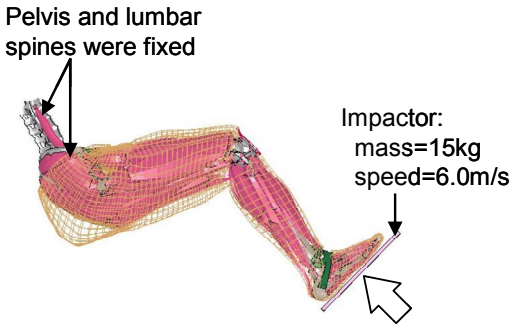

Figure 10. Simulation setup for foot impact

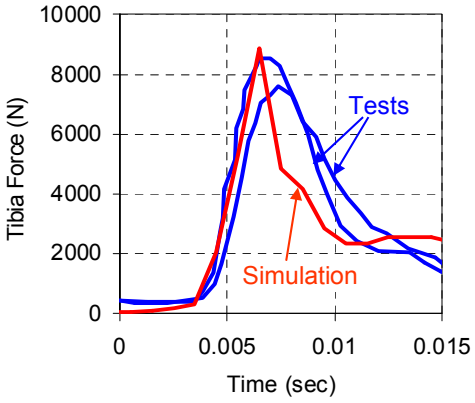

Figure 11. Comparison of tibial axial force between simulation result and test data

The femur was positioned and rotated to correct for the natural valgus angle at the knee such that the long axis of the tibia would be aligned with the direction of the impact direction when the foot was placed on the footplate. A 9.5mm thick piece of foam padding was placed between the foot and the footplate to damp out oscillation. The effect of occupant bracing was simulated externally with a harness placed over the knee which was attached to a spring via a pulley. Immediately before impact, the harness was tightened until the axial load in the specimen reached half of the specimen's body weight. Impacting energy was generated by a rigid pendulum with an effective mass of 15kg and the average impact speed of 6.0m/s (Crandall et al, 1996[13]).

Figure 10 shows a simulation setup using the human leg FE model with muscles for foot impact. A 9.5mm thick footplate including foam padding with a mass of 15kg was modeled as an impactor to reproduce abovementioned experimental setup. In this study, to represent occupant bracing, muscle models in the right lower extremity were activated by using EMG data of right lower extremity in braking motion, which were obtained from a volunteer test we conducted as shown below. The femur model was fixed in braking motion before impact while pelvis and lumbar spine were fixed. After the preload predicted at the tibia reached a preload of about 300N measured at the tibia in the test, the footplate was impacted with the initial velocity of 6.0m/s and then the femur was released to reproduce cadaver's leg responses. Figure 11 shows comparison of tibial axial force between simulation result and test data. The simulation result shows good agreement with test data.

VOLUNTEER TEST

Activity of each muscle is critical to simulate a bracing situation in pre-impact by using a developed human body FE model with muscles. Since no data of muscle activity for bracing situations were found, we developed an experimental test apparatus in our laboratory to obtain muscle activity for a selected bracing situation. In real-world accidents, drivers show various types of bracing situations. Audrey et al. (2009)[3] conducted a series of volunteer test to analyze driver behavior during critical events using a driving simulator. Eighty subjects who are aged between 22 and 30 years old have participated to the test. They found that more than 67% of subjects moved backward with right leg extended to a brake pedal and arms extended to a steering to anticipate the crash. According to their findings, we selected a bracing situation in which a volunteer subject pushes his right foot on a brake pedal and his hands on a steering with maximal voluntary force.

In this study, a volunteer test with one healthy male subject of 33 years old whose height was 176.5 cm and weight was 75 kg, similar to AM50, was conducted to obtain physiological information in a bracing situation with braking under his informed consent based on the Helsinki Declaration. All procedures were approved by the institutional ethics committee. In this test, the subject was asked to push his right foot on a brake pedal and his hands on a steering with his maximal voluntary force in the developed test apparatus fixed on the laboratory. Figure 12 shows a diagram of developed measuring system. Six data sets were obtained using the system:

(1) 3D motions of the subject
(2) 24 electromyography (EMG) from skeletal muscles of upper and lower extremities (cf. Table 1)
(3) Pressure distributions on seats
(4) Pedal force
(5) Right and left separated steering forces
(6) Reaction force on seats.

The obtained volunteer test data were analyzed and each joint angle during braking motion was calculated from measured 3D motions of the subject. Figure 13 shows time history of pedal force measured in the test. The subject's maximal braking

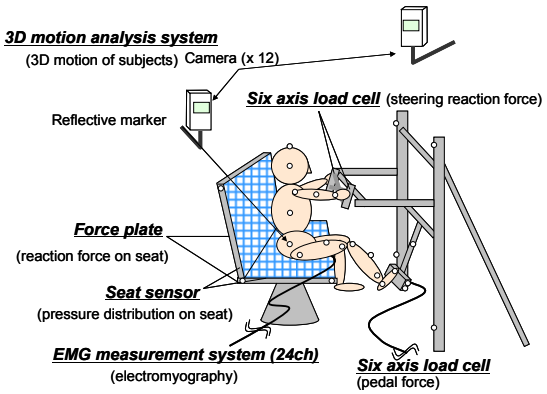

Figure 12. Diagram of developed measuring system

Table 1. Muscles measured in test

Muscles (Lower ex.)	Muscles (Upper ex.)
Soleus	Pectoralis Major
Tibialis Ant.	Deltoid Ant.
Gastrocnem Med.	Deltoid Lat.
Gastrocnem Lat.	Deltoid Post.
Vastus Med.	Infraspinatus
Vastus Lat.	Biceps Brachii
Rectus Femoris	Brachialis
Adductor Longus	Triceps Brachii
Biceps Femoris	Flexor Carpi Radialis
Semitendinosus	Flexor Carpi Ulnaris
Gluteus Maximus	Brachioradialis
	Extensor Carpi Radialis
	Extensor Carpi Ulnaris

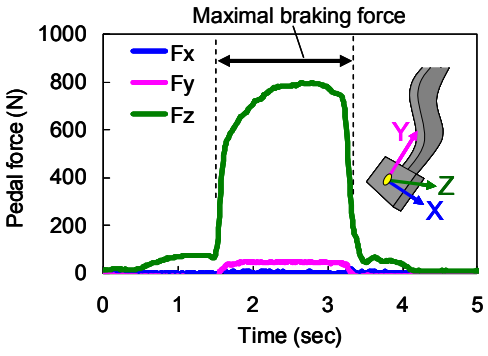

Figure 13. Measured pedal force

force was reached to 750N, which was comparable with previously reported values of 700-1000N for emergency braking situation (Audrey et al., 2009[3], Owen, C. et al., 1998[28], Palmertz C. et al., 1998[29]). Figure 14 shows activation levels of Soleus, Tibialis Anterior, Biceps Femoris (Long Head), and Rectus Femoris in right lower extremity. The activation levels were normalized by dividing EMG signal of each muscle measured in the test by

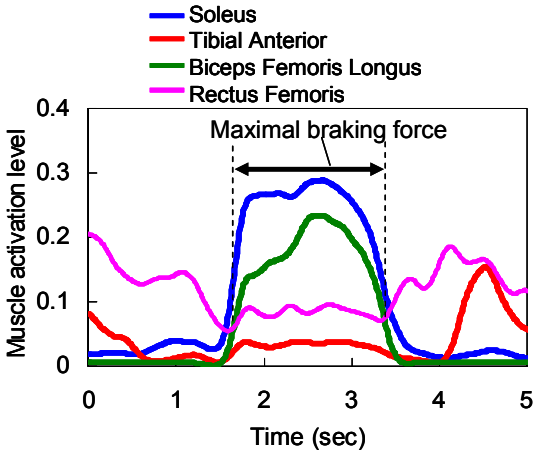

Figure 14. Measured muscle activation levels of right lower extremity

the maximal EMG signal, which was obtained from other tests on maximal voluntary force conducted using the same subject in the same day. The Soleus and Tibialis Anterior are extensor and flexor muscles of ankle joint, respectively. Biceps Femoris (Long Head) and Rectus Femoris are flexor and extensor muscles of knee joint as well as extensor and flexor muscles of hip joint, respectively. In the braking motion, activation levels of extensor muscles of ankle joint and hip joint were increased to 25-30% while those of flexor muscles of ankle joint and hip joint were less than 10%. The muscle activity suggests that right lower extremity was extended in the braking motion. Therefore, the selected braced situation was appropriately reproduced in this test.

FRONTAL IMPACT SIMULATIONS

In frontal automotive accidents, drivers made evasive maneuvers on braking and steering to reduce their vehicle speeds and avoid crashes. In such emergency cases, drivers also might brace their body with their muscle activity to prepare the upcoming impacts. In this study, a frontal crash situation was selected to find out differences of an adult male driver's behaviors and injury outcomes in post-crash between a living human body and a cadaveric human body, which have not been estimated so far. We selected a crash situation which an adult male driver made an evasive maneuver of braking with a deceleration of 0.7G for 600 ms in pre-crash and then he sustained a frontal impact with a speed of 50km/h. In pre-crash phase, he pushed his right foot on a brake pedal and his hands on a steering with his maximal voluntary force and simultaneously braced his body to reduce the impact speed and protect his body for the impact. In post-crash phase, he could not do anything for the impact, although he kept his muscle activity until 85ms after impact. We simulated this situation using

the developed human FE model with muscles as described in following sections.

In the selected crash situation, the driver made an emergency braking and reduced his vehicle speed. However, we do not have experimental volunteer test data on emergency braking using a vehicle or a simulated vehicle which should include a driver's motions, EMG data of some muscles, and reaction forces of a brake pedal, a steering, a seat cushion, a seat back and so on for reconstruction of a driver's kinematic and kinetic responses. These kinds of experimental volunteer tests are not easy to be conducted due to risks for volunteers. Therefore, this study adopted an alternative method to reconstruct the pre-crash situation. We simulated a driver's kinematic and kinetic responses in his emergency braking using a deceleration of 0.7G automatic braking obtained from the literature (Ejima et al. 2010[16]) and the volunteer test data on a bracing motion with a maximum voluntary force conducted in the laboratory static apparatus as mentioned previously.

As shown in Figure 15, in the simulation setup, the developed human FE model with muscles was set to a sitting position with rigid seats while the right foot was positioned on a brake pedal and the hands was positioned to get a grip on a steering in order to reproduce the volunteer test setup. A 3-point belt model with a force-limiter of 4kN and a pretension was also equipped with the simulation setup. The normalized EMG activity of 24 muscles measured in right lower extremity and right upper extremity was

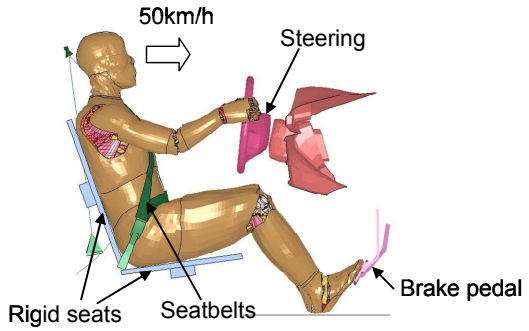

Figure 15. Simulation setup of frontal impacts

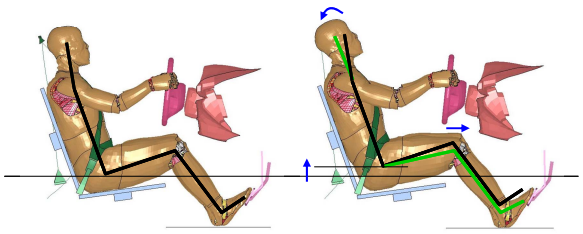

(a) 200ms (b) 800ms

Figure 16. Comparison of occupant postures before a braking motion and before an impact

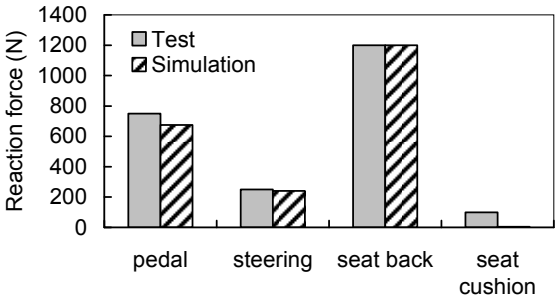

Figure 17. Comparison of reaction forces between simulation results and volunteer test data

directly inputted to the corresponding muscle model. Muscle activity of other muscles in the right lower extremity and the upper extremities which were not measured in the test was estimated to reproduce forces on a brake pedal and a steering, respectively. The method to estimate the activation levels of muscles is almost the same as described above. Since muscle activity of the left lower extremity was not measured in the test, we assumed the muscle activity as similar to that in the right lower extremity. In addition, muscle activity of the trunk and neck was also not measured in the test. Therefore, we assumed activation levels of most muscles in the neck and trunk as 10-20% because activity of some muscles such as Sternocleidomastoid in the neck and Rectus Abdominis in the trunk presented 10-20% in other experimental volunteer tests conducted in our laboratory. Activation levels of Longus Colli, Scalenus Anterior, and Sternohyoid associated with neck flexion were assumed as 50% to reproduce the volunteer's neck motion.

In the simulation, only an acceleration of gravity was given to have the human FE model sit on the seat from an onset of the simulation until 200ms and after 200ms a deceleration of 0.7G was inputted to a sled model including the rigid seats, the brake pedal, the steering, the seatbelt, and the floor for a period of 600ms. After 800ms, an acceleration of 50km/h shown in Figure 8 was applied to the sled model in order to reproduce a frontal impact situation. The activity of each muscle was given to the muscle model at 100ms after the onset of the simulation and was assumed to be kept as a constant value until the end of simulation after the pedal force reached the maximum. This is because we do not have EMG data of volunteers during brake deceleration and frontal impact sled deceleration.

Figure 16 shows a comparison of the driver's postures at 200ms before the braking motion and at 800ms before the impact. Comparing with the posture before the braking motion, the hip displaced upward and the right leg displaced forward and downward while the head rotated rearward in the

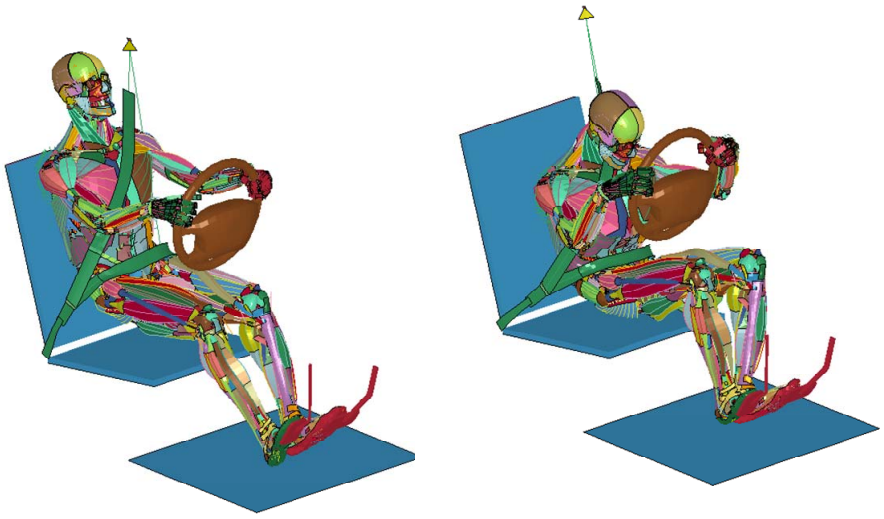

(a) before impact (b) 85ms after impact

Figure 18. Occupant motions predicted by active human model (50km/h)

posture before the impact. This predicted braking motion was similar to that observed in the volunteer test. Figure 17 shows a comparison of reaction forces between simulation results and volunteer test data. Predicted forces of the pedal, the steering, and the seat back showed good agreement with test data. Predicted force of the seat cushion was zero while the force was 100N in the test. This inconsistency is because the hip was completely apart from the seat cushion in braking motion of the simulation.

In this study, we are interested in the difference of a driver's behaviors and injury outcomes between a living human body with muscle activity and a cadaveric human body without muscle activity. We are also interested in the rate dependency of muscular effects for the driver's behaviors and injury outcomes. Therefore, four parametric simulations on frontal impact situations were performed to find out the difference and the rate dependency. Case 1 represents a crash situation for an active human body with an impact speed of 50km/h. Case 2 represents that for a cadaveric human body with the same speed of 50km/h. Case 3 represents that for an active human body with an impact speed of 25km/h. Case 4 represents that for a cadaveric human body with the same speed of 25km/h. For the cadaveric human body, all muscles were assumed not to be activated. However, when the muscle model was given as zero of activation level, the model caused instability. Therefore, less than 1% of activation levels were inputted to the muscles of the cadaveric human body model. An acceleration time history for impact speed of 25km/h was determined using that of 50km/h. Figure 18 shows occupant motions predicted by the active human model with 50km/h. The skin models were removed to show muscle models clearly. From Figure 18, the active human model braced his body to push his arms on a steering and right foot on the brake pedal before impact. After impact, the active human model continued to brace his body and kept his head from approaching the steering. Figure 19 shows the driver's postures at 85ms after impact for the four cases. The posture of the active human body

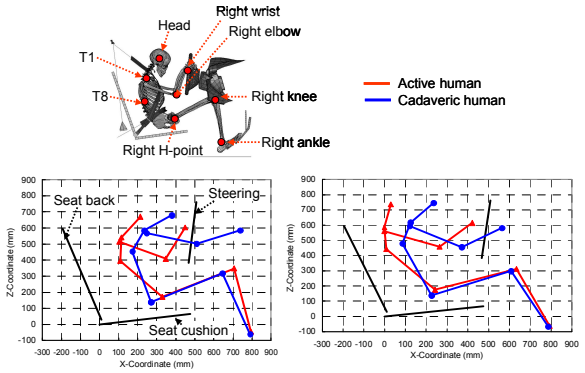

(a) 50km/h (b) 25km/h

Figure 19. Occupant postures at 85ms after impact

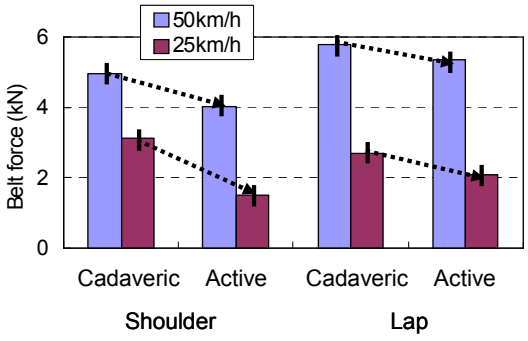

Figure 20. Comparison of maximum forces at shoulder and lap belts

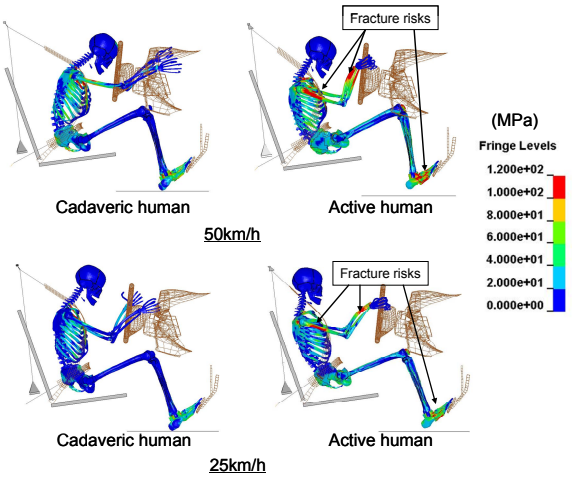

Figure 21. Comparison of stress distribution at 85ms after impact

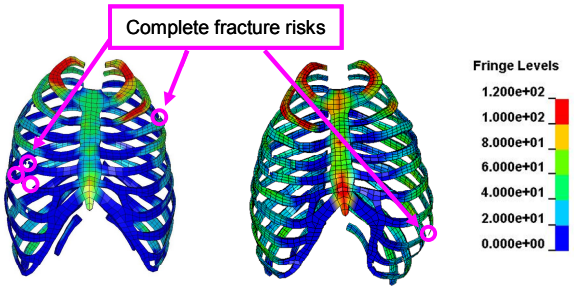

(a) Cadaveric human (b) Active human

Figure 22. Comparison of rib fractures between cadaveric human body and active human body

was different from that of the cadaveric human body in both 50km/h and 25km/h. In comparison with the cadaveric human body, the knee and hip went forward while the upper body including upper extremities went backward in the active human body. In addition, difference of the driver's postures between the active human body and the cadaveric human body in lower speed of 25km/h was larger than that in higher speed of 50km/h. Figure 20 shows comparison of maximum forces at a shoulder belt and a lap belt for four cases. In both the shoulder and lap belts, maximum belt forces of the cadaveric human body were larger than those of the active human body at 50km/h. The similar trend was found at 25km/h. Figure 21 compares Von Mises stress distribution of skeletal parts at 85ms after impact for four cases. The active human body sustained more fracture risks at upper and lower extremities than the cadaveric human body. Figure 22 shows comparison of Von Mises stress distribution in the ribcage between the cadaveric human body and the active human body. The figure includes locations of complete fractures. The simulation result of cadaveric human body was obtained from the validation results using frontal sled cadaver test data with an impact speed of 50km/h conducted by Vezin et al. (2001)[39] as shown previously. The simulation result of the active human body was obtained from the simulation results of frontal impact simulation for the active human body with 50km/h. The comparison shows that the cadaveric human body sustained more rib fractures than the active human body.

DISCUSSION

It is one of challenging issues to predict a driver's injuries and activate his muscles simultaneously during pre-impact and post-impact using human FE models. However, it is critical to understand how drivers sustain injuries in real-world accidents. In past decade, a lot of human body FE models have been developed and validated against existing cadaver test data (Iwamoto et al., 2002[21], Vezin et al., 2005[40], Ruan et al., 2005[31] etc.). However, these models could not be used to analyze muscular effects in pre-impacts for injury outcomes in post-impacts due to lack of active muscles in these models. On the other hand, some human multi-body models with active muscles have been developed (SIMM[34], AnyBody[4], etc.) and used for predicting muscular force and fatigue in human motions such as exercise, driving, ingress, and sports. In most of these models, skeletal parts, anatomical joints, and muscles were simplified to rigid bodies, mechanical joints, and line segments, respectively. Therefore, these models could not be used to analyze occupant injury risks in post-impacts. Some researchers tried to combine both benefits and analyze muscular effects in pre-impacts and post-impacts (Chang et al., 2008[11], Sugiyama et al., 2007[36]). They incorporated muscles modeled by bar elements into an existing human FE model and predict bone fracture risks with muscle activity. However, the muscle model represented by bar elements has less accuracy for injury analyses because of the following three reasons. Firstly, the model cannot represent exact interactions of muscle-to-muscle, muscle-to-bone, muscle-to-skin. Secondly, the model cannot represent stiffness changes in the transverse plain to a muscular action line according to activation levels. Finally, unrealistic stress concentrations could occur because the muscle bar elements have to be connected with rigid elements defined in skeletal parts. On the contrary, each muscle model developed in this study was represented as a hybrid model of solid elements with muscular 3D geometry and bar elements with active muscular properties. Therefore, the muscle model has more accuracy for injury analyses.

This study selected the most typical bracing situation among volunteer tests using eighty subjects and a driving simulator performed by Andrey et al. (2009)[3] to investigate bracing effects in pre-impacts. A male volunteer subject pushed his

right foot on a brake pedal and his hands on a steering with maximal voluntary force in static laboratory apparatus to reconstruct the bracing situation. Then, muscle activity in the upper and lower extremity was measured and inputted to muscles of the developed human model to simulate the bracing situation. However, the muscle activity measured in the test is that for a bracing situation in a static condition and might be different from that for a bracing situation in a dynamic condition such as deceleration of braking or impact. Recently, some volunteer tests have been conducted under deceleration of braking or impact (Ejima et al., 2009[15], Beeman et al., 2010[5]) and EMG data were measured in the tests. Unfortunately, they did not make clear the difference of muscle activity between a dynamic situation and a static situation. Postural control could change the muscle activity under the deceleration and a driver's mental state could affect the muscle activity in cases of panic braking. However, this study focused on investigating the difference of a driver's behaviors and injury outcomes between a living human body with muscle activity and a cadaveric human body without muscle activity. Although further studies are needed to investigate effects of a driver's postural control and mental state on muscle activity of whole body, the muscle activity used in this study is good enough to investigate the difference between a living human body and a cadavaric human body.

The simulation results using the developed human body FE model with muscles demonstrated that an active human body kept the position of the upper body backward and also kept the position of the lower extremities forward for the braking deceleration comparing with a cadaveric human body as shown in Figure 19. These occupant behaviors are similar to those observed in comparison between tensed volunteers and relaxed volunteers conducted under a braking deceleration of 0.7G (Ejima et al.,2010[16]). From the difference on occupant behaviors, forces of the shoulder and lap belts in the active human body were a little bit smaller than those in the cadaveric human body, although shoulder belt force of the active human body was much smaller than that of the cadaveric human body at the lower speed of 25km/h (Figure 20). Therefore, the active human body had less rib fracture risks than the cadaveric human body at 25km/h. Since muscular forces in upper and lower extremities of the active human body increased and the lower extremities had more forward positions, the active human body had more bone fracture risks in the upper and lower extremities comparing with the cadaveric human body (Figure 21). The difference of injury outcomes between the active human body and the cadaveric human body appeared more remarkably at the lower speed of 25km/h.

Kallieris et al. (1995)[23] compared 29 sled tests with belted cadavers and 24 accident cases with 24 belted drivers and 6 belted front passengers at the configuration of the frontal collision with impact speeds of about 50km/h. They found fractures of the radius in the upper extremities as result of reinforcement against the steering wheel during the collision phase in the accident cases while no injuries were observed in the cadaver tests. They also found some leg injuries including fractures at the femur, tibia, fibula, foot, and ankle joint while no injuries were observed in the cadaver tests. Additionally they reported that the cadaver tests showed a rib fracture frequency twice as high as for the accident cases. Since the cadaver tests conducted by Kallieris et al.[23] did not include braking deceleration, injury outcomes in the cadaver sled tests might correspond to those for cadaveric human body simulated in the validation using cadaver test data conducted by Vezin et al. (2001)[39]. On the other hand, injury outcomes in accident cases might correspond to those for active human body with a braking deceleration of 0.7G and an impact speed of 50km/h. In the simulations, the active human body had more fracture risks in the upper and lower extremities while the cadaveric human body had no fracture risks. In addition, the active human body had less fracture risks in the ribcages than the cadaveric human body as shown in Figure 22. Injury outcomes predicted by the developed human body FE model with muscles show good agreement with those reported by Kallieris et al.[23]. Therefore, the model is a useful tool to investigate the bracing effects in pre-impacts of real-world accidents on injury outcomes.

A lot of researchers have investigated traffic accident data and have tried to find injury patterns and the mechanisms. Some injury mechanisms are still unknown. However, if we consider muscular effects of occupants in pre-impacts and post-impacts, we might be able to elucidate such injury mechanisms. Carroll et al. (2010)[10] reported that occupants seated in the front passenger seat tended to sustain more torso injuries compared with the driver's seat. This mechanism can be explained from the simulation results (see Figure 22). Different from a driver, an occupant seated in the front passenger seat does not push his foot on a pedal and his hands on a steering. If an occupant in the front passenger and a driver are regarded as the cadaveric human body and an active human body with respect to the impact responses, respectively, the occupant is likely to sustain more rib fracture risks than the driver. Rudd (2009)[32] reported that the majority of the foot and ankle injuries occur at lower crash severities with delta-V of less than 30km/h. This mechanism can be also explained from the simulation result that the bone fracture risks in the lower extremities were predicted even in 25km/h for the active human body

(see Figure 21). In addition, as Kent et al. (2003)[24] reported, elderly occupants sustain more thoracic injuries in frontal impacts due to weakness of their skeletal parts. Different from younger occupants, elderly occupants have less muscular power and less muscle activity, besides of the weakness of bone properties. If an elderly occupant and a younger occupant are regarded as the cadaveric human body and the active human body with respect to the impact responses, the elderly occupant could sustain more rib fracture risks than the younger occupant (see Figure 22). Therefore, the active human body FE model has potential for better understanding of unclear injury mechanisms of occupants in automotive crashes.

LIMITATIONS

This study has the following limitations.

- Validation of muscle stiffness was performed for only Biceps Brachii because the volunteer test data were not obtained for other muscles such as Rectus femoris in the leg. Although the hybrid model has possibility to reproduce muscular stiffness change, more data are needed for complete validation of muscle stiffness.
- EMG data of trunk and neck muscles were not measured in the bracing situation of this study because it was not so easy to measure EMG activity of muscles in trunk and neck regions. Therefore, we estimate the activity to reproduce measured reaction forces. Further studies are needed to measure activity of trunk and neck muscles and activity of inner muscles.
- Data of muscle activity under dynamic situations such as brake deceleration and sled deceleration were not obtained in this study. Further study is needed to obtain muscle activity from volunteer test data conducted under such dynamics situations.
- This study selected a bracing situation. However, in real-world accidents, there are some bracing situations including panic condition. Therefore, more investigation is needed for understanding of drivers' behaviors in pre-impacts.
- Muscle activity used in this study was estimated based on EMG data from a volunteer test. Therefore, the activity did not include effect of muscular reflex and posture stabilization. Further study on muscle controller based on neural science is necessary.
- No airbags were included in the frontal impact simulations performed in this study. This indicates that injury outcomes predicted in this study cannot be applied for current commercial vehicles.

CONCLUSIONS

An active human body FE model with 3D geometry of muscles was developed to investigate muscular effects in pre-impact for injury outcomes. The muscle was modeled as a hybrid model of solid elements with passive properties and bar elements with active properties. The muscle model reproduced muscular stiffness change according to muscle activation levels. The developed human body FE model, which had originally a standing posture, was changed to a driver's sitting posture by activating each muscle of whole body. The model was validated against cadaver test data on frontal impacts for the thorax using a 3-point seatbelt and hub impactor. Force-displacement responses predicted by the model fell within test corridors. The model was also validated against cadaver test data on frontal sled impacts using occupants equipped with seatbelts. Acceleration of the head, thoracic spines, and pelvis predicted by the model showed good agreement with those obtained from test data. In addition, the model was used for foot impact simulations with a preload representing braking effect and was compared with cadaver test data obtained from the literature.

This study investigated the bracing effects in pre-impacts for injury outcomes in frontal impacts by frontal impact simulations with pre and post impacts using the developed human body model. A volunteer test was conducted to reproduce a bracing condition, which could occur in real-world accidents, using static laboratory apparatus with rigid seats, a steering, and a brake pedal. Muscle activity obtained from the test was inputted to the muscle models. The model reproduced the bracing condition because predicted reaction forces of the pedal, steering, and seat back agreed well with those of test data. Comparisons between an active human model and a cadaveric human model indicate that muscle activity with the bracing condition could constrain upper body for frontal impacts and cause more bone fracture risks in upper and lower extremities. From frontal impact simulations performed at the impact speed of 50km/h, the cadaveric human model could sustain more rib fracture risks than the active human model. These findings correspond to conclusions from comparison of injury outcomes between real-world accident data and cadaver test data with the same speed of 50km/h. Therefore, the model has possibility to make the detailed investigation of muscular effects in pre-impact for injury outcomes. Although further studies are needed to model the muscular reflex and posture stability control as well as to obtain muscle activity under dynamic situations of brake deceleration and sled deceleration, the active human body FE model would be a useful tool for better understanding of unexplained injury mechanisms in real-world automotive accidents.

REFERENCES

[1] Accident Analysis Report (JAPAN) Institute for Traffic Accident Research and Data Analysis (ITARDA) 2007.

[2] Agur, A.M.R., Dalley II, A.F., 2005. Grant's Atlas of Anatomy; 11th Edition, Lippincott Williams & Wilkins, Baltimore, Maryland.

[3] Andrey, H.-D., Frederic, R., Pascal, D., Herve, M., 2009. "Pre-Crash Phase Analysis using a Driving Simulator. Influence of Atypical Position on Injuries and Airbag Adaptation" 21th ESV Conference, No.09-0534.

[4] AnyBody, http://www.anybodytech.com

[5] Beeman, S., Kemper, A., Madigan, M., Duma, S. 2010. "Effects of Muscle Activation on Occupant Kinematics in Frontal Impacts" 6th Annual Injury Biomechanics Symposium.

[6] Begeman, P., King, A.I., Levine, R., Viano, D.C. 1980. "Biodynamic Response of the Musculoskeletal System to Impact Acceleration" Stapp Car Crash Conference, No.801312, 479-509.

[7] Behr, M., Arnoux, P-J., Serre, T., Thollon, L., Brunet, C. 2006. "Tonic Finite Element Model of the Lower Limb" Journal of Biomechanical Engineering, Vol. 128, 223-228.

[8] Brumbelow, M. L., Zuby, D.S. 2009. "Impact and Injury Patterns in Frontal Crashes of Vehicles with Good Ratings for Frontal Crash Protection", 21st ESV Conference, No.09-0257.

[9] Carlson, G.D., Botte, K.J., Josephs, M.S., Newton, P.O., Davis, J.L.W., Woo, S.L-Y. 1993. "Morphologic and biomechanical comparison of tendons used as free grafts", Journal of hand surgery, Vol.18A, No.1, 76-82.

[10] Carroll, J., Adolph, T., Chauvel, C. Labrousse, M., Trosseille, X., Pastor, C., Eggers, A., Smith, S., Hynd, D. 2010. "Overview of Serious Thorax Injuries in European Frontal Car Crash Accidents and Implications for Crash Test Dummy Development" IRCOBI Conference, 217-234.

[11] Chang, C-Y., Rupp, J., Kikuchi, N., Schneider, L. 2008. "Development of a Finite Element Model to Study the Effects of Muscle Forces on Knee-Thigh-Hip Injuries in Frontal Crashes", Stapp Car Crash Journal, Vol. 52, 475-504.

[12] Choi, H.Y., Sah, S.J., Lee, B., Cho, H.S., Kang, S.J., Mun, M.S., Lee, I., Lee, J. 2005. "Experimental and numerical studies of muscular activations of bracing occupant" 19th ESV Conference, Paper No.05-0139-O.

[13] Crandall, J., Portier, L., Petit, P., Hall, G., Bass, C., Klopp, G., Hurwitz, S., Pilkey, W., Trosseille, X., Tarriere, C. 1996. "Lassau, J.; Biomechanical Response and Physical Properties of the Leg, Foot, and Ankle" 40th Stapp Car Crash Conference, No.962424, 173-192.

[14] Du Bois, P.A..2003. "A simplified approach to the simulation of rubber-like materials under dynamic loading" Proc. 4th European LS-DYNA Users Conference, D-1, 31-45.

[15] Ejima, S., Zama, Y., Ono, K., Kaneoka, K., Shiina, I., Asada, H. 2009. "Prediction of Pre-Impact Occupant Kinematic Behavior Based on the Muscle Activity during Frontal Collision" 21st ESV Conference, No.09-0913.

[16] Ejima, S., Zama, Y., Ito, D., Ono, K., Kamiji, K., Yasuki, T. 2010. "Effect on posture maintenance with muscle activity during pre-impact braking" JSAE spring annual meeting, No. 20105212 (in Japanese).

[17] Funk, J.R., Crandall, J.R., Tourret, L.J., MacMahon, C.B., Bass, C.R., Khaewpong, N.K., Rppinger, R.H. 2001. "The effect of active muscle tension on the axial injury tolerance of the human foot/ankle compex" 21st ESV Conference, Paper No. 237, 1-14.

[18] Gans, C. 1982. "Fiber architecture and muscle function" Exercise and Sports Sciences Reviws, 10, 106-107.

[19] Hedenstierna, S., Halldin, P., Brolin, K. 2007. "Development and Evaluation of a Continuum Neck Muscle Model", 6th European LS-DYNA User's Conference, Session 2, 80-99.

[20] Hedenstierna, S., Halldin, P., Brolin, K. 2008. "Evaluation of a combination of continuum and truss finite elements in a model of passive and active muscle tissue", Computer Methods in Biomechanics and Biomedical Engineering, Vol. 11, No.6, Dec., 627-639.

[21] Iwamoto, M., Kisanuki, Y., Watanabe, I., Furusu, K., Miki, K., Hasegawa, J. 2002. "Development of a Finite Element Model of the Total Human Model for Safety (THUMS) and Application to Injury Reconstruction" IRCOBI Conference, 31-42.

[22] Iwamoto, M., Nakahira, Y., Kimpara, H.

Sugiyama, T. 2009."Development of a Human FE Model with 3-D Geometry of Muscles and Lateral Impact Analysis for the Arm with Muscle Activity", SAE paper, No. 2009-01-2266.

[23] Kallieris, D., Otte, D., Mattern, R., Wiedmann, P. 1995 "Comparison of Sled Tests with Real Traffic Accidents" 39th Stapp Car Crash Conference, No.952707, 51-58.

[24] Kent, R., Patrie, J., Poteau, F., Matsuoka, F., Mullen, C. 2003. "Development of an Age-dependent Thoracic Injury Criterion for Frontal Impact Restraint Loading" 18th ESV Conference, No.72.

[25] Kent, R., Lessley, D., Sherwood, C. 2004. "Thoracic Response to Dynamic, Non-Impact Loading from a Hub, Distributed Belt, Diagonal Belt, Double Diagonal Belts" Stapp Car Crash Journal, Vol.48, 495-519.

[26] Kitagawa, Y., Pal, C. 2001. "Development and Evaluation of a Human Lower Extremity Model" 17th ESV Conference, No. 282.

[27] Levine, R.S., Patrick, L.M., Begeman, P.C., King, A.I. 1978. "Effect of quadriceps function on submarining" Proc. of the 22th Conference of Association for the Advancement of Automotive Medicine (AAAM), 319-329.

[28] Owen, C., Roberts, A., Manning, P., Lowne, R. 1998. "Positioning and bracing of the lower leg during emergency braking – A volunteer study" IRCOBI Conference, 147-159.

[29] Palmertz C., Jakobsson, L., Karlsson A.-S. 1998. "Pedal Use and Foot Positioning during Emergency Braking" IRCOBI Conference, 135-146.

[30] Pioletti, D.P., Rakotomanana, L.R., Benvenuti, J.-F., Leyvraz, P.-F. 1998. "Viscoelastic constitutive law in large deformations: application to human knee ligaments and tendon", Journal of Biomechanics, Vol.31, 753-757.

[31] Ruan, J.S., El-Jawahri, R., Barbat, S., Prasad, P. 2005."Biomechanical Analysis of Human Abdominal Impact Responses and Injuries through Finite Element Simulations of a Full Human Body Model" Stapp Car Crash Journal, Vol.49, 343-366.

[32] Rudd, R.W. 2009. "Updated Analysis of Lower Extremity Injury Risk in Frontal Crashes in the United Sates" 21st ESV Conference, No.09-0556.

[33] Shigeta, K., Kitagawa, Y. Yasuki, T. 2009. " Development of Next Generation Human Body FE Model Capable of Organ Injury Prediction" 21st ESV Conference, Paper No. 09-0111-O.

[34] SIMM, http://www.musculographics.com /products/simm.html

[35] Simamura, M., Ohhashi, H., Yamazaki, M. 2003. "The Effects of Occupant Age on Patterns of Rib Fractures to Belt-Restrained Drivers and Front Passengers in Frontal Crashes in Japan" Stapp Car Crash Journal, Vol.47, 349-365.

[36] Sugiyama, T. Kimpara, H., Iwamoto, M., Yamada, D., Nakahira, Y., Hada, M. 2007. "Effects of muscle tense on impact responses of lower extremity" IRCOBI Conference, 127-140.

[37] Tennyson, S.A., King, A.I. 1976. "A Biodynamic Model of the Human Spinal Column" SAE Paper No. 760771.

[38] Thelen, D. G. 2003. "Adjustment of Muscle Mechanics Model Parameters to Simulate Dynamic Contractions in Older Adults" Transaction of the ASME, Vol.125.

[39] Vezin, P., Bruyère, K., Bermond, F. 2001. "Comparison of Head and Thorax Cadaver and Hybrid III Responses to a Frontal Sled Deceleration for the Validation of a Car Occupant Mathematical Model" 17th ESV Conference, No.114.

[40] Vezin, P., Verriest, J.P. 2005."Development of a Set of Numerical Human Models for Safety" 19th ESV Conference, Paper No. 05-0163.

[41] Winters, J.M. 1990. "Hill-Based Muscle Models" A System Engineering Perspective; Multiple Muscle Systems: Biomechanics and Movement Organization, Winters, J.M. and Woo. S. (eds.), New York, Springer, 69-93 and 726-749.

[42] Yamada, H. 1970. Strength of Biological Materials; Williams & Wilkins Company.

IMPLEMENTATION OF REACTIVE HUMAN BEHAVIOR IN A NUMERICAL HUMAN BODY MODEL USING CONTROLLED BEAM ELEMENTS AS MUSCLE ELEMENT SUBSTITUTES

Adrian Prüggler
Philipp Huber
Andreas Rieser
Kurt Steiner
Virtual Vehicle Research and Test Center
Austria
Stefan Kirschbichler
Graz University of Technology, Vehicle Safety Institute
Austria
Arno Eichberger
Graz University of Technology, Institute of Automotive Engineering
Austria

ABSTRACT

The reduction of road casualties and injury risk is a major goal of automotive engineering. Manufacturers are confronted with increasing safety regulations, stricter exhaust gas pollution regulations and strong competition. Hence, cost efficiency is a significant concern of automotive industry. Furthermore the development of innovative safety systems such as adaptive restraints and collision avoidance systems calls for new methods for system design and evaluation beyond laboratory crash tests.

Cost efficiency is achieved with numerical simulations using Multibody System (MBS) or Finite Element Method (FEM) techniques partly substituting full vehicle testing. Focus has been on simulations of the crash phase but innovative safety systems call for consideration of the low g pre-crash phase. Therefore the use of crash test dummies and their numerical representations which are designed for higher loading, is not satisfying. The use of numerical human body models is a promising approach to further improve bio-fidelity. Nevertheless, for pre-crash simulations the influence of muscle activity on the passenger kinematics induced by the vehicle motion is no longer negligible for real life safety.

Hence the OM4IS ("Occupant Model for Integrated Safety") project was initiated by a large consortium including scientific partners (Virtual Vehicle Research and Test Center, Graz University of Technology, Bundesanstalt für Straßenwesen-BASt) and industry partners (Partnership for Dummy Technology and Biomechanis, Robert Bosch GmbH, Toyoda Gosei Europe, TRW Automotive, DYNAmore GmbH). The challenge is to identify human movement and behavior patterns (position and muscle activity) during pre-crash phase and implement these patterns into a suitable human body model. The present paper describes first results to implement muscle activity into a simplified version of the numerical model **T**otal **HU**man **M**odel for **S**afety (**THUMS**) developed by Toyota Motor Corporation and Toyota Central R&D Labs. This model represents a 50th percentile American Male (AM50) and is implemented into the explicit finite element software LS-Dyna.

As a starting point, the reactive behavior of humans in two distinct load cases, an emergency braking maneuver and a single lane change are investigated. Movement and behavior patterns as well as muscle activity are analyzed by volunteer tests on sled and full vehicle level. An infrared based 3D motion capturing system and an electromyography measurement (EMG) system are used. Methodology and results of this behavior pattern analysis is presented in a separate paper.

A simplified FE model that qualitatively reproduces human motion patterns in the selected load cases is developed. The first version of the model features a simplification of the THUMS model replacing the deformable parts by rigid body parts and using kinematic joints. Major muscle groups are implemented as beam elements which can be controlled using coupling of LS-Dyna software and Matlab/Simulink. The model should be able to reproduce volunteers' movements for two load cases (acceleration in frontal and lateral direction) and in the second modeling step identified human movement and behavior pattern should be implemented qualitatively which is presented in a separate publication.

At this stage computing time efficiency, numerical stability and implementation in the automotive development process were not of first priority. Furthermore the study concentrates on occupants' acceleration induced reactions and not on active movements.

INTRODUCTION

Basically, there are two methods of modelling the real system, namely Multi Body (MBS) and Finite Element Method (FEM). MBS represents the real system via rigid segments, the so-called bodies. These bodies are connected via kinematic joints with a defined number of degrees of freedom (DOF). Centre of gravity, inertial properties and a local coordinate system are assigned to each of the segments. Professional simulation software automatically generates the equations of motion for the system. Using the boundary conditions and a numerical solution approach the equations of motion are solved [1]. For contact definitions between the bodies, simple, non-deformable geometric elements are dedicated to the bodies. Due to the simplicity of this approach the computing power needed is low and it can be used for parameter variations.

The basic principle of FEM is to divide a continuous body into discrete small elements with simple geometry. The adjacent elements are connected on the nodes of the element. The system of nodes and elements is called a mesh. Properties are assigned to the nodes. The solid mechanics problem of the body is solved by using approximating functions. To relate deformations to internal forces a constitutive material law is used (e.g. [2], [3]). Therefore the FEM approach offers the chance to investigate the displacements and stresses in a structure. Due to discretization and the complexity of solving the differential equations of the system, the needed computing power is considerably higher than a comparable system using the MB modelling technique. For simulations of the pre-crash phase the deformations of vehicle structure and the deformations of the occupant are not the primarily concern. Hence the use of FE models for pre-crash applications is not very widespread. Especially for the crash phase, FE simulations have become an important development tool. Two main aims are defined in the OM4IS project: The characterization of reactive behavior in low load pre-crash phase and the implementation of reactive behavior into numeric human body models. In the last decades passive and active safety of automobiles have been developed more or less separately, nowadays as the consideration of the pre-crash phase gains importance the simulation of this phase also becomes relevant. Using a MBS model for the pre crash phase and a FE model for the crash phase causes costs and the transfer of model kinematics from pre crash to crash phase simulation is difficult. Using an "integrated" FE model for pre crash and crash phase would decrease cost and may simplify the transfer of kinematic results from pre crash to crash phase. Hence the basis for the OM4IS is a FE human body model, namely the **T**otal **HU**man **M**odel for **S**afety (**THUMS**) developed by Toyota Motor Corporation and Toyota Central R&D Labs. As a starting point for identifying human behavior and movement patterns, the OM4IS consortium has agreed on two maneuvers. The first one is an emergency braking maneuver and the second one is a single lane change maneuver. For both maneuvers the acceleration level in longitudinal as well as in transversal direction vehicle is in the range of 1g.

METHODS

Testing

Sled tests were carried out at the Vehicle Safety Institute of Graz University of Technology. All in all eleven males which were close to the 50th percentile male have been tested. For all tests, a reference seat mounted on a sled has been used. This seat has been a serial production seat with removed cushions which were replaced by wooden plates mounted on seat and back rest. These wooden plates have been covered with leather to increase friction between the volunteer and the seat. The modifications have been done in order to eliminate the influence of the deformable seat cushion and therefore simplify the boundary conditions for the numerical simulation. Due to the fact that the sled acceleration can only be controlled in a single direction and the aim of the investigations was to simulate a braking and an evasive maneuver, the seat has been either mounted backwards to simulate the braking maneuver, or for evasive lateral maneuver, the seat has been mounted perpendicular to the acceleration direction. Figure 1 shows a principle setup of the sled tests for simulation of the braking maneuver.

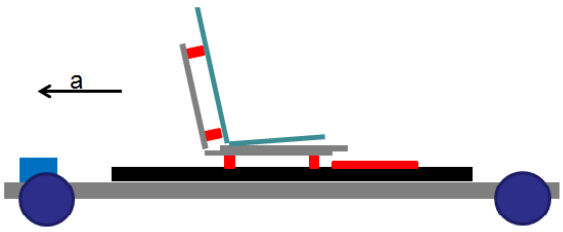

Figure 1. Principle sled test setup. Symbol a is the sled acceleration during the test.

For further information concerning the test set up and the results refer to [4].

Simulation

Muscles The human body consists of more than 300 muscles. For detailed simulation of human kinematics and to gain insight into the resulting stresses in the human body it is necessary to implement the muscles in a realistic manner. There are basically two approaches- the biophysical cross-bridge model of Huxley [5] and the phenomenological Hill model [6]. The Huxley model is based on the attachment and detachment of action and myosin filaments. The model describes the muscle activity on a microscopic level and takes the chemical and physical processes within the sarcomere into consideration [5]. The Hill model describes the muscle as a combination of springs and non linear contractile elements. Due to the fact that the Huxley model describes the muscle activity on microscopic level, this model is more complex than the Hill model. Hence the Hill model is usually the preferred approach for muscle modeling. In the present project another approach was chosen. The first focus of the OM4IS project is on the identification of human behavior patterns and its implementation into a numeric human body model. The accuracy of resulting stresses is in this phase of lower priority. An application of Hill model is therefore not essential. The approach described below simplifies also the fulfillment of another project requirement: it should be applicable to other human body models.

Controller and Co-simulation A promising approach which fulfills the project's requirements is the use of a coupling between Matlab/ Simulink and the explicit FE solver LS-DYNA. The concept is shown in Figure 2. As it can be seen there are two blocks. The first one is the explicit FEM solver block named "LS-DYNA" and the second one is the "Matlab, Excel" block. The two blocks communicate via an interface. . LS-DYNA provides the translational and rotational values of predefined nodes for the Matlab, Excel block. On basis of this values and the chosen controller concept the controller software (Matlab, Excel…) calculates force values and sends them back to LS-DYNA. Those force values are applied on predefined bar elements in axial direction. The time increment for data exchange can be determined by the user. It depends on the time step as used in the FE calculation. Theoretically, the information could be exchanged after each FE time step. In order to increase the speed of calculation the exchange interval can be increased. The exchange parameters are then frozen [7].

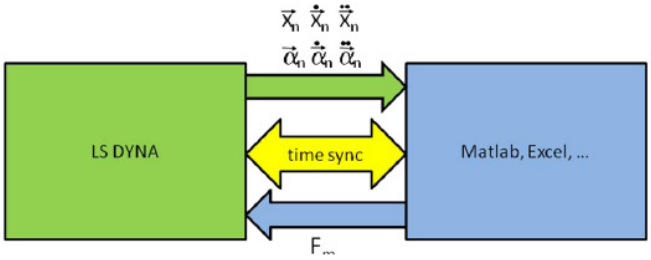

Figure 2. Coupling Exchange parameters

Modeling

After having defined how to implement muscle activity into the numeric human body model the method has been investigated. This first two modeling steps had two main objectives. The first objective was to validate if the coupling approach (Coupling between Matlab/Simulink and Explicit FE solver) could be used for this field of application. The second objective was to find a modeling technique which allows a fast adjustment of the controller when using another Finite Element model. First simulations to validate the coupling have been carried out on basis of a simple model equivalent of the lower extremity. Foot, shank and thigh have been modeled as rigid shell elements connected via revolute joints. Muscles have been included using controlled beam elements. Origin and insertion of the muscle elements was not anatomically correct.

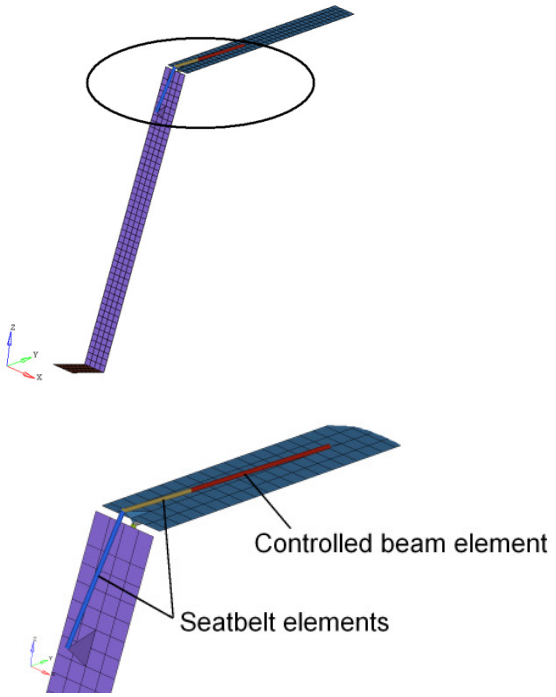

Figure 3. Leg model substitute, detail muscle modeling with seatbelt elements and controlled beam element

Simulations showed that a muscle modeling approach with seatbelt and controlled beam

elements works sufficiently. For further controller development controlled beam elements connecting directly the two body parts would also be adequate. Modeling approaches using seatbelt, slipring and controlled beam elements could be used in a later project phase. Further simulations showed that the use of the coupling between Matlab/Simulink and the explicit FE solver is very sensitive in terms of the Matlab/Simulink release. Due the fact that this coupling was one essential part for the further work we have decided to simplify coupling process. Matlab/Simulink was substituted by a C++ code. The control algorithms have therefore been modeled in C++ which offers two chances. The first one is the desired independence of software releases and the second advantage is the simplification concerning automation (for initializing and parameter calculations, loops can be used).

The next model of higher complexity consisted of parts of the H3 Dummy model and the BIORID II model. Similar to the first model, joints have been modeled as kinematic joints with one DOF. The extremities as well as the spine were modeled as rigid bodies.

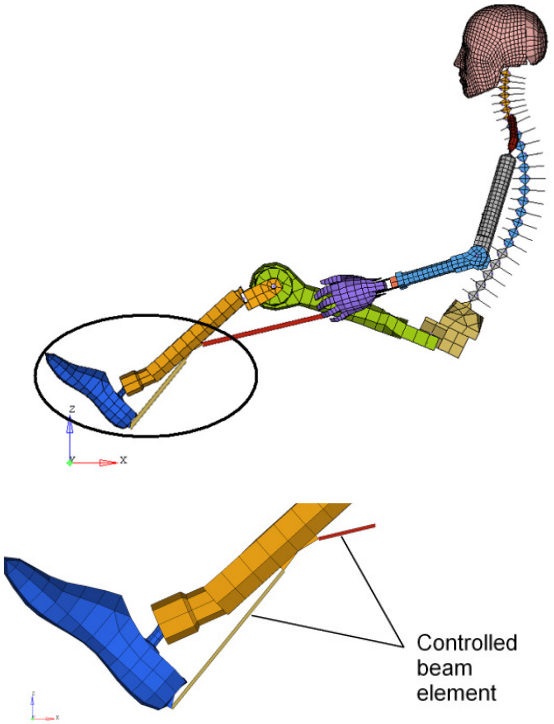

Figure 4. Model consisting of BIORID II and H3 dummy parts, detail muscle implementation

The model was also equipped with beam muscle elements which could be directly controlled. Again the focus of this modeling step was on control of the lower extremity of the model. Hence the hip, the spine as well as the head and the upper extremities have been fixed. The aims of this step were to work on a model with more realistic geometry, to find a muscle modeling approach which could also be used for the upper parts of the human body and to find a suitable modeling approach which allows also a change of the FE model without having too much adaption effort. Figure 4 shows the model. The most promising modeling approach was to directly use nodes of the FE model for muscle origin and insertion. The muscle element directly connects the shank with the thigh. Results of the first sled tests showed that the movements of occupants' lower extremities are negligible. Further simulations therefore focused on the kinematics of occupants upper body parts. Figure 5 shows the model response to a 50 ms 4 g square pulse, applied at time zero. The aim of this investigation was to check if the model is able to return to initial position after being exposed to a single perturbation in x direction. Gravity has not been included.

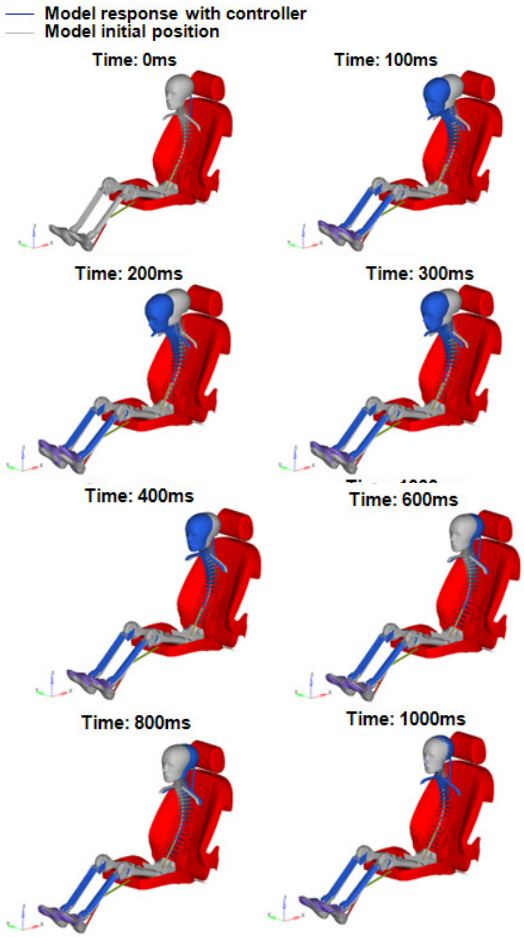

Figure 5. Model response to a 50 ms 4 g square pulse

After 1000 ms the models reaches its initial position.

THUMS model and necessary model simplifications

As already mentioned the THUMS model should serve as basis for research. THUMS is an advanced simulation model that has been developed to estimate injury mechanisms and injuries in traffic accident situations. It is a FE model of the mid-size adult male occupant. It consists of all deformable human body parts with anatomical geometry and biomechanical properties [8], [9]. While the first versions of the THUMS model were initially developed for the explicit finite element code PAM-CRASH (ESI Group), it is now solely developed for the software LS-DYNA (LSTC). The THUMS version of 2002 had more than 80.000 total elements [8]. The latest version of THUMS which is called THUMS4 has more than 1.7 million elements. According to [10] the model offers Toyotas' accident researchers more than 14 times more information than the previous THUMS version. Obviously one of the disadvantages of a finite element model is the high calculation time compared to a multi-body model.

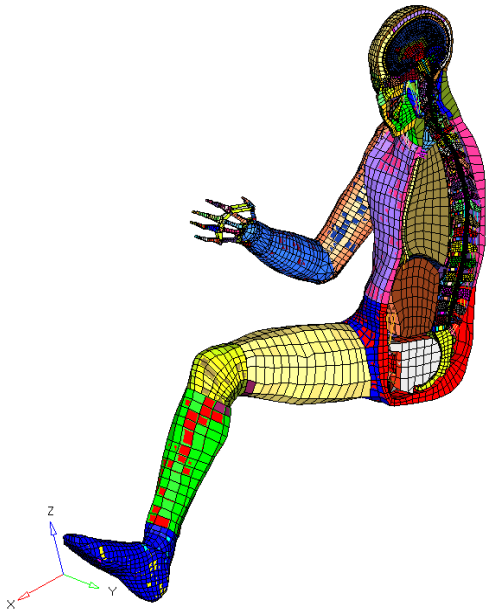

Figure 6. Section cut of THUMS

The development of a controller strategy demands a high number of iterations and this is why the use of the original THUMS would cause calculation time and costs, which is not satisfying in practical application. Therefore, the original THUMS had to be modified. The bones of the model have been extracted. After extraction, the bones have been set rigid and additional masses have been added to the bones to fit the masses and inertias of the new model to the original THUMS. In case of the original THUMS, joints are modelled via contacts. For the described bone model the joints have been modelled as kinematic joints. All in all 12 joints have been defined. Two for the left and right ankle, two for the left and right knees, two for the left and right hip, one for lumbar vertebrae, one for the cervical vertebrae, two for left and right shoulder, two for left and right elbows, see Figure 7. For all joints except the shoulder and hip joints muscles have been included. Due to the fact, that the models rotational and translational DOF's have been locked in pelvis region and the kinematics of upper region has been in focus of interest, muscles have only been defined for the two vertebrae joints. The muscle origins and insertions have been adjusted to joint locations and are therefore not anatomically correct. In contrast to real muscles which can only contract, the muscle elements can contract as well as elongate to control the movement of upper body region.

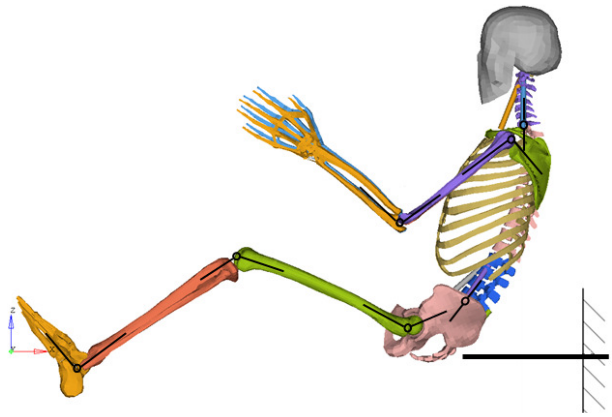

Figure 7. Extracted bone model for controller development

Figure 8 shows the sled acceleration characteristics for one volunteer in 3 different trials, which is needed to reproduce the occupants sled test kinematics. As it can be seen, the characteristics is similar for the second and third trial, the first trial shows a small offset of approximately 50 ms. For an implementation of the acceleration pulse into the simulation a mean acceleration pulse has been created. For the simulation the acceleration up to about 700 ms was used.

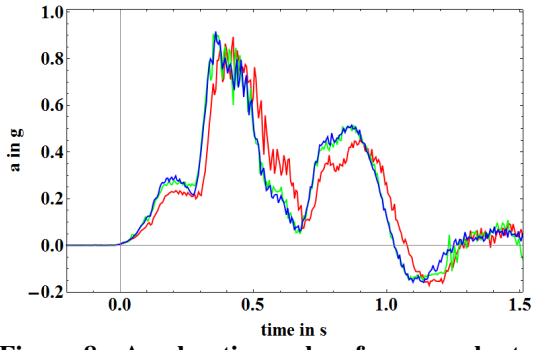

Figure 8. Acceleration pulses for one volunteer (3 trials: red=first, green= second and blue= third trial)

RESULTS

Figure 9 shows the first simulation results using the simplified THUMS model and the sled test acceleration pulse. Blue is volunteers' lumbar angle during the sled test. Red is the calculated lumbar angle during simulations. As it can be seen the angles show a good accordance up to 500 ms. At this point in time one can see that the acceleration depicted in green is already decreasing. Further work will concentrate on the adjustment of the controller in order to be able to simulate volunteers kinematics up to about 1000 ms.

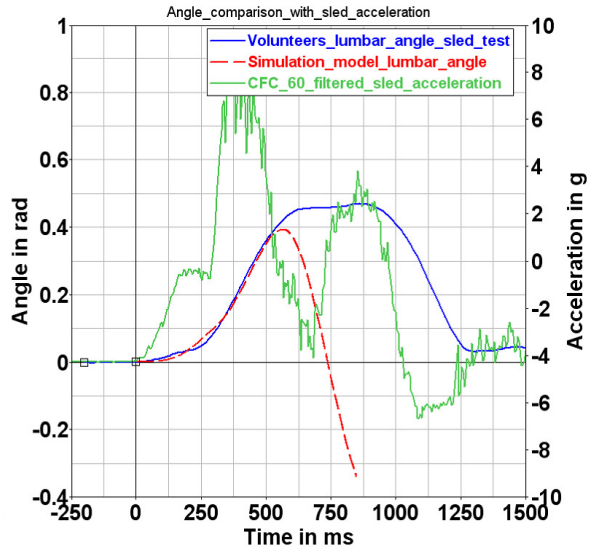

Figure 9. Sled test acceleration and volunteer lumbar angle in during sled test and simulation

DISCUSSION AND CONCLUSION

The current paper presents the aim and the first modeling approaches of a research project of a large consortium called OM4IS. This project focuses on the modeling of kinematic reactive behavior of an occupant during pre crash phase especially for two defined maneuvers. A frontal emergency braking and a single lane change maneuver. First simulations started with a simple substitute of the lower extremity. Muscle modeling approach has been tested using a model consisting of parts of BIORID II and H3 dummy model. For current controller development a FE human body model developed by Toyota Central R&D Lab serves as a basis. The reasons for choosing a FEM model instead of a MBS model are that the level of detail of FE models compared to MBS models is very high and using a FE model also for pre crash phase reduces the number of used models and may lead to a simplification of the development process. On the other hand the use of such a model especially in pre crash leads to two problems. The first one is that the use of a FE model instead of a MBS model increases the calculation time and the second is the numerical stability during the long pre crash phase (up to 1.5 s) compared to the collision phase. In order to reduce the calculation time and to have a stable numeric model for controller development the FE human body model has been modified in that way that it is similar to a MBS.

For the implementation of human muscle activity, actively controlled beam elements have been included. The beam elements are controlled using a coupling between Matlab/Simulink respectively a C++ routine and the explicit FE controller. This modeling approach splits the controller with its intelligence and the model information. It offers the chance to change the model without losing or destroying parts of the controller. In order to develop a method which could also be used for other FE models and also for MBS models the controller intelligence has been excluded from the FEM code. As described, the current model has only been used for the simple test data and with focus on the frontal braking maneuver. Future work will concentrate on simulation of full vehicle maneuvers which were carried out in November 2010. The presentation of the results and a more detailed description of the controller concept will be subject of future publications.

ACKNOWLEDGEMENT

The authors would like to acknowledge the financial support of the "COMET K2 - Competence Centres for Excellent Technologies Programme" of the Austrian Federal Ministry for Transport, Innovation and Technology (BMVIT), the Austrian Federal Ministry of Economy, Family and Youth (BMWFJ), the Austrian Research Promotion Agency (FFG), the Province of Styria and the Styrian Business Promotion Agency (SFG).
We would furthermore like to express our thanks to our supporting industrial and scientific project partners, by names in alphabetical order: Bundesanstalt für Straßenwesen-BASt (DI Andre Eggers), Robert Bosch GmbH (Dr.-Ing. Gian Antonio D'Addetta), DYNAmore GmbH (Dr.-Ing. Dirk Fressmann), Daimler AG (DI Christian Mayer), BMW Group (Dr. Katja von Merten; DI Philipp Wernicke), TRW Automotive (DI(FH). Thomas Herpich; DI Simon Kramer), Toyoda Gosei Europe (Dr.-Ing. Jörg Hoffmann; DI Michael Freisinger), Partnership for Dummy Technology and Biomechanics (Dr. Norbert Praxl); Graz University of Technology, Vehicle Safety Institute (DI Dr.techn. Wolfgang Sinz), Ludwig-Maximilians-Universität Munich (Dr.-Ing Steffen Peldschus).

REFERENCES

[1] MADYMO (2004). MADYMO Theory Manual Version 6.2.1 TNO Road Vehicles Institute, Delft, The Netherlands.

[2] Bathe, K. J: "Finite-Elemente-Methoden." Springer, Berlin; Auflage: 2, 2007

[3] Steinke, P: "Finite-Elemente-Methode." Rechnergestützte Einführung. Springer-Verlag GmbH & Co. KG, 2.Auflage ,2007

[4] Kirschbichler. et al. 2011. "Detailed Analysis of 3D Occupant Kinematics And Muscle Activity During The Pre-Crash Phase as Basis For Human Modeling Based On Sled Test .".Manuscript to be submitted to the 22nd International Conference on the Enhanced Safety of Automobiles Conference, June13-16. Washington, USA

[5] Huxley, A. F. 1957. "Muscle structure and theories of contraction." Prog. Biophy. Biophy. Chem. 7, 255-318.

[6] Hill AV. 1938. "The heat of shortening and the dynamic constants of muscle." Proc. R. Soc. Lond.
B. 126:136–195.

[7] Cresnik, R. et al. 2009. "Dynamic Simulation of Mechatronic Systems." 7th European LS-Dyna Conference, Graz, Austria

[8] Iwamoto, M. et al. 2002. "Development of a Finite Element Model of the Total Human Model for Safety (THUMS) and Application to Injury Reconstruction." International IRCOBI Conference on the Biomechanics of Impact, September 18-20. Munich, Germany

[9] Article published on 08-02-2010. " Total Human Model for Safety (THUMS)." URL-http://www.toyota.com/esq/articles/2010/THUMS.html, Accessed on 10-12-2010

[10] Article published on June 9 2010. "THUMS 4 -Toyota optimiert seine virtuellen Crashtest-Dummys." URL-http://www.unfallzeitung.de /zeitung/thums-4-toyota-optimiert-seine-virtuellen-crashtest-dummys, Accessed on 15-01-2011